Distinct element modelling of pipe–soil interaction for offshore pipelines on granular soils

Giulia Macaro

Exeter College
Department of Engineering Science
University of Oxford

A thesis submitted for the degree of
Doctor of Philosophy

Hilary Term 2015

Abstract

Distinct element modelling of pipe–soil interaction for offshore pipelines on granular soils
by Giulia Macaro — Exeter College, University of Oxford
Hilary Term 2015

Offshore on-bottom pipelines are subjected to cycles of thermal and pressure-induced axial expansion, which can cause them to buckle laterally. For an elegant and cost-effective solution, lateral buckling is allowed in a controlled manner. Of the various design parameters, the soil resistance has the greatest associated uncertainty.

Previous studies of lateral pipe–soil interaction have used laboratory model tests and continuum-based numerical methods. However, they are economically and computationally expensive, and have mostly been restricted to pipes on undrained clay. To overcome this limitation, this thesis introduces the distinct element method (DEM) as a novel numerical tool for the study of lateral pipe–soil interaction for partially embedded offshore pipelines on sandy seabeds.

The DEM directly models the particulate nature of sandy soils, allowing large displacements of discrete bodies and providing insights into the mechanics of the soil at a particle level. Pipe–soil interaction is studied by DEM analyses through four separate research stages: (i) mechanical characterisation of the soil, (ii) specimen preparation and pipeline implementation, (iii) small displacement pipe loading tests and (iv) large displacement pipe loading tests.

The soil is modelled as an assembly of spherical particles exchanging contact forces, energy and momentum when they interact. At the microscopic scale, a novel moment–relative rotation contact law is introduced to account for the irregular shape of real sand grains. At a macroscopic scale, the mechanical behaviour of the sand is calibrated using experimental triaxial test data.

Additional work includes the numerical preparation of a soil assembly and the implementation of a pipeline object in the open-source DEM code Yade. A novel specimen preparation technique is developed to assemble a homogeneous sample at a desired relative density. The pipeline is implemented as a cylindrical body with a continuously curved surface and a specific mass.

Small displacement loading tests are performed, with a segment of the pipeline interacting with a 3D prismatic soil domain, replicating plane strain conditions. The influence of particle size, domain thickness, loading velocity and damping are investigated. The findings provide valuable recommendations for performing DEM simulations of this problem, balancing numerical accuracy and computational effort.

Large displacement loading tests are performed to validate the DEM approach and to obtain detailed insights into the nature of the pipe–soil interaction. Monotonic vertical and lateral loading simulations are quantitatively compared with laboratory results. To replicate realistic loading conditions of the pipeline on the seabed, cyclic large displacement tests are also performed. Both the monotonic and the cyclic tests show a good level of agreement with experimental results obtained in previous research. Moreover, the numerical analyses provide insights into the evolution of particle motion and the failure mechanism within the soil.

Acknowledgments

There are a number of people I want to thank for their support and encouragement throughout my doctoral studies.

I would like to thank my supervisors, Stefano Utili and Chris M. Martin, for their professional guidance during the research and writing-up process. Their encouragement and constant interest in my work motivated me to carry out this research and provided me with invaluable experience for pursuing my future career. Stefano conceived the overall programme of research. I am indebted to him for introducing me to the fascinating topic of granular materials, for pushing me beyond my limits, and his useful suggestions throughout. Chris has taught me how to tackle complicated problems into manageable ones. I am sincerely grateful to him for his invaluable expertise and practical advices on pipelines and numerical modelling.

I am also grateful to my examiners, Helen Cheng and Byron W. Byrne, for thorough review and constructive comments that contributed to the improvement of this thesis. I am very grateful to the Engineering and Physical Sciences Research Council (EPSRC) and BP for the financial support. I would also like to express my gratitude to the Engineering Department and Exeter College for enabling me to present my work at the International Symposium on Geomechanics from Micro to Macro.

I would like to thank my colleagues in the Civil Engineering Group. Particularly, I am indebted to Dr Richard Sandford for sharing the experimental data on pipe-soil interaction, which was necessary for validating the DEM model proposed in this thesis. I would also like to thank Dr Chia Weng Boon for his support during the implementation of the pipeline object. I am grateful to all the users and developers of DEM Yade code for invaluable discussions on modelling of granular materials. In particular, I would like to acknowledge Dr Vaclav Šmilauer and Dr Bruno Chareyre for answering the many questions I had while learning to use Yade.

Many of the simulations reported in this thesis were run on the high performance computer managed by the Advanced Research Computing facility at the University of Oxford. I would also like to acknowledge the help and patience of their support staff, in particular Dr Mihai Duta.

I am grateful to the friends and colleagues of Jenkin Room 11 for making the time spent in the office much more enjoyable. Many thanks to the unofficial *engineering music appreciation society*, the tunes shared and the gigs attended have been the ideal soundtrack to this research.

Thank you to my friends, for their understanding and sustained friendship. No matter if for a quick chat or a long phone call, bringing a scary gift, wandering around known places or going on memorable trips to new ones, for a dance class or a fun run. Thanks for being there for me unconditionally, especially when most needed.

Finally, I would like to thank my parents and brother for their patience and support.

Contents

Notation

Symbol used in this thesis, with the exception of those used only once

Roman Symbols

C_n	Normal viscous damping constant	kg/s
C_s	Shear viscous damping constant	kg/s
D	Pipe diameter	m
D_{50}	Median grain size of sand	m
q	Deviatoric stress	$\mathrm{N/m^2}$
E	Particle Young's modulus	$\mathrm{N/m^2}$
E^*	Equivalent Young's modulus of contacting particles	$\mathrm{N/m^2}$
E_P	Pipe Young's modulus	$\mathrm{N/m^2}$
$\mathbf{F}_c$	Resultant contact force vector	N
$\mathbf{F}_d$	Damping contact force vector	N
$\mathbf{F}_n$	Normal contact force vector	N
$\mathbf{F}_s$	Shear contact force vector	N
$\mathbf{F}_{max}$	Maximum shear contact force vector	N
$\mathbf{F}_{n,el}$	Elastic component of normal contact force vector	N
$\mathbf{F}_{n,v}$	Damping component of normal contact force vector	N
$\mathbf{F}_{s,el}$	Elastic component of shear contact force vector	N
$\mathbf{F}_{s,v}$	Damping component of shear contact force vector	N
$\mathbf{g}$	Gravity acceleration vector	$\mathrm{m/s^2}$
G	Particle shear modulus	$\mathrm{N/m^2}$
G^*	Equivalent shear modulus of contacting particles	$\mathrm{N/m^2}$
H	Horizontal pipe–soil load	N

$\mathbf{I}$	Moment of inertia tensor	kg m^2
I	Inertial number	
I_{uf}	Unbalanced force ratio	
K_n	Normal secant contact stiffness	N/m
k_n	Normal tangential contact stiffness	N/m
k_p	Vertical plastic stiffness	N/m^2
k_r	Rolling contact stiffness	Nn
k_s	Shear contact stiffness	N/m
$\mathbf{L}$	Contact torque vector	Nm
L	Pipe length	m
$\mathbf{M}$	Rolling moment	Nm
$\mathbf{M}_{el}$	Elastic component of the rolling moment	Nm
m	Particle mass	kg
m^*	Equivalent mass of contacting particles	kg
$\widehat{\mathbf{n}}$	Unit normal vector	
n	Specimen porosity	
N_c	Number of contacts	
N_p	Number of particles	
$\widehat{\mathbf{p}}$	Unit vector of pipe axis	
P	Normal elastic force of contacting bodies	N
p	Confining pressure	N/m^2
$\mathbf{\Delta q}$	Particle rotation quaternion	
$\mathbf{q}$	Particle orientation quaternion	
R	Overloading ratio of pipe (Chapter 7 only)	
R	Particle radius	m
R^*	Equivalent radius of contacting particles	m
R_P	Pipe radius	m
Δt	Time step increment	s
Δt_{crit}	Critical time increment	s

$\widehat{\mathbf{t}}$	Unit tangential vector	
$\mathbf{T}_c$	Contact torque vector	Nm
T	Shear force of contacting bodies	N
t	Time	s
ΔU_s	Incremental shear displacement	m
$\dot{\mathbf{U}}_n$	Relative normal velocity	m
$\dot{\mathbf{U}}_s$	Relative shear velocity	m
u	Horizontal pipe displacement	m
U_c	Uniformity coefficient	
U_n	Overlapping depth	m
U_s	Shear displacement	m
V	Vertical pipe–soil load (positive for penetration)	N
v	Pipe loading rate	m/s
V_{max}	Maximum vertical pipe–soil load during the previous loading event	N
w	Vertical pipe displacement (positive for penetration)	m
$\ddot{\mathbf{x}}$	Particle linear acceleration vector	$\mathrm{m/s^2}$
$\dot{\mathbf{x}}$	Particle linear velocity vector	m/s
$\mathbf{x}$	Particle centre position vector	m
$\mathbf{x}_C$	Contact point position vector	m
$\mathbf{x}_P$	Pipe centre position vector	m
Z	Specimen height	m
Z_m	Mechanical coordination number	

Greek Symbols

α	Non-viscous damping coefficient	
β_r	Rolling stiffness coefficient	
δ	Pipe–soil interface angle of friction	$^\circ$
$\dot{\varepsilon}$	Strain rate	$\mathrm{s^{-1}}$
ϵ	Percentage error	

ϕ_μ	Angle of interparticle friction	$^\circ$
γ'	Soil self weight	$\mathrm{N/m}^3$
η	Plastic moment coefficient	
κ	Stiffness number	
μ	Coefficient of interparticle friction	
ν	Particle Poisson's ratio	
ν_P	Pipe Poisson's ratio	
$\dot{\boldsymbol{\omega}}$	Angular acceleration vector	$\mathrm{rad/s}^2$
$\boldsymbol{\omega}$	Angular velocity vector	rad/s
ρ	Particle density	$\mathrm{kg/m}^3$
σ	Standard deviation	
$\sigma_1, \sigma_2, \sigma_3$	Principal stresses, $\sigma_1 > \sigma_2 > \sigma_3$	$\mathrm{N/m}^2$
ε_1	Vertical strain	
ε_2, ε_3	Lateral strain	
ε_a	Axial strain	
ε_v	Volumetric strain	
$\boldsymbol{\theta}$	Relative rotation vector	rad
$\boldsymbol{\theta}_r$	Rolling component of relative rotation vector	rad
$\boldsymbol{\theta}_t$	Twisting component of relative rotation vector	rad
ζ	Viscous damping ratio	
ζ_n	Normal viscous damping ratio	
ζ_s	Shear viscous damping ratio	

Superscripts

$\tilde{}$	Local coordinate system
$^\circ$	Current time step
$^\ominus$	Previous mid-step
$^\oplus$	Next mid-step
$^-$	Previous step

$^{+}$ Next step

Acronyms / Abbreviations

ALE Arbitrary Lagrangian-Eulerian

DEM Distinct element method

FELA Finite element limit analysis

FEM Finite element method

HP High pressure pipelines

HPC High performance computer

HT High temperature pipelines

LB Leighton Buzzard

LDFE Large-deformation finite element

MPI Message Passing Interface

OpenMP Open Multi-Processing

PIV Particle image velocimetry

PSD Particle size distribution

RD Relative density

REV Representative elementary volume

Chapter 1

Introduction

1.1 Background

1.1.1 Offshore pipelines

Crude oil is a mixture of gases and petroleum liquids, e.g. hydrocarbons and organic compounds, which are isolated in the refining process. The first lamp burning kerosene was invented in England in 1847, but modern commercial exploitation of oil wells began only in the late 1850s in the United States. Gradually, oil wells began to be drilled in water: in the mid-1890s, off piers in Summerlands (California, USA) and near Baku (Azerbaijan, in the Caspian Sea); in the 1910s from fixed platforms in the lakes of Louisiana and Ohio (USA); and in the 1930s in the shallow waters immediately off the beaches of Texas and Louisiana, at only a wading distance from land.

In order to beat the competition from onshore oil extraction fields in the USA, Kerr-McGee Oil Industries went offshore into the "deep" waters on Block 32, 17 km off the Louisiana coast, in the Gulf of Mexico. Those waters were only 6 m deep, but, for

the first time, an oil extraction well was built out of sight of land. Not long after, in 1954, the first pipeline was laid in the waters of the Gulf of Mexico (Braestrup et al., 2005).

Even before the offshore platform in the Gulf of Mexico, the forerunners of modern offshore pipelines had already been laid during the Second World War on the bed of the English Channel between England and France. The project, named Operation PLUTO (acronym for Pipe Line Under The Ocean), was commissioned in 1942, and aimed to supply fuel to the Allied forces for the invasion of the European continent (Mitchell, 2006; Palmer and King, 2008). The pipe was laid across the Channel in 10 hours by a special floating drum of 9.14 m diameter, called Conundrum. By August 1944, two lines were completed crossing the channel over a distance of 130 km, followed by 17 other lines 50 km long. Although it was certainly a great achievement as it was the first oil pipeline running on the seabed, the value of PLUTO is still disputed, as it appears that only a small part of the required oil was brought to France through it.

Initially, offshore pipelines were laid in shallow water depths, accessible to divers, as many construction operations were carried out with their help. Then, with the constantly increasing oil demand, the oil industry moved far beyond these depths. Randolph and Gourvenec (2011) define "deep waters" as those where the depth is greater than 500 m, and "ultra deep waters" as those reaching 1500 m. In fact, oil and gas developments in water depths of 1000 m are now routine, but they can also reach 2500 m.

Nowadays, the major offshore oil and gas development areas are found in the Gulf of Mexico, the South California coast and the North Sea, where the seabed is mostly made of siliceous sand and clay, and the North West Shelf of Australia, the Middle

Table 1.1: Selected pipeline projects, globally and in the North Sea.

	Start-up year	Length (km)	Max water depth (m)	Notes
Block 32 Gulf of Mexico	1947	~ 30	6	First offshore field worldwide – Pipeline laid in 1954 (Braestrup et al., 2005)
Norpipe Oil North Sea	1975	354	70	First pipeline in the North Sea (Tormodsgard, 2014)
Perdido Gulf of Mexico	2010	172	2450	Deepest pipelines worldwide (Shell, 2009)
Ormen Lange North Sea	2007	120	1100	Deepest pipeline in the North Sea (Tormodsgard, 2014)
Nord Stream Baltic Sea	2011	1224	213	Longest pipeline worldwide (Espoo, 2009)
Langeled North Sea	2006	1166	385	Longest pipeline in the North Sea (Tormodsgard, 2014)
Galsi Mediterranean Sea	-	185	2824	Planned (Edison, 2010)
MEIDP Arabian Sea	-	1300	3383	Under study (Nash and Roberts, 2011)

East, the Indonesian archipelago and the South China Sea, where the seabed is generally composed of calcareous sand. Overall, there are about 10 000 offshore platforms worldwide (Chakrabarti, 2005), 4000 of which are in the US sector of the Gulf of Mexico. Around them, a network of pipelines extends for tens of thousands of kilometres. Exact numbers are difficult to estimate, however, more than 11 000 km of pipelines are expected to be built by 2018 (Beaubouef, 2014). These offshore pipelines carry oil and liquefied natural gas from a field under the sea to shore or to a floating production, storage and offloading unit (export pipelines), or from one place to another (transmission pipelines), forming the "arteries of the oil and gas industry" (Palmer and King, 2008). Representative pipeline projects are summarised in Table 1.1. In the Table, together with the most significant at a worldwide level, particular attention is given to pipelines in the North Sea, since it is the closest field to the United Kingdom. Oil and

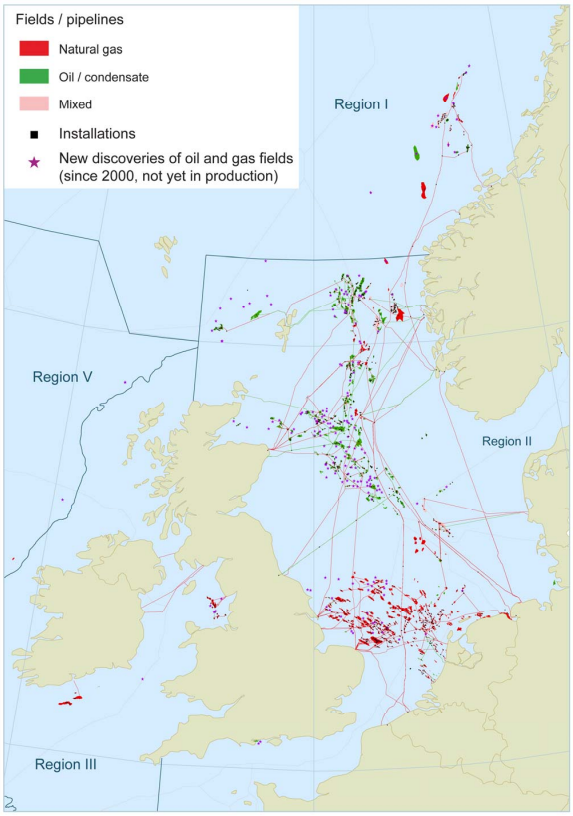

Figure 1.1: Pipelines in the North Sea (Erik and Stokke, 2009).

gas pipelines in the North Sea are also shown in Figure 1.1.

1.1.2 Axial compressive loading in high pressure/high temperature pipelines

During operation, offshore pipelines are generally subject to high compressive forces in the longitudinal direction. These forces are related to the pressure and to the temperature of the fluid being transported. For a generic pipeline of average radius $\overline{r}$ and wall thickness $\bar{t}$, the difference between the internal and the external pressure Δp induces a circumferential (hoop) stress in the pipe wall equals to (tension positive):

$$\sigma_h = \frac{\overline{r}\Delta p}{\bar{t}}. \tag{1.1}$$

This force tends to enlarge the pipe diameter, and as a consequence to contract the pipe longitudinally. If the pipe is fully restrained, contraction is prevented, and a longitudinal tensile stress arises. Under a thin-walled shell idealization the radial stress can be neglected, and the longitudinal stress is derived from the stress–strain relation for a linear elastic isotropic material and a fully restrained pipe:

$$\sigma_{p,w} = \nu\sigma_h = \nu\frac{\overline{r}\Delta p}{\bar{t}} \tag{1.2}$$

where ν is the Poisson's ratio of the wall material. This stress is applied on the cross sectional area of the pipe wall $A_w = 2\pi\overline{r}\bar{t}$. The fluid content produces also a compressive pressure differential $\sigma_{p,c} = \Delta p$ acting over the area occupied $A_c = \pi\overline{r}^2$. The total (compression positive) pressure-induced longitudinal force in the pipe is given from the summation of the two contributions in the wall $\sigma_{p,w}$ and in the fluid content $\sigma_{p,c}$ (Palmer and King, 2008):

$$F_{l,p} = \sigma_{p,c}A_c + \sigma_{p,w}A_w = \pi\overline{r}^2(1-2\nu)\Delta p. \tag{1.3}$$

Given that $\nu < 0.5$ for all wall materials, an increase in pressure produces a compressive longitudinal force in the pipe.

The difference in temperature ΔT between the external temperature and the pipe contents tends to expand the pipe in all directions (both circumferentially and axially). In the longitudinal direction, assuming axial movement is prevented, it produces a compressive force that is:

$$F_{l,T} = \alpha E \Delta T A_w \tag{1.4}$$

where α is the linear thermal expansion coefficient and E the Young's modulus of the wall material.

Combining the last two equations together, the resultant longitudinal force in a

pipe that is fully restrained against axial displacement may be computed (Palmer and King, 2008):

$$F_l = \pi \bar{r}^2 (1 - 2\nu)\Delta p + 2\pi \bar{r} \bar{t} \alpha E \Delta T. \tag{1.5}$$

This represents the compressive longitudinal force produced by an increase in pressure and temperature that causes the pipe to expand.

Subsea pipelines can transport oil and gas from reservoirs with a pressure exceeding 69 MPa and a temperature above 120 °C (Bai, 2001). In this case they are defined high pressure/high temperature pipelines (HP/HT pipelines). These pipelines typically run on seabeds where the water is at an ambient temperature ranging from 1.7 to 7.5 °C (Guo et al., 2005).

Since pipelines are slender structural elements, when subject to a high compressive axial load F_l, they are susceptible to buckling. Buckling occurs in the direction where the pipe is less constrained, hence the horizontal direction.

1.1.3 Lateral buckling of on-bottom pipelines

Typically lateral buckling involves displacements of up to 10 or 20 pipe diameters, which corresponds to an absolute displacement of 2 to 10 m, with the length of the pipe affected by the lateral displacement ranging between 100 and 300 m (Bruton et al., 2007). During its lateral displacement, the pipe scrapes the seabed, remoulding the soil ahead of the buckle crown, and building up a berm of soil at its front (see Figure 1.2). The magnitude of the displacement depends on the pipe stiffness and on the resistance of the soil berms to the pipe movement.

The loading conditions in offshore pipelines, corresponding to the high pressure and high temperature mentioned above, are not constant. During their lifespan, pipelines

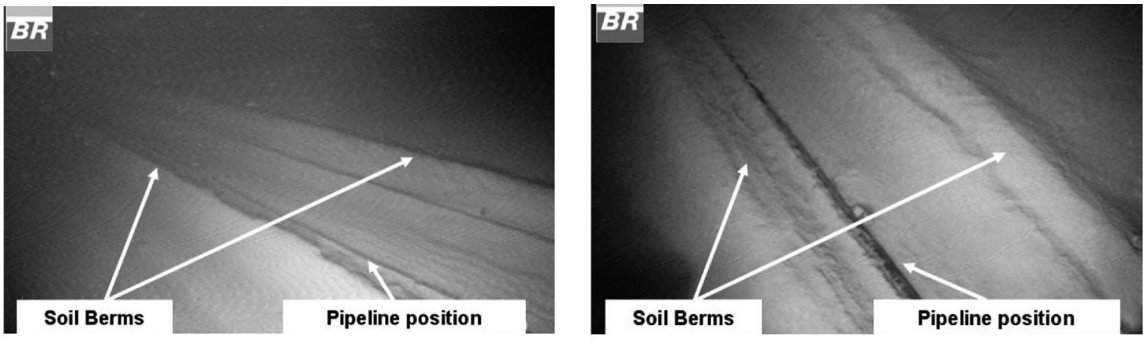

(a) (b)

Figure 1.2: Lateral buckling of on-bottom pipelines (Cardoso and Silveira, 2010).

experience several cycles of start-up and shut-down for general maintenance, and consequently they experience cyclic increasing and decreasing of internal pressure and temperature. Cheuk et al. (2008) report that typically 1000 cycles occur during the life of the pipeline, which is usually of 25 to 30 years. During a shut-down event, the pipe experiences a decrease in load, which makes a laterally buckled pipe move back towards the as-laid position. Lateral movement in the opposite direction will occur again at the following start-up. Hence, cycles of high pressure and high temperature make the pipeline undergo large cyclic lateral displacements. In addition, a hydrotest is carried out before starting the normal operating conditions, to verify the strength of the pipeline and the integrity of the connections. During this preliminary test, the pipeline is filled with seawater at a certain pressure, to check for an eventual pressure drop. Thereafter the pipeline is subject to repeated cycles of high and low pressure and temperature, which give rise to axial expansion and contraction, causing cyclic lateral buckling.

Depending on the magnitude of the lateral displacement, lateral buckling may have serious consequences for the integrity of the pipeline. Excessive lateral displacements may lead to stress localisation at the crown of the buckle and accumulation of fatigue

damage due to the large number of cyclic movements experienced. An incident for failure of the pipeline as a consequence of buckling has been reported by Pasqualino et al. (2001). The pipeline was shallowly buried in soft mud off the coast of Brazil and carried hot oil at a temperature of 95 °C and pressure of 40 MPa. On approaching the coast at Guanabara Bay, it buckled laterally displacing up to 4 m from its original position. The pipe kinked and ruptured, leading to an oil spill of about 1×10^6 litres into the bay. At least two other incidents occurred because of buckling, one in the North Sea and one in West Africa (Bruton and Carr, 2011).

1.2 Motivation

The offshore industry has attempted to prevent lateral buckling by trenching or burying the pipeline, rock-dumping, or by relieving the stress with expansion tools at regular intervals along the pipeline. More recently engineers began to adopt a more efficient solution, that is to "work with rather than against the pipeline" (Bruton et al., 2005), by allowing and controlling the formation of buckles along the pipeline. Furthermore, controlled lateral buckling is currently the only economic solution at high temperature and pressure, or in very deep waters. Specific installation techniques aim at initiating buckles at a controlled spacing in order to minimize the build-up of compressive force in the pipe. These include (i) snake-lay, where the pipe is laid with regular large radius route curves, (ii) sleepers to raise the pipe off the seabed, and (iii) distributed buoyancy at regular intervals.

The response of on-bottom pipelines to thermal- and pressure-induced axial expansion depends on the magnitude of the operating pressure and temperature, the

structural properties of the pipe, the initial lay configuration, and the soil resistance. Among these, assumptions concerning the mobilised soil resistance play a crucial role in the modelling of pipe–soil interaction. Accurate modelling is required for a cost-effective design, allowing the buckling, but preventing excessive plastic deformations and fatigue.

As it is difficult to obtain data from case history data from laterally buckled offshore pipelines in the field, a valid alternative is to gather data from laboratory tests. Typically, a pipeline segment is pushed into the soil specimen and moved laterally to replicate the movement it is subjected to during buckling. It is then moved cyclically back and forth, typically under constant vertical load, to recreate cyclic large lateral displacements occurring during start-up and shut-down cycles. Centrifuge tests (Zhang et al., 2001a; White, 2010) and small-scale $1\,g$ model tests (Sandford, 2012) have been performed to gain a deeper knowledge of the pipeline response on sandy seabeds during large cyclic movements of the pipe. Based on these tests, empirical force–displacement relationships have been developed to describe the soil resistance to lateral movements of the pipeline (Verley and Sotberg, 1994; Zhang et al., 2002a; Tian and Cassidy, 2011). Corresponding centrifuge and laboratory tests have been performed and similar pipe–soil interaction models have been developed for pipelines on clay. However, due to the different response of sandy and clayey soils, tests on clay do not contribute directly to the understanding of the pipe–soil interaction of pipes on sand.

In addition, it is costly to obtain high quality data from physical modelling, especially regarding the failure mechanisms within the soil. The repeatability of physical tests is not always maintained, as it is impracticable to carry them out on identical specimens. The behaviour of sandy soils is extremely dependent on the initial relative

density, which is also highly variable. For these reasons, numerical analyses, mainly using the continuum-based finite element method (FEM), are becoming more attractive for the investigation of pipe–soil interaction (e.g. Wang et al. (2010)). Although these numerical approaches succeed in predicting the pipeline response under certain conditions and can reveal failure mechanisms in the soil, they have mostly been restricted to the analysis of pipes on undrained clay. Moreover, these analyses are greatly expensive due to the necessity for remeshing, to account for the large deformations occurring during lateral buckling. When the finite element method is applied to sandy soils, the computational cost increases due to the adoption of a non-associated flow rule, which can cause numerical instability, loss of mesh objectivity and generally increased computational demand (Sandford, 2012).

In summary, the main limitation to physical and continuum numerical (FEM) modelling of the pipe–soil interaction on sand lies in the cost necessary to replicate the large movements of the pipe: economical cost for the physical modelling, and computational cost for the FEM modelling. Moreover both the approaches lack the possibility of gaining high quality insight into the sand behaviour at a particle level.

1.3 Research purpose

This thesis describes work carried out to overcome the shortcomings of the physical and continuum modelling approaches for the study of lateral pipe–soil interaction on sand. Another approach is proposed herein to model the pipe movements at large amplitude and in a variety of loading conditions.

The aim of this work was to employ the distinct element method (DEM) as a viable

alternative for the study of lateral pipe–soil interaction for offshore pipelines on sandy seabeds. Numerical simulations were carried out using the DEM, taking advantage of the particulate nature of granular soils. The sandy specimen was modelled as an assembly of spherical particles, and the pipeline segment as a cylinder. The DEM was initially developed by Cundall (1971) for the study of rock mechanics, and applied to granular materials by Cundall and Strack (1979). Since then, it has proven to be a powerful tool in the study of granular materials to gain insight into the interactions occurring at the particle level, and to simulate problems where large plastic displacements are involved. Although it has been mainly used to understand soil response by simulations of element tests, the use of the DEM as a tool to replicate boundary value problems is still an open debate.

This thesis will demonstrate that the DEM can be applied to the study of lateral pipe–soil interaction for partially embedded pipelines. This is a complete novelty for the field of pipe–soil interaction of laterally buckled pipelines. The problem is challenging, as the numerical model should be able to replicate the formation of the soil berm of progressively increasing volume as the pipe sweeps back and forth across the seabed during heating and cooling episodes. In addition, the pipe is constantly in contact with the soil surface, which itself is constantly undergoing intense (but highly localised) plastic deformations. Capturing the interaction of the pipeline with the surrounding soil is fundamental for replicating the structural pipeline response accurately.

In this work, the DEM was developed and applied to pipe–soil interaction problems, to achieve the primary objectives as follows:

- to mimic the contact of sand grains. This first objective was achieved by understanding the mechanics of grains in contact, and implementing a fictitious

contact moment able to model irregular-shaped grains using spherical particles;

- to replicate the mechanical behaviour of a sand sample. Numerical triaxial tests on cuboidal particle assemblies were carried out for this purpose, and the micromechanical parameters characterizing the numerical soil were calibrated against available laboratory tests;
- to obtain a numerical specimen with initial conditions similar to those of a physical sand specimen. The particle assembly was created and an initial simulation was performed to reproduce the sample preparation technique usually carried out in the laboratory;
- to obtain a numerical object replicating the pipeline. A new object was implemented in the DEM open-source code specifically for this purpose;
- to develop a numerical approach for studying pipe–soil interaction. This objective was completed by carrying out an extensive test programme of small displacement tests of the pipeline on the numerical specimen. The intention of these tests was to establish which parameter values allowed stable and accurate numerical loading tests of the pipe;
- to simulate pipe–soil interaction by the DEM. The tools developed and the information gathered from all the previous steps of this research were used together. pipe–soil interaction was modelled by performing numerical simulations of a plane strain pipe segment subject to larger lateral displacements, both in monotonic and cyclic conditions, under both vertical displacement control and vertical load control.

1.4 Thesis outline

The thesis is organised into eight chapters. This first chapter has introduced the topic of laterally buckled pipelines, highlighted the need for more research and presented the scope of this work.

Chapter 2 (*Review of pipe–soil interaction models*) presents a review of the most relevant literature on modelling and predicting pipe–soil interaction. Physical and numerical investigations of the pipeline response in existing research are illustrated. A review of various pipe–soil models for predicting the force–displacement relationship is also presented.

Chapter 3 (*Numerical modelling methodology*) introduces the distinct element method (DEM) as a novel tool for addressing the pipe–soil interaction problem. It then describes the features and the performance of the DEM code used for this research. The algorithms more relevant for this work are described in detail.

Chapter 4 (*Calibration of DEM analysis parameters*) presents a procedure used to calibrate the micromechanical properties of the soil samples used in the DEM analyse. The numerical results are discussed at the macro- and micro-level.

Chapter 5 (*DEM model: specimen generation and pipeline implementation*) illustrates two more features of the DEM code employed during this research. A numerical specimen is created to reproduce laboratory sand pluviation techniques. An object to replicate the pipeline is also implemented in the code.

Chapter 6 (*Pipe–soil interaction: small displacement analyses*) reports the results of DEM analyses carried out on the pipe loaded for small displacements. Tests were performed varying each of the numerical and geometrical parameters affecting the

simulations.

Chapter 7 (*Pipe–soil interaction: large displacement analyses*) presents the results of DEM analyses carried out on the pipe loaded to larger displacements, both in monotonic and cyclic conditions. The pipe–soil interaction is investigated through the force–displacement relationships and through graphical post-processing of the particle motions, to investigate the pipe–soil interaction both at the macro- and the micro-scale.

Chapter 8 (*Conclusions*) summarises the main findings of this research and provides some suggestions for future work.

Chapter 2

Review of pipe–soil interaction models

This chapter provides a review of the most relevant literature on the modelling of pipe–soil interaction. Physical and numerical tests on pipelines are presented. Although most attention is given to unburied pipelines on sand, tests on buried pipelines in sand and pipelines on clay are also mentioned, where these are significant for understanding the overall gradual progress in the field. The focus is mainly on the motivations, the soil and the pipe properties, the dimensions of the pipe, the loading conditions and the displacements the pipe is subjected to, and eventually the limitations of these tests.

The findings of the loading tests on the pipe are summarised in a review of the available force–displacement relationships for predicting the lateral movements of on-bottom pipelines. Within these predictive models, both empirical and macro-element models are illustrated.

2.1 Modelling of pipe–soil interaction

2.1.1 Physical modelling

Experimental tests on pipelines are necessary to obtain a good understanding of how an offshore pipeline interacts with the seabed soil, and to derive force–displacement curves on which design guidelines are based. A review of the most significant tests is given here. In general, only tests on sand are described. A few tests on clay are also reported, when these bring an additional value to the general understanding of pipe–soil interaction.

It is relevant to understand the difference between tests conducted on sand or clay, and when in sand, whether it is a siliceous or calcareous sand. Clayey soils are generally deformed under undrained conditions during a buckling event, so the effect of excess pore pressure on pipeline response should be taken into account. The build up of excess pore pressures may result in decay of soil stiffness and a softer response. Instead sandy soils, for most of cases of practical interest, can be assumed to deform under drained conditions. However, sandy soils behave in different ways: siliceous and calcareous sands are different in their origin, components, and behaviour.

Siliceous sands consist of terrigenous marine sediments, which are transported from land after the erosion of rocks. They are found in the North Sea and in the Gulf of Mexico. Their grains are of silicate-based minerals such as quartz and feldspar, and are characterised by a sub-rounded shape (Figure 2.1(a)). Calcareous sands, instead, consist mostly of biogenous pelagic marine sediments, formed from organic particles (typically made of calcium carbonate) that settle through the water. These derive mainly from the insoluble remains of marine organisms such as shells, skeletons and

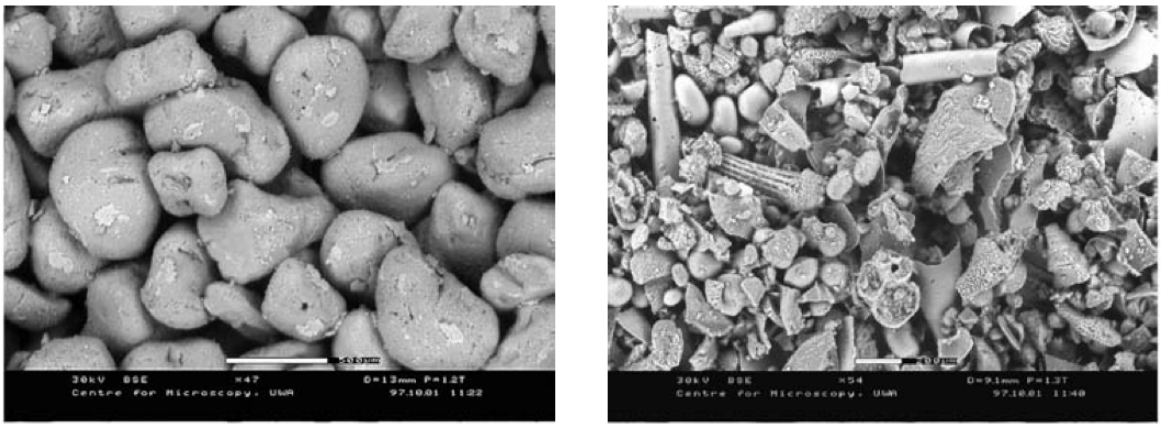

(a) (b)

Figure 2.1: Grains of (a) silica sand and (b) calcareous sand (Randolph and Gourvenec, 2011).

teeth. They are found off the coasts of Australia (North-West Shelf), Brazil (Campos and Santos Basins), and in the Middle East regions. Their particles are angular, rough and crushable, and tend to settle in an open structure with a larger void ratio than in siliceous soils (Figure 2.1(b)). In compression, a densely packed silica sand tends to dilate at all stress levels, while the calcareous sand dilates at low stress levels and contracts at high stress levels because of crushing. When loaded cyclically, the structure, the shape and the crushability of the calcareous sand leads to collapse of the structure, with a overall response more compressible and less dilatant than siliceous sands (White, 2010).

Originally, lateral loading tests on pipelines were conducted to investigate their response to sliding on the seabed surface. These were both small- and large-scale tests (the scale is related to the pipe dimensions), and they were restricted to small lateral displacements of the pipe. The motivation was to understand the pipeline response during hydrodynamic loading, and the aim was essentially to establish a frictional (Coulomb) correlation between the lateral load and the vertical load. These consisted

of plane strain tests on a short segment of the pipeline, loaded monotonically on silica sand.

Lyons (1973) conducted small-scale tests on a pipe submerged in water pulled at a 3:4 ratio of vertical force to horizontal force, for various pipe surface roughnesses and sand gradations. Small tests were performed on a 0.025 m diameter pipe, and larger tests were performed on 0.229 and 0.406 m diameter pipes. Lyons found that a frictional coefficient between the horizontal force and the vertical force was essentially constant, with very little effect of the pipe diameter, pipe roughness and sand size. The friction coefficients provided should be used only when the same loading conditions are applied on the pipe. In fact, as no attempt was made to analyse the pipe response in more general loading conditions, the results are mainly of qualitative significance.

Lambrakos (1985) performed *in-situ* tests in the Gulf of Mexico, with one pipe 3.05 m long to simulate the sliding mechanism, and a pipe 1.83 m long to simulate rolling. Both of them had a diameter of 0.61 m and were moved on the seabed by towing them from a boat on the sea surface. Two locations were chosen for the tests on sand, in water depths of 9 and 18 m. The tests could not be well controlled, and although the results had a large scatter, they were generally in accordance with those found by Lyons.

Brennodden et al. (1986) performed large-scale tests to investigate pipe–soil interaction for various loading histories and loading conditions. The tests were conducted on pipe sections of 0.5 and 1.0 m of diameter, and 1.6 m long, on saturated soils, of four different types: loose silty fine sand, loose and dense medium/coarse sand, soft clay and stiff clay. Different loading histories were given: simple breakout (lateral loading to failure), breakout after force-controlled oscillations, and breakout after displacement-

controlled oscillations. Frictional behaviour was confirmed for the simple breakout tests. However, it was recognised for the first time that cyclic loading affected the lateral resistance, and that it could not be described by a single friction coefficient. In particular, different trends were found depending on the density and the type of sand. In medium/coarse sands the cycling prior to breakout produced an increase of the lateral resistance; this increase was more in the loose than in the dense sand. In loose silty fine sand, instead, the breakout resistance increased after small load-controlled oscillations, but decreased after longer displacement-controlled oscillations.

Other large-scale tests were conducted for various research projects, such as the Pipeline Stability Design project (PIPESTAB, conducted by Wagner et al. (1987)), the American Gas Association project (AGA, by Allen et al. (1989)) and the Danish Hydraulic Institute project (DHI, by Palmer et al. (1988)).

Wagner et al. (1987) improved the database created by Brennodden et al. (1986), and observed that, in general, any loading history that increases the penetration leads to an increasing of the lateral resistance. As the pipe penetrates it mounds soil to the sides, and produces an increase of the lateral earth pressure resistance.

Palmer et al. (1988) recognised the necessity of testing the pipeline under more realistic hydrodynamic conditions. Although no attempt was made to simulate the full loading history (depending on the laying process, seabed profile, tidal currents, hydrostatic test and operating conditions), they simulated a sequence of vertical and lateral cyclic conditions to represent the loading of a pipeline under surface waves during the rapid onset of a storm. Large-scale tests were performed with a 0.295 m diameter and 1 m long pipe, on saturated sand for various force-controlled loading conditions, pipe roughness and particle size. While a small effect was found for the

sand size, the roughness of the pipe affected the pipe–soil interaction. In particular, the rough pipe was reported to sink more under identical conditions, and to mobilise a higher lateral force. An interpretation was given, suggesting that the smooth pipe slips across the surface, deforming the surface only superficially. The rough pipe, instead, engages the sand and creates much deeper deformations, hence mounding more soil in front of itself. The cyclic tests confirmed that the soil resistance is generally higher with respect to the static test. It was also observed that the pipe sinks more in the cyclic tests. Hence the pipe penetration into the sand must influence the lateral resistance. Finally, Palmer et al. (1988) pointed out that a full understanding of lateral resistance would require detailed investigations of soil deformation mechanics in the vicinity of the pipe. Hence a different kind of investigation was suggested, possibly involving X-ray techniques.

Zhang (2001) and Zhang et al. (2001a) conducted an extensive experimental programme of centrifuge tests involving pipe–soil interaction on calcareous sand under various loading conditions. A series of 50 tests with a pipe section of diameter $D = 20$ mm (1 m at prototype scale) were performed. These included vertical loading tests, sideswipe tests (lateral displacement at constant embedment), and probe tests (lateral displacement at constant vertical load). Both monotonic and cyclic loading conditions were explored, and tests were performed for various overloading ratios, i.e. the ratio between the maximum vertical load and the initial vertical load of the current loading event. As with the previous researchers, the aim was still to understand the soil resistance to assess the stability of on-bottom pipelines under the action of environmental forces such as current and waves. Most of the experiments were performed in small displacement tests, with the pipe subject to a small lateral displacement (up to $0.2D$).

Only a few probe tests were performed for medium/large displacements (up to $2.5D$). However, the large amount of data were of high significance. In fact those were used to calibrate a theoretical macro-element model to describe the pipe–soil interaction as a whole (Zhang et al., 1999; Zhang, 2001; Zhang et al., 2002a,b).

It is appropriate to emphasise that all the tests described above were performed to address the stability issue of on-bottom pipelines due to environmental (hydrodynamic) loads. The issue of lateral stability under thermal and pressure-induced loadings leading to buckling was not yet a major concern, yet. Only in 2002 was the Joint Industry Project (JIP) entitled SAFEBUCK created to investigate pipe–soil interaction during pipeline buckling and walking, and to develop design guidelines in this area (Bruton et al., 2005).

Within the SAFEBUCK project, a set of large displacement lateral pipe–soil interaction tests was performed by Cheuk et al. (2007). The tests were conducted on clay, which behaves differently from sand during rapid loading, and hence they are beyond the immediate interest of this thesis. However, the results still provide interesting qualitative insights. These tests were carried out on a pipe of diameter of $D = 0.283\,\mathrm{m}$, which was subjected to the following loading conditions. It was moved vertically for a small embedment ($0.081D$), then, while keeping the vertical load constant, displaced laterally for up to $7.5D$, moved laterally back and forth 10 times, and finally moved outward to a displacement of $10D$. The displacement path and the lateral load–displacement curve are illustrated in Figure 2.2. The tests allowed the identification of four main stages. At the beginning of the lateral movement (breakout), the load–displacement response is stiff, due to the increase of the lateral resistance. Then there is a sudden drop due to the separation of the pipe from the soil (suction release). As the

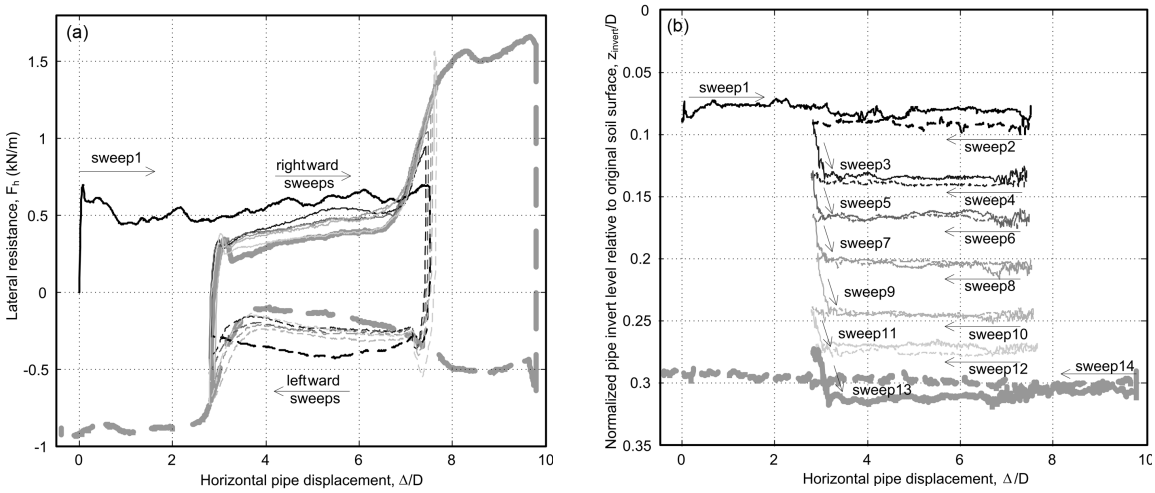

(a) (b)

Figure 2.2: Experimental results from large displacement cyclic tests on clay (Cheuk et al. (2007), with permission of Canadian Science Publishing).

pipe moves laterally, an "active" berm forms in front of it, leading to a gradual increase of the resistance (steady berm growth). In the final cycle, the load–displacement curve becomes steeper and then levels off, as the pipe collects the material of the "dormant" berm left from the previous cycles and accumulates it into the active berm (dormant berm collection).

As part of the phase of SAFEBUCK project dedicated to sandy soils, White (2010) ran monotonic and cyclic tests of a pipe segment on sandy calcareous soils in a geotechnical centrifuge. The cyclic response was investigated by running up to 50 cycles for each test, with lateral displacement up to 6 times the pipe diameter. As-laid embedment, breakout, residual and cyclic lateral resistance were measured and compared with the current SAFEBUCK guidelines. These tests were of considerable significance as they covered loading conditions and amplitudes of displacement which had not been investigated before on sand. Overall, the results highlighted an under-prediction of soil resistance at breakout, and an over-prediction of the residual lateral resistance after

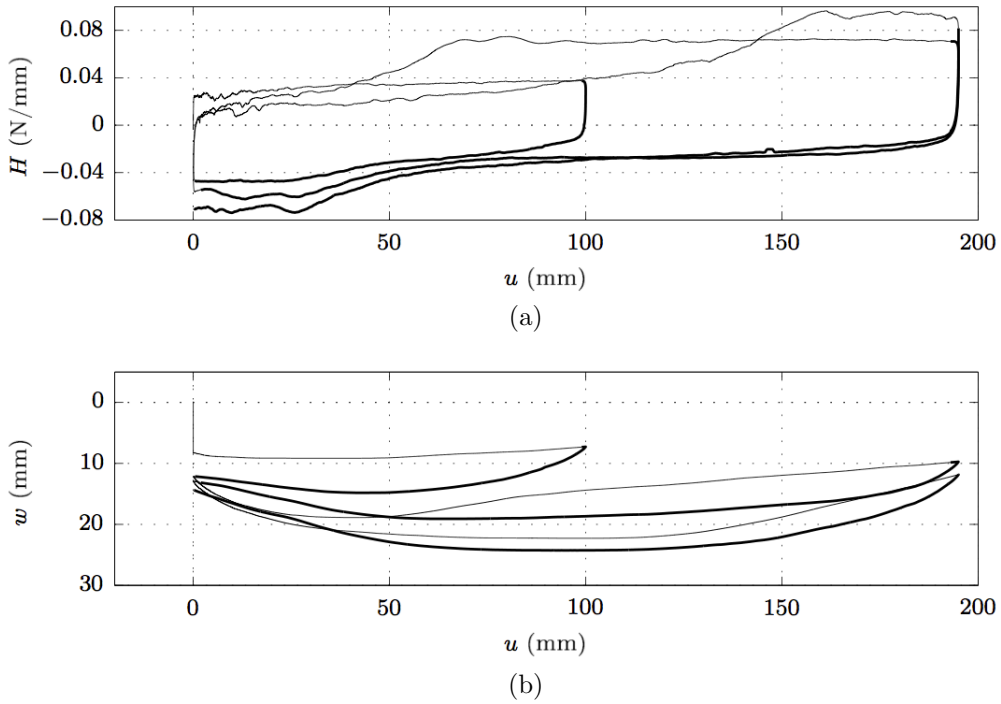

Figure 2.3: Experimental results from large displacement cyclic test on sand (Sandford, 2012).

several cycles due to the increase of the passive resistance offered by the berm. White found a significant difference in the response depending on the soil type, and suggested a likely effect of the pipe roughness. However, he also emphasised the non-applicability of the results to pipelines on soils different from those tested, and also stressed the need for further investigations to understand which soil and pipe–soil interface properties control these differences.

Sandford (2012) conducted a series of lateral loading tests of a model pipe on siliceous sand under a large variety of loading conditions. The tests were conducted at unit gravity with a pipe segment of diameter $D = 0.05\,\mathrm{m}$. Particle image velocimetry (PIV) apparatus was used to provide details of the sand movements, and to investigate the failure mechanisms occurring. The test programme consisted of monotonic vertical loading tests, small displacement swipe and probe tests, large lateral displacement tests at constant vertical displacement, circular loop tests, and cyclic large lateral

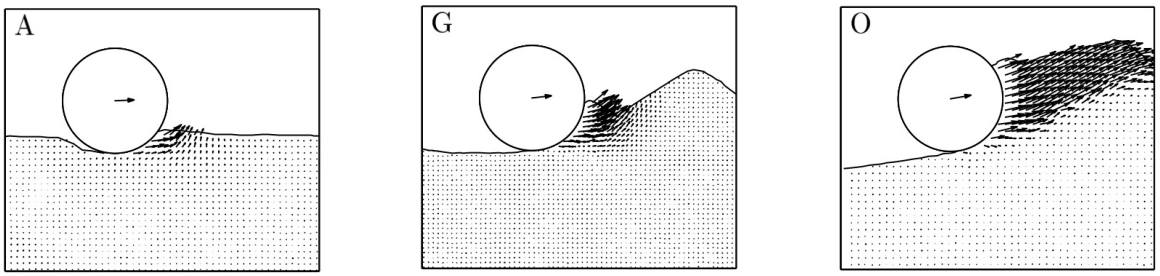

(a) (b) (c)

Figure 2.4: Velocity field at various stages of the large displacement cyclic test on sand (Sandford, 2012). (a) Beginning of lateral displacement, (b) merging of active and dormant berms, and (c) maximum lateral displacement.

displacement tests at constant vertical load. The last test consisted of a stage of monotonic vertical loading, followed by a sequence of lateral displacements at constant vertical load: an initial displacement up to $2D$, back to the pipe initial position, then two cycles of displacements to $4D$. A summary of Sandford's large displacement test is reported in Figure 2.3, and an example of the velocity vector field from the PIV apparatus is in Figure 2.4.

2.1.2 Numerical modelling

Numerical modelling of pipe–soil interaction is becoming more and more attractive. The reasons are mainly in the high cost and time-consuming nature of physical experiments. So far, numerical investigations have been done mostly on cohesive soils (clays). Although pipe–soil interaction on clay is not the objective of this thesis, a review of previous numerical studies on clay is still relevant to appreciate the effort, and to understand the difficulties of the numerical modelling in this field.

Small-strain finite element analyses were performed by Aubeny et al. (2005) and Merifield et al. (2008). Their studies are focused on the as-laid condition and have some limitations for application to lateral buckling. The pipe is assumed "wished in

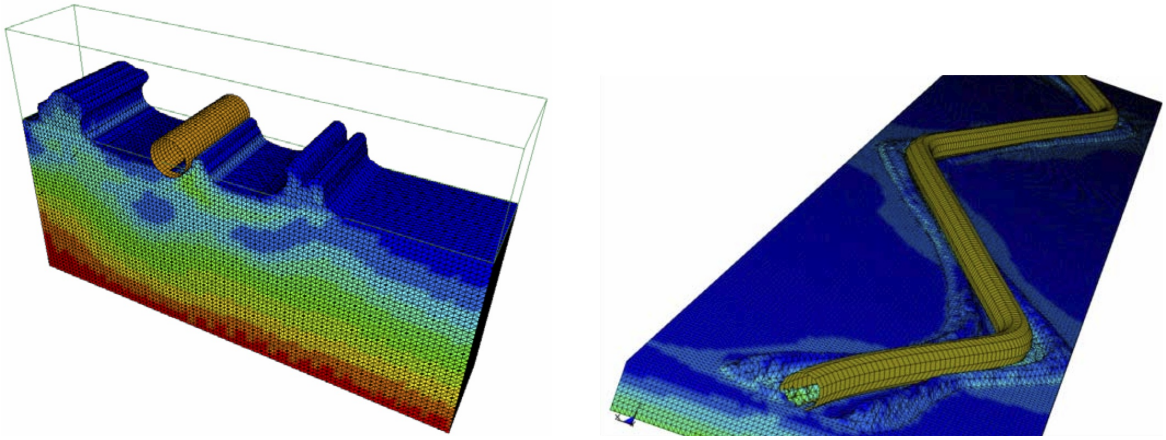

(a) (b)

Figure 2.5: Continuum FE analysis of pipe–soil interaction: (a) 3D plane strain and (b) full 3D model (Konuk and Yu (2007), with permission of ASME).

place", which means that soil heave is neglected, with a consequent underestimation of the vertical penetration resistance. In addition, only infinitesimal pipe movements are analysed, hence the results cannot provide any information about the pipe–soil interaction behaviour at large displacements.

Yu and Konuk (2007) performed large-deformation finite element analyses in 3D, using an arbitrary Lagrangian-Eulerian (ALE) approach. First they performed a test of a rigid pipe segment in a prismatic continuum domain (3D plane strain test) to investigate the influence of the soil and pipe properties on the pipe–soil interaction (Figure 2.5(a)). They then performed a full 3D analysis involving a long but shallow block of soil taken as a continuum, and a pipe with manufactured bends to encourage lateral buckling. The objective was to study both the response of the soil and the flexural and torsional response of the pipe (Figure 2.5(b)).

Large-deformation finite element (LDFE) analyses were performed by Wang et al. (2010), making use of the "remeshing and interpolation technique with small strain" (RITSS). The method was similar to the work of Yu and Konuk (2007), but a simpler soil model was used, and it was applied to 2D simulations only. The merit of the

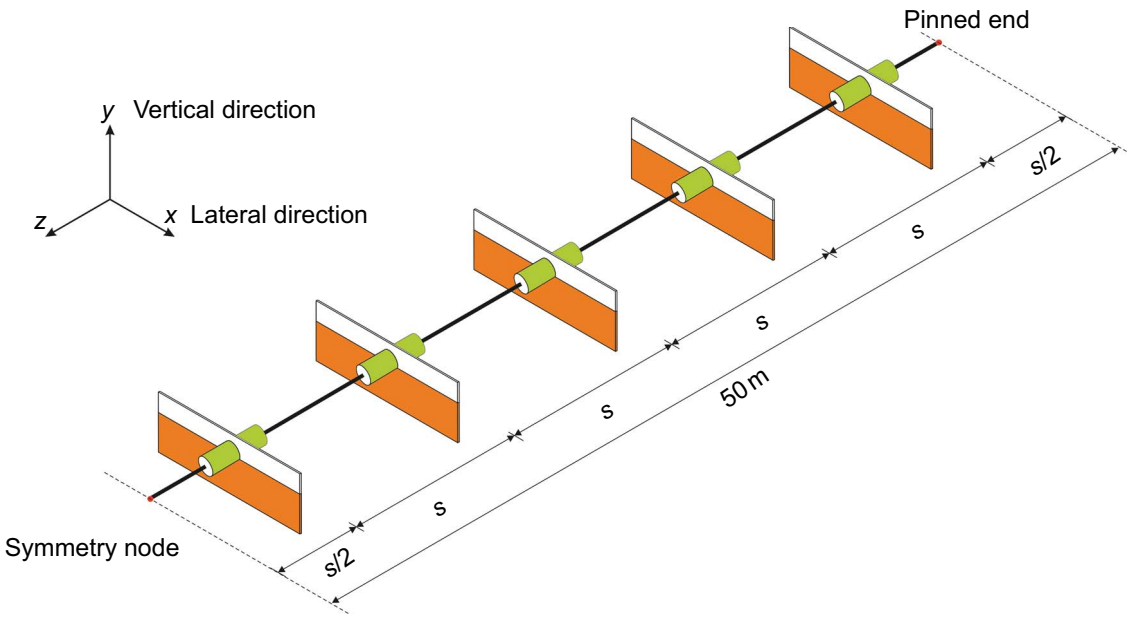

Figure 2.6: Coupled Eulerian-Lagrangian (CEL) FE analysis of lateral pipe–soil interaction (Martin et al. (2013), with permission of ICE Publishing).

analyses was to study large lateral displacements (up to $3D$) and to find a reasonable agreement between the numerical results and corresponding experimental data. The comparison was conducted both qualitatively in terms of soil profile and failure mechanisms, and quantitatively in terms of load–displacement curves.

Martin and White (2012) conducted finite element limit analyses (FELA) using the program OxLim, developed at the University of Oxford, which computes lower- and upper-bound plasticity solutions with automated mesh refinement. The tests were performed in a 2D plane strain domain. The pipe segment was 'wished in place' and subjected to vertical penetration, uplift, and various combinations of vertical and lateral displacement. The results were in terms of the vertical resistance during penetration and uplift, together with combined load failure envelopes for various soil and pipe properties.

Martin et al. (2013) performed Coupled Eulerian-Lagrangian (CEL) finite element

analyses of a pipeline undergoing lateral displacements of up to one pipe diameter. They combined several 2D continuum domains, representing the soil, with a 3D model of the pipeline (Figure 2.6). Although this novel modelling approach is still at a very early stage, it compares well with other numerical methods.

All the numerical studies mentioned so far were conducted on undrained clay. At the time of writing this thesis, only Sandford (2012) has studied lateral pipe–soil interaction numerically on sandy soils. Together with the experimental work described in the previous section, he carried out a programme of numerical tests using both finite element limit analysis (FELA) and displacement finite element analysis (FEA). FELA was used to derive combined load failure envelopes for vertical and lateral loading, but this required the assumption of associated plastic flow. The displacement FEA simulations were necessary to account for a non-associated flow rule in the sand model.

In the context of numerical studies of pipe–soil interaction, it is worth citing a few previous applications of the distinct element method (DEM) to uplift and lateral movements of buried pipelines in sand (to the author's knowledge there is no previous DEM work on partially embedded pipes in sand, which is the topic of this thesis).

Calvetti et al. (2001) and Calvetti et al. (2004) performed DEM tests with the commercial software PFC^{3D} on a buried pipe segment in a prismatic soil domain, to replicate a 3D plane strain test (Figure 2.7(a)). In the DEM, instead of the level of mesh refinement, the key parameters are the number of bodies in the domain and the dimension of the particles representing the soil. Calvetti and co-workers used about 7000 spheres with a median size $D_{50} = 0.02\,\mathrm{m}$. With the pipe diameter D equal to $0.05\,\mathrm{m}$, the ratio D/D_{50} is only 2.5, which is not a realistic value of the real

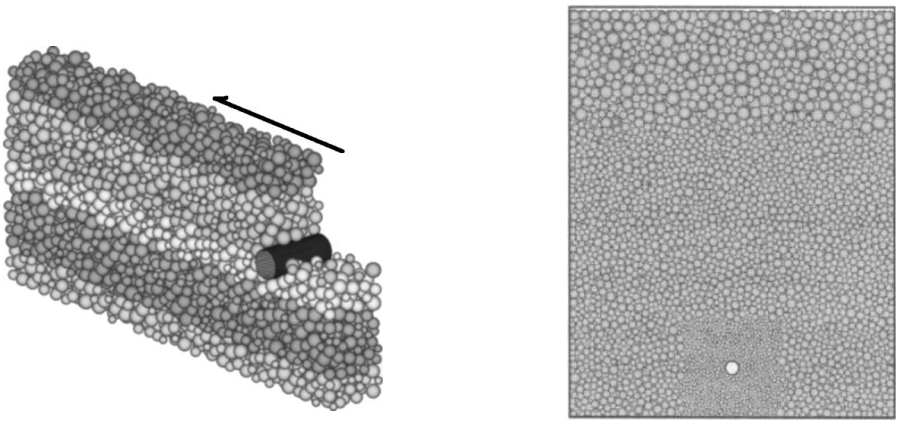

(a) (b)

Figure 2.7: Distinct element analysis of a buried pipeline: (a) from Calvetti et al. (2004) and (b) from Yimsiri and Soga (2006). Figures reproduced with permission of ASCE and SEAGS.

pipe/grain size ratio for these problems. However, they found a good match between the experimental and numerical results, if taken in the form of a dimensionless factor. They did not show the comparison of load–displacement curves, but only a normalised force, conceptually similar to a bearing capacity factor, at four different embedment depths.

Similar tests were performed by Yimsiri and Soga (2006), again using PFC^{3D}. The tests were on a pipeline subjected to lateral and upward movements. The pipeline was buried in medium and dense sand samples, at various embedment ratios. The largest sample consisted of about 180 000 spherical particles. The pipe diameter was 0.12 m, and the particle dimension was varied such that is was smaller in the vicinity of the pipe, and larger far from it (Figure 2.7(b)). Even in this way, the ratio between the pipe diameter and the median grain size D/D_{50} was varying between 4.8 and 1.6. Although this is far for being realistic (the particle size was scaled up by a factor varying from 50 to 75) they stated that preliminary analyses showed only 8 % difference in the force on the pipe when only larger particles were used. In addition, the following inconsistencies

emerge from their paper. Firstly, they described three-dimensional simulations, but they did not specify the thickness of the domain. Secondly, due to the different scaling factors in the same test, it is likely that there was some penetration of smaller particles into the region formed by bigger particles. Thirdly, the pipe roughness was said to have a negligible effect on the force–displacement curve, which is in contrast with experimental observations (Palmer et al., 1988). Finally, no direct comparison with experimental data is shown, but only a comparison against FEM results. However, the DEM results are consistent with the FEM results, both during lateral and upward movement in medium samples. A non-negligible difference was found in dense samples, but no reason was proposed.

It is appropriate to recognise that no further studies were conducted by Calvetti or Yimsiri and their co-workers on pipe–soil interaction through DEM. In their works, they emphasised the advantages of the DEM over FEM to simulate large displacements of the pipe. However, there does not appear to have been any follow-on work to exploit this advantage. For instance, a logical continuation of these studies would have been the application of the DEM to pipe segments in sand under a larger variety of loading conditions, considering both buried and partially embedded pipelines.

2.2 Pipe–soil predictive models

The physical and numerical modelling studies described in the previous sections are generally conducted with the aim of extrapolating the pipe–soil behaviour and developing empirical force–displacement relationships to predict the soil resistance to lateral movements of the pipeline. Although developing a pipe–soil interaction model is bey-

ond the scope of this research, a brief overview of these models is provided here. This will help to contextualise the DEM analyses of pipe–soil interaction described in the later chapters.

Predictive models for lateral pipe–soil interaction have been developed using different theoretical approaches: (i) a single friction factor model, (ii) a two component model based on a frictional and a passive term, and (iii) a plasticity-based macro-element model.

The single component model is based only on a Coulomb friction resistance, and it is extremely conservative, since it underestimates the lateral soil resistances. However, an "equivalent friction factor" can be used to account for embedment and berm size. The two-components model can reproduce with good agreement the lateral soil response during monotonic loading, and it is currently applied in design codes. However, the friction factor models are both developed by empirically fitting experimental test data, and they cannot reliably account for cyclic loading conditions. Hence they are often referred to as empirical models.

The macro-element approach aims at a better understanding of the whole pipe–soil interaction mechanism during monotonic and cyclic loading conditions, but still requires further development to handle large displacements. pipe–soil macro-element models are based on an analogy with the modelling of shallow foundations, in particular infinitely long strip footings. The analogy was recognised for the first time by Small et al. (1971), and adopted more recently by Zhang and Erbrich (2005). However White and Gaudin (2008) highlighted some discrepancies between pipeline geotechnics and conventional foundation engineering. In particular, they observed that, compared with a strip foundation, in a pipeline (i) the geometry is less controlled and less predictable,

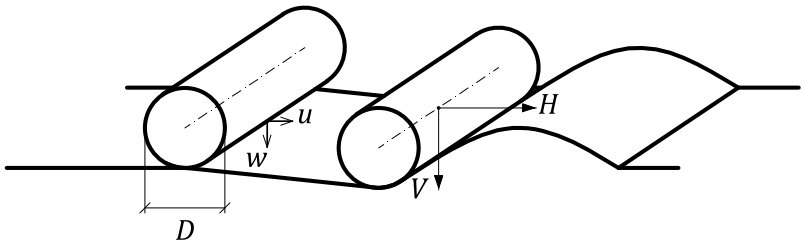

Figure 2.8: Sign convention for loads (V, H) and displacements (w, u).

(ii) the amplitude of the movements is larger, (iii) the surrounding soil conditions can be significantly affected by the operations of lay-out, and (iv) very large plastic soil displacements take place. Hence any pipe–soil interaction model developed in analogy with the modelling of shallow foundations should account for these differences as well.

The sign conventions for the vertical and horizontal loads V and H applied by the pipeline to the soil (per unit length), and the corresponding displacements w and u, are shown in Figure 2.8.

2.2.1 Empirical models

Simple predictive models have been developed by empirically fitting data from large-scale tests, with little theoretical basis. They were primarily proposed to establish the ultimate soil resistance and the final settlement of the pipe, so they do not provide any information about the soil resistance at smaller displacements.

The first models for pipe–soil interaction, formulated in the 1970s and 1980s, assumed frictional behaviour where the lateral resistance of the soil to the pipe movement at breakout is proportional to the submerged vertical force (Lyons, 1973; Brennodden

et al., 1986):

$$H = \mu V. \tag{2.1}$$

Successive models (Wagner et al., 1987) consisted of a frictional term and a passive term superimposed:

$$H = H_f + H_p \tag{2.2}$$

where H_f takes into account the resistance to sliding of the pipe along the seabed surface, and H_p accounts for the restraint offered by the wedge of soil in a passive state lying ahead of the laterally displacing pipe. Various formulations of H_p were provided by Wagner et al. (1987), Verley and Sotberg (1994) and White (2010).

The lateral resistance of the soil for large amplitude monotonic lateral displacements is predicted by calculating the lateral force from Eq. 2.2, assuming that the residual embedment is half of the embedment at the breakout (Verley and Sotberg, 1994). White (2010) compared this formulation with experimental results and observed a general overprediction.

With regard to the cyclic lateral response, there is no theoretical formulation, although White (2010) observed a significant increase of the lateral resistance as the pipe encroaches on the lateral berms. This behaviour is not captured by any of the traditional models described so far, and hence it is not even included in current design codes.

2.2.2 Macro-element plasticity models

The first macro-element models were developed for spudcan footings (Schotman, 1989; Tan, 1990; Martin, 1994) and strip footings (Nova and Montrasio, 1991; Gottardi et al.,

1999). Since then, different models have been suggested for shallowly buried pipes in calcareous sands (Zhang et al., 1999) and clays (Zhang and Erbrich, 2005), and for buried pipes in clays (Di Prisco et al., 2004). A typical macro-element model is described by four components:

(i) a yield surface in the combined loading space V-H defining the allowable loading combinations. The formulation of the yield surface is often taken from experimental sideswipe tests, which consist of a monotonic vertical loading, then a monotonic horizontal loading while the embedment depth is kept constant;

(ii) a hardening law describing the expansion of the yield surface with the vertical plastic displacement increment. This is taken from the derivative of the expression relating the vertical bearing capacity and the embedment;

(iii) an elastic matrix describing the response for load combinations within the yield surface, in general with no cross coupling between the vertical and horizontal directions;

(iv) a flow rule (formulated as a plastic potential) describing the direction of the incremental displacement vector during an elasto-plastic event. Experimental results from sideswipe tests on sand suggest that the plastic potential is very different from the yield surface, i.e. the flow rule is strongly non-associated.

Four force-resultant models with increasing sophistication have been developed in the last decade by researchers from the University of Western Australia, the so-called UWAPIPE models (Tian and Cassidy, 2010). The four components of each model have been developed on the basis of centrifuge loading tests, with their parameters calibrated for calcareous sand. These models are: the elasto-plastic model (Zhang et al., 1999), the bounding surface model (Zhang et al., 2002b), the kinematic hardening model

(Zhang et al., 2002a; Tian and Cassidy, 2010), and the radial hardening model (Tian and Cassidy, 2011).

2.3 Summary

This chapter has provided a review of experimental tests and numerical simulations available in the literature to analyse lateral pipe–soil interaction.

Initially the experimental tests were carried out to investigate the pipe response to environmental (hydrodynamic) loads. Later they were performed to address the stability of pipelines under thermal and pressure-induced loadings leading to buckling. The tests were similar, except that they involved larger lateral displacements and a larger number of loading cycles. Overall, the experimental work has highlighted which geometrical factors and loading conditions play important roles in determining the pipe–soil response. These are:

- The soil type, whether it is clay or sand (either calcareous or siliceous).
- The pipe dimensions and roughness. Experiments were performed with a pipe of diameter varying between 0.025 and 0.050 m in small-scale tests, and between 0.2 and 1 m in large-scale tests. The roughness of the pipe was also varied, although detailed results were not available.
- The loading conditions, either monotonic or cyclic, and force- or displacement-controlled.

On a parallel path, researchers have attempted to investigate lateral pipe–soil interaction through numerical modelling. Using continuum-based approaches, the main issue with numerical modelling of unburied pipelines on sandy soils is the difficulty

of capturing severe plastic deformations in the soil during the large (often cyclic) displacements of the pipe. The distinct element method (DEM) has been tested for the study of pipe–soil interaction, but only for buried pipelines in sand. The researchers praised the capability of the DEM to reproduce the large displacements of the pipe and to capture the micromechanisms within the sand. These features will enable DEM to be employed in the next chapters of this thesis to study pipe–soil interaction problems of partially buried pipes on sand.

Although it is beyond the scope of this thesis, the chapter has included a review of pipe–soil interaction models for predicting the soil resistance to vertical and lateral movements of a pipe segment. Empirically fitted models and macro-element plasticity models were discussed. These were illustrated to show a direct application of the numerical pipe–soil interaction analyses which are the object of this thesis.

Chapter 3

Numerical modelling methodology

This chapter presents the main features of the numerical method used for the simulations performed during this research. Firstly, relevant literature covering the particulate nature of the soil is reported. Secondly, the distinct element method (DEM) is introduced, and evidences are presented for its use as a suitable numerical tool for the study of particulate materials. The main features of the DEM code used for this research are highlighted, with an investigation of its performance on the available computer resources. The last part of the chapter is dedicated to the description of the code, and the algorithms most relevant to this research. Among them, the contact model is presented in detail. Particular attention is also given to the description of a moment–relative rotation contact law, introduced to take into account the irregular shape of sand grains.

3.1 Modelling of granular soils

3.1.1 Soil as a granular material

Soil is often regarded as a continuous medium, in which stress and strain are regarded as uniform over a small volume, and the relative movements and rotations at particle level are not considered. In spite of this, the opening of Lambe and Whitman 's (1969) book "Soil mechanics" makes use of a basic example to clarify the nature of soil: the authors encourage the young student approaching the field of soil mechanics for the first time to observe a handful of beach sand with the naked eye. It is straightforward to note that the sand consists of individual particles. The nature of the beach sand does not differ much from that of the sandy seabeds in deep seas, where the pipelines that are the object of this thesis are located. Both are soils which can be regarded as particulate systems, i.e. "pertaning to a system of particles" (Lambe and Whitman, 1969). They consist of distinct grains, translating and rotating independently from one another, and interacting with each other solely at contact points. Spaces between grains are filled with air and/or water, and these constituents influence the transmission of forces between grains. Hence the soil is also a multiphase system.

Feda (1982) refers to the solid particles of a particulate system as "structural units", for they are individual bodies forming the soil's skeleton, moving as single units and in mutual contact. When the individual units are visible to the naked eye, these are called grains, and the respective particulate materials are called granular media. Even clay is made of particles, although they are not clearly visible without the aid of the microscopy. Soils, in general, are particulate materials. What differentiates clay from sand is only the shape and the size of the grains (Terzaghi (1925), reported in Clayton

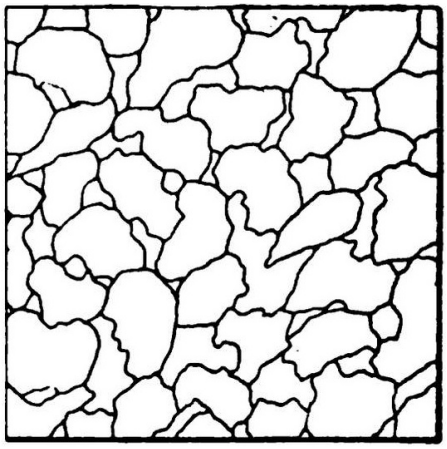

Figure 3.1: Structure of a compacted sand (Terzaghi, 1920).

et al. (2009)).

The particulate nature of soils was also discussed by Terzaghi (1920) while studying the earth pressure on a retaining wall. *"The fundamental assumptions of the traditional earth-pressure theories cannot, in fact, stand even superficial examination. The fundamental error was introduced by Coulomb, who purposely ignored the fact that sand consists of individual grains, and who dealt with the sand as it were a homogeneous mass with certain mechanical properties. Coulomb's idea proved very useful as a working hypothesis for the solution of one special problem of the earth-pressure theory, but it developed into an obstacle against further progress as soon as its hypothetical character came to be forgotten by Coulomb's successors. The way out of the difficulty lies in dropping the old fundamental principles and starting again from the elementary fact that sand consists of individual grains."*. Terzaghi used a primitive but functional apparatus to measure the pressure exerted by the sand against a wall, and pieces of aluminium sheet to observe the structure of the sand and the intergranular movements (Figure 3.1). He recognised that the intensity of the earth pressure depends not only on the elastic properties of the sand, but also on its structure.

Once the particulate nature of soil is recognised, it is easy to accept that the existence of contacts between the grains restricts their movement and controls the strength and the rigidity of the whole granular material. These characteristics then depend on the number, orientation and mechanical characteristics of the contacts, which themselves depend on the nature and strength of the particles. Feda (1982) differentiates the mechanical behaviour of particulate materials from that of continuous media. In particulate materials the behaviour is controlled by relative sliding and rolling of individual particles (intergranular deformation), whereas in continuous media, instead, the deformation is caused by deformation of the structural units (intragranular deformation).

3.1.2 The irregular shape of grains

The particulate nature of soil motivates us to consider firstly the behaviour and the characteristics of the individual grains, then to analyse the relationships among these grains, and finally to observe their response at a macroscopic scale. The particle shape, taken as the "expression of external morphology" (Barrett, 1980), is defined according to the scale of observation (Figure 3.2). Sphericity (also eccentricity or form) refers to the macroscopic scale, describing the the overall shape of a particle and reflecting variations of its proportions. Roundness (or angularity) is a measure of the major surface irregularities, such as corners and edges. Roughness (or smoothness) refers to the smallest scale of surface irregularities related to the particle surface texture. The particle shape influences the mechanical behaviour of a sand, not only the stiffness and strength, but also other state variables and phenomena such as density, dilation and particle rearrangement (Santamarina and Cho, 2004).

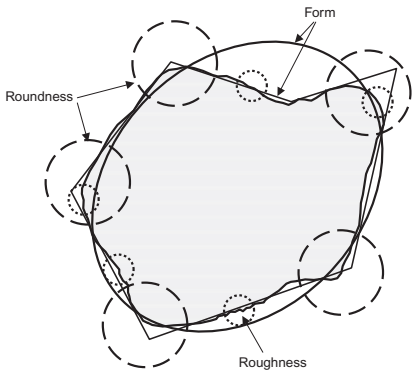

Figure 3.2: Elements of particle shape (Clayton et al. (2009) with permission from ICE Publishing, after Barrett (1980)).

Cavarretta et al. (2010) demonstrated that, while there is a clear relationship between particle surface roughness and inter-particle friction, the material macro-response is only slightly dependent on them. The material response, instead, is much more dependent on the particle shape. Cho et al. (2006) extensively investigated the influence of the particle shape on index properties and macroscopic behaviour of soils. They observed that a decrease of roundness and sphericity (i.e. a decrease regularity of particle shape) increases the extreme void ratios $e_{\max}$ and $e_{\min}$, basically limiting the ability of the particles to rearrange themselves and to form dense packings. It also decreases the stiffness of the material at low strains, increases the resistance to particle rotation and hence the dilation, and increases the friction angle at the critical state. When considering particle shape, convexity should also be taken into account. In fact, with non-convex particles, multiple points of contact can develop between grains, resulting in an increase of strength and stiffness in comparison with convex particles.

Because of these reasons, it is essential to recognise that particle shape is a determining parameter in soil behaviour. Therefore, even before describing in detail the numerical method used for this work, attention should be paid to the shape of the numerical particles employed. It is also appropriate to note that compromises must be

made when aiming at replicating soil behaviour through numerical models. Spherical particles are the simplest numerical representation of sand grains. Other particles geometries include clusters of spheres, which may either touch or overlap. Spheropolygons are defined as the Minskowski sum of a base polygon and a disk, and examples of their application can be found in Pournin et al. (2005). Superquadric particles can take various smooth shapes defined by a generic function, and include ellipsoids (Ng, 2006; Kozicki et al., 2012). The advantage of ellipsoids is that although they are still convex particles, the resistance to rotation is increased by the non-collinearity of the vector connecting the centroids of two contacting particles (branch vector) and the vector defining the contact plane (normal vector). A promising recent development is the use of potential particles, which are defined as a polynomial function constructed from an assembly of planes, forming polyhedrons with slightly rounded corners, edges and faces (Houlsby, 2009; Harkness, 2009). Moving towards even more realistic geometries, the morphology of real particles can be captured using X-ray computed tomography and reproduced numerically using non-uniform rational basis splines (NURBS) (Andrade et al., 2012). The granular element method (GEM) proposed by Andrade could be very appealing for its ability to reproduce the exact shape, sphericity and roundness of the particles. However, it is very limited by its enormous computational cost due to the contact algorithm.

Despite being aware of all these possible numerical representations of sand particles, in this thesis spherical particles were employed. Very long runtimes were expected due to the large number of particles needed to perform simulations with the pipe (Chapter 5). Hence the computational cost could not be increased any further by the use of more realistic particles. A way of taking into account their non-spherical shape

is introduced with the contact model in Section 3.3.2.2.

3.1.3 Numerical methods

Continuum models take into account the stresses acting on the sides of an infinitesimally small cube of soil which is composed of homogeneous material. In reality, the cube of soil in only statistically homogeneous, and it is meaningful to look at the microscopic stress and strain only if these vary little over distances which are of the order of magnitude of the size of the largest particle. In other words, the assumption of continuous soil is only valid when the dimension of the microstructure of the soil is much smaller than that of the the objects of study. Whenever the dimension of interest is of similar order of magnitude to the dimensions of the grains forming the soil itself, a discrete approach is more appropriate. This is the case when studying pipe–soil interaction, where the pipe diameter and the grain size differ only of one to three orders of magnitude.

Assemblies of discrete particles can be modelled numerically by a discrete element method, following the movement of each individual particle forming the medium. The discrete element method attempts to replicate the behaviour of the soil in a way that Lambe and Whitman (1969) believed to be impossible few decades ago, by considering the behaviour at each contact.

Discrete element methods are divided in two groups according to the way in which they treat the mechanical interaction in the normal direction of motion (Cundall and Hart, 1992; Duran, 2000; Zhu et al., 2007; O'Sullivan, 2011b). These are the hard contact approach and the soft contact approach, as shown in Figure 3.3.

In the hard contact simulations there is neither interpenetration between the particles

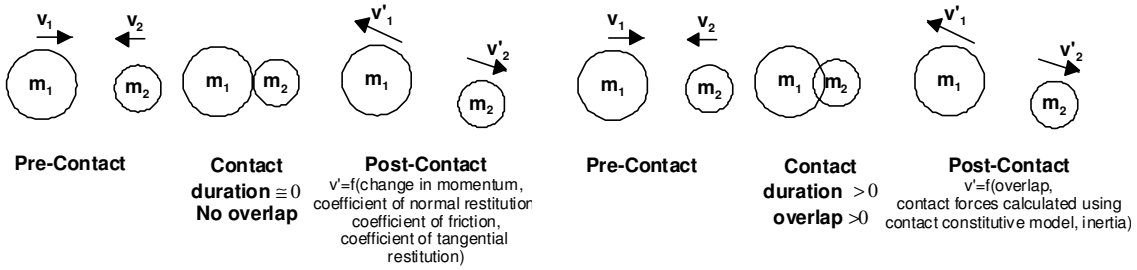

Figure 3.3: Hard contact and soft contact approaches for discrete element modelling (O'Sullivan, 2002).

nor deformation of the particles. The interactions are processed as a sequence of collisions, which are instantaneous. The collisions are solved numerically by imposing conservation of linear and angular momentum, preserving a coefficient of restitution. This approach is the basis of the collisional or event driven methods (for a more detailed description, refer to Brilliantov et al. (1996)). It is appropriate in simulations of molecular dynamics, where there are numerous bodies moving and colliding at high speed. The disadvantage of the hard contact approach is that when it is applied to the study of granular materials, it fails to capture important details of the response for dense packings, where multiple contacts occur simultaneously and the effect of these multiple collisions can no longer be neglected.

In soft contact simulations, instead, there is an attempt to replicate the minute elastic deformations that real grains suffer when they are in contact. In order to account for these deformations, in the numerical method the particles are allowed to overlap slightly at each contact point. The overlapping and the relative positions between each pair of contacting particles are then used to calculate the forces between them, and from the integration of the Newton's second law over a time increment, the new position of each particle is obtained. Unlike hard contact simulations, soft contact

models are intended to handle several particle contacts at the time, which makes them appropriate for the study of dense systems. This is the main reason for choosing the soft contact approach for the analyses described in this thesis.

There are also other particulate numerical methods worth mentioning, potential based molecular dynamics methods. In molecular dynamics (Alder and Wainwright, 1959), the particles representing the molecules are modelled as point-like centres, which interact through interaction potentials.

3.1.4 The distinct element method (DEM)

Before reviewing the main features of the distinct element method, a clarification regarding the terms discrete and distinct element method seems necessary. As pointed out by Cundall and Hart (1992), the term "discrete element method" refers in general to a computer program that (a) allows finite displacements and rotations of discrete bodies, including complete detachment, and (b) recognises new contacts automatically as the calculation progresses. The distinct element method (DEM), developed originally by Cundall and Strack (1979), is a discrete element method based on the soft contact approach and explicit time integration. Another discrete element method is, for example, the discontinuous deformation analysis method (Thomas, 1997; Shi and Goodman, 1985).

The distinct element method, also referred throughout this thesis as DEM, was initially developed by Cundall (1971) for the study of rock mechanics. In his paper, Cundall proposed a computer program (the term DEM was not used yet) for simulating progressive failure of a jointed rock system, emphasizing as a unique feature, that there is no limit to the amount of displacement or rotation of each block. This is a key

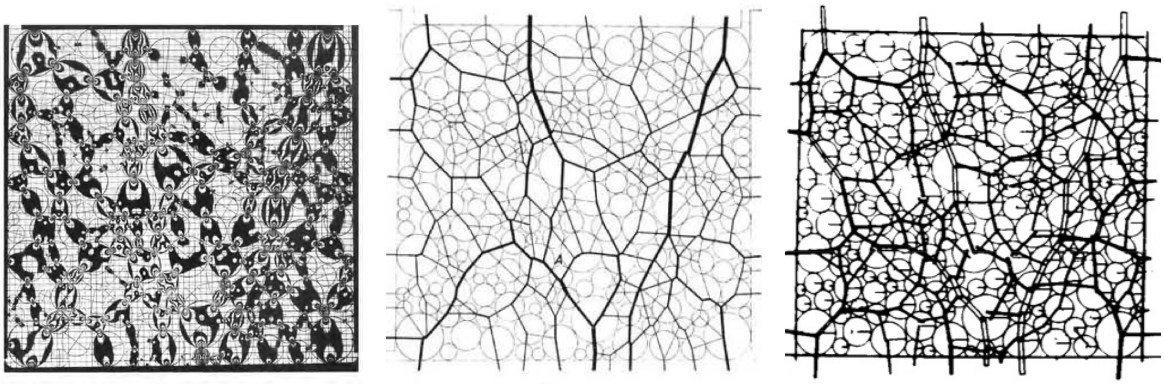

(a) (b) (c)

Figure 3.4: Distribution of contact forces: (a) photographs of the discs and (b) contact forces from the experiment (de Josselin de Jong and Verruijt (1969), with permission of Springer); (c) numerical results (Cundall and Strack (1979), with permission of ICE Publishing).

feature of the the method, as it allows modelling of phenomena where large rigid body translations and rotations, as well as large plastic deformations, are involved.

Cundall and Strack (1979) applied DEM to granular materials. They validated their computer program BALL by independently reproducing a physical test on an assembly of 197 discs reported by de Josselin de Jong and Verruijt (1969). In the physical experiment, the assembly of discs was made of optically sensitive material in order to determine the magnitude and the direction of contact forces, as well as the displacements and rotations of the individual discs. The verification was done by means of visual comparison of force vector plots produced numerically and experimentally (Figure 3.4). Although the verification was primarily qualitative, it demonstrated the potential of the distinct element method as a tool for the study of granular assemblies.

Although it was developed with the aim of studying rock mechanics, DEM soon began to be applied to various engineering applications, such as mining engineering, food technology, manufacturing, pharmaceutical, and also to other disciplines, such as geology, materials science, mathematics, and physics. For a detailed review of

DEM applications see Zhu et al. (2008). Moreover, the increase in computer processor performance, together with the use of high performance (multi-core) computers, has rapidly increased the interest in DEM among researchers (Zhu et al., 2007; O'Sullivan, 2015).

The attractiveness of DEM is the possibility of describing the mechanics of the particulate nature of soils, using a relatively small number of parameters. Since simulation data is accessible at any stage of an analysis, DEM can provide useful qualitative details of the evolution of particle displacements and rotations, and particle interactions, that cannot be directly observed in the laboratory (Thornton, 2000). It also facilitates soil specimen reproducibility.

As pointed by Zdravkovic and Carter (2008), DEM is mainly used to understand soil response by the simulation of element tests. These analyses have demonstrated that DEM can capture characteristic features of the soil behaviour. An exhaustive list of applications is given in Zhu et al. (2008) and, from a geomechanics perspective, in Cundall (2001) and O'Sullivan (2011a, 2015).

3.2 The open-source code Yade

There are many distinct element codes available for geomechanics applications. Ball is the DEM code developed originally by Cundall and Strack (1979) for 2D simulations. Trubal (Cundall, 1988) expanded the computations to 3D applications. ELLIPSE3D (Lin and Ng, 1997) is a modified version of Trubal. Particle Flow Code PFC^{2D} and PFC^{3D} (Itasca, 2008) are commercial DEM codes based on the original Trubal. Another commercial software becoming increasingly popular is EDEM (DEM Solutions, 2013),

primarily in the field of mining and chemical engineering. Open-source DEM codes involve Oval (Kuhn, 2006), EsyS-Particle Simulation (Weatherley et al., 2014), Yade (Šmilauer et al., 2010), and LIGGGHTS, which is a granular code from the molecular dynamics package LAMMPS (Kloss and Goniva, 2011).

Yade (acronym for Yet Another Dynamic Engine) is the software used for the analyses presented in this thesis. Yade is an open-source code, written in C++, and using Python for scene construction, simulation control and post-processing. It allows three-dimensional discrete simulations, and it is based on OpenMP parallelization. Yade was chosen for the present work for the following reasons. It had already been employed with promising results by Kozicki and Donzé (2008), Catalano et al. (2014) and Kozicki et al. (2014) among others. Its open source nature allows the implementation of new algorithms, e.g. contact laws and bodies with specific shapes. Moreover, Yade is continuously evolving thanks to the contribution of a wide community of users.

3.2.1 Parallel computation

Yade is parallelized using Open Multi-Processing (OpenMP), that is an application programming interface that supports shared memory multiprocessing programming. Hence it runs on a single workstation or node with multiple cores. As it does not use any Message Passing Interface (MPI) specifications, its performance does not improve from running on distributed memory systems (i.e. clusters with multiple nodes). The basic difference between OpenMP and MPI parallelization is that the former divides the loops between the available processors, while the latter divides the domain into parts and each of them is calculated by one node. Further detailed information about OpenMP is available in Chapman et al. (2008).

The parallelism is executed in Yade in every simulation, by splitting some loops into different processors. This includes the looping over all contacts for solving the interactions (contact solution), and over all bodies to solve the equations of motion (time integration). Some limitations arise since not everything in the code can be parallelized, hence the performance also depends on the efficiency of those algorithms that run on a single processor. At the time that most of the simulations necessary for this work were performed, the algorithm for the contact detection was still not parallelized, and therefore took a large portion of the total time of simulations with a great number of particles. In addition, when many processors are used, the amount of communication needed between them increases, which tends to slow the simulation speed. Finally, the efficiency of the parallelism is problem-dependent, that is, related to the number of bodies and to the interactions among them. This implies that each simulation has its optimum number of processors, depending on computer resources.

Two computer workstations were used for the DEM simulations during this research. These were:

(i) a Intel®Xeon(R) CPU E5-2687W v2 with $3.40\text{GHz} \times 16$ CPUs and 32 GB of RAM;

(ii) a Intel®Xeon(R) CPU E5640 with $2.67\text{GHz} \times 8$ CPUs and 12 GB of RAM.

Some simulations were also performed using the Advanced Research Computing facility at the University of Oxford. The high performance computer (HPC) was a Xeon SandyBridge with 1728 cores of 2.0GHz and 68.7 GB of RAM for 80 nodes. As Yade is parallelized with OpenMP, the runtime did not benefit from running on the HPC. However, the multiple nodes were beneficial for performing several simulations at the same time.

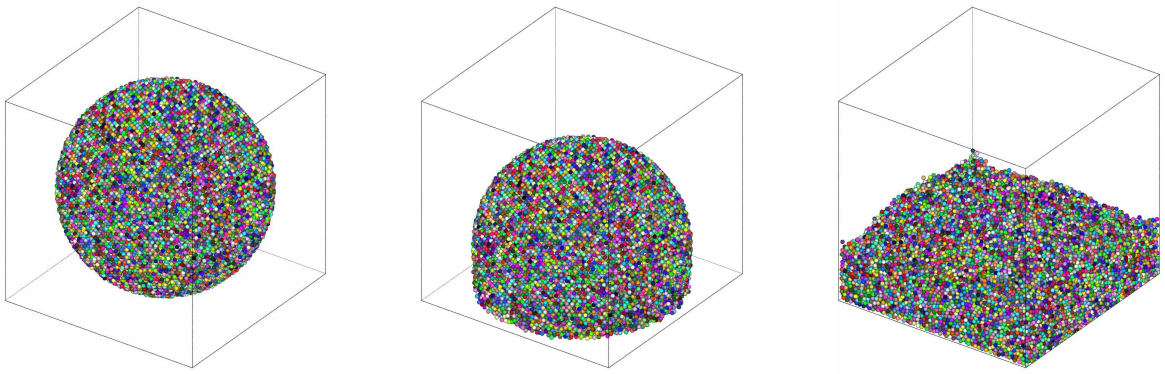

(a) (b) (c)

Figure 3.5: Snapshots at different stages of the performance test with 50 250 spheres.

3.2.2 Performance of Yade

The performance of Yade with the available computer resources was assessed by performing a simple simulation using various numbers of processors. The test consisted of the generation of particles, arranged along a hexagonal grid, to fill the volume of a sphere. The particles are then allowed to settle under gravity in a cubic box for a certain number of steps (Figure 3.5). The test is automatically run for a growing number of bodies (from 5000 to 502 000), repeated three times for each number, and the average results are calculated. It was carried out using the two workstations available for this work: one of 16 CPUs (GM1) and the other of 8 CPUs (GM2). This specific test was chosen as it is the one regarded by the Yade developers as a good reference test to evaluate the performance of each user's workstation. Hence, benchmark values for this test are available to the user community (Thoeni and Eulitz, 2014).

Figure 3.6 shows the computational time required to perform the test on pc GM1 for various number of processors with an increasing number of bodies. The results are shown only up to 200 000 particles, omitting the runtime necessary to perform the test with 500 000 particles for an easier visualization. Irrespective of the number of

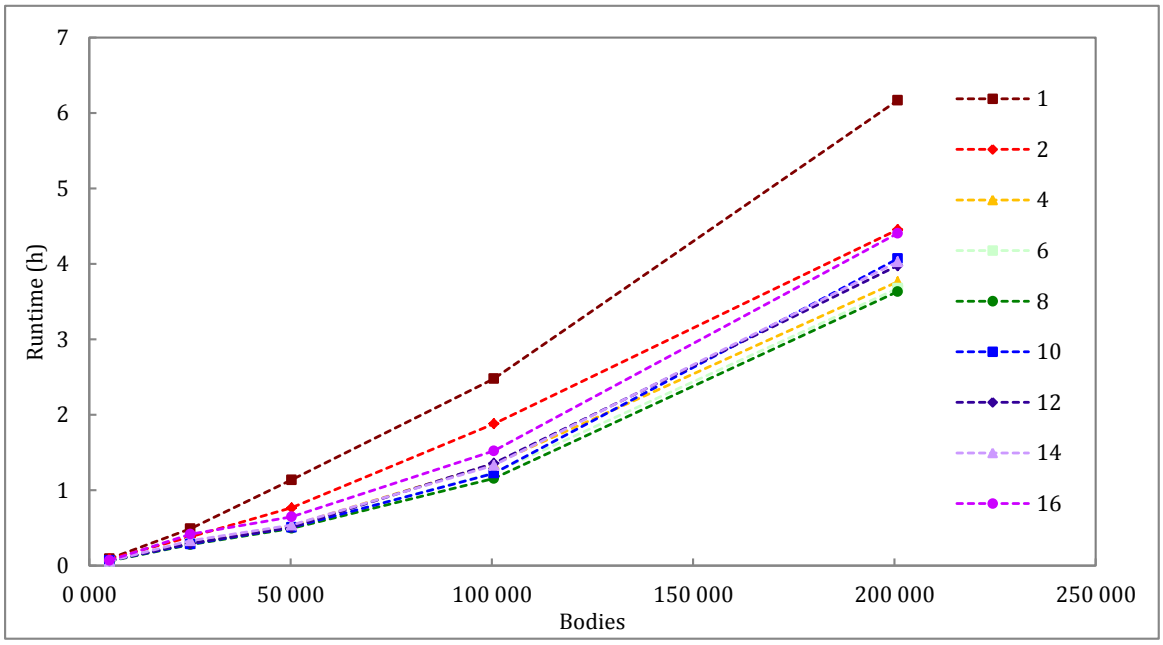

Figure 3.6: Runtimes of the performance test on pc GM1 for various number of processors.

processors used, the dependency between number of particles and time is, in practice, never linear. This is due to some algorithms slowing the simulations even further (Šmilauer et al., 2010).

The primary aim of these tests was to assess the overall performance of the workstations, and to identify the optimal number of processors for each simulation, depending on the number of particles required. The results are illustrated in Figures 3.7 and 3.8 for the two workstations (GM1 and GM2). The results from the same test performed by another Yade user (Thoeni and Eulitz, 2014) are also included for comparison. As the number of bodies spanned over a wide range, for an easier visualization, the results are separated into two figures showing the speed of the simulations on small and large assemblies. For the same reason, Table 3.1 is provided with the speed of the simulations on the workstation GM1. Even when hyperthreading was a possible option, it was always disabled, as better performance could be achieved without it.

Table 3.1: Speed of the simulation (iterations/sec) during the performance test on pc GM1.

CPUs \ spheres	5037	25 103	50 250	100 467	200 813	502 006
1	299.021	56.777	24.420	11.212	4.504	0.1930
2	308.083	72.872	36.228	14.770	6.236	0.1947
4	406.444	94.787	52.297	20.589	7.382	0.1981
6	**495.699**	94.759	54.688	22.566	7.556	0.1977
8	455.736	**99.796**	**56.432**	**24.047**	**7.646**	0.1978
10	411.772	97.321	54.798	22.691	6.827	**0.1995**
12	426.647	93.656	54.520	20.496	6.984	0.1983
14	464.908	83.874	51.570	20.858	6.894	0.1975
16	401.743	66.714	42.956	18.264	6.306	0.1986

In general, the velocity of the simulation increases for an increasing number of processors, until it reaches the limit when about 8 processors are used. For a further increase of the number of processors, the simulations do not benefit, as anticipated in the previous section. The optimal number of processors increases from 6 to 10 as the number of particles increases. Considering that for the simulations in this research a number of particles ranging from 5000 to 40 000 was used, the optimal number of processors is around 8.

Comparing the performances of the two workstations, when the same number of processors are used, the machine with 16 CPUs and 32 GB of RAM (GM1) is faster than the machine with 8 CPUs and 12 GB of RAM (GM2). Depending on the number of particles, the machine GM1 is between 20 and 57 % faster when running with 1 processor, and between 16 and 35 % faster when running with 8 processors.

The speed of the simulation for different numbers of bodies and processors is comparable also with the results from Thoeni and Eulitz (2014). While GM1 performed better with a small number of particles, the computer of the other Yade user was faster when 500 000 particles were used. However, simulations with that many particles were

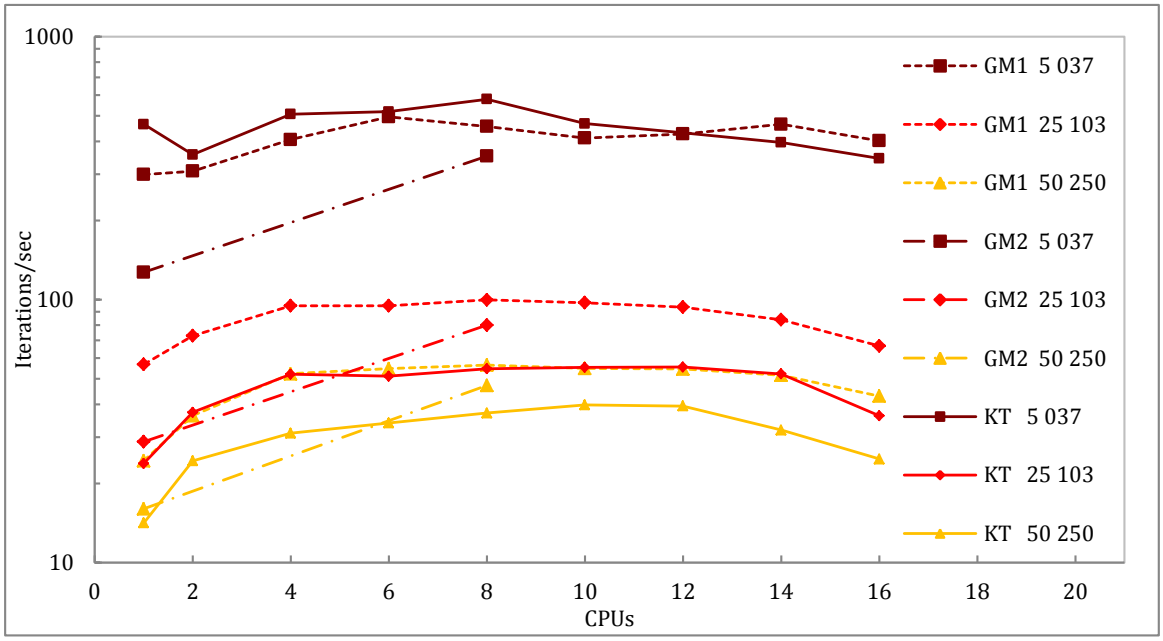

Figure 3.7: Performance of Yade on small assemblies on different workstations: GM1 (- - -), GM2 (— · —) and another Yade user (——, Thoeni and Eulitz (2014)). Note vertical axis uses a base 10 logarithmic scale.

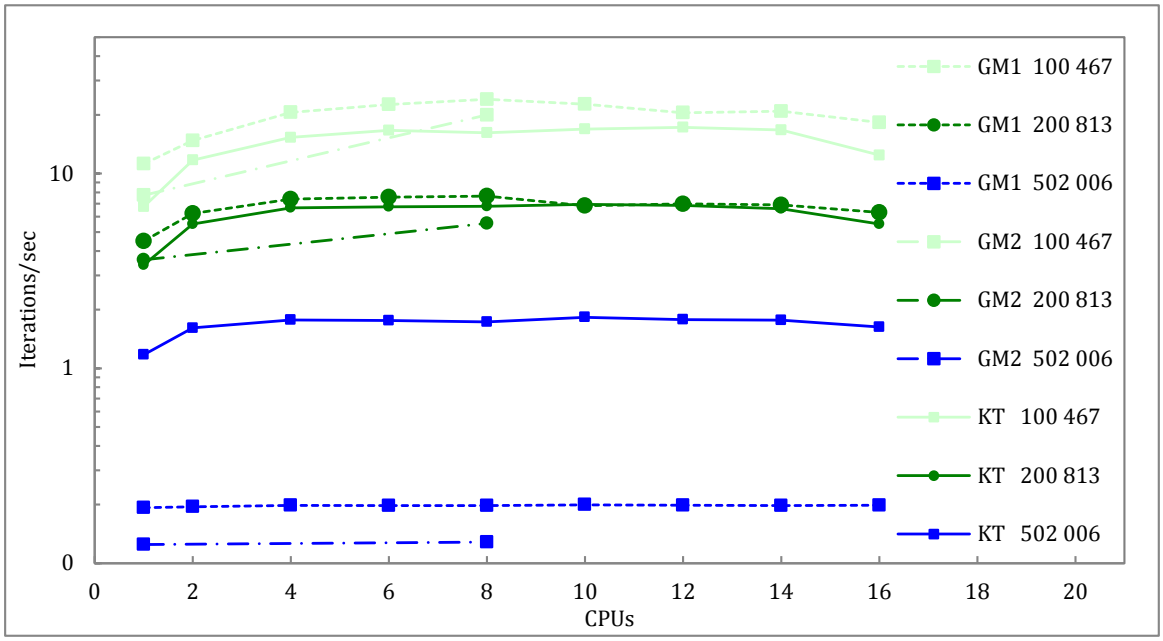

Figure 3.8: Performance of Yade on large assemblies on different workstations: GM1 (- - -), GM2 (— · —) and another Yade user (——, Thoeni and Eulitz (2014)). Note vertical axis uses a base 10 logarithmic scale.

not performed in this research.

Finally, it should be pointed out that the results above illustrated are valid for this specific simulation. Performance tests should be run for every type of simulation, so that the optimal number of processors can be identified, as shown in Section 5.1.2 for the preparation of the numerical soil specimen used for the pipe loading test.

3.3 Modelling granular soils with Yade

Yade is a DEM code based on the explicit time integration scheme. The solution is taken from the dynamic equation of motion of the individual particles, rather than solving the system of stiffness equations for all the particles. The calculation cycle and the fundamentals of the method relevant for understanding the work presented in the next chapters, are described below. The complete documentation can be found at Šmilauer et al. (2010), but other references are also Kozicki and Donzé (2008) and Šmilauer (2010). The documentation is continuously evolving and improving, however some parts are covered in more detail in the documentation of WooDem[1], a forked version of Yade.

3.3.1 The computational cycle

In Yade, and in general in the DEM, the interactions between the particles are solved incrementally, over a number of time steps. The DEM cycle is summarised in Figure 3.9. At the beginning, the geometry and the contact model are defined, and the bodies are generated. Then, for each time step, the interactions are solved through two consecutive phases. The first phase consists of a neighbour searching, and aims at identifying the

[1] `http://woodem.eu/doc/`

pairs of particles that might be in contact (contact detection). This is achieved by considering the position of approximate volumes, the axis-aligned bounding boxes, containing each particle. In the second phase, the contact interactions are solved by considering the exact geometry of pairs of neighbouring particles (contact resolution). The goal is to calculate geometrical features of the interaction, such as the overlapping and the relative displacement between each pair.

Then the specific contact model chosen by the user is used to calculate the contact forces. In general, an interaction law relates the relative displacement between each pair of particle to the contact force. Further details regarding the contact law used for this research are provided in the next section. The calculated forces are then applied to the particles, including body and external forces such as gravity.

The translational and rotational accelerations are obtained by integrating the translational and rotational equations of motion for each particle, which read:

$$m\ddot{\mathbf{x}} = \sum_{c=1}^{N_c} \mathbf{F}_c + m\mathbf{g} \tag{3.1}$$

$$\mathbf{I}\dot{\boldsymbol{\omega}} = \sum_{c=1}^{N_c} \mathbf{T}_c \tag{3.2}$$

where m, $\ddot{\mathbf{x}}$ and $\dot{\boldsymbol{\omega}}$ are respectively the mass, the linear and the angular acceleration vectors of the particle, $\mathbf{g}$ the gravitational acceleration acting on the particle, $\mathbf{I}$ is the inertia tensor of the particle, and $\mathbf{F}_c$ and $\mathbf{T}_c$ are the force and the torque generated from the contact between the particle and either other particles or the boundaries, calcutated for all the bodies N_c in contact with it. These equations of motion are integrated in a leapfrog scheme to calculate the particle accelerations, velocities, displacements and rotations. The leapfrog (or Verlet) scheme implies that the even derivatives, such as positions and accelerations, are computed at each time step, and the odd derivatives,

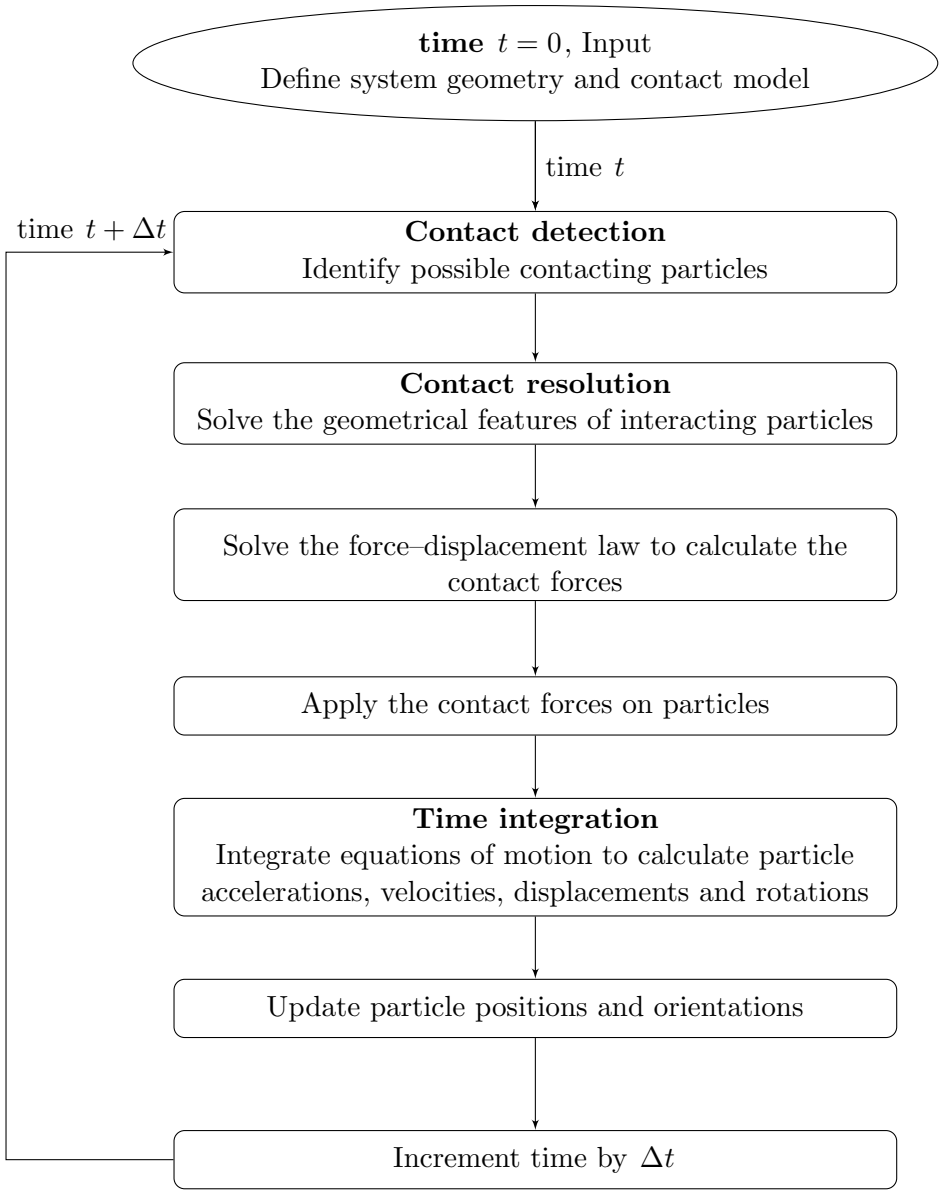

Figure 3.9: Computational cycle in a DEM simulation.

i.e. the velocities, are computed at the mid time steps. Herein the superscript $^\circ$ is used to refer to a variable at the current time step t, $^\ominus$ and $^\oplus$ for a variable at the previous and next mid-step $t - \Delta t/2$ and $t + \Delta t/2$, and $^-$ and $^+$ for a variable at the previous and next step $t - \Delta t$ and $t + \Delta t$. Throughout this thesis, when it is not explicitly specified, the variables refer to the current time step t, i.e. the superscript $^\circ$ may be omitted.

The integration of the equations of motion is carried out as follows. By integration of the accelerations $\ddot{\mathbf{x}}^{\circ}$ and $\dot{\boldsymbol{\omega}}^{\circ}$ at the current step t, the velocities at the next mid-step $t + \Delta t/2$ are computed:

$$\dot{\mathbf{x}}^{\oplus} = \dot{\mathbf{x}}^{\ominus} + \ddot{\mathbf{x}}^{\circ}\Delta t \tag{3.3}$$

$$\boldsymbol{\omega}^{\oplus} = \boldsymbol{\omega}^{\ominus} + \dot{\boldsymbol{\omega}}^{\circ}\Delta t \tag{3.4}$$

where $\dot{\mathbf{x}}$ and $\boldsymbol{\omega}$ are the linear and angular velocities. It should be noticed that the passage from Eq. 3.2 to 3.4 is immediate only for spherical bodies, where the diagonal elements of the inertia tensor are identical. The algorithm for non-spherical bodies is introduced when the pipe implementation is described (Section 5.2). A further integration gives the particle position $\mathbf{x}^{+}$ and orientation $\mathbf{q}^{+}$ at the next time step $t + \Delta t$:

$$\mathbf{x}^{+} = \mathbf{x}^{\circ} + \dot{\mathbf{x}}^{\oplus}\Delta t \tag{3.5}$$

$$\mathbf{q}^{+} = \Delta\mathbf{q} \cdot \mathbf{q}^{\circ} \tag{3.6}$$

where $\Delta\mathbf{q}$ is the quaternion representing the rotation vector $\boldsymbol{\omega}^{\ominus}\Delta t$.

The particle positions and orientations are hence updated. At the end of the cycle, the time is incremented by Δt, and the cycle is run again.

3.3.2 The contact model

The contact model is used in DEM to describe numerically the contact forces developing between adjacent particles. These contact forces can be resolved into components normal and tangential to the contact surface.

In a physical contact between two grains, the individual grains slightly deform in the area close to the contact point, leading to an enlargement of the contact area itself, so

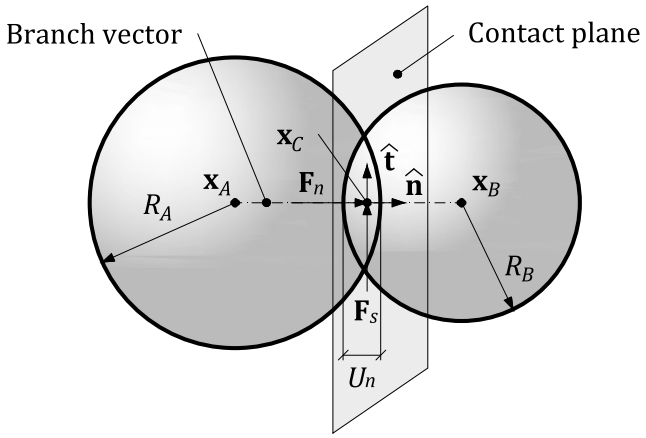

Figure 3.10: Contact between two spherical particles.

that the centres of the grains come closer together. In addition, when the shear force at the contact becomes larger than the shear resistance, the grains will experience relative sliding. The overall behaviour of the soil will depend on the deformation of the individual grains, and on the relative sliding. Because sliding is a non-linear and irreversible deformation, the force–displacement behaviour at the contact will be strongly non-linear and irreversible.

The contact between two spherical particles is illustrated in Figure 3.10. Each particle is defined by the position of its centre $\mathbf{x}$ and its radius R. The contact point $\mathbf{x}_C$ is defined as the point within the interpenetration volume of the two spheres along the branch vector, that is, the line between the particle centres. This point identifies a contact plane defined by the unit normal vector $\widehat{\mathbf{n}}$. A tangential unit vector $\widehat{\mathbf{t}}$ is instead defined such that $\widehat{\mathbf{t}} \cdot \widehat{\mathbf{n}} = 0$. In order to simulate the deformations occurring between two physical grains, the numerical particles are allowed to overlap by a small distance, the overlapping depth U_n, defined as:

$$U_n = R_A + R_B - |\mathbf{x}_A - \mathbf{x}_B| \tag{3.7}$$

where R_A and R_B are the radii, and $\mathbf{x}_A$ and $\mathbf{x}_B$ the positions of the centres of the

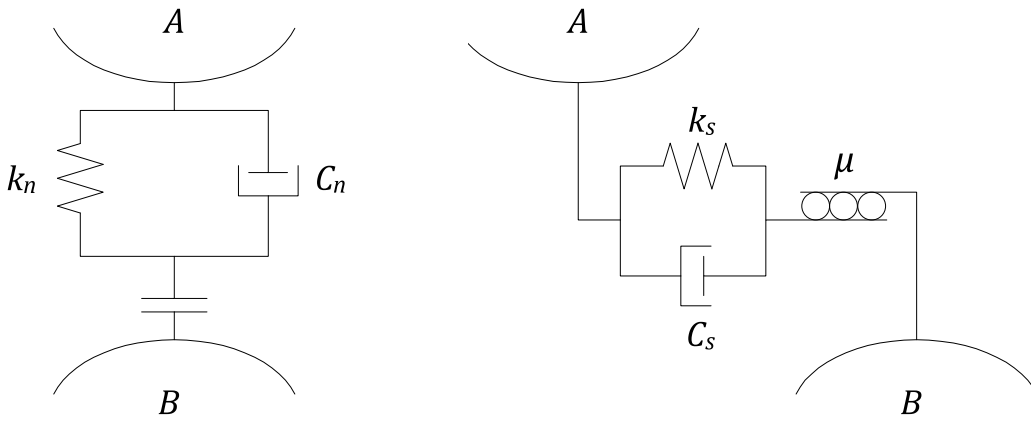

(a) (b)

Figure 3.11: Schematic of the contact model in the normal (a) and shear (b) direction.

two spheres (note that there is overlapping if $U_n > 0$). From the overlapping and the relative shear displacement between the particles, the contact model is used to compute the contact forces. This is decoupled into the normal component $\mathbf{F}_n$ acting along the direction of the normal vector, and the shear (tangential) component $\mathbf{F}_s$ acting along the contact plane, in the direction of the tangential vector. The normal and shear contact forces can be envisioned as a system of springs, sliders, dividers, and dashpots in the normal and tangential direction (Figure 3.11). Springs of stiffness k_n and k_s are used in both directions to simulate the elastic behaviour induced by the slight overlap between the two particles. The dashpots with coefficients C_n and C_s are introduced to simulate viscous damping. The divider in the normal direction is added to simulate no transmission of traction when the particles are no longer in contact, in other words, to prevent the development of tensile forces. The shear force instead includes a slider to simulate the plastic slip condition, that is, the particles start undergoing irreversible relative sliding displacement when the frictional resistance, given by μ, is exceeded.

The Hertz–Mindlin no micro-slip solution (Mindlin, 1949) was adopted as a force–

displacement law in this research. This is a simplified version of the Hertz–Mindlin and Deresiewicz theory, developed to describe the physics of the contact between elastic bodies. More specifically, Hertz (Hertz, 1881; Johnson, 1985) provided the normal force–displacement relationship for elastic contact between frictionless spheres subjected to a normal force; Mindlin (1949) proposed a relation for an elastic-frictional contact between spheres subjected to a normal force and a varying shear force; Mindlin and Deresiewicz (1953) recognized the occurrence of micro-slips at the edges of the contact surface and suggested a solution for the incremental shear force–displacement relation for spheres subjected to varying normal and shear forces.

The Hertz–Mindlin model was chosen for its ability to reproduce realistically the behaviour of spherical bodies in contact. The solution without micro-slips was preferred to that from Mindlin and Deresiewicz to keep the model simple and computationally affordable. A more complex constitutive law would have required more computational time to complete simulations. In addition, the Hertz–Mindlin contact law directly takes into account the mechanical properties of the particle material, hence realistic values of the elastic parameters are expected to replicate the behaviour of an assembly of physical particles realistically.

Evidence of the ability of the Hertz–Mindlin model to replicate the contact between particles is provided, among others, by Di Renzo and Di Maio (2004) and Thornton et al. (2011). They performed DEM simulations of a sphere undergoing elastic-frictional collision from oblique impact with a flat wall. Three contact models were compared: the linear contact model, the Hertz–Mindlin–Deresiewicz model, and a simplified Hertz–Mindlin model. Di Renzo and Di Maio (2004) showed that the linear contact model is capable of modelling only the macroscopic characteristics of the collision, i.e. the

rebound angle and the rotational velocity. At the microscopic scale, however, the evolution of the forces, velocities and displacements estimated both with the linear and the simplified Hertz–Mindlin models provided considerable discrepancies with the exact analytical solution. A good agreement was found with the Hertz–Mindlin–Deresiewicz model. Thornton et al. (2011), however, recognised the capability of the linear model to predict results in good agreement with the more complex Hertz–Mindlin and Deresiewicz model, provided an appropriate value of the ratio of the shear and normal stiffnesses is used. Despite this, they also observed that the calibration of the stiffnesses ratio might be more difficult for problems different from the collision of a single sphere. Therefore they recommended the use of a simplified Hertz–Mindlin and Deresiewicz model, which does not require the above-mentioned calibration and uses parameters based on the grain properties (Young's modulus and Poisson's ratio). In addition, they clarified the need for an incremental approach for the shear force–displacement law in non-linear models, since the shear spring stiffness is always changing due to the varying of the normal force (Eq. 3.18).

3.3.2.1 Simplified Hertz–Mindlin formulation

The formulation of the Hertz–Mindlin no micro-slip solution for the contact law was introduced for DEM by Cundall (1988), as a simplified version of that proposed by Mindlin and Deresiewicz (1953).

The normal component is implemented on the basis of Hertz theory (Hertz, 1881; Johnson, 1985). Hertz studied the elastic deformation of solid bodies, identifying a surface and a distribution of pressure between them. He described analytically the growth of the surface and the distribution of pressure on it by analogy with electric

potential theory. He reduced it to a boundary value problem, and found an expression of the potential that would satisfy certain boundary conditions. These conditions are:

- each contacting body is treated as an elastic half-space;
- the contact area is assumed to be small in comparison to the dimensions of the contacting bodies, and the stress is sufficiently small so that the material response remains elastic;
- the surfaces in contact are perfectly smooth, i.e. only a normal pressure acts between the two bodies;
- the normal pressure is zero outside the surface of pressure (no tensile force is allowed) and equal and opposite inside;
- the pressure on the contacting surface is distributed over an ellipse.

The solution of the posed boundary problem can be summarised as follows.

For two contacting spheres, the ellipse of pressure is a circle, and the distribution of the normal pressure on the contacting surface can be written as (Johnson, 1985):

$$p = p_0 \left[1 - \left(\frac{r}{a}\right)^2\right]^{1/2} \tag{3.8}$$

where p_0 is the pressure at the centre of the surface, r the distance from the centre, and a the radius of the surface. The total force on the surface is given by the integral of p over the surface of pressure:

$$P = \int_0^a p(r) 2\pi dr = \frac{2}{3} p_0 \pi a^2. \tag{3.9}$$

The last formula can also be written as a function of the overlapping U_n as

$$P = \frac{4}{3} E^* \sqrt{R^*} U_n^{3/2} \tag{3.10}$$

where the overlapping U_n is calculated as in Eq. 3.7, and R^* and E^* are the equivalent

radius and equivalent Young's modulus of the contacting spheres, defined as:

$$\frac{1}{R^*} = \frac{1}{R_A} + \frac{1}{R_B} \tag{3.11}$$

$$\frac{1}{E^*} = \frac{1-\nu_A^2}{E_A} + \frac{1-\nu_B^2}{E_B} \tag{3.12}$$

where R_A and R_B are the radii of the spheres, E_A and E_B their Young's moduli, and ν_A and ν_B their Poisson's ratios. The equivalent radius expresses a summation of curvatures (inverse radii), which is assumed to be positive for a convex surface, and negative for a concave surface. The equivalent contact modulus expresses the elastic properties of bodies A and B as a combination of springs.

It is important to note that even if the material response is assumed to be linear elastic, the relationship between the force P and the displacement U_n is non-linear, because it depends on the area of the contact surface, which increases non-linearly with the contact deformation, as $a^2 = U_n R^*$.

In Yade, the normal component of the force at the current time step (the superscript $^\circ$ is omitted, but implied here) can be decomposed into an elastic component and a damping component:

$$\mathbf{F}_n = \mathbf{F}_{n,el} + \mathbf{F}_{n,v}. \tag{3.13}$$

The elastic component is exactly that force defined from Hertz theory, which in vectorial form reads:

$$\mathbf{F}_{n,el} = K_n U_n \widehat{\mathbf{n}} = \frac{4}{3} E^* \sqrt{R^*} U_n^{3/2} \widehat{\mathbf{n}}. \tag{3.14}$$

The first formulation in the above equation, with the secant stiffness K_n, is generally used in DEM literature to represent the contact through springs, where the particles can slightly overlap and the contact force is proportional to the overlapping through the spring stiffness K_n. The damping component in Eq. 3.13 is discussed in Section 3.3.3.

It is worth stressing again that where the superscripts are not defined explicitly, $^\circ$ is implied. Hence the normal force denotes the normal force $\mathbf{F}_\mathbf{n}^\circ$ calculated at the current time step, from the current contact normal $\widehat{\mathbf{n}}^\circ$.

The shear (tangential) component is calculated following the Mindlin no-slip solution, described in Mindlin (1949), and regarded as a simplified version of the Mindlin-Deresiewicz model (Mindlin and Deresiewicz, 1953). The basic assumptions are that (i) the particles are in contact through Hertzian normal force, and (ii) this normal force does not influence the shear force. In the latter paper, they described the presence of partial slips at particle contact, such that the force–displacement relationship depends on the instantaneous rate of change of the contact forces, and thus on the whole loading history. Since the application of the Mindlin-Deresiewicz solution in discrete element modelling involves complex algorithms and requires the state of each contact to be stored in memory, which can be extremely expensive, the simplified version (the so-called Hertz–Mindlin no-slip solution) is generally adopted in DEM simulations, and herein as well.

Although the terms shear and tangential force are usually used interchangeably in the literature, shear is preferred here to describe the force mobilised in the direction perpendicular to the contact normal. The reason is to avoid confusion with the tangent stiffness at the contact (both in the normal and shear direction), which represents the current stiffness calculated incrementally.

The shear force describes the material response before sliding occurs between two particles subject to normal and shear contact forces. If the load is smaller than the Coulomb frictional limit, micro-slips occur over part of the contact surface while the remaining area surface remains stuck. Those micro-slips are disregarded in the simpli-

fied Hertz–Mindlin model. The load T on the part of contact surface where no relative movement occurs is expressed as

$$T = 8G^* \sqrt{R^* U_n} U_s \tag{3.15}$$

where U_s is the relative movement in the direction perpendicular to the contact normal, and G^* is the equivalent shear modulus, defined from the shear moduli of the particles in contact:

$$\frac{1}{G^*} = \frac{2-\nu_A}{G_A} + \frac{2-\nu_B}{G_B}. \tag{3.16}$$

The formulation of the shear force in Yade , in analogy with the normal force, includes an elastic component and a damping component:

$$\mathbf{F}_s^\circ = \mathbf{F}_{s,el} + \mathbf{F}_{s,v}. \tag{3.17}$$

The damping component is described in detail in Section 3.3.3. The elastic component is formulated in an incremental fashion to take into account the cumulative shear displacement ΔU_s, that is the sum of the incremental displacements at the contact that occurs from the time the contact is formed. Further justifications of the adoption of the incremental form can be found in O'Sullivan and Bray (2003) and Thornton et al. (2011). Specifically,

$$\mathbf{F}_{el} = \mathbf{F}_s^- + \mathbf{\Delta F}_{s,el} \tag{3.18}$$

where the incremental shear force is defined starting from Eq. 3.15:

$$\mathbf{\Delta F}_{s,el} = k_s \mathbf{\Delta U}_s = 8G^* \sqrt{R^* U_n} \mathbf{\Delta U}_s \tag{3.19}$$

where k_s is the tangent shear stiffness of a virtual spring at the contact between two bodies, and the vector $\mathbf{\Delta U}_s$ is the incremental relative displacement in the direction perpendicular to the normal contact, defined from the relative shear velocity at the

previous mid time step

$$\boldsymbol{\Delta}\mathbf{U}_s = \dot{\mathbf{U}}_s^{\ominus}\Delta t. \tag{3.20}$$

Sliding between the particles occurs when the shear force exceeds the plastic limit. The limit of the shear force is given from the Coulomb failure criterion such that

$$\mathbf{F}_s = |\mathbf{F}_n|\mu\frac{\mathbf{F}_s^{\circ}}{|\mathbf{F}_s^{\circ}|} \qquad \text{if} \quad |\mathbf{F}_s^{\circ}| \geq |\mathbf{F}_{\max}| = \mu|\mathbf{F}_n| \tag{3.21}$$

where $\mu = \tan\phi_\mu$ is the coefficient of interparticle friction.

3.3.2.2 Moment–relative rotation contact law

A rolling resistance model can be incorporated in DEM to account for the non-sphericity of real sand grains, as already anticipated in Section 3.1.2. When real non-spherical sand grains are in contact a moment arises from the from non-collinearity of the branch vector with the contact normal (Figure 3.12(a)). This means that the normal component of the contact force does not pass through the particle centroids. On the contrary, when spheres are in contact, the normal component of the contact force passes through the centroids of the particles, without imparting any additional moment (Figure 3.12(b)); there is only a moment contribution from the shear component. Intuitively, it is straightforward to recognise that spherical particles can rotate more easily than ellipsoids or other particles with more irregular and angular shapes. Therefore a fictitious moment can be added at the contact, which opposes the particle rotation.

Particle rolling is not a minor kinematic mechanism (Oda et al., 1982). Thus, it cannot be neglected. The relative motion between grains, or more generally between two bodies, can be regarded as a combination of sliding, rolling and spinning. Sliding occurs when there is a relative linear velocity between the surfaces of the two bodies.

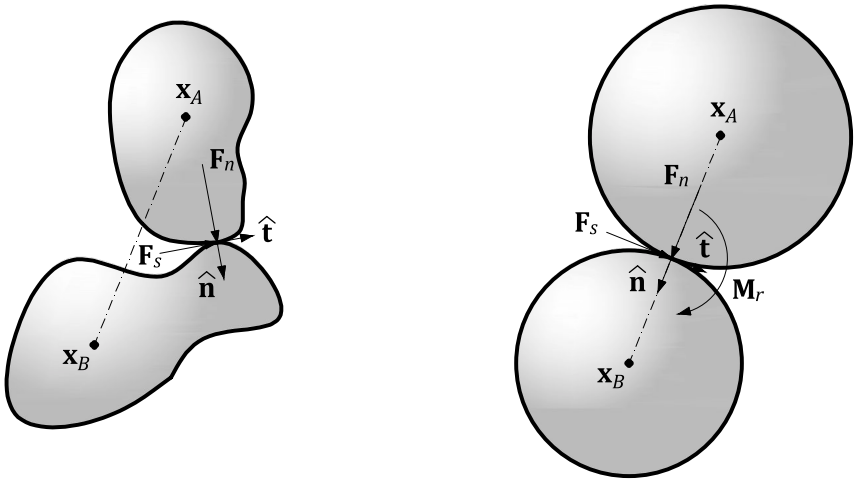

(a) (b)

Figure 3.12: Contact between (a) non-spherical and (b) spherical particles.

Rolling occurs when there is a relative angular velocity between two bodies about an axis lying in the tangent plane, and spinning occurs when there is relative angular velocity about the common normal. Evidences of particle rolling are discussed by Oda et al. (1982). They performed biaxial compression tests on oval rods, and observed that large voids and high rotational gradients occur during the formation of shear bands, suggesting than rolling, not sliding, is the major deformation mechanism. In addition, the rolling mechanism controls not only the peak strength, but also leads to extensive dilatancy of granular materials. Free rolling is defined in Johnson (1985) as rolling motion where the spin and shear forces at the contact are zero. Resistance to rolling is associated with a couple which arises form the asymmetry of the pressure distribution at the contact. The rolling resistance can arise from several sources, including micro-slip and friction at the contact interface, energy dissipation due to plastic deformation and viscous hysteresis, surface adhesion between particles, and shape effects. Ai et al. (2011) define all the first sources as "traditional mechanisms" of rolling resistance. The shape effect cannot strictly be classified as such, since it is not related to the physical

characteristics of the contacts. The particle shape effect is a pure geometrical feature, but it plays an important role in DEM modelling when idealised spherical particles are used.

Where it is not expressly specified, discrete element simulations are in general performed on spheres free to rotate. As a consequence, the rotations that numerical particles experience exceed the rotations that real particles experience in the soil. It is also worth noticing that, in order to correct grain rolling, contact laws that partially or totally block the rotations can be found in the literature. Completely blocking off the particles rotations might be a reasonable option for DEM simulations, as shown by Calvetti et al. (2004). They blocked the rotations of the particles, and found an appropriate fictional value for the interparticle friction angle. However, it does not reproduce the correct kinematics, therefore it does not correspond to the physical reality. O'Sullivan (2011b) noted that when rotation is inhibited, the contact conditions are different. Specifically, the particle assembly is not in (dynamic) rotational equilibrium, hence the fabric stress tensor will not be necessarily symmetric. Reproducing realistic conditions at a particle level is crucial for the scope of this research. It is necessary, for example, to reproduce the correct kinematics to simulate the formation and the growth of the berm of soil created by the laterally moving pipe. It is important to stress that the use of rolling resistance models is still a controversial argument among DEM users. Here it was only employed as an expedient to account for the different shapes between spherical DEM particles and irregular shaped sand grains.

Review of previous rotational resistance models

A review of the most popular rolling resistance models was done at the beginning of this work in order to choose the one that was more appropriate for the geometry analysed, and which was also consistent with the non-linear behaviour described by the Hertz–Mindlin contact law. The main findings are summarised below.

Bardet and Huang (1993) introduced the first analytical model to estimate a value for rolling stiffness from experiments on cylinders placed between two rigid plates. The expression was based on the two-dimensional theory of elastic contact, and it was found that the rolling stiffness was proportional to the cylinder radius and to the normal components of the contact force.

Iwashita and Oda (1998) proposed a two-dimensional model to account for rolling resistance in DEM. They recognised that the relative movement between two particles can be decomposed into sliding (ΔU_s) and rolling (ΔU_r) incremental components. The incremental rotation between two spheres is defined by:

$$\theta_r = \frac{\Delta U_r}{R} \tag{3.22}$$

where R is taken as the mean radius of the two spheres $R = (R_A + R_B)/2$. The contact model is described by a rolling spring for the elastic moment, a dashpot to account for the damping effect, a slider for the limiting moment, and a divider to simulate no transmission of moments when the particles are no longer in contact.

Jiang et al. (2005) derived a 2D model extending the Iwashita–Oda model, in which the rolling resistance depends on the contact area. The area is accounted for by introducing a shape parameter to represent the contact width between two particles. Plassiard et al. (2009) and Belheine et al. (2009) extended the Iwashita and Oda model

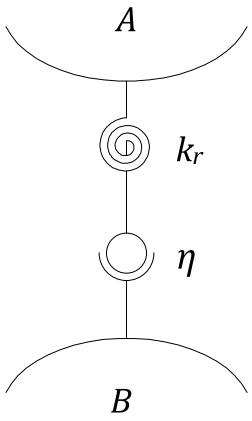

Figure 3.13: Schematic illustration of the rotational resistance contact model.

to spherical particles in 3D.

Proposed rotational resistance model

The rolling resistance model adopted for this study is based on the aforementioned models. It consist of a rolling spring to account for the elastic moment, and a rotational slider that starts working when the plastic limit is reached (Figure 3.13).

The elastic rolling moment $\mathbf{M}_{el}$ was implemented in an incremental form to account for the history of previous rotations (as for the shear component of the contact force). The notation $^{\circ}$, $^{\ominus}$ and $^{\oplus}$, $^{-}$ and $^{+}$ is used again to refer to a variable known at the current time step, at the previous and next mid-step, and at the previous and next step (Section 3.3.1). The rolling moment at the current time step is defined as

$$\mathbf{M}_{el}^{\circ} = \mathbf{M}^{-} + \Delta\mathbf{M}_{el} \tag{3.23}$$

where $\mathbf{M}^{-}$ is the moment at the previous step and $\Delta\mathbf{M}_{el}$ is the incremental elastic moment, defined as

$$\Delta\mathbf{M}_{el} = -k_r\boldsymbol{\theta}_r^{\ominus} \tag{3.24}$$

where k_r is the rolling stiffness and $\boldsymbol{\theta}_r^{\ominus}$ is the rolling component of the relative rotation

vector between two particles in contact. The total relative rotation vector $\boldsymbol{\theta}^{\ominus}$ consists of rolling and a twisting contributions, $\boldsymbol{\theta}_r^{\ominus}$ and $\boldsymbol{\theta}_t^{\ominus}$, calculated as:

$$\boldsymbol{\theta}_r^{\ominus} = \boldsymbol{\theta}^{\ominus} - \boldsymbol{\theta}_t^{\ominus} \tag{3.25}$$

$$\boldsymbol{\theta}_t^{\ominus} = \left(\boldsymbol{\theta}^{\ominus} \cdot \widehat{\mathbf{n}}^{\ominus}\right) \widehat{\mathbf{n}}^{\ominus}. \tag{3.26}$$

Prior to this research, the formulation for the rolling stiffness β_r had not yet been implemented in Yade. Some considerations are necessary regarding this parameter. Firstly, as suggested by Iwashita and Oda (1998), the incremental moment generated from the shear displacement at the contact and the incremental moment generated from the rolling displacement are of the same order of magnitude under the condition $\Delta U_s \approx \Delta U_r$:

$$\mid \Delta \mathbf{F}_{s,el} \mid R \approx \mid \Delta \mathbf{M}_{el} \mid . \tag{3.27}$$

Secondly, it is desirable that the adopted formulation of the moment–relative rotation law be consistent with the Hertz–Mindlin formulation for the normal and shear forces. Hence the rolling stiffness adopted here is different from Iwashita and Oda (1998) and Plassiard et al. (2009), where a linear law was used instead.

The rolling stiffness k_r was implemented in Yade by substituting Eq. 3.19, 3.24 and 3.22 in Eq. 3.27, where

$$\mid \Delta \mathbf{F}_{s,el} \mid R = k_s \sqrt{U_n} \Delta U_s \tag{3.28}$$

$$\mid \Delta \mathbf{M}_{el} \mid = \mid k_r \boldsymbol{\theta}_r^{\ominus} \mid = k_r \frac{\Delta U_r}{R}. \tag{3.29}$$

This leads to

$$k_s \sqrt{U_n} \Delta U_s = k_r \theta_r. \tag{3.30}$$

The rolling stiffness is then obtained as

$$k_r = \beta_r k_s \sqrt{U_n} R^2 \tag{3.31}$$

where $R = (R_A + R_B)/2$ is the mean radius of the two particles in contact, and β_r is the rolling stiffness coefficient, which needs to be calibrated. It is worth noting that with such a formulation, the relationship between the moment and the incremental relative rotation is linear only if k_s and (indirectly) k_n are constant. The limiting plastic moment is described by a formulation analogous to the Coulomb criterion:

$$\mathbf{M} = \frac{\mathbf{M}^{\circ}_{el}}{\mid \mathbf{M}^{\circ}_{el} \mid} \eta R \mid \mathbf{F}_n \mid \qquad \text{if} \quad \mid \mathbf{M}^{\circ}_{el} \mid \geq \eta R \mid \mathbf{F}_n \mid \tag{3.32}$$

where η is a coefficient for the plastic moment, which needs to be calibrated. Its physical meaning is similar to the interparticle friction coefficient $\tan \phi_\mu$, and controls the maximum rolling resistance that can be generated at the contact point.

3.3.3 Damping

Damping may be divided in two categories: local (also known as contact) damping and global damping (Cundall and Strack, 1979). Local damping is applied at the contact between particles, and operates on relative variables, such as the relative velocities. It is evaluated at the contact level, during the solution of the force–displacement law. It is introduced in the calculations in Eq. 3.13 and 3.17, recalled below:

$$\mathbf{F}_n = \mathbf{F}_{n,el} + \mathbf{F}_{n,v} \tag{3.33}$$

$$\mathbf{F}_s = \mathbf{F}_{s,el} + \mathbf{F}_{s,v}. \tag{3.34}$$

The subscript $_v$ in the normal and shear components of the damping force anticipates that, generally, local damping is of the viscous type. Further clarifications follow in

the next paragraph.

Global damping, instead, is applied on particles' absolute variables, such as absolute velocity and absolute acceleration. It is introduced in the integration of the equations of motion Eq. 3.1 and 3.2, which become:

$$m\ddot{\mathbf{x}} = \sum_{c=1}^{N_c} \mathbf{F}_c + m\mathbf{g} + \mathbf{F}_d \tag{3.35}$$

$$\mathbf{I}\dot{\boldsymbol{\omega}} = \sum_{c=1}^{N_c} \mathbf{T}_c + \mathbf{T}_d. \tag{3.36}$$

It should be pointed out that the above definition of local and global is different from the nomenclature used by Itasca (2008), where local damping is applied on each particle, and viscous damping is meant to be applied at the contact and is proportional to the relative velocity. Itasca's definition is given for completeness, but is not used in this thesis.

Furthermore, the form of damping can be viscous or non-viscous, depending on whether or not it is applied in proportion to the velocities (either absolute or relative) of the particles. The local (generally viscous) damping leads to energy dissipation at the contact level. The global damping is a purely numerical device which leads to energy dissipation throughout the model, and directly calms the entire system down.

Although slightly different, local and global damping are both used in DEM, but there is still a great uncertainty in the literature regarding the choice of the appropriate type, and the range of realistic parameter values. A description of the most common types of damping follows below, so that the peculiarities of the damping used for the work in this thesis can be appreciated.

3.3.3.1 Global damping

Global damping was first introduced by Cundall and Strack (1979) as a form of viscous damping, which decreases the magnitude of the absolute velocities of the particles. It is introduced in the equation of motion. The damping force in Eq. 3.35 reads

$$\mathbf{F}_d = -C_{Cundall}\dot{\mathbf{x}} \tag{3.37}$$

where $C_{Cundall} = \alpha_C m$ is the coefficient of global damping. with units of mass/time, taken proportional to the mass m of the particle, and a coefficient α_C. Its effect is to damp all the particles according to their velocity and their mass. In other words, it can be seen as the effect of a dashpot connecting each particle to the ground. The equation of motion (Eq. 3.35) can be then rewritten with the damping term, and solved for velocity $\dot{\mathbf{x}}^{\oplus}$. As observed by Cundall (1987), the main limitations of this formulation are that (i) all the particles are equally damped, (ii) it introduces body forces, and (iii) the proportional coefficient α_C depends on the solution of an eigenvalue problem. In fact, the optimal α_C is related to the solution of a system of a mass, damping force and resultant contact force, and it depends on the natural frequency (and hence on the stiffness) of the system.

Therefore Cundall (1987) suggested a different form of global damping. This is non-viscous, but proportional to the resultant force acting on each particle, with a sign ensuring that the vibrational (but not the steady) modes are damped:

$$\mathbf{F}_d \propto |\mathbf{F}_c| \mathrm{sgn}\left(\dot{\mathbf{F}}\right) \tag{3.38}$$

where $\dot{\mathbf{F}}$ is the rate of change of the resultant force, which includes the summation of

the contact forces of each particle, including gravity:

$$\mathbf{F} = \sum_{c=1}^{N_c} \mathbf{F}_c + m\mathbf{g} \tag{3.39}$$

The global non-viscous damping in Yade is based on the formulation of Cundall (1987) and Itasca (2008). This type of damping is a purely numerical device to dissipate energy, to facilitate rapid convergence to quasi-static equilibrium in problems of that type. The idea behind it is to decrease those forces that increase the particle velocities, and to increase those forces that are opposed to the motion. This is achieved by comparing the sign of the acceleration (force) and the velocity. The damping force is expressed as

$$\mathbf{F}_{d,k} = -\alpha|\mathbf{F}_k|\mathrm{sgn}\left(\mathbf{F}_k\dot{\mathbf{x}}_k^{\ominus}\right), \quad k \in \{x, y, z\} \tag{3.40}$$

where α is a dimensionless non-viscous damping coefficient and $\mathbf{F}_k$ is the resultant force on the particle. The calculation is done per component, hence the subscript k. Being a purely numerical device, its influence on the numerical solution needs to be investigated and quantified in each simulation.

3.3.3.2 Contact viscous damping

Contact damping was also introduced by Cundall and Strack (1979) in addition to the global damping, as a more realistic way to suppress particle oscillations.

The contact damping operates on the particle relative velocities, so it is viscous-type damping. It is calculated at the contact level, during the calculation of the contact forces, hence it is also referred to as local damping. It may be envisioned as dashpots acting in the normal and shear directions at the contact between two particles. The

contact damping forces in Eq. 3.33 and 3.34 read

$$\mathbf{F}_{n,v} = C_n \dot{\mathbf{U}}_n \tag{3.41}$$

$$\mathbf{F}_{s,v} = C_s \dot{\mathbf{U}}_s \tag{3.42}$$

where $\dot{\mathbf{U}}_n$ and $\dot{\mathbf{U}}_s$ are the relative velocity vectors at the contact in the normal and shear directions (i.e. the current rate of change overlap and of relative shear displacement), and C_n and C_s are damping constants (units: mass/time). In the original Cundall and Strack (1979) formulation the damping coefficients are proportional to the contact tangent stiffnesses through coefficients ζ: $C_{n,Cund} = \zeta_n k_n$ and $C_{s,Cund} = \zeta_s k_s$ in the normal and shear directions. This derives from the condition of a critically damped single degree of freedom system of a mass, spring and a dashpot.

Tsuji et al. (1992) related the damping coefficients C_n and C_s to the coefficient of restitution ϵ, which is a constant of a more physical nature, via the following equations

$$C_{n,Tsuji} = \gamma \sqrt{m^* k_n} U_n^{1/4} \tag{3.43}$$

$$C_{s,Tsuji} = \gamma \sqrt{m^* k_s} U_s^{1/4} \tag{3.44}$$

where m^* is the effective mass of the particles in contact given by

$$m^* = \frac{m_A m_B}{m_A + m_B}. \tag{3.45}$$

The variable γ is related to the coefficient of restitution ϵ, defined as the ratio of the relative velocities after and before a collision between two particles:

$$\gamma \propto \epsilon = -\frac{v_1}{v_0}. \tag{3.46}$$

There is, in Tsuji et al. (1992), only a suggestion to read the value of the parameter γ from a $\gamma(\epsilon)$ graph, but there is no analytical expression relating the two. Antypov and Elliott (2011), instead, derived an analytical form starting from the equation of

motion, for a collision of bodies when a Hertzian model is used to describe the contact. The solution is represented by

$$\gamma = \frac{-\sqrt{5}\ln\epsilon}{\sqrt{\ln^2\epsilon + \pi^2}}. \tag{3.47}$$

Although dimensionally inconsistent with Eqs. 3.43 and 3.44, this formulation is certainly more specific and immediate than the graph proposed by Tsuji et al. (1992), and it uses the coefficient of restitution ϵ, which is a realistic parameter. However, the coefficient ϵ needs to be evaluated from calibration tests.

Itasca (2008) proposed a simplified version of the coefficient of contact viscous damping. This formulation is also used in Yade. It is based on a damped spring-mass system where the damping coefficients in the normal and shear directions are a fraction of the critical damping coefficient of the system :

$$C_n = \zeta_n C_{n,crit} = \zeta_n \cdot 2\sqrt{m^* k_n} \tag{3.48}$$

$$C_s = \zeta_s C_{s,crit} = \zeta_s \cdot 2\sqrt{m^* k_s} \tag{3.49}$$

where k_n and k_s are the tangent normal and shear stiffnesses and ζ_n and ζ_s are the damping ratios. It should be noticed that, although the formulation of the contact damping is linear, since the contact law in non-linear, a tangent contact stiffness needs to be computed at each time step in each direction:

$$k_n = \frac{\partial F_n}{\partial U_n} = 2E^*\sqrt{R^* U_n} \tag{3.50}$$

$$k_s = \frac{\partial F_s}{\partial U_s} = 8G^*\sqrt{R^* U_n} \tag{3.51}$$

It should be pointed out that, although the solution provided by Tsuji et al. (1992) and Antypov and Elliott (2011) is more realistic because it aims at relating the damping to the coefficient of restitution, its use among DEM researchers is still at an early stage.

Validations and further studies might be necessary, which could be the starting point for future work. Therefore the solution proposed by Itasca (2008) and used in Yade (as in Eq. 3.48 and 3.49) was considered sufficient for this work. A more detailed viscous damping model and its implementation in Yade was not in the scope of this thesis. However, since there is not a fixed value for the damping ratios ζ_n and ζ_s, their values need to be verified by checking that these do no affect the results of the simulation significantly.

3.3.4 Concluding remarks on the contact model

Once all the components of the contact model have been introduced, it is useful to re-examine them all together. The normal component was implemented on the basis of the Hertz theory (Hertz, 1881). The shear component was calculated following the Mindlin no-slip solution (Mindlin, 1949). In both directions, a viscous damping contribution was added to improve numerical stability by providing energy dissipations. A moment–relative rotation law was included to account for the effect of the non-spherical shape of sand grains (Iwashita and Oda, 1998). The contact law formulation is summarised in the Table 3.2 and the non-viscous component of the force–displacement relations are illustrated in Figure 3.14.

The contact law needs only five parameters to be assigned by the user. The Young's modulus E, the Poisson's ratio ν, and the interparticle friction μ are taken from the elastic and frictional properties of the sand grains. The rolling stiffness coefficient β_r and the plastic moment coefficient η are calibrated to match experimental behaviour of real sand. For this research, the parameters of the contact law were calibrated against triaxial tests performed by Schnaid (1990) on Leighton Buzzard sand. The calibration

Table 3.2: Summary of the contact model.

	Normal component	Shear component	Moment
Force (or moment)	$\mathbf{F}_n = \mathbf{F}_{n,el} + \mathbf{F}_{n,v}$	$\mathbf{F}_s^{\circ} = \mathbf{F}_{s,el} + \mathbf{F}_{s,v}$	
Elastic component	$\mathbf{F}_{n,el} = K_n U_n \widehat{\mathbf{n}}$	$\mathbf{F}_{s,el} = \mathbf{F}_s^{-} + \Delta\mathbf{F}_{s,el}$	$\mathbf{M}_{el}^{\circ} = \mathbf{M}^{-} + \Delta\mathbf{M}_{el}$
		$\Delta\mathbf{F}_{s,el} = -k_s \Delta\mathbf{U}_s$	$\Delta\mathbf{M}_{el} = -k_r \boldsymbol{\theta}_r^{\ominus}$
Stiffness coefficient	$K_n = \frac{4}{3} E^* \sqrt{R^* U_n}$	$k_s = 8G^* \sqrt{R^* U_n}$	$k_r = \beta_r k_s \sqrt{U_n} R^2$
Viscous component	$\mathbf{F}_{n,v} = C_n \dot{\mathbf{U}}_n$	$\mathbf{F}_{s,v} = C_s \dot{\mathbf{U}}_s$	
Damping coefficient	$C_n = \zeta_n 2\sqrt{m^* k_n}$	$C_s = \zeta_s 2\sqrt{m^* k_s}$	
Plastic criterion		if $\lvert\mathbf{F}_s^{\circ}\rvert \geq \mu \lvert\mathbf{F}_n\rvert$	if $\lvert\mathbf{M}_{el}^{\circ}\rvert \geq \eta R \lvert\mathbf{F}_n\rvert$
		$\mathbf{F}_s = \mu \lvert\mathbf{F}_n\rvert \frac{\mathbf{F}_s^{\circ}}{\lvert\mathbf{F}_s^{\circ}\rvert}$	$\mathbf{M} = \eta R \lvert\mathbf{F}_n\rvert \frac{\mathbf{M}_{el}^{\circ}}{\lvert\mathbf{M}_{el}^{\circ}\rvert}$

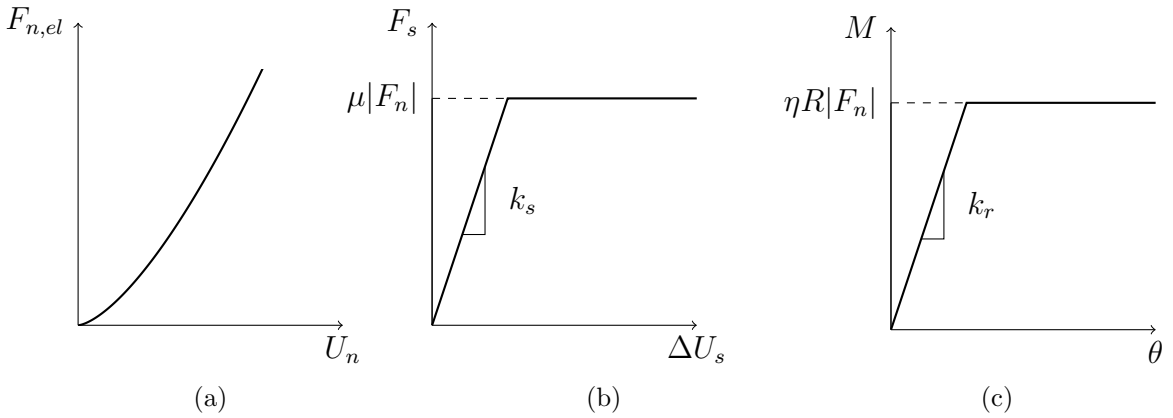

Figure 3.14: Non-viscous components of force–displacement and moment–relative rotation relationships (the shear force and the moment–relative rotation contact models are shown for constant particle overlapping).

procedure is presented in the next chapter.

3.3.5 Critical time step and computational time

To maintain numerical stability, the time step in a DEM simulation should always be smaller than a critical value Δ_{crit}. The reason is to ensure that during a single time step the disturbance cannot propagate from one particle further than its immediate

neighbouring particles.

In DEM the critical time step increment is estimated in analogy with the critical time step of a one dimensional mass-spring system. The critical time step of a particle of mass m on a spring of stiffness k is $\Delta t_{crit} = T/\pi = 2\sqrt{m/k}$, where T is the period. Although the basic idea is equivalent, the formulation for a system of particles becomes less trivial. The formula for the critical time step is taken as the minimum critical time step over all the particles, and as the minimum for each degree of freedom, assuming these are uncoupled (Hart et al., 1988):

$$\Delta t_{crit} = \min_{w} \left\{ \min_{i} \sqrt{\frac{m_i}{K_{i,c}}} \right\} \quad w \in \{x, y, z\} \tag{3.52}$$

where m_i is the mass of particle i, and $K_{i,c}$ is the sum of the contributions of the stiffnesses of all contacts in which particle i participates. This condition gives $\Delta t_{crit} = \infty$ when there are no contacts. Although it is formally correct, it is not acceptable, since it implies that the contact stiffness remains constant throughout the simulation. For the tests described in this thesis, the condition of zero contacts would have occurred not only at the start of the simulations, but also during a long part of the specimen preparation. In fact, the specimens were generated on purpose with non-contacting particles, and then they were slowly adjusted to reach an isotropic state (Section 4.2.1) or to settle under gravity (Section 5.1).

In order to ensure an appropriate time step during these preparation tests, a slightly different formulation was chosen for this work. The time step was then kept constant and used throughout all the simulations. The formulation was still based on Equation 3.52, but it was derived from an estimation of the critical time based on future interactions. It was already implemented in Yade, and its formula reads (Šmilauer

et al., 2010):

$$\Delta t_{crit} = \min_i R_i \sqrt{\frac{\rho_i}{E_i}} \tag{3.53}$$

where R_i is the radius of the particle i, ρ_i its density, and E_i its Young's modulus. Some observations regarding this formulation are necessary. Firstly, simulations with systems characterised by small and stiff particles are performed in longer computational times. Secondly, the critical time step does not directly depend on the number of contacts of each particle in the system. Šmilauer (2010) compared the critical time steps obtained from Eq. 3.52 and 3.53, and found that when a coefficient of 0.3 is applied to the latter equation, the two are approximately equal. Therefore for this work, the same coefficient was applied. In addition, it was verified that the chosen time step produced a stable and accurate solution.

3.3.6 Boundary conditions

Two types of boundary conditions were used for the DEM analyses in this thesis: rigid walls and periodic boundaries.

Rigid walls are planar surfaces of finite stiffness and no volume nor inertia, hence they cannot move as a result of the application of a force. In the thesis, they were used mainly in the tests with the pipe loaded on sand (Chapters 5, 6 and 7).

Periodic boundaries were also used for this work. The domain, i.e. the periodic cell, is surrounded by identical copies of itself. These boundaries allow particles to move out of the cell and to be remapped into the cell at a symmetrical location on the opposite face. The particles are remapped when their center falls outside the cell; if a particle lies near a face, an image (or "ghost") particle is introduced onto the opposite face. Each remapped particle carries all the micromechanical information of

the original one, except for the position. The advantage is a reduced computational time and no influence of geometric boundaries.

Periodic boundaries were used for the triaxial tests (Chapter 4) and for some tests with the pipe (Chapter 6). While for the pipe loading tests the boundary were fixed, the periodic boundary in the triaxial test were dynamic, to deform the sample according to a specific loading path. The load was applied by enforcing a uniform strain field in the periodic cell, which was applied to both the particles and the periodic cell boundaries. The stress on the boundaries was adjusted through a servo-control algorithm, in which the stress rate $\dot{\varepsilon}$ is defined according to Cundall (1988):

$$\dot{\varepsilon} = \dot{\varepsilon} + g\Delta t(\sigma_g - \sigma_c) \tag{3.54}$$

where σ_g and σ_c are the desired and the current stress on the boundaries of the cell, and g the gain parameter, estimated as (Radjaï and Dubois, 2011)

$$g = \frac{L_{cell}}{M_{tot}} \tag{3.55}$$

where L_{cell} is the dimension of the cell, and M_{tot} the total mass of the specimen.

3.3.7 Quasi-static simulations

The triaxial tests described in Chapter 4 were performed under the condition of quasi-static equilibrium. This condition ensures that the simulation is not rate-dependent, and it is performed through a succession of states of static equilibrium.

When attempting to replicate a quasi-static laboratory experiment, it is important that these conditions are also ensured throughout DEM simulations. Quasi-staticity in DEM simulations has been investigated in 2D by Roux and Combe (2002), and in 3D by Roux and Combe (2010). In order to provide sufficient inertial damping so that

quasi-static simulations can be performed in a reasonable time scale, Thornton and Antony (1998) suggest to scale the particle density up by a factor of up to 10^{12}.

The quasi-staticity of a simulation is evaluated in Yade by measuring the so-called unbalanced force ratio, similar to Ng (2006):

$$I_{uf} = \frac{|\sum_{i}^{N_p} \mathbf{F}_i^{in}|}{|\sum_{i}^{N_i} \mathbf{F}_i^{c}|} \tag{3.56}$$

where $\mathbf{F}_i^{in}$ represents the resultant of all the inertial forces on all the particles N_p, and $\mathbf{F}_i^{c}$ is the contact forces arising at the each interaction N_i. Under the conditions of perfect static equilibrium, the resultant forces on all bodies are zero, since those from interactions cancel out, hence $I_{uf} = 0$. Particles have no acceleration, and the total kinetic energy of the system is nil. In practice, quasi-static conditions are deemed to be achieved when $I_{uf} < 1\%$ (Ng, 2006). In this sense, the unbalanced force is a measure of the departure from the static equilibrium.

3.4 Specimen preparation techniques

The described DEM model will be employed in the next chapters to perform simulations of numerical assemblies replicating soil specimens. As the preparation of a physical specimen requires several considerations, similarly the preparation of a numerical sample can be very challenging. This section is dedicated to a review of specimen preparation techniques available in literature.

The most obvious way is to replicate the laboratory specimen preparation's procedure, which generally is performed by pluviation. The particles of the granular material (sand) fall gently under the gravity force either through water (wet pluviation) or air

(dry pluviation). Replicating these procedures in the DEM could be computationally extremely expensive, since large deformations are involved in the simulation, and continuous updates of the contact lists are required. Therefore, a simplified procedure to prepare sample within an affordable runtime is needed.

Specimen preparation methods can be distinguished in two categories: the constructive and the dynamic techniques (Bagi, 2005). Constructive techniques are called those methods where the particles are placed into the domain in a pre-determined medium-dense configuration. Dynamic techniques are instead called those methods where the particles are placed into the domain and then a further modification of their position is performed through DEM calculations. A detail description of the most employed specimen generation techniques are given by Bagi (2005), O'Sullivan (2011b) and Radjaï and Dubois (2011). A brief description is also included in this thesis, to illustrate the approaches more significant for the work described in this thesis, to understand their advantages and their limitations, and to legitimate the choice made for the preparation of the numerical sandy seabed.

3.4.1 Constructive techniques

In the constructive methods the particles are placed in the domain according to purely geometrical algorithms before the simulation starts, without any DEM calculation cycles. They are usually developed for two-dimensional circular particles, and often their extrapolation in three dimensions is not trivial.

The closed form and the open form advancing front approaches developed by Feng et al. (2003) are capable of producing an isotropical 2D arrangement. However large gaps may remain at the edges of the domain. Similarly in the inwards packing method

proposed by Bagi (2005) for 2D assemblies, the density can be only slightly varied. Cui and O'Sullivan (2003) developed a triangulation based approach, both for disks and spheres. Its major drawback is that no user-defined particle size distribution can be inserted. On the other hand, the main advantage is that it is a relatively faster method, and it is useful when it is needed to generate dense packings in irregular geometries.

The main feature of these methods is that they take a rather short computational time to obtain stress-free assemblies of grains exactly touching each other (i.e. with no overlaps) characterized by low density. The particle size distribution might not always be defined, and they all, apart from the triangulation based approach, are implemented solely for 2D problem.

3.4.2 Dynamic techniques

In the dynamic method the particles are placed in the domain randomly or in a pre-defined simple geometry, and then a large amount of calculation cycles are performed to modify the system up to a state of static equilibrium or to a desired state of stress. In this section, particular attention is paid to those procedures used in this thesis.

The most typical approach is the radius expansion method. The particles are placed in a volume, with their diameters smaller than their final size. A simulation is then performed to gradually increase their diameters until a dense packing is reached (Itasca, 2008). The complementary procedure is the isotropic compression method, where the particles are placed with the final size in the domain and the walls are moved inwards until the desired density is obtained. This procedure is largely used for DEM simulations of triaxial tests, when a dense packing at an isotropic state in absence of body forces is needed. A drawback is that the movements of the walls propagates

a compaction front within the sample, generating non-homogeneous specimens with a looser centre and a denser periphery. The multi-layer compaction method proposed by Jiang et al. (2003) aims at generating homogeneous dense samples

A valid alternative is to perform the isotropic compression combined with periodic boundaries conditions, and to apply a uniform strain field to each of the particles, rather than to the walls. In this way the anisotropic effect is reduced. This method was used for the preparation of the numerical sample used in the triaxial test (Section 4.2.1).

The gravitational method introduced by Thomas (1997) for two-dimensional simulations aims at replicating numerically the dry pluviation performed in the laboratories to assemble physical specimens. The particles are created above the domain and are allowed to fall under the gravity force until the system reaches a condition of static equilibrium. The numerical simulation is very expensive, especially due to the large deformations involved during the deposition, which require a frequent update of the contact list. Hence, instead of placing the particles above the domain, it is often preferred to place them already in the domain that will be used for the main simulation, which is only higher to account for the void spaces due to the initial non-contacting particles. The advantages of the gravitational method are that (i) it can be easily employed in three-dimensional simulations and (ii) it allows a natural soil fabric to develop. As the direction of loading (gravity) is only vertical, the specimen obtained is certainly anisotropic. Compaction by vibration can be replicated by prescribing a velocity to the the rigid boundaries. The porosity at the end of the deposition can be controlled by varied the interparticle friction angle

The "dumping" method proposed by Radjaï and Dubois (2011) is based on the gravitational approach, but the gravity is suddenly plugged in. The drawback of this

method is that, due to the sudden increase of the gravity, the obtained assembly is inhomogeneous and characterized by an unrealistic decrease of the density in the bottom layers. They justify it suggesting that an elastic wave travelling upward is generated when the particles hit the bottom, decreasing the density in that area.

In the approach proposed by Marketos and Bolton (2010) one particle at a time is moved vertically until it is in contact with pre-existing particles and forced to move laterally until a position of stable equilibrium is reached. Although it requires a high computational effort, it allows to generate anisotropic assemblies, looser at the top and denser at the bottom.

Gravitational approaches for particles falling form a hopper are proposed by Feng et al. (2003) in 2D and by Radjaï and Dubois (2011) in 3D. These pluviation methods, however, require extremely high computational costs, as the particles are subject to very large deformations, more than in the other gravitational approaches.

As also pointed by O'Sullivan (2002), the disadvantages of the gravitational and pluviation methods are the difficulties of obtaining homogeneous specimens and their computational costs, not only during the generation stage to avoid overlapping of particles, but especially during the settlement. However they are still capable of reproducing laboratory assembling techniques and obtaining natural soil fabric at various densities.

3.5 Summary

This chapter has demonstrated that dry sandy soils are particulate materials, and that the distinct element method (DEM) is an attractive method for simulating the

mechanical behaviour of such soils. In principle the DEM, as a particulate numerical method, is able to capture the behaviour of each grain forming the soil.

The open-source DEM code Yade was introduced and its performance was investigated. As numerous particles are necessary to replicate the soil response in boundary value problems, the computational demand may be very high. Employing the OpenMP environment and the specific parallelization of some loops, it was found that optimal performances could be obtained from Yade by using a number of processors varying from 6 to 8.

The last section of the chapter was dedicated to a brief overview of the DEM features of Yade. The description of the numerical method and its theoretical derivation allowed reasonable choices regarding the type of contact model, damping, and time step. A simplified version of the Hertz–Mindlin contact model was chosen, together with damping of viscous or non-viscous type, depending on the simulation characteristics. As the shape of grains affects the mechanical behaviour of sands, a moment–relative rotation contact law was implemented. As will be shown in Chapters 4 and 7, this law will be crucial for replicating correctly the behaviour of the sand of interest and to validate the DEM model against experimental data. On the basis of the review of specimen preparation techniques, one will be chosen in Chapter 5 and employed to prepare numerical sand specimens for the pipe–soil interaction analyses.

Chapter 4

Calibration of DEM analysis parameters

This chapter presents the procedure employed to calibrate the micromechanical parameters of the spherical particles. The procedure to generate an isotropic sample is then illustrated. The results of dimensional analysis of the parameters controlling the simulation and the macroscopic response of the material are presented. A calibration procedure is proposed, and finally the results at the macroscopic and microscopic level are discussed.

4.1 Soil characteristics

The tests were carried out on a numerical sample reproducing the characteristics of white Leighton Buzzard (LB) sand 14/25, fraction B. The LB sand was chosen for its widespread use in research for laboratory testing. In addition, the silica grains are characterised by a high resistance against crushing (Section 2.1.1), which is favourable

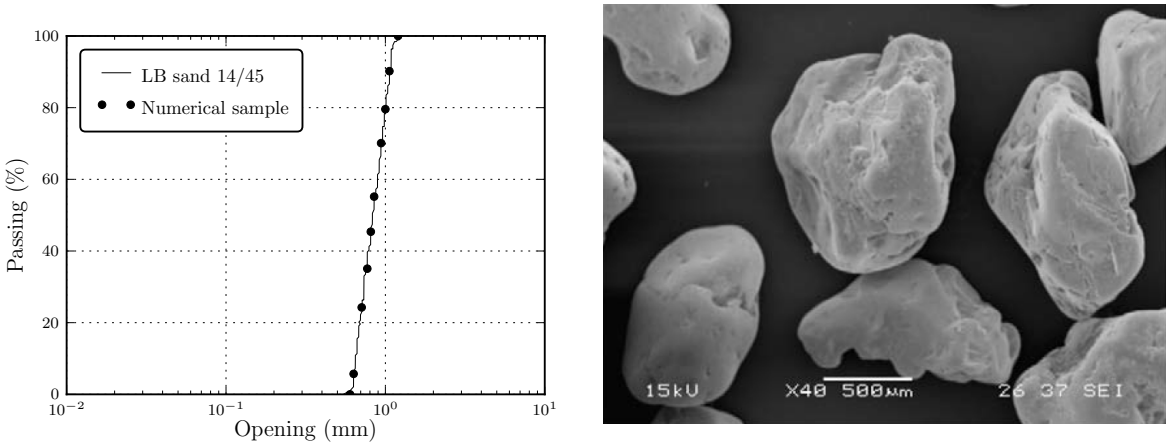

(a) (b)

Figure 4.1: (a)Particle size distribution of LB sand fraction B, replotted after Schnaid (1990). (b) Scanning electron micrograph of LB sand fraction B (Cabalar (2010) with permission of Springer).

Table 4.1: Physical and mechanical properties of the LB sand, taken form Schnaid (1990).

Specific gravity G_s	Max void ratio $e_{\max}$	Min void ratio $e_{\min}$	Diameter D_{50} (mm)	Friction angle ϕ_{crit} (°)
2.65	0.774	0.479	0.8	34.3

as the adopted numerical model does not account for particle breakage.

LB sand 14/25 passes through the No. 14 British Standard sieve (1.18 mm) and is retained on the No. 25 sieve (0.6 mm), being in the category of medium-coarse sand, as shown by the particle size distribution (PSD) in Figure 4.1(a). Individual grains are mostly mostly silica (quartz) minerals, with subangular to subrounded shape (Figure 4.1(b)). Key properties of the LB sand are summarised in Table 4.1. The uniformity of soil can be expressed by a uniformity coefficient $U_c = 1.3$, which is defined as the ratio of D_{60} and D_{10}.

The interparticle friction angle ϕ_μ is defined as the inverse tangent of the average coefficient of kinetic friction at which particles start sliding over each other. It is

Table 4.2: Interparticle friction angle of quartz grains.

	ϕ_μ (°)	comments
Rowe (1962)	22 - 31	water-saturated particles on flat
Bromwell (1966)	27	block on block, various conditions and cleanliness
Procter and Barton (1974)	17.4	dry particle on flat
Procter and Barton (1974)	22	water-saturated particle on flat
Procter and Barton (1974)	26	water-saturated particle-particle

usually measured experimentally between two or few particles. Measured friction angles of quartz grains are summarised in Table 4.2. Rowe (1962) measured the friction angle between a few water-saturated quartz particles on a flat surface, obtaining values ranging between 22 and 31°, consistent with measurements from other researchers. Bromwell (1966) attributed most of the changes of the interparticle friction angle to the level of surface cleanliness. He observed a gradual decrease of ϕ_μ with the increasing of the time spent drying the clean quartz grains, suggesting that the contamination occurs very rapidly. The effect of the cleaning process depends on the roughness of the surface. On average, Bromwell obtained for rough quartz particles $\phi_\mu = 27°$. Procter and Barton (1974) measured 26° for the particle-particle contact of saturated quartz grains, and 22 and 17.4° for the particle-flat contact of saturated and dry grains respectively. Also, Procter and Barton (1974) pointed out that, in general, it is more difficult to measure the interparticle friction angles of dry particles, as those were also cleaned to remove superficial grease. Particles exposed to the atmosphere are contaminated with dust, organic compounds and gases which act as lubricants. Cleaning with water removes these and increases the surface friction. The effect of the organic compounds, however, depends on both the efficiency of the cleaning technique, and on the roughness of the particles.

In general, quartz particles are never perfectly clean, and 26° is a value widely accepted for describing the interparticle friction angle of both dry and wet quartz grains (Mitchell and Soga, 2005). Therefore $\phi_\mu = 26^\circ$ was chosen to represent the friction angle between the LB sand grains in the DEM analyses.

4.2 Numerical simulations of triaxial tests

4.2.1 Specimen preparation

It is common practice that specimens for triaxial compression tests are prepared by isotropic compression. In general, particle assemblies for numerical simulations in geomechanics can be obtained using various procedures. These were more exhaustively described in Section 3.4. Realistic triaxial simulations may be performed when the same experimental specimen preparation procedure is replicated, so that the initial numerical particle assembly is comparable with the real specimen.

Numerical particle assemblies and real specimens may be conveniently compared using the relative density, rather than the absolute density. This is because the arrangement of real angular grains differs from that of numerical spherical particles. The relative density, however, is computed relative to the loosest and densest possible conditions for a given set of particles, reducing the influence of the angularity of real grains. The relative density is defined as:

$$RD = \frac{n_{\max} - n}{n_{\max} - n_{\min}} \cdot \frac{1 - n_{\min}}{1 - n} \tag{4.1}$$

where n is the porosity of the specimen, and $n_{\max}$ and $n_{\min}$ are the porosities at its loosest and densest state respectively.

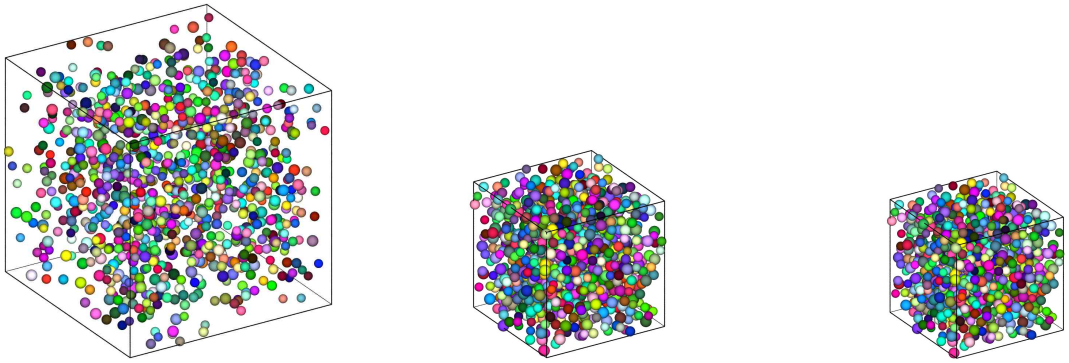

(a) (b) (c)

Figure 4.2: (a) Generation of the sample and evaluation of (b) the maximum and (c) the minimum porosities.

Hence the triaxial tests described herein were run on numerical samples whose relative density was compared to the relative density of the experimental samples used to calibrate the DEM model. The maximum and minimum porosities, required for the determination of the relative density, were estimated with a procedure based on the radius expansion-friction method decrease proposed by Chareyre and Villard (2005) and Salot et al. (2009). Also Thornton (2000) used a similar procedure, generating loose and dense assemblies of sphere by adopting high and low interparticle friction angles.

The method consists of generating the numerical sample in a periodic cell with a very high interparticle friction angle ($\phi_{\mu 0} = 80°$) and no initial contact among particles (Figure 4.2(a)). A uniform strain rate field is then applied to all the particles of the periodic cell, leading to a gradual increase of confining pressure up to 1 kPa. In these conditions, the sample is considered to be at its loosest state (maximum porosity, Figure 4.2(b)). The value of 1 kPa is chosen as a reference. The results are not affected by its value, as long as it is small enough in comparison to the confining pressure used in the triaxial tests. Then the friction angle is gradually reduced to

0°, where the numerical sample is considered to be at its densest state (minimum porosity, Figure 4.2(c)). Knowing the maximum and minimum porosities, a sample with a desired relative density can be generated by decreasing the friction angle at a constant confining pressure of 1 kPa until the porosity corresponding to the desired relative density is achieved. Then the confining pressure is gradually increased up to the value required in the shear phase.

4.2.2 Representative elementary volume

Periodic boundaries were used during the triaxial test simulations in order to reduce the number of particles necessary to avoid boundary effects, hence greatly reducing the computational time.

A particle assembly with the PSD as in Figure. 4.1(b) was generated in a cuboidal volume whose size needed to be assessed. A representative elementary volume (REV) is defined as the minimum volume of soil sample for which a given parameter is independent of the sample size. Hence the REV size is considered adequately representative when it does not affect the response in terms of macroscopic parameters, e.g. the elastic modulus and the peak friction angle of the material. The size of this REV should be large enough, with respect to the individual grain size, in order to define overall continuum quantities such as stresses and strains. Moreover, the capability of reproducing the real behaviour of a sample, hence the size of the REV, needs to be balanced with the necessity of a reasonable timescale to simulate it.

Samples with same micromechanical properties, but different numbers of particles were tested to assess the proper number to be used in the following triaxial test simulations. Cubic periodic samples formed of 1000, 5000, 10 000 and 20 000 particles were

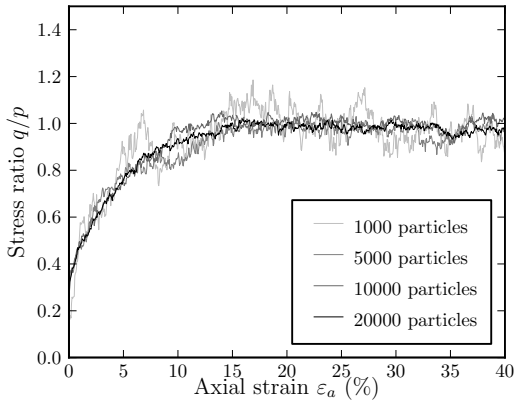

Figure 4.3: Evolution of stress ratio for numerical samples with different numbers of particles at a confining pressure of 100 kPa.

tested. The results are shown in Figure 4.3. The deviatoric stress was calculated as $q = (\sigma_1 - \sigma_3)$, σ_1 and σ_3 being the major and minor principal stresses. All the stresses are effective stresses, as all the DEM analyses were conducted without pore fluid. The axial strain was calculated as $\varepsilon_a = \varepsilon_1$ and the volumetric strain as $\varepsilon_v = (\varepsilon_1 + \varepsilon_2 + \varepsilon_3)$, ε_1 being the vertical strain and ε_2 and ε_2 the lateral strains. Compressive stresses and strains are taken as positive in accordance with the classical convention of soil mechanics.

Figure 4.3 shows that the mechanical response does not change if 5000, 10 000 or 20 000 particles are employed. Larger oscillations are observed for decreasing number of particles, which is expected due to the particulate nature of the assembly. The chosen size of the REV for the triaxial simulations is 5000 particles. This REV is appropriate to represent the converged macro-response, but might not be sufficient to replicate the micro-mechanisms occurring at a particle level (see Section 4.6). Since the main objective of these triaxial simulations was to calibrate the DEM contact model against the macroscopic response of the material, an REV size of 5000 was considered sufficient.

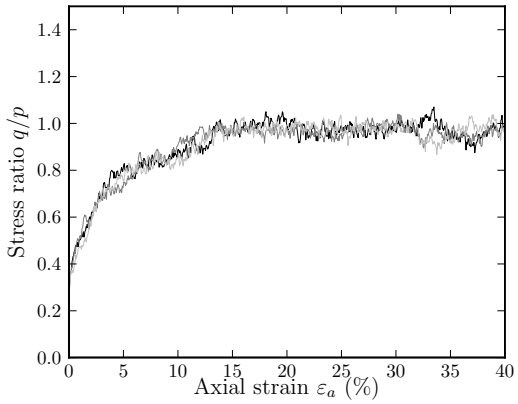

Figure 4.4: Evolution of stress ratio for samples randomly generated at a confining pressure of 100 kPa.

4.2.3 Influence of sample variability

The aim of these preliminary tests was to verify that the macroscopic response of the simulation was not affected by the initial random process of the generation of the sample, as long as the particle size distribution remained constant. Therefore triaxial test simulations were repeated three times, using samples with the PSD as in Figure 4.1(a) and identical micromechanical properties. The generation process, due to its random algorithm, might have created slightly different samples.

The results are illustrated in Figure 4.4 and show very similar stress–strain behaviours, suggesting that the simulations are reproducible. The slight differences observed are entirely realistic, as the sample variability is a real physical property. In fact the variability would be expected to decrease further with an increase of the number of particles, in the same way that it decreases for larger real soil samples. It was also checked, although it was expected, that identical assemblies, generated with the particles in the exact same initial locations, exhibited very similar behaviour. Little differences are still expected, and these are due to the parallelism of the code (Šmilauer et al., 2010).

4.3 Dimensional analysis

The theory of dimensional analysis allows scaling correctly the values of the DEM parameters in order to reduce the computational time while ensuring numerical stability throughout the simulation. Some parameters were considered to have an important effect on the macroscopic response of the sand. These parameters are listed as follows:

- porosity n [-] of the sample;
- density $\rho\,[\mathrm{ML}^{-3}]$ of the particles;
- contact parameters, which are the Young's modulus $E\,[\mathrm{ML}^{-1}\mathrm{T}^{-2}]$, the Poisson's ratio ν [-], and the friction angle ϕ_μ [-]. Initially the particles were free to roll. When, from the numerical results, the inadequacy of the model with no resistance to rolling became evident, the moment–relative rotation contact law was introduced. Hence the effects of the two coefficients for the rolling resistance model were assessed as well. These are the rolling stiffness coefficient β_r [-] and the coefficient for the plastic moment η [-];
- parameters controlling the simulation, i.e. the confining pressure $p\,[\mathrm{ML}^{-1}\mathrm{T}^{-2}]$ during the shear phase and the strain rate $\dot{\varepsilon}\,[\mathrm{T}^{-1}]$ applied to the periodic cell.

It was also convenient to include the number of particles N_p and the particle diameter D_{50} among the control parameters, even if they were not varied.

According to dimensional analysis theory (Palmer, 2008), the outcome of a physical or a numerical experiment, if expressed in dimensionless quantities (stress ratio, strain, porosity, etc.), depend only on dimensionless combinations of the parameters of the problem. As a general rule, the Buckingham πtheorem relates the number n_π of independent (dimensionless) groups, to the total number n_p of dimensional physical

variables and to the number n_k of independent dimensions:

$$n_\pi = n_p - n_k. \tag{4.2}$$

Separating the dimensionless variables (N_p, n, ν and ϕ_μ) from the dimensional ones (ρ, E, p, $\dot{\varepsilon}$ and D_{50}), it follows that $n_p = 5$. The independent dimensions are M, L and T, giving $n_k = 3$. Hence the previous equation becomes $n_\pi = 5 - 3 = 2$, and provides the number of dimensionless groups for the five dimensional variables.

Assuming as fundamental variables D_{50}, $\dot{\varepsilon}$, and p, and isolating the stiffness parameters, the two dimensionless groups for the remaining dimensional variables can be derived. These are the inertial number I and the stiffness number κ.

The inertial number I is defined similarly to Radjaï and Dubois (2011), as

$$I = \dot{\varepsilon} D_{50} \sqrt{\frac{\rho}{p}}. \tag{4.3}$$

The formula is derived from the ratio of the characteristic time scales of the simulation: microscopic inertial time t_i and the macroscopic deformation time $t_{\dot{\varepsilon}} = 1/\dot{\varepsilon}$. The inertial time is estimated as the time required for a particle of density ρ and diameter D_{50} to travel a distance equal to its diameter when subjected to a force pD_{50}^2, hence $t_i = \sqrt{m/pD_{50}} = \sqrt{\pi/3} \cdot D_{50}\sqrt{\rho/p}$. This number represents the amount of inertia of the system. In ideal quasi-static conditions, $I = 0$. In attempting to find a compromise between accuracy and computational effort, I is practically close, but never equal, to zero. The value taken by the inertial number for a particular simulation is a measure of the departure from static equilibrium.

Assuming non-linear Hertzian contacts, as used in the DEM analyses in this research, the formula for the stiffness number κ reads:

$$\kappa = \frac{D_{50}}{U_n} = \left[\frac{E}{3(1-\nu^2)p}\right]^{2/3}. \tag{4.4}$$

This is derived from the ratio between median particle size and overlapping, hence it estimates the fraction of a particle's size which is expected to experience overlapping. Therefore it characterises the elastic stiffness of the particle assembly.

In addition to I and κ, Radjaï and Dubois (2011) suggest to also to compare the tangent shear and normal stiffnesses, using the ratio k_s/k_n (from Eq. 3.14 and 3.19):

$$\Pi_\nu = \frac{k_s}{k_n} = \frac{2(1-\nu)}{2-\nu}. \tag{4.5}$$

Therefore the expected response of the material can be expressed in terms of dimensionless quantities as basic quantities before derived:

$$\left(\frac{q}{p}, \varepsilon_a\right) = \left(N_p, n, I, \phi_\mu, \kappa, \Pi_\nu\right). \tag{4.6}$$

Tests conducted during the present study showed that the Poisson's ratio affects the mechanical response only slightly. This was also noted by Plassiard et al. (2009) and Radjaï and Dubois (2011). The same happened to be true for the range of values of interparticle friction angle tested here (from 21 to 36°), in agreement with Cavarretta et al. (2010). Hence these two parameters have not been included in the dimensional analysis presented below.

The effect of the remaining dimensionless parameters was investigated against a benchmark simulation. The reference simulation was run with 5000 particles and was characterised by the micromechanical properties of the LB sand (illustrated in Section 4.1). For the elastic parameters, typical values for silica were chosen, hence a Young's modulus of $E = 70\,\text{GPa}$ and a Poisson's ratio of $\nu = 0.3$. The interparticle friction angle ϕ_μ was taken as 26° (Rowe, 1962; Procter and Barton, 1974; Mitchell and Soga, 2005). This gives a coefficient $\mu = \tan\phi_\mu = 0.49$. The density was scaled up by a factor of 10^9, which gives $\rho = 2650 \times 10^9\,\text{kg/m}^3$. Scaling the particle density up

Table 4.3: DEM input parameters of the reference test.

Parameter	Symbol	Value	Units
Number of particles	N	5000	
Median particle size	D_{50}	0.8×10^{-3}	m
Particle density	ρ	2650×10^{9}	kg/m^3
Confining pressure	p	100	kPa
Strain rate	$\dot{\varepsilon}$	1.0×10^{-4}	s^{-1}
Time step	Δt	5.8×10^{-4}	s
Damping coefficient	α	0.5	
Young's modulus	E	70	GPa
Poisson's ratio	ν	0.30	
Interparticle friction coefficient	μ	0.49	
Rolling stiffness coefficient	β_r	0	
Plastic moment coefficient	η	0	

in order to complete simulations within a reasonable timescale is a common practice in DEM (Thornton, 2000). However, a preliminary analysis is necessary to assess the combination of strain rate and density to keep the simulation in quasi-static conditions. A non-viscous damping coefficient $\alpha = 0.5$ was used during the simulation (Eq. 3.40). Since all the simulations were quasi-static, the particle kinetic energy remained very small at all times. The time step was chosen as a fraction of the time that an elastic wave takes to propagate within a given particle (Eq. 3.53). Following the suggestion from Šmilauer (2010), an additional safety coefficient of 0.3 was taken, which gives a time step of 5.8×10^{-4} s. All the simulations were run at a constant confining pressure p equal to 100 kPa. A summary of the input parameters of the reference test is given in Table 4.3.

It is important to stress that performing these preliminary simulations was not merely a parametric exercise, but was necessary for identification of the correct values to be assigned to the mechanical parameters and the characteristic times. This set of parameters included firstly the scaling factor for the particle density, and the strain

rate. Once the numerical simulation was found to be stable, simulations to calibrate the contact parameters were performed.

4.3.1 Influence of inertial number

As already mentioned in Eq. 4.3, the inertial number depends on the particle size and density and loading conditions. Therefore triaxial test simulations were run for different values of I, varying both particle density and strain rate. The input parameters are summarised in Table 4.4. Particle density was varied between 2650×10^8 and $2650 \times 10^{10}\,\mathrm{kg/m^3}$, and the strain rate between 3.2×10^{-5} and $3.2 \times 10^{-4}\,\mathrm{s^{-1}}$.

The values were chosen such that the density was respectively one order of magnitude smaller (TX02) and larger (TX03) than the reference simulation (TX01). Then two other tests (TX04 and TX05) were performed at fixed particle density, but at strain rates such that the product $\dot{\varepsilon}\sqrt{\rho}$ remained constant. Therefore in Tests TX02 and TX04 the inertial number was equal to 1.3×10^{-4}, and they were performed with low particle density and high strain rate respectively. In Tests TX03 and TX05 the inertial number was equal to 1.3×10^{-3}, and they were performed with high particle density and low strain rate respectively.

The results are presented in Figures 4.5 and 4.6. Firstly, the effect of the particle density and the strain rate is illustrated in Figure 4.5. There is not an evident influence of the density, which proves the adequacy of its scaling factor (Figure 4.5(a)). There is, however, an effect of the strain rate, and this is more evident as the strain rate is higher (Figure 4.5(b)). This result implies that for certain loading rates the system is strain rate dependent, even in those simulations when inertial number is as small as $I \simeq 10^{-4}$. Roux (2005) and Radjaï and Dubois (2011), however, suggested that

Table 4.4: Summary of analyses performed with different values of the inertial number.

Test	ρ (kg/m^3)	$\dot{\varepsilon}$ (s^{-1})	I (-)
TX01	2650×10^{9}	1.0×10^{-4}	4.0×10^{-4}
TX02	2650×10^{8}	1.0×10^{-4}	1.3×10^{-4}
TX03	2650×10^{10}	1.0×10^{-4}	1.3×10^{-3}
TX04	2650×10^{9}	3.2×10^{-5}	1.3×10^{-4}
TX05	2650×10^{9}	3.2×10^{-4}	1.3×10^{-3}

the quasi-static limit is approached for $I \leq 10^{-3}$. It should be mentioned that, with respect the Eq. 4.3, those researchers defined the inertial number as $I\sqrt{\pi/6}$. Their formulation slightly decreases the value of I, but does not vary the order of magnitude of the number itself.

Interesting considerations can be drawn when the five simulations are plotted together, as shown in Figure 4.6. Tests with identical inertial number I and performed with small strain rates (such that they are not rate dependent) give rise to the same macroscopic response (Tests TX02 and TX04). This is in agreement with the dimensional analysis theory, where the response of the material changes only when the dimensionless group I varies, regardless of the values of the dimensional variables ρ and $\dot{\varepsilon}$. The slight discrepancy between TX02 and TX04 is due more to the variability of the simulation itself, rather than to the difference in the input parameters.

On the contrary, tests with identical inertial numbers but high strain rates (such that they are strain rate dependent) give rise to two different macroscopic responses (Tests TX03 and TX05). This is in contrast with the dimensional analysis theory, as the input parameters of the two tests provided identical I. As the unbalanced force ratio is a lot greater than 1 %, the simulations are not in quasi-static conditions. Hence parameters such as the damping coefficient or the scaled density might affect

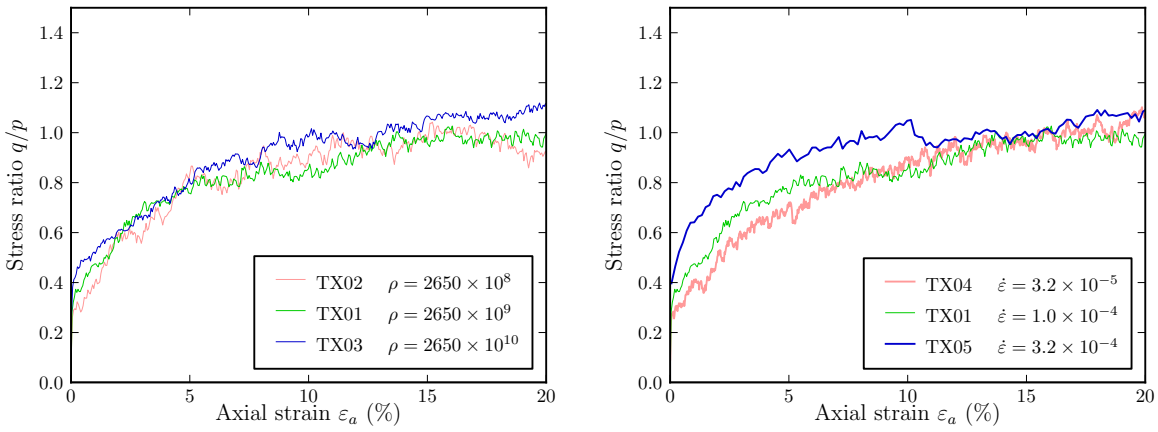

(a) (b)

Figure 4.5: Influence of (a) particle density and (b) strain rate.

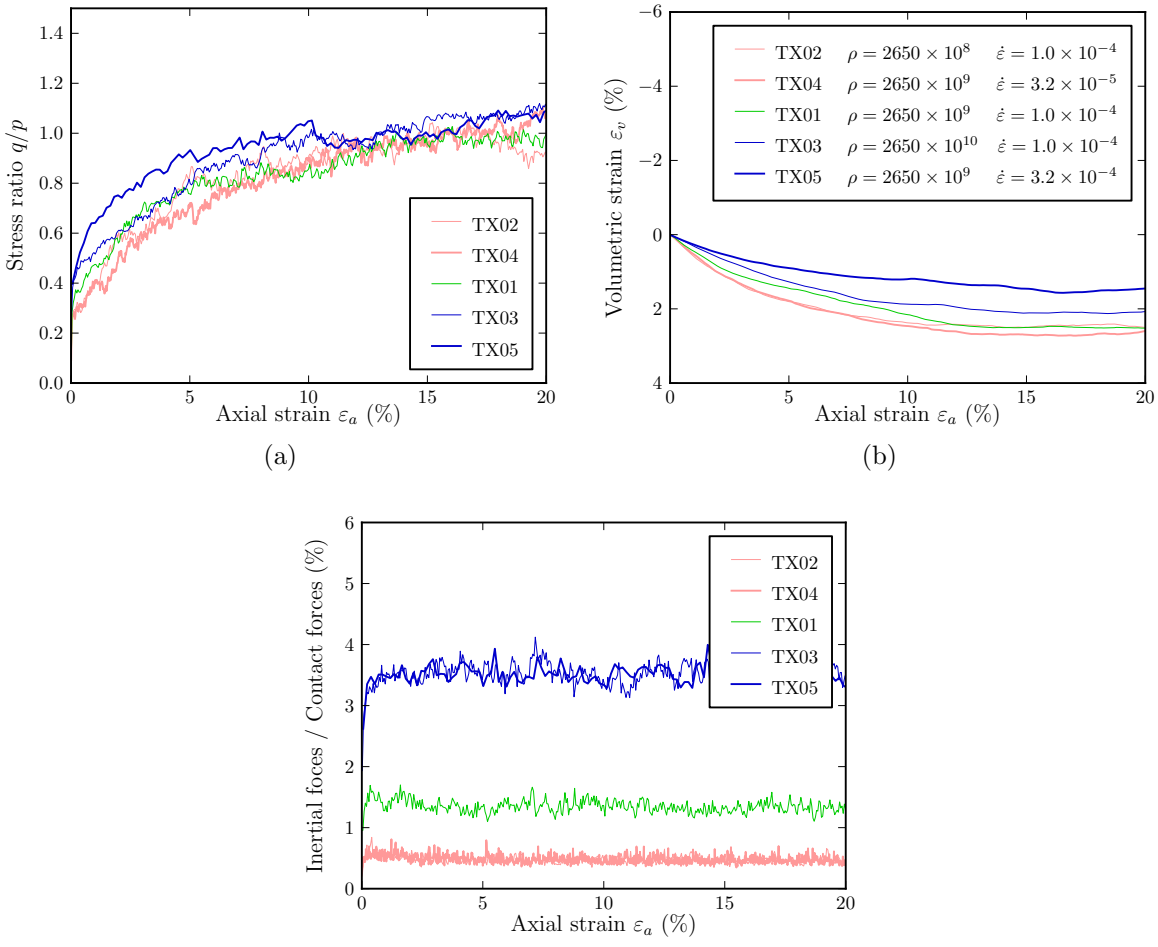

(a) (b)

(c)

Figure 4.6: Evolution of (a) stress ratio, (b) volumetric strain, and (c) unbalance force for samples with different inertial numbers. Curves of same colour correspond to identical inertial number: — $I = 1.3 \times 10^{-4}$, — $I = 4.0 \times 10^{-4}$, — $I = 1.3 \times 10^{-3}$.

Table 4.5: Summary of tests performed with different values of the stiffness parameter.

Test	E (GPa)	p (kPa)	κ (-)
TX01	70	100	4036
TX06	0.7	100	187
TX07	7	100	870
TX08	7	1000	187
TX09	7	10	4036

the results.

As expected, the unbalanced force, i.e. the ratio between inertial and contact forces, is the same in each pair of tests with identical inertial number (TX02-TX04 and TX03-TX05). In other words, the inertial number I is capable of quantifying the equilibrium of the system during the simulation, described by the value of the unbalanced force.

Summarizing, the inertial number provides a measure of the departure from static equilibrium during the simulation. The value $I \leq 10^{-3}$ ensures a stable system, e.g. in terms of small unbalanced force, but is not always sufficient for obtaining an accurate solution.

4.3.2 Influence of stiffness number

The stiffness number in Eq. 4.4 depends on the particle Young's modulus E and external applied pressure p. To investigate the influence of this number, two sets of triaxial test simulations were performed, as summarised in Table 4.5. In the first set (Tests TX06, TX07 and TX01) the Young's modulus was varied between 0.7 and 70 GPa while the confining pressure was kept fixed. In the second set (Tests TX08, TX01 and TX09) the confining pressure was varied between 10 and 1000 kPa while the Young's modulus was kept unchanged.

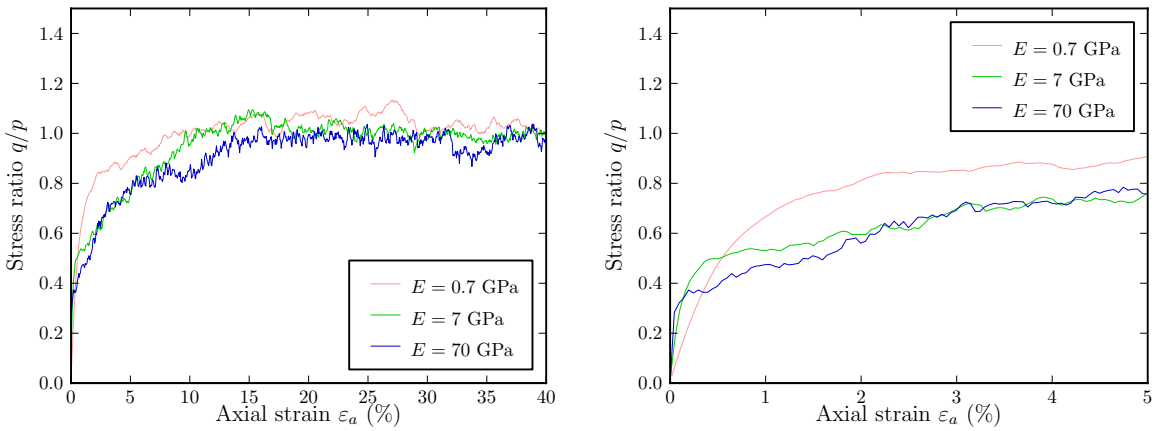

Figure 4.7: Evolution of stress ratio for samples with different Young's modulus.

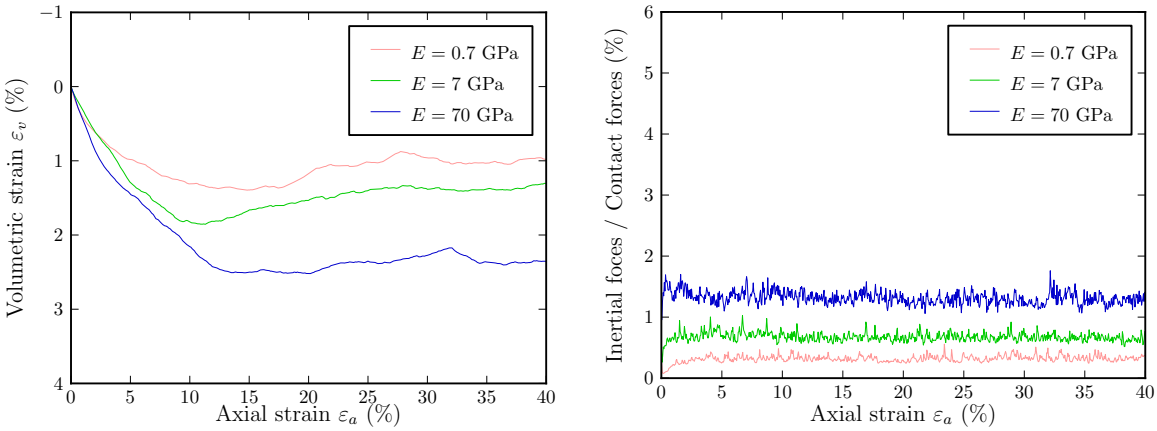

Figure 4.8: Evolution of (a) volumetric strain and (b) porosity for samples with different Young's modulus.

The results of the first set presented in Figure 4.7 and 4.8 show a slight increase of the initial macroscopic Young's modulus with the corresponding microscopic parameters, which is expected as the system is becoming stiffer. However, at larger strains the strength of the system is slightly lower for higher microscopic E. This is probably related to the porosity of the system. Starting from the same relative density during the isotropic phase, the three samples reach the beginning of the shear phase with different porosities, which are higher for higher E: the stiffest sample can be deformed less and

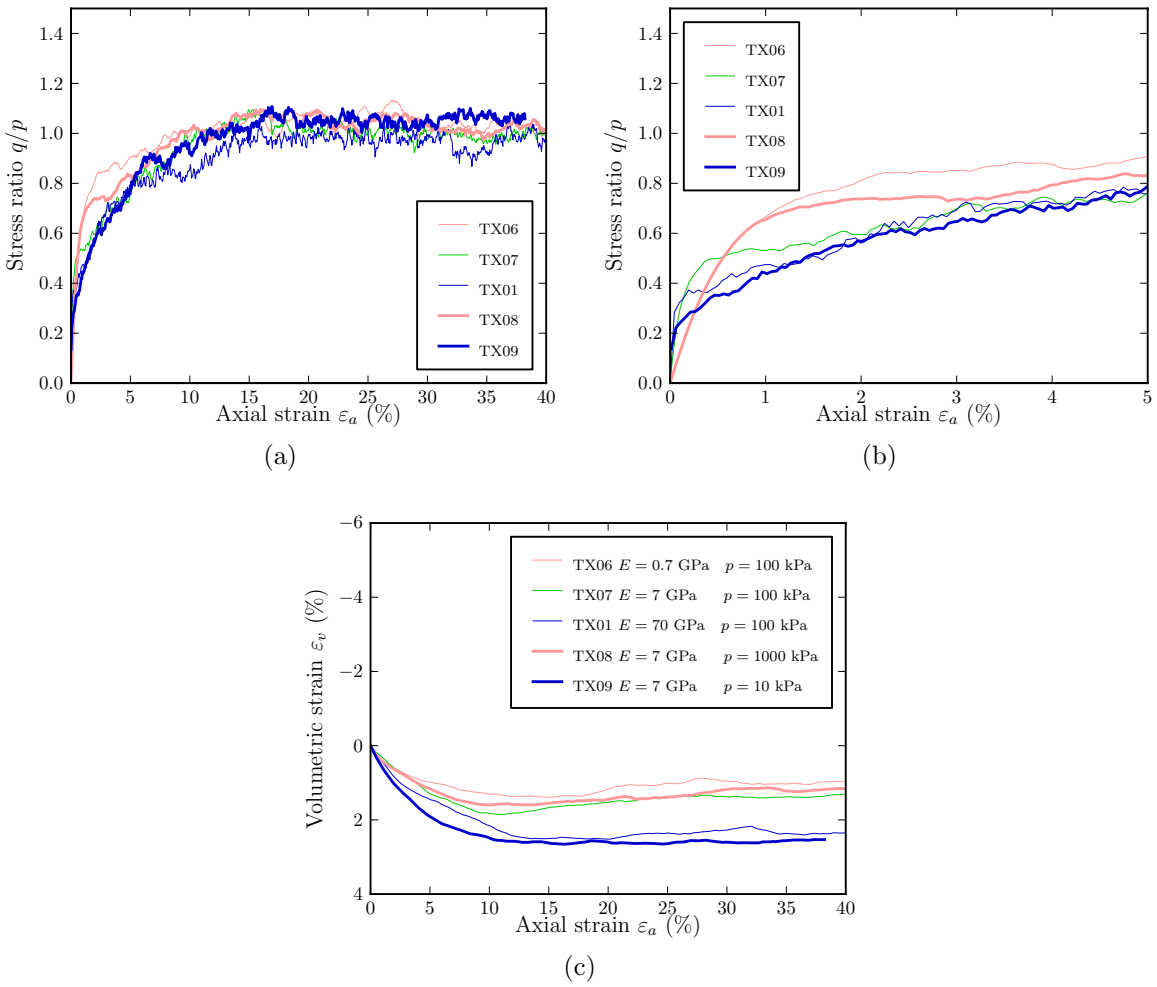

Figure 4.9: Evolution of (a) and (b) stress ratio and (c) volumetric strain for samples with different stiffness numbers. Curves of same colour correspond to identical stiffness number: — $\kappa = 187$, — $\kappa = 869$, — $\kappa = 4036$.

is then less compacted. Hence it is reasonable that the stiffest sample is characterised by lower strength. The evolution of the strain follows the trend just described.

Results for first and second set of simulations are presented in Figure 4.9, so that the effect of the stiffness number can be observed. The results are shown in different colours such that simulations with same stiffness numbers but different E and p can be clearer identified. Tests with identical stiffness numbers produce the same stress–strain behaviour (Figures 4.9(a), (b) and (c)). This is visible both at small and at large strains, and it is in agreement with the dimensional analysis theory. The small

difference between each pair of curves is due to the variability of the simulations.

4.3.3 Influence of rolling parameters

The numerical triaxial tests illustrated in the previous sections were performed using a simplified Hertz–Mindlin contact law, as described in Section 3.3.2 . No moment–relative rotation law was added at the contact. It should be noted that the highest critical state friction angle ϕ_{cs} obtained from these tests was 19.5°, which is much lower than the values exhibited by real sands. As reference, Schnaid (1990) obtained $\phi_{cs} = 35.3°$ for laboratory triaxial compression tests on a Leighton Buzzard sand with the same PSD adopted in these numerical simulations. In order to increase the strength of the numerical material, and hence to match the experimental behaviour, a moment–relative rotation law was introduced. It is convenient to recall the formulation proposed for the rolling model, as presented in Eq. 3.23 and 3.32:

$$\mathbf{M}^{\circ}_{el} = \mathbf{M}^{-} - k_r \boldsymbol{\theta}^{\ominus}_r \tag{4.7}$$

$$\mathbf{M} = \frac{\mathbf{M}^{\circ}_{el}}{\mid \mathbf{M}^{\circ}_{el} \mid} \eta R \mid \mathbf{F}^{\circ}_n \mid \qquad \text{if} \quad \mid \mathbf{M}^{\circ}_{el} \mid \geq \eta R \mid \mathbf{F}^{\circ}_n \mid \tag{4.8}$$

where the rolling stiffness is expressed as $k_r = \beta_r k_s \sqrt{U_n} R^2$, and β_r and η are the rolling stiffness coefficient and the coefficient for the limiting plastic moment. The aim of the tests presented below was to understand the effects of β_r and η on the macroscopic response.

Numerical triaxial tests were performed for different value of β_r, ranging between 0.01 and 1.0, for a loose specimen (Figure 4.10) and for a dense specimen (Figure 4.11). Only the stress–strain curves are reported here, as the influence of the rolling parameters on the volumetric strain was very limited. From the figures it is clear that at

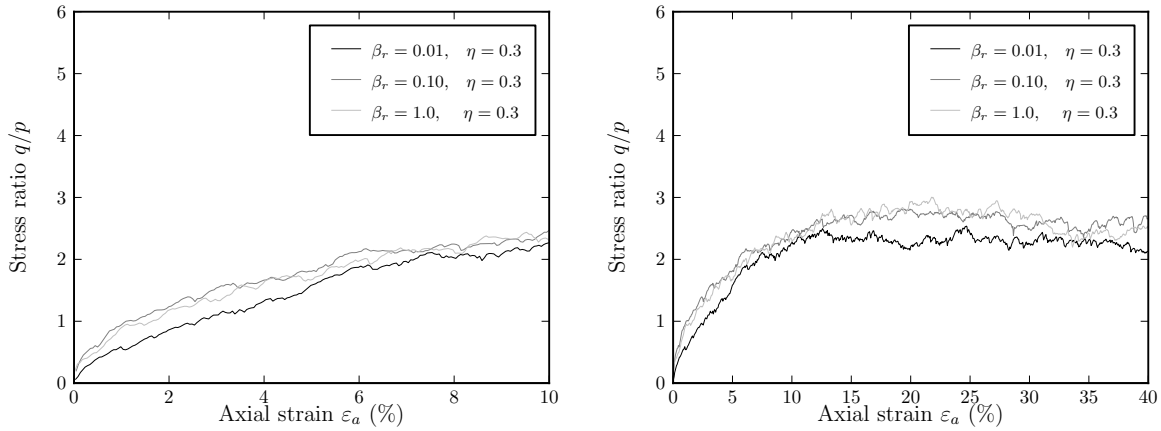

Figure 4.10: Evolution of stress ratio and volumetric strain in loose specimens for different values of β_r, with $\eta = 0.3$. Response at (a) small strains and (b) critical state.

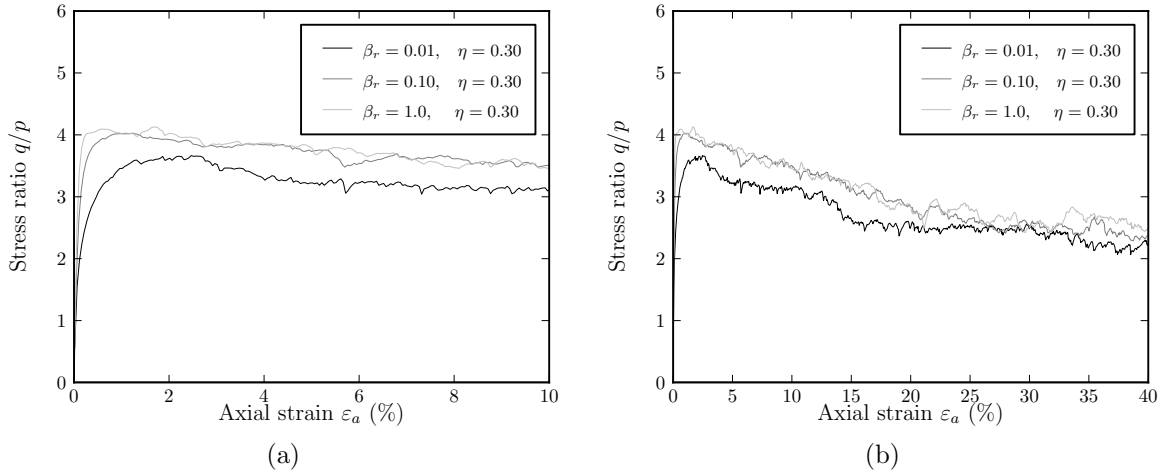

Figure 4.11: Evolution of stress ratio and volumetric strain in dense specimens for different values of β_r, with $\eta = 0.3$. Response at (a) small strains and (b) critical state.

small strains the elastic stiffness of the system increases with increasing β_r. This is in agreement with the formulation of the contact law, as β_r controls the elastic moment–rotation stiffness. The response of the dense specimen at the peak state suggests that a higher peak friction angle is reached with higher β_r. Moreover, for $\beta \geq 0.1$ no further increases occur, in other words, the system reaches its rolling rigidity limit. No influence can be observed at the critical state, for either the loose or dense specimens.

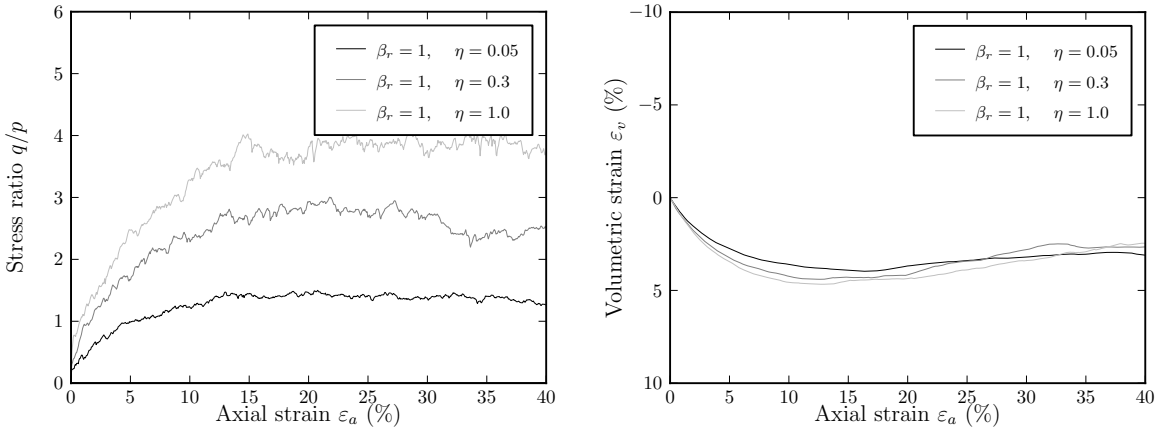

(a) (b)

Figure 4.12: Evolution of stress ratio and volumetric strain in loose specimens for different values of η_r, with $\beta = 1.0$.

Additional tests were then performed on numerical specimens with different values of the plastic moment coefficient η, ranging from 0.05 to 1.0. The results are presented in Figure 4.12 and 4.13 for loose and dense specimens respectively. It is evident η has a strong effect on the critical state stress: the higher the coefficient η, the greater is the mobilised friction angle, for both initially loose and initially dense assemblies. A slight influence on the volumetric strain is observed, but only in dense specimens and for very small values of η. These findings are in agreement with the proposed formulation of the moment–relative rotation contact law. The coefficient η in Eq. 4.8 is the coefficient limiting the maximum plastic moment exhibited by the particles during their rotations. The results show that when η increases, the residual strength of the system increases as well.

The results obtained from various rolling parameters are now briefly compared with available literature. Plassiard et al. (2009) performed numerical triaxial tests on spherical particles with a linear (non-Hertzian) law for the normal component and a linear elasto-plastic law for the shear and rotational component of the contact law.

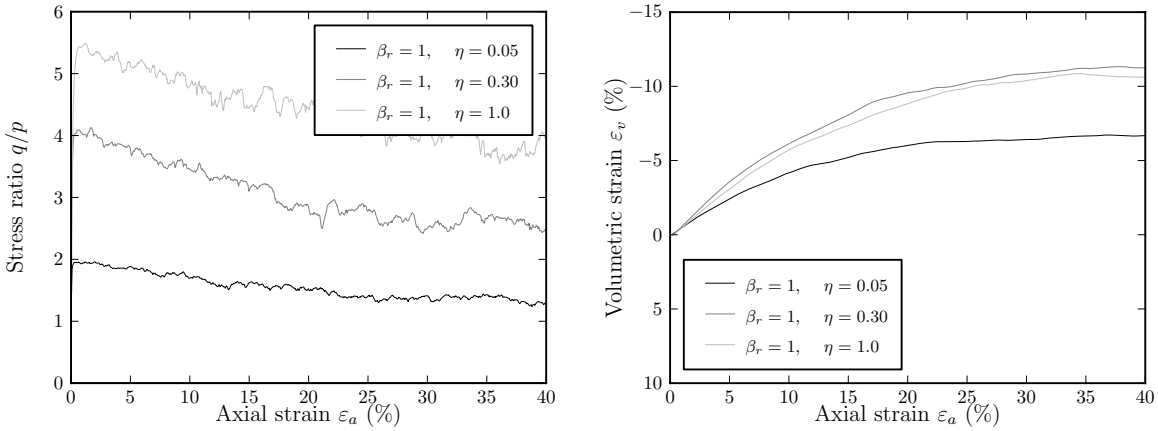

(a) (b)

Figure 4.13: Evolution of stress ratio and volumetric strain in dense specimens for different values of η_r, with $\beta = 1.0$.

They main difference was that the overlapping does not affect the normal, shear and rolling stiffnesses, as it does in the model used in this thesis and illustrated in Eq. 3.14, 3.18 and 3.31. They found a strong effect of β_r on the peak and critical state strengths, and an influence of η on the peak strength only. Widuliński et al. (2009), using a different DEM code but the same type of contact as Plassiard et al. (2009), found the same behaviour. This trend is in contrast with the findings shown in this work. Mohamed and Gutierrez (2010) performed 2D triaxial tests using a linear contact law and a simplified version of the moment–relative contact law, in which only the plastic moment coefficient η needed to be calibrated. For this parameter, they found a strong influence on the peak strength. This is in accordance with the results obtained here. No direct comparison can be done with Zhang et al. (2013), as they not only used a linear contact model, but they also adopted a different formulation for the rolling resistance model, which is based on the contact area between the particles. Although these references are all valuable, they used formulations of the rolling coefficient k_r different from each other, and from the one used in this work. Therefore the mentioned

dissimilarities of the results are justified. Only the analyses of Plassiard et al. (2009) and Widuliński et al. (2009) were performed with the same formulation of k_r, and, as expected, they provided similar trend between them.

4.3.4 Summary of results

The dimensional analysis has demonstrated the importance of determining a suitable size for the REV and an appropriate inertial number I. It has also identified the particle density ρ and the strain rate $\dot{\varepsilon}$ as key parameters necessary for running stable and accurate simulations. Lastly, it has shown the influence of several key micromechanical parameters (Young's modulus E, the rolling stiffness coefficient β_r and the plastic moment coefficient η) on the macroscopic response. The main findings are summarised here, and some preliminary conclusions are drawn.

- When periodic boundaries are used, a specimen of 5000 particles is sufficient to replicate the typical macroscopic response of a granular material subjected to a numerical triaxial test using DEM. The results are not significantly influenced by the random generation of the particles at the beginning of each test, hence the repeatability is ensured.
- With the given PSD, stable and accurate simulations can be performed when the inertial number $I \leq 4 \times 10^{-4}$. It corresponds to a combination of $\rho = 2650 \times 10^9\,\mathrm{kg/m^3}$ and $\dot{\varepsilon} = 1 \times 10^{-4}\,/\mathrm{s}$. The value for the density corresponds to a scaling factor of 9 orders of magnitude on the density of the real sand. However, it was demonstrated that since the simulations were performed in the absence of gravity and in a quasi-static condition, the density scaling does not affect the macroscopic response of the system.

- The interparticle friction angle has a limited influence on the response for the range of values examined (21 to 36°). Hence $\phi_\mu = 26°$ was chosen, as representative of quartz grains.
- The Poisson's ratio has practically no influence on the macroscopic response, and the Young's modulus instead has only a limited influence. For this reason typical values for silica sand were chosen: $E = 70$ GPa and $\nu = 0.3$.
- With the chosen non-linear law employed to describe the contact forces and the contact moment, the parameters controlling the moment–relative rotation contact law influence the macroscopic response as follows. The coefficient β_r increases the elastic stiffness, and the coefficient η controls the strength at the critical state. In addition, both β_r and η control the peak strength. These need to be calibrated against results from laboratory tests.

4.4 Calibration methodology

The calibration was performed against experimental results obtained by Schnaid (1990) on specimens of Leighton Buzzard (LB) sand (see Section 4.1). These were performed on a loose and on a dense specimens at a cell pressure of 100 kPa. The LB sand was already described in Section 4.1, and its PSD ws shown in Figure 4.1(a). The specimens had an initial relative densities $RD = 25$ and 64 %.

4.4.1 Calibration of moment–relative rotation contact law

The plastic moment coefficient η was varied between 0.1 and 1.0, while keeping the rolling stiffness coefficient β_r constant and equal to 0.5. The aim was to match the

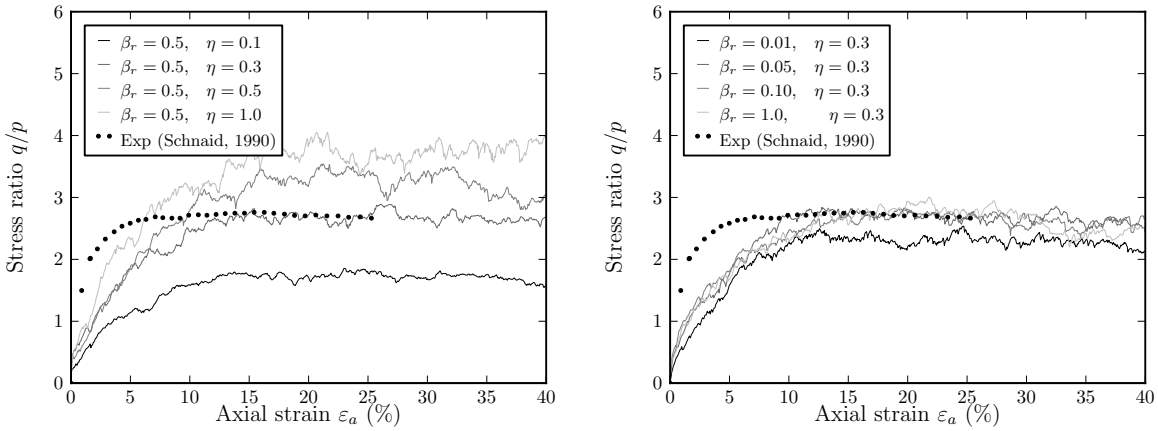

Figure 4.14: Influence of the rolling coefficients on the loose sample

critical stress ratio obtained experimentally. The results in terms of stress–strain in Figure 4.14(a) show that $\eta = 0.3$ matches the experimental curve well .

The coefficient β_r was then varied between 0.01 and 1.0, while keeping the coefficient η constant and equal to 0.3. The results in Figure 4.14(b) show that for $\beta_r \geq 0.05$ the initial elastic stiffness of the material does not change any longer. Hence $\beta_r = 0.05$ was chosen.

4.4.2 Effect of initial porosity

Numerical triaxial tests on samples with different porosities at the beginning of the shear phase were performed. The specimens were generated with a porosity ranging between 0.477 and 0.389, corresponding to a numerical relative density ranging between 25 and 90 %. The goal was to find the values of porosity giving rise to response matching the experimental curves. The results are presented in Figure 4.15.

The figures show good agreement with the general behaviour of loose and dense sands, and with numerical triaxial tests that others researchers have performed using DEM (Thornton, 2000; Salot et al., 2009). As expected, the initial shear modulus

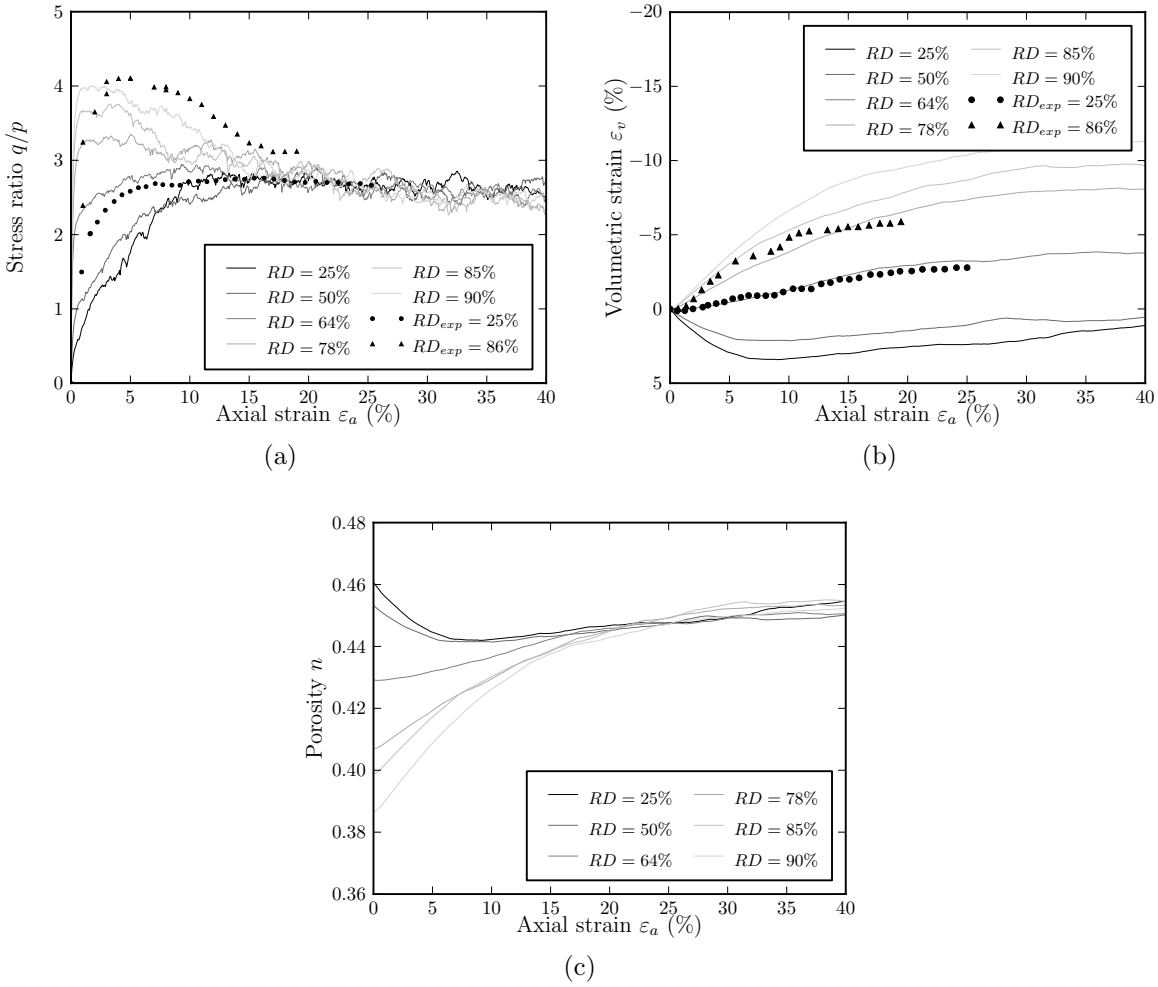

Figure 4.15: Evolution of stress ratio and volumetric strain for different initial porosities, with β_r=0.05, η=0.3.

(initial slope of the curve in Figure 4.15(a)) is higher for the dense samples, which exhibit a peak and then softening behaviour. The volumetric strain shows compression for loose samples, and expansion for the dense ones. The porosity, which is different at the initial state in each simulation, approaches a common, steady value when the axial strain reaches approximately 20-25%. This means that the critical state has been reached. From these figures, two values of the porosity were chosen to replicate the experiments performed on the loose and dense samples. These are $n = 0.427$ ($RD = 64\,\%$) and $n = 0.389$ ($RD = 90\,\%$).

It worth pointing that RD is the numerical relative density calculated from the

porosities of the numerical samples at the densest ($RD = 100\,\%$) and loosest ($RD = 0\,\%$) states, and generated following the procedure described in Section 3.4.

4.4.3 Comparison with experimental results

The numerical results at the end of the calibration process are compared with the experimental results in Figure 4.16. They show the general behaviour exhibited by a granular material during shearing. The loose specimen reaches a flat maximum stress at around $10\,\%$ axial strain, exhibiting a slight dilatant behaviour, which is observed in the experiment as well. The dense specimen reaches the peak stress at around $\varepsilon_a = 2\,\%$ ($5\,\%$ in the experiment) followed by a softening behaviour, during which the soil dilates. As the numerical specimens reach the critical state, the volumetric strain no longer varies and the stress ratios of the two specimens converge at the same level.

Comparison of the results curves between the experiments and the numerical tests shows that a good match is obtained between the two curves for the loose specimen. A good agreement is observed for the stress curve of the dense test, while the numerical specimen is found to be more dilatant than in the experiment at large strains. This might be due to the non-spherical shape of real sand grains, which produces a different arrangement, hence a different volumetric behaviour, especially in dense packings. Aggregates of particles or other non-spherical bodies may be required to achieve a better agreement using DEM. This is a current limitation of the numerical method presented. It should be considered however, that the soil samples used in laboratory experiments to study the pipe–soil interaction are mainly characterised by small relative densities. Samples tested in the pipe–soil interaction experiment of Sandford (2012), for example, had a relative density ranging from 25 to $32\,\%$, which is not very far to the relative

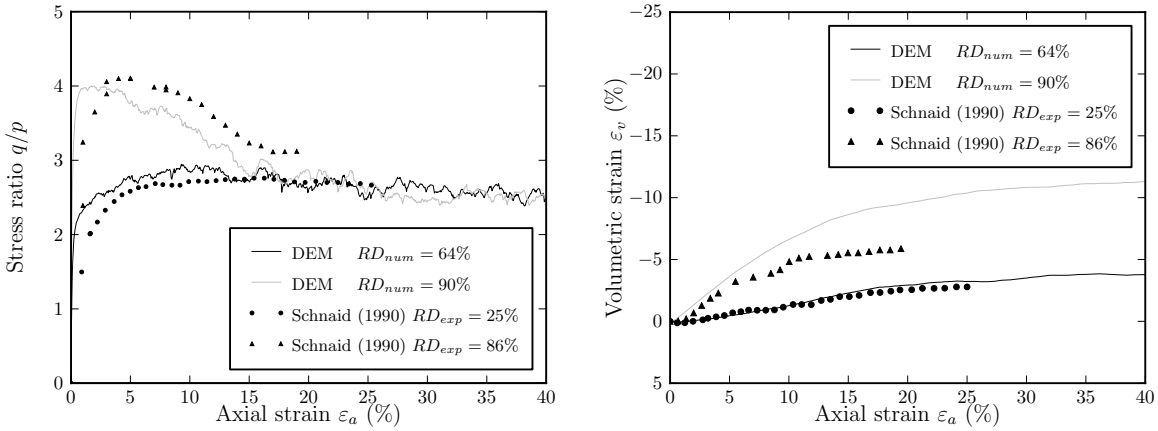

Figure 4.16: Evolution of stress ratio and volumetric strain for loose and dense samples after the calibration.

density of the loose sample reproduced here. Moreover, it is appropriate to emphasise that this comparison was done using numerical specimens whose only difference was the porosity before shearing. This is a key point of the calibration procedure presented herein. Once the calibration was performed, the validation against experimental triaxial tests was done adjusting only one parameter, that is the specimen initial porosity.

A very satisfactory agreement was found for the mobilised friction angles between the numerical and experimental triaxial tests. The calculated value of peak friction angle ϕ_p for the loose specimen was 36.5° for the numerical test and 35.3° for the experiment. A good agreement was also found for the ϕ_p of dense samples which were 41.8° (numerical) and 42.1° (experimental). The friction angle mobilised at the critical state ϕ_{cs} was 34.4°, which corresponds closely to the one found in the experiments by Schnaid (1990).

Summarizing, the salient features of the triaxial stress–strain curves of Leighton Buzzard sand, with the exception of dilatancy at large strains for dense samples, were successfully reproduced using DEM for both loose and dense samples.

4.5 Validation of DEM model

The predictive capability of the calibrated DEM model was validated using some further experimental triaxial tests carried out by Schnaid (1990) on the same LB sand as the tests mentioned already in this chapter. For the validation, the relative density and the confining pressure of the tests were different from those used to calibrate the model. The numerical parameters obtained from the calibration as described in the previous sections were left unchanged, and no further adjustments were made for these simulations.

4.5.1 Triaxial tests at various relative densities

A numerical test was performed to replicate the experimental results of a triaxial test with a relative density $RD_{exp} = 59\,\%$. The specimen was prepared following the procedure described in Section 4.2.1. In brief, the spheres were generated with no contacts and with a high interparticle friction angle ϕ_μ. The confining pressure was gradually increased up to $p = 1\,\text{kPa}$. Then ϕ_μ was decreased, while keeping p constant, until reaching the porosity corresponding to the desired relative density.

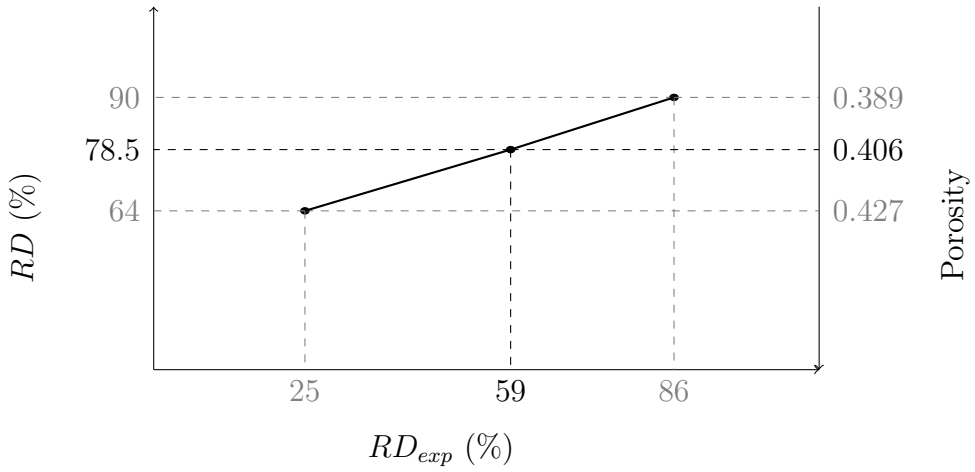

Figure 4.17: Relationship between experimental and numerical relative density.

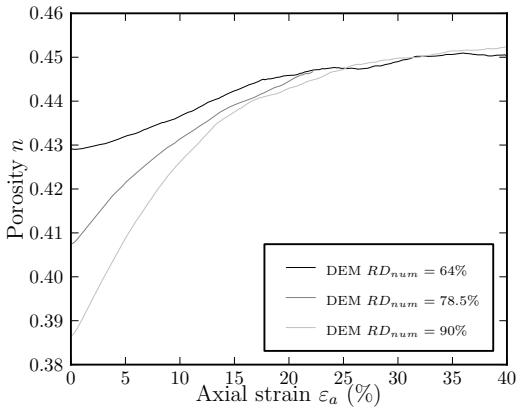

Figure 4.18: Evolution of porosity during triaxial test simulations on samples at different relative densities, with a confining pressure 100 kPa.

To establish the value of the desired porosity and numerical relative density, the relation between numerical and experimental relative density obtained from the calibration was used. In Section 4.4, a match was found between the experimental and numerical curves of the loose specimen ($RD_{exp,loose} = 25\,\%$ and $RD_{loose} = 64\,\%$) and the dense specimen ($RD_{exp,dense} = 86\,\%$ and $RD_{dense} = 90\,\%$). This range was used to evaluate the numerical relative density corresponding to an experimental relative density of 59 %. A linear interpolation was used, such that:

$$RD = \frac{RD_{dense} - RD_{loose}}{RD_{exp,dense} - RD_{exp,loose}} \cdot (RD_{exp} - RD_{loose}). \tag{4.9}$$

Then, for the interpolated numerical relative density of $RD = 78.5\,\%$, the porosity was estimated through the same procedure, as also summarized in Figure 4.17.

Figure 4.18 shows the evolution of the porosity during the triaxial test simulations beginning from different relative densities. The porosities start from values of 0.389 (dense specimen), 0.406 (medium dense specimen) and 0.427 (loose specimen). They all approach a unique value on reaching the critical state.

Figure 4.19 shows the results of the triaxial test simulations performed at a confining pressure $p = 100$ kPa, with $RD = 78.5\,\%$. The respective experimental test ($RD_{exp} =$

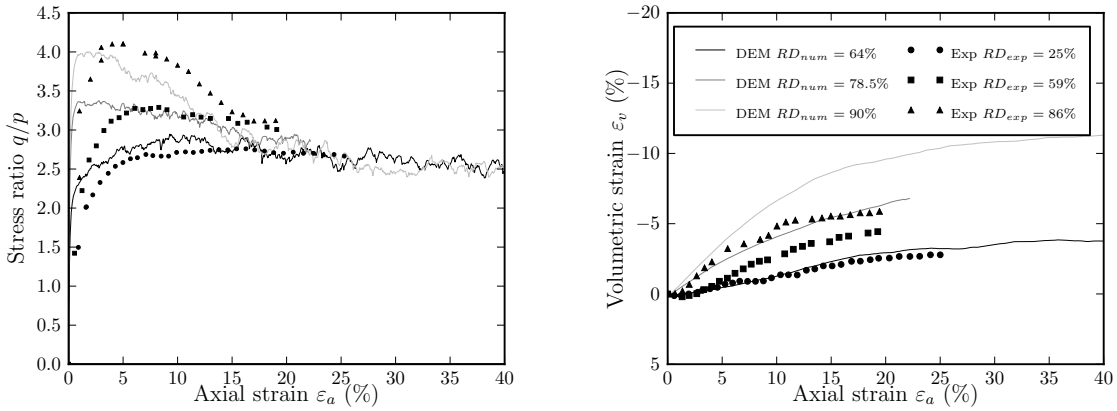

Figure 4.19: Triaxial tests on samples at different relative densities, with a confining pressure 100 kPa for DEM simulations and experiments (Schnaid, 1990).

59 %) is also shown. For reference, the results from the simulations and experiments used for the calibration (Section 4.4.3) are also illustrated. Overall, the stress–strain response for the intermediate relative density is reproduced with good agreement. The curves shows an initial dilation, reaching a peak stress ratio $q/p = 3.38$ (3.28 in the experiment), followed by softening behaviour until reaching the same stress ratio as that obtained in the loose and dense tests. The peak friction angle is 38.9° in the numerical test and 38.4° in the experimental test. The axial-volumetric strain curve is reproduced with less agreement. This is an expected outcome, as the volumetric response was not correctly reproduced for the triaxial test simulation on the dense specimen either.

4.5.2 Triaxial tests at various confining pressures

Triaxial test simulations were performed to replicate experimental results from tests on samples at a common relative density of $RD_{exp} = 59\,\%$, but with different confining pressures. The numerical specimen was prepared at a relative density $RD = 78.5\,\%$,

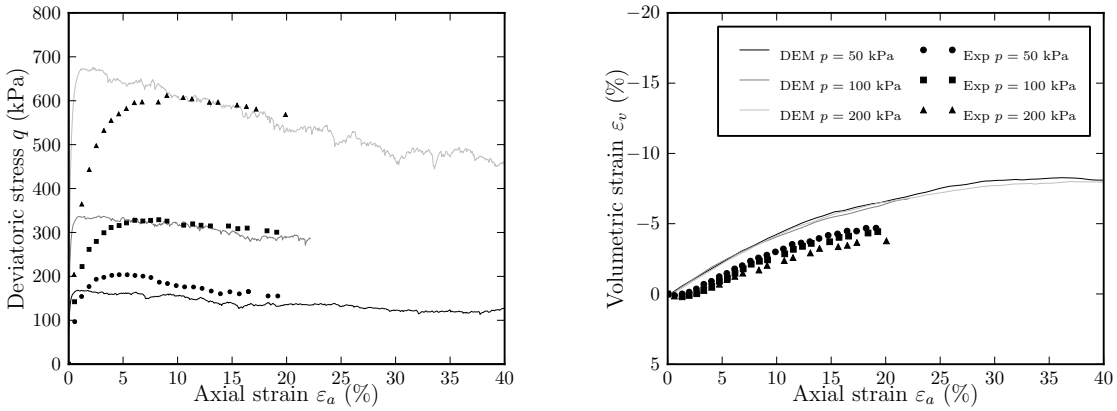

Figure 4.20: Triaxial tests on medium dense samples ($RD_{exp} = 59\,\%$, $RD = 78.5\,\%$) at various confining pressures, for DEM simulations and experiments (Schnaid, 1990).

as described in the previous section. Two tests were performed at confining pressures $p = 50$ and 200 kPa.

The results of the numerical and experimental tests are shown in Figure 4.20. For reference, the results from the simulation and experiment performed at $p = 100$ kPa on the sample at the same relative density, and presented in the previous section, are also illustrated. The numerical results replicate the observed stress–strain response with good agreement. The peak friction angles of the numerical tests are almost identical, namely $\phi_p = 38.9^\circ$ for the 100 and 200 kPa tests, and $\phi_p = 38.8^\circ$ for the 50 kPa test. There is some variability in the experimental results, were ϕ_p assumes values of 42.1°,38.4° and 37.2° for the tests at 50, 100 and 200 kPa respectively. The response at critical state is replicated well by the DEM, with friction angles of 35.9°, 36.3° and 34.8° for the numerical tests with increasing confining pressure. These are estimated from the stress at an axial strain of 20 %, so that they can be compared with the experimental results at an equal strain. The corresponding critical state friction angles from the experiments are 37.1°, 36.9° and 35.9°. The axial-volumetric strain response

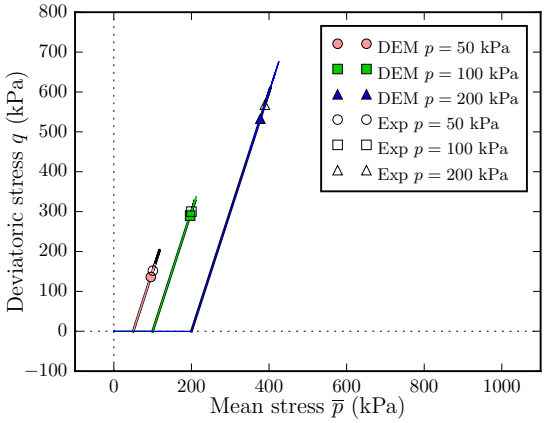

Figure 4.21: Stress paths during triaxial tests on medium dense samples ($RD_{exp} = 59\,\%$, $RD = 78.5\,\%$) at various confining pressures, for DEM simulations and experiments (Schnaid, 1990). The stress levels at critical states are also annotated.

is relatively close to the experiments, with some difference that was expected as in the previous tests.

Figure 4.21 shows the results from the triaxial tests run at various confining pressures, in terms of mean and deviatoric stresses. For this purpose, the mean stress was calculated as $\overline{p} = (\sigma_1 + \sigma_2 + \sigma_3)/3$ where $\sigma_1 > \sigma_2 > \sigma_3$ are the principal stresses. The values at critical state, estimated at $\varepsilon_a = 20\,\%$ are also annotated for both numerical and experimental tests. The plots in the $\overline{p}$–q plane confirm good agreement between the numerical and the experimental results.

It is worth stressing that these results were obtained with no further adjustment or tuning of any DEM parameters. Based on the results obtained from the calibration, new triaxial test simulations were performed with the intention of predicting the soil response. Only subsequently were the numerical results compared with the experiments. These analyses demonstrate that the proposed DEM model can capture realistically the soil response at various relative densities under different confining pressure in the range 50 to 200 kPa.

4.6 Interpretation of results at microscopic scale

4.6.1 Results at a particle level

One attraction of the distinct element method is the ability to gain an insight into the deformation processes occurring at a microscopic level. In attempting to analyse the micromechanisms in the specimen both at peak state and at critical state, the results of the triaxial test on the dense sample were elaborated to produce particle location plots, velocity fields and contact force networks. These were obtained using Python scripts embedded in the graphical software POV-Ray (Persistence of Vision Pty. Ltd., 2004).

Two larger samples were used for the analysis of the microstructure of the specimen during numerical triaxial test: a cubic sample of 13 000 spheres, and a parallelepiped sample (aspect ratio 1:1:2) of 26 000 spheres. As shown in Figure 4.22, the shape of the sample had a very limited effect on the macroscopic response of the material.

Plots of the particle locations for the two larger tests are presented in Figures 4.23 and 4.24 at three different times: as they start shearing ($\varepsilon_a = 1.0\,\%$), when they reach the peak strength ($\varepsilon_a = 1.5\,\%$), and as they approach the critical state ($\varepsilon_a = 20\,\%$). Plots were made for $\varepsilon_a = 1.5\,\%$, which is the closest available point to the exact peak point of the simulations, reached at $\varepsilon_a = 1.72\,\%$ for 13 000 sphere test and at $\varepsilon_a = 1.47\,\%$ for 26 000 sphere test. Instead of the three-dimensional figure, a slice of the domain was considered with a thickness of 0.88 mm, equivalent to $1.1D_{50}$. Only the particles whose centres fell within the slice are plotted in the figure. Hence about 500 and 1300 spheres are shown for the cubic and the parallelepiped samples respectively. The thickness of the slice is the same for all the following figures in this chapter.

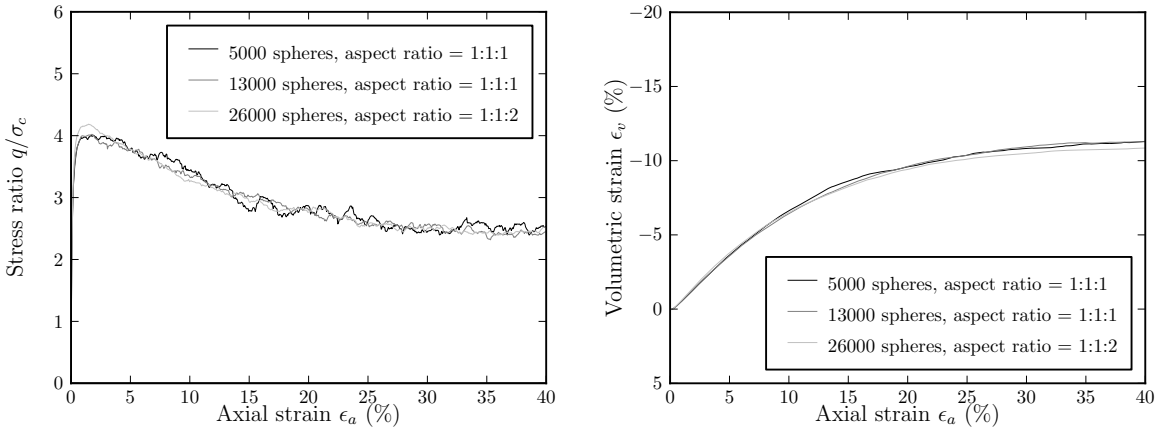

(a) (b)

Figure 4.22: Triaxial tests on samples with different numbers of particles and different aspect ratios.

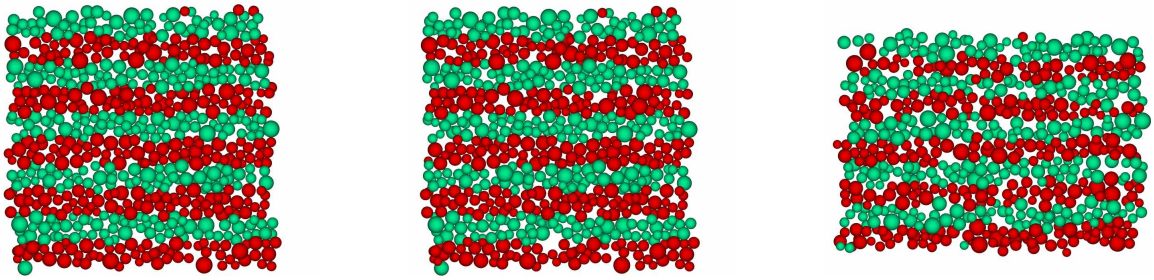

(a) $\varepsilon_a = 1.0\,\%$ (b) $\varepsilon_a = 1.5\,\%$ (c) $\varepsilon_a = 20\,\%$

Figure 4.23: Particle configuration during triaxial test on 13 000 spheres: (a) start of shearing, (b) peak, and (c) approaching the critical state.

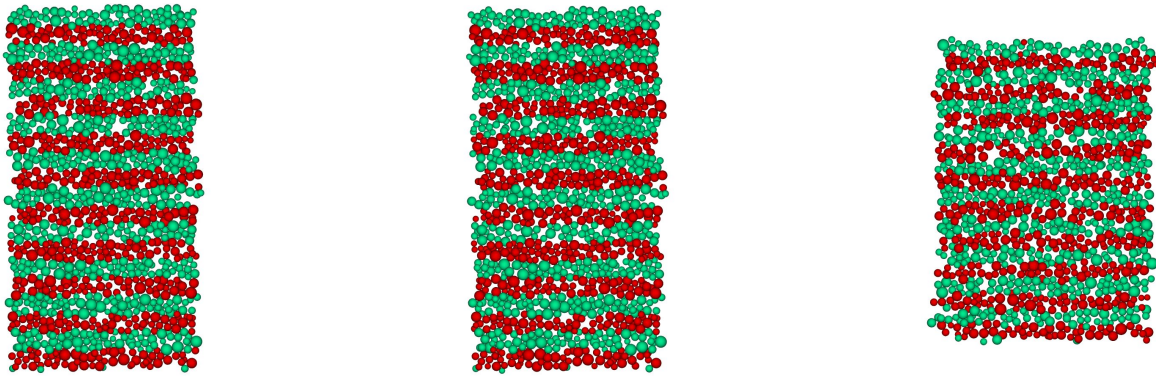

(a) $\varepsilon_a = 1.0\,\%$ (b) $\varepsilon_a = 1.5\,\%$ (c) $\varepsilon_a = 20\,\%$

Figure 4.24: Particle configuration during triaxial test on 26 000 spheres: (a) start of shearing, (b) peak, and (c) approaching the critical state.

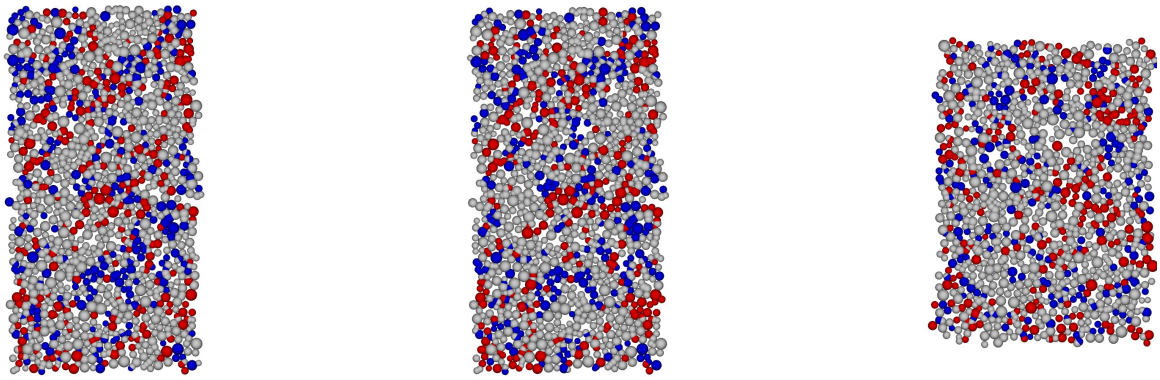

(a) $\varepsilon_a = 1.0\,\%$ (b) $\varepsilon_a = 1.5\,\%$ (c) $\varepsilon_a = 20\,\%$

Figure 4.25: Particle rotations during triaxial test on 26 000 sphere sample. Red spheres indicates an absolute clockwise rotation larger than the absolute mean value, blue spheres indicates an absolute anticlockwise rotation larger than the absolute mean value.

The particles are coloured in layers according to their initial position prior to shearing. From the figures, the deformation pattern is evident. As the deviatoric stress increases, the specimens become shorter and wider. As the coloured horizontal layers remain parallel to each other, it can be inferred that a roughly uniform deformation occurred throughout the test.

An attempt was made to assess whether strain localisation and shear band formation could be observed with the proposed method. Therefore the response at a microscopic scale in the parallelepiped sample was analysed in more detail.

The particle rotations were examined as they can be related to shear band formation. It is experimentally observed that particle rotation is a major microscopic mechanism (Oda et al., 1982). It is also numerically demonstrated that particle rotations concentrate in shear bands (Bardet and Proubet, 1992; Oda and Kazama, 1998). Those numerical simulations were in 2D, and this might have facilitate shear bands formation. Figure 4.25 shows that, for the numerical test presented herein, the magnitude of the particle rotation was uniformly distributed throughout the sample.

(a) $\varepsilon_a = 1.0\,\%$

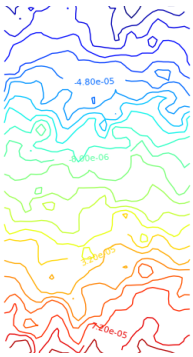

(b) $\varepsilon_a = 1.5\,\%$

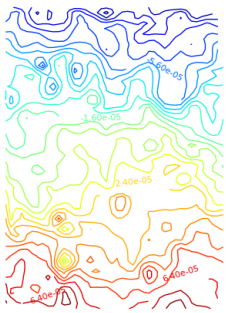

(c) $\varepsilon_a = 20\,\%$

Figure 4.26: Vertical displacement increment contours during triaxial test on 26 000 sphere sample.

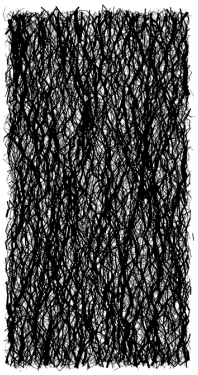

(a) $\varepsilon_a = 1.0\,\%$

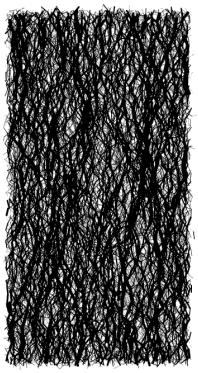

(b) $\varepsilon_a = 1.5\,\%$

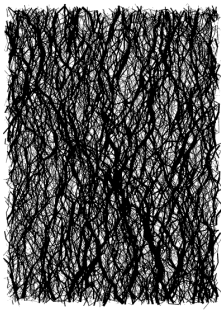

(c) $\varepsilon_a = 20\,\%$

Figure 4.27: Contact force network during triaxial test on 26 000 sphere sample.

Figure 4.26 shows the vertical displacement increments, calculated based on the method presented by Thornton and Zhang (2006). A grid was created on a vertical slice of the specimen. Particles closest to each node were chosen as markers, and then the incremental displacement of the markers was recorded. The contours of the displacement increments (Figure 4.26) showed no evidence of shear bands, confirming the deformation pattern observed from the particle plots.

The contact force network was generated by connecting the centroids of contacting particles with a cylinder whose thickness was proportional to the magnitude of the normal contact force. For a more immediate visualization, the network shown in

Figure 4.27 was generated from the three-dimensional specimen, considering all the spheres in contact, and not solely those ones on a thinner slice of the domain. The figure shows a predominance of vertical forces, linked in chains parallel to the major principal stress direction.

4.6.2 Comparison with published work

In the DEM analyses presented here there is no evidence of the formation of shear bands during failure of the assembly. To confirm this finding, two additional numerical triaxial tests were performed. One was without any form of damping, and the other was performed without any moment–relative rotation law, i.e. the particles were free to roll. The micro-mechanisms observed were similar to those presented above. As the deviatoric stress increased, the assemblies became shorter and wider, experiencing a uniform deformation with no localised shear bands forming.

These findings confirm that the numerical model proposed here is only capable of reproducing the macroscopic response of a sandy specimen during a triaxial test. This is reasonable because in a periodic cell the load is applied both to its boundaries and the particles within it (see Section 3.3.6), preventing strain localisation and shear bands formation. This is also in agreement with the work of Thornton (2000) (as in many others of his papers) where he restricts his analysis to an investigation of the macroscopic stress–strain response and to the soil fabric, asserting that strain localisation cannot occur in a periodic cell as the strain field is uniform. As also pointed out by Cheung and O'Sullivan (2008), whereas the the macroscopic response is less sensitive to the lateral boundary conditions, these play a crucial role in the micromechanisms occurring in a numerical triaxial specimen at a particle level.

It should also be pointed out that, where DEM is employed to investigate the behaviour of the soil at a particle level, little effort is made to calibrate the contact laws and to reproduce the macroscopic stress–strain response as well. For example, the majority of DEM studies on soil behaviour at a particle level are carried out using numerical triaxial tests performed with flexible boundaries (see for example the works of Bardet and Proubet (1992), Oda and Iwashita (2000) and Cheung and O'Sullivan (2008)) or bonded specimens of spheres enclosed by rigid boundaries (Cheung and O'Sullivan, 2008). Investigations at the microscopic scale on assemblies enclosed with periodic boundaries were only performed in 2D by Kuhn (1999) and Thornton and Zhang (2006). Kuhn (1999) found thin oblique bands (microbands) of void cells within which slip deformation was most intense, that might (although it was not shown) become a localised shear band. Instead Thornton and Zhang (2006) observed strain localisation performing the test on as many as 5000 particles. The work of Thornton and Zhang goes beyond their earlier studies (Thornton, 2000) demonstrating the existence of shear bands during periodic boundaries simulations. It should be noted that the two-dimensional domain might have facilitated the strain localisation and shear bands formation. In addition, 5000 particles is a larger number than what was used for this thesis, where 5000 particles were used in a three-dimensional domain. It is also appropriate to mention that none of the those studies was capable of reproducing quantitatively the macroscopic behaviour of the granular material tested. They all replicated qualitatively the behaviour of the soil in terms of stress–strain, but their main focus was on the particulate mechanisms.

On the other hand, none of the the works mentioned throughout this chapter in which DEM analyses were calibrated against experiments (Belheine et al. (2009), Salot

et al. (2009) and Widuliński et al. (2009) among others) investigated the granular material response at the microscopic scale. It is evident that researchers aim at replicating either qualitatively the micro-response, or quantitatively the macro-response of a granular material.

This is because different numerical models should be developed according to the final goal of the investigations. Specific assumptions and simplifications should be made depending on the type of behaviour that needs to be captured (O'Sullivan, 2011a). The DEM methodology adopted in this thesis is able to replicate the macroscopic response of a granular assembly subject to triaxial compression. However, investigation of the microscopic mechanisms has suggested that these cannot be realistically reproduced due to the periodic boundary conditions employed here. These findings contributed also to avoid using periodic boundary conditions to reproduce more realistic microscopic mechanisms for the pipe–soil interaction analyses described in the following chapters.

4.7 Summary

In this chapter, the mechanical behaviour of soil specimens subject to triaxial tests was simulated using DEM analyses. The distinct element method introduced in details in the previous chapter was employed to analyse the effect of DEM parameters expressed in dimensionless form, and to calibrate the parameters of the contact law. The calibration was carried out using available experimental results for triaxial tests on loose and dense specimens of Leighton Buzzard sand. Then the calibrated DEM parameters were used to predict experimental results for a medium dense specimen subject to triaxial testing under various cell pressures.

Analysis of the numerical results at microscopic scale illustrated the variety of graphical information attainable from DEM simulations. Particle plots, rotation plots, contact force networks, and incremental displacement fields were produced for this purpose. These were used to investigate the possibility of the onset of strain localisation and the consequent formation of shear bands, but no evidences of such behaviour was found. The likely reason for this lies in the periodic boundary conditions of the numerical sample. It was also pointed that it is very challenging to reproduce, with the same numerical soil, both the macromechanical and the micromechanical response of a granular material. Compromises must be made when running DEM simulations, as each different model can replicate a specific behaviour.

The calibrated DEM model will be used in the following chapters to simulate the macroscopic behaviour of a sandy seabed in lateral pipe–soil interaction analyses. The methodology developed for studying the microscopic response will be essential for analysing the detailed mechanics of the pipe–soil interaction at a particle level.

Chapter 5

DEM model: specimen generation and pipeline implementation

This chapter describes features of the numerical method employed for studying pipe–soil interaction, which is the main objective of this thesis. The gravitational approach is chosen to prepare the numerical specimen. Specimens at various relative densities are prepared, and the influence of damping is assessed. The implementation of the numerical object representing the pipeline is then described in detail.

5.1 Deposition of spherical particles under gravity

The preparation of the numerical specimen representing the seabed for the pipe–soil tests was performed using a gravitational approach similar to those proposed by Thomas (1997) and Radjaï and Dubois (2011). This approach was chosen among the others presented in Section 3.4.2 after the following considerations. As the simulations were three-dimensional, most of the constructive approaches (with the exception of

O'Sullivan's triangulation method) were not suitable for the scope. The geometry constraints, given from the sand being packed in a parallelepiped with a thickness much smaller than all the other dimensions, made Feng's closed front method impractical, as a large number of gaps would have been created at the edges of the domain. For the same reason, the compression method was discarded, as the limited thickness would not have allowed an isotropic compression, producing higher density in the out-of-plane direction.

Moreover since it was necessary to replicate a specific particle size distribution (PSD), the triangulation approach was unsuitable. The specific PSD was necessary to validate the DEM model against experimental data after the calibration through triaxial test simulations (Sections 4.4.3 and 4.5) and through comparison with laboratory pipe–soil interaction tests (Sections 7.2, 7.3 and 7.4.2). In addition, there was the crucial need of obtaining samples with a specific range of particle dimensions, so that the diameter ratio between sand spheres and pipeline was constant, even in samples with different densities. Therefore the radius expansion method was not considered as a valid option.

The necessity of obtaining samples at different relative densities, ideally using the same procedure, was also taken into account. Hence the constructive approaches were discarded, as they were only able to produce loose specimen, and not able to vary their density within a large range. In general, the ability of the gravitational methods to replicate the soil fabric and the stress conditions of seabeds in the field was very appealing. The drawback of the significant computational cost was acknowledged, but not seen as a limit. Preliminary simulations were performed to optimize the available computer resources. Details of the specimen preparation procedure are as follows.

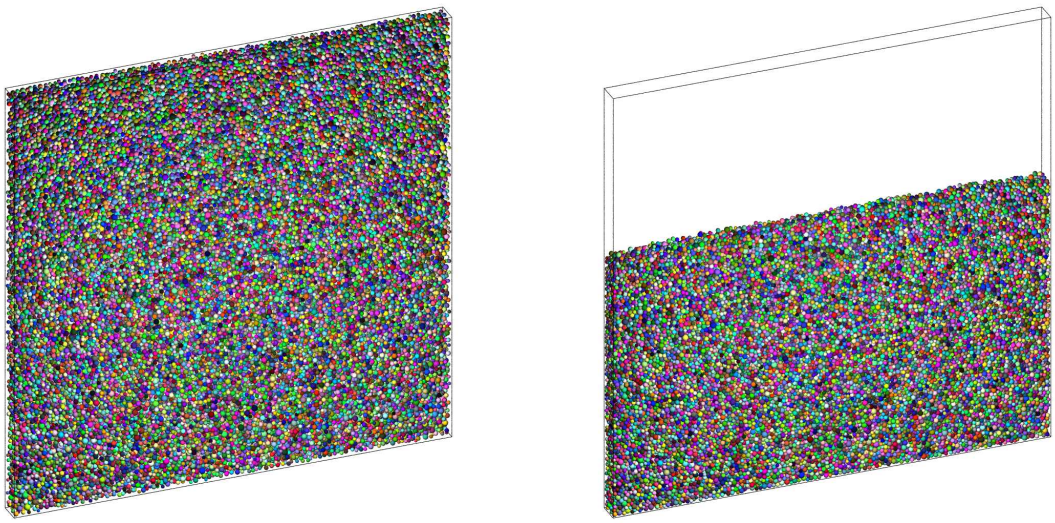

(a) (b)

Figure 5.1: 3D view of particle positions: (a) initial location and (b) after settlement.

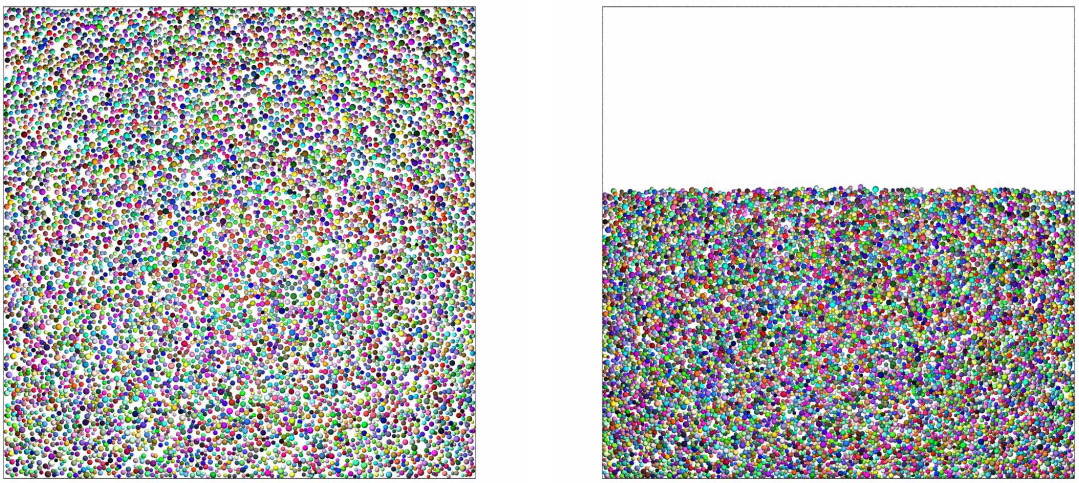

(a) (b)

Figure 5.2: Front view of particle positions along a central vertical slice: (a) initial location and (b) after settlement.

The preparation of the numerical sample was carried out allocating 36 961 spheres randomly in space, without any contacts, in a volume higher than the one needed for the pipe–soil tests (see Figure 5.1(a)). The random number generator used a seed number, which by default was taken from the computer clock. Alternatively a fixed value of the seed number could be inserted manually, to generate repeatable particle

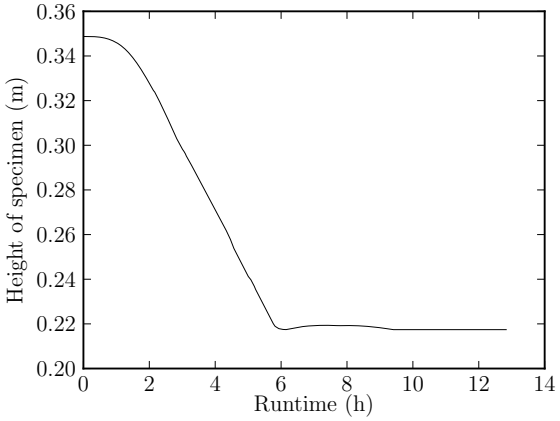

Figure 5.3: Evolution of the height of the highest particle of the sample during the settlement

configurations.

The number of spheres was chosen so that, after the deposition, they would occupy a volume about 7 pipe diameters long, 4 pipe diameters high, and 5 times the median particle diameter thick in the out-of-plane direction ($7D \times 4D \times 5D_{50}$). The pipe segment dimension and the particle size distribution were chosen to replicate those in small-scale laboratory pipe–soil interaction tests used later in this work to validate the DEM model (Section 7.1). Given a pipe diameter $D = 50\,\text{mm}$ and median particle size $D_{50} = 0.8\,\text{mm}$, the dimensions of the domain after the deposition were approximately $350\,\text{mm} \times 200\,\text{mm} \times 4\,\text{mm}$. It is worth pointing out that the measure of the height was only approximate as it depended on the final porosity of the sample.

A gravitational body force was then gradually applied, in 100 steps, allowing the particles to settle (see Figure 5.1(b)). This was to avoid inhomogeneities of the sample, as observed in Radjaï and Dubois (2011). Finally the particles were allowed to settle until the system reached static equilibrium.

The positions of the particles intersecting a central vertical slice $1.1D_{50}$ thick, before and after the deposition, are shown in Figure 5.2. Figure 5.3 shows the evolution of

the height of the sample during the deposition process. As expected, the trend is that the height is decreasing with time. Bouncing of a few particles was observed, but did not affect the final height and porosity of the specimen.

5.1.1 Evaluation of specimen's homogeneity

A reference numerical specimen was prepared following the described procedure. The numerical properties of the particles replicating the sand were taken from the results of the calibration through triaxial test simulations (Section 4.4.3). The same parameters will be used to validate the DEM model for pipe–soil interaction analyses (Section 7.2).

The homogeneity of the specimen was assessed by evaluating its spatial porosity distribution within ten horizontal strips. The height of the specimen Z after the deposition was 0.217 m, just slightly above the target $4D$ necessary to run pipe–soil interaction simulations. Hence each one of the strips (except the top one which was slightly higher) was 0.02 m high, corresponding to 5.5 times the median particle diameter, and containing about 3400 spheres.

The porosity in each of the strips was then evaluated, as shown in Figure 5.4(a). Only those particles whose centre was in the layer were considered for the evaluation of the porosity of that specific layer. When particles were shared by two adjacent layers, the entire particle was attributed to the layer where its centre was located (Figure 5.4(b)). It was believed that, on average, there was an equal number of particles split between two adjacent layers, so that they would balance out. This assumption was justified by the large number of particles in each layer.

A more rigorous approach was followed by Jiang et al. (2003), to evaluate the porosity within 11 layers of a 2D specimen of 620 disks. They considered each of the

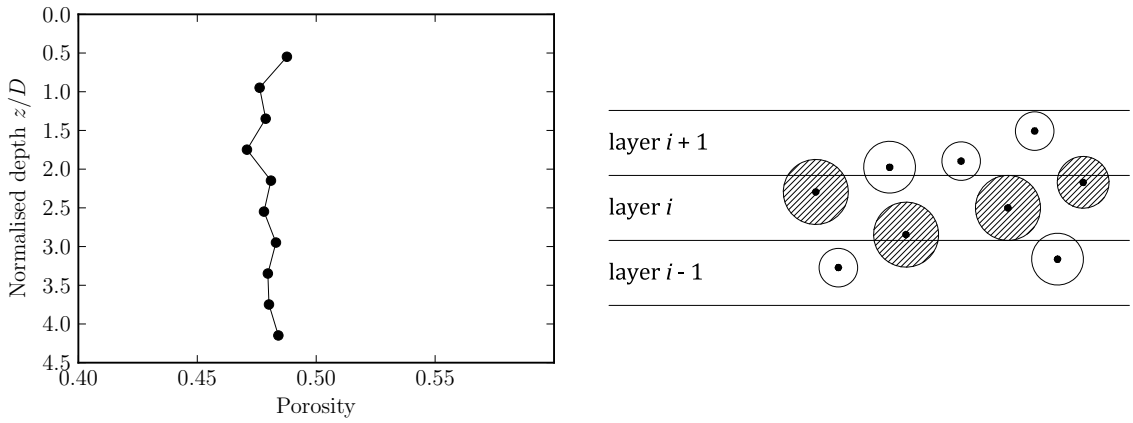

(a) Distribution of the porosity.

(b) Location of the particles in horizontal layers.

Figure 5.4: Analysis of the porosity in 10 horizontal layers of the specimen after the deposition.

two parts into which the particle was divided by two adjacent layers. Such approach was necessary in their work, as the specimen was considerably smaller, with each layer consisting of about 56 disks. For comparison, it is worthwhile to stress that the specimen described in this thesis consisted of about 3400 spheres in each layer, that, divided by the out-of-plane thickness ($5D_{50}$), gave about 680 spheres per D_{50} of thickness (12 times bigger than the number of disks in each of Jiang's layers). Therefore the procedure followed for particles split between two layers was legitimate.

The distribution of the porosity in the specimen (Figure 5.4(a)) showed that the minimum and maximum porosity varied from 0.471 to 0.487 (average 0.480). This finding suggested that a homogeneous sample can be obtained from the proposed gravitational deposition method with a gradual increase of gravity.

A way of assessing quantitatively the variation of porosity (or void ratio) in the specimen is suggested by Jiang et al. (2003), by defining a parameter S^2 called the sample variance of the void ratio:

$$S^2 = \frac{1}{N_{layer} - 1} \sum_{i=1}^{N_{layer}} (e_i - e)^2 \tag{5.1}$$

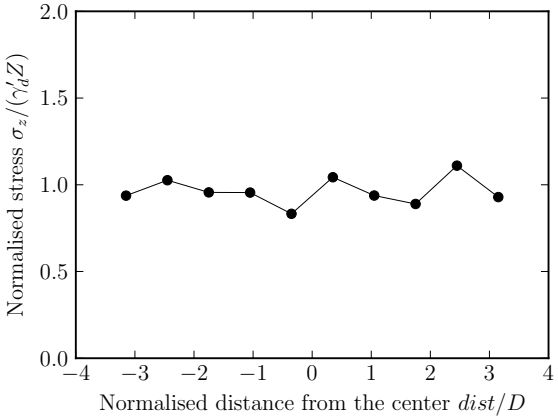

Figure 5.5: Vertical stresses at the bottom of the specimen after the deposition.

where N_{layer} is the number of layers into which the specimen is divided, e is the overall void ratio, and e_i is the void ratio in each layer. Although they did not provide a specific value of sample variance to distinguish between homogeneous and non-homogeneous specimens, they observed that values below 3 % ensure homogeneous samples. The value of the variance for the deposited specimen in this work was equal to 1.6 %, which is smaller than the one suggested in the literature.

It is also interesting to compare the obtained specimen with the results described by Radjaï and Dubois (2011) using the dumping method. They observed an increasing porosity while approaching the bottom floor, due to an elastic wave propagating upwards as the particles bounce off the floor (see Section 3.4.2). Instead Figure 5.4(a) shows a porosity profile that is nearly constant, even at the bottom of the specimen. This result confirms that no significant particle bouncing occurred during the deposition procedure described herein. The reason for this difference is in the way the gravity was applied: suddenly in Radjaï and Dubois (2011) and gradually, in a step-wise fashion, in this work. This finding suggests that the application rate of the gravity influences the homogeneity of the specimen, and that a gradual increase of the gravity allowed the preparation of a homogeneous numerical sample.

Another variable to consider when assessing sample homogeneity is the distribution of vertical stress σ_z on the bottom floor (see Figure 5.5). This is essentially constant, suggesting that no influence of the boundary occurred during the deposition. It also shows homogeneity of the sample along the horizontal direction. The vertical stress may be expressed in context of the soil dry self weight and the specimen height $\sigma_z/(\gamma'_d Z)$, where the γ'_d is a function of the soil self weight and the specimen final porosity $\gamma'(1-n)$. In this case, the normalised vertical stress varies from 0.83 to 1.2, assuming a value of 0.96 on average.

Another assessment involves the lateral stresses σ_y on the walls, and the stress ratio σ_y/σ_z (Figure 5.6). The lateral stresses were calculated from the interaction forces exchanged between walls and particles in each layer. The vertical stress was instead calculated based on the density of the sand particles and on the porosity in each layer. The results indicate that the vertical stress increases linearly with depth, and the stresses of the right and the left walls are almost identical. The stress ratio K_0 fluctuates around 0.60 (Figure 5.7).

Lastly, Figure 5.8 shows a histogram of the contact orientations in the sample after the deposition. Only half of the circle is plotted, as contacts lay along a direction, so θ and $\theta + 180°$ are plotted with the same orientation. The distribution is characterized by a rather small level of anisotropy and describes an elliptic shape. The dominant direction of contact is the vertical one, which is expected, as the specimen was prepared using a gravitational deposition technique.

The above results focus on evaluating the homogeneity of one specific numerical specimen, namely the one used to perform large displacement pipe–soil interaction analyses (described in Chapter 7). To evaluate the sensitivity of these homogeneity

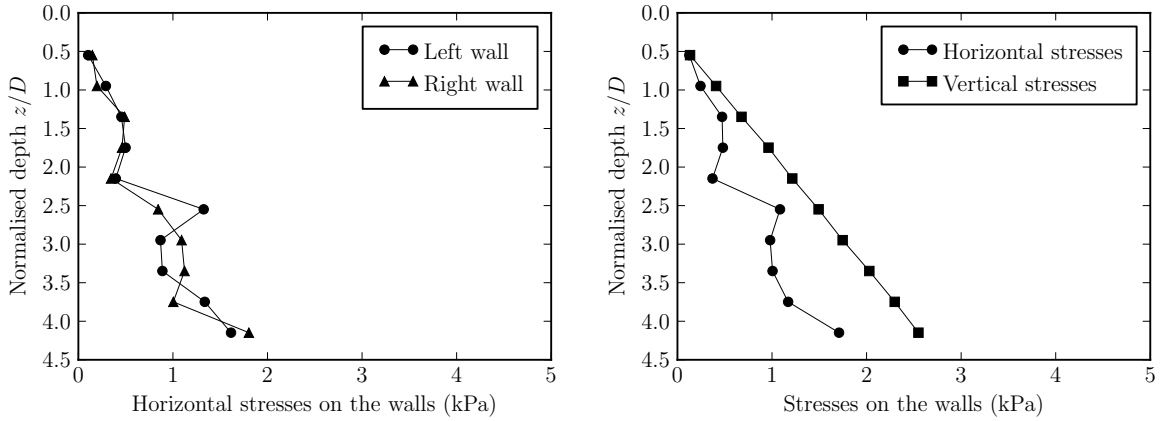

(a) Horizontal stresses on the left and right wall.

(b) Vertical stress and horizontal stress averaged between the two lateral walls.

Figure 5.6: Analysis of the stresses after the deposition, within 10 horizontal layers.

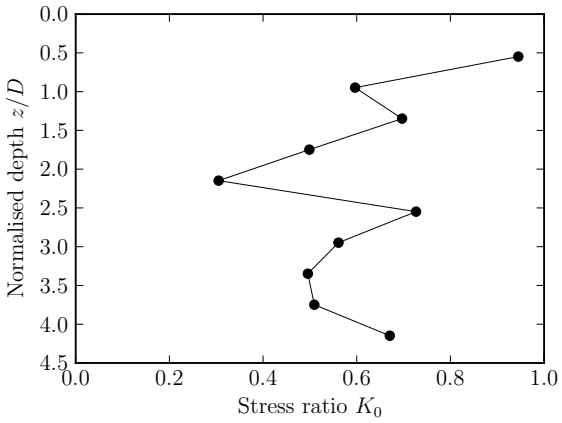

Figure 5.7: Ratio of the lateral and vertical stresses.

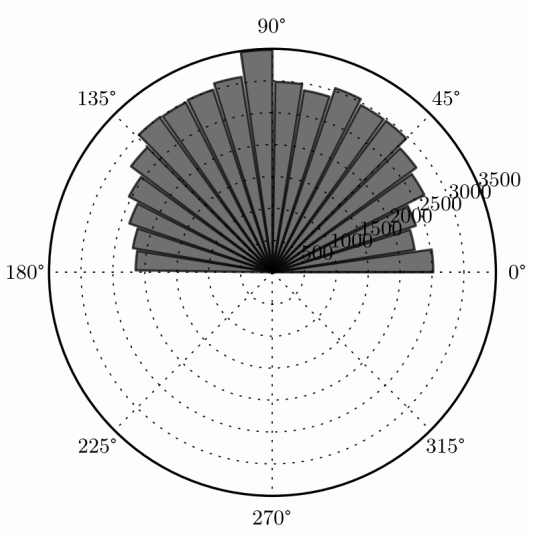

Figure 5.8: Distribution of the contact orientations after the deposition in the y–z plane. The dotted lines correspond to an isotropic fabric.

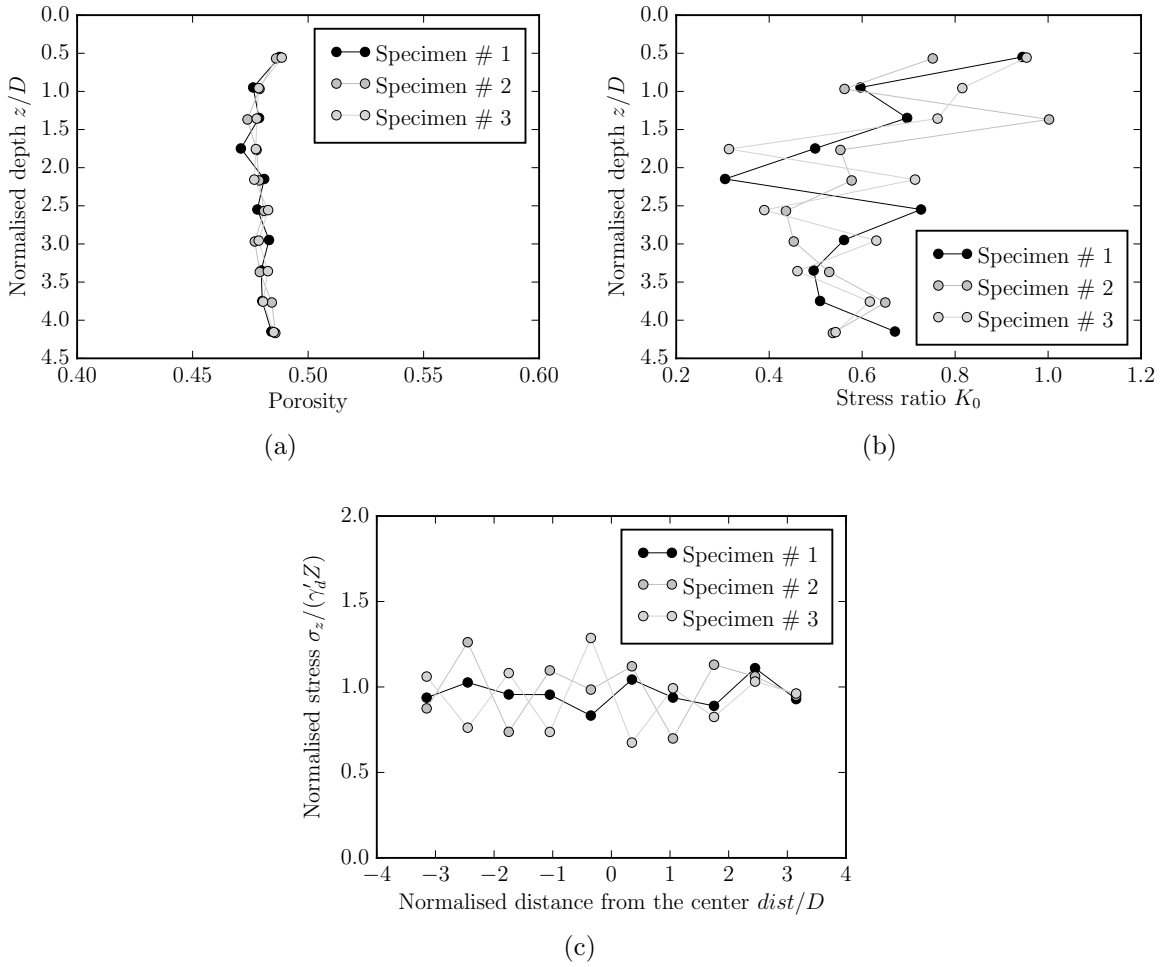

Figure 5.9: Evaluation of homogeneity of randomly generated specimens.

assessments to the seed number used to randomise the initial particle layout, two other specimens were prepared. A non-identical initial position was assigned to the particles in the two specimens, and then deposition commenced. After they reached static equilibrium, the specimens' homogeneity was assessed.

Figure 5.9 summarises the results. "Specimen # 1" refers to the specimen whose homogeneity has been already discussed and illustrated in Figures 5.4, 5.5 and 5.7. The specimens generated with different random seed numbers are referred to as "# 2" and "# 3". The porosity profile with depth remains almost unchanged in the three specimens, with an average value changing from 0.480 to 0.481 (Figure 5.9(a)). The

stress ratio fluctuates in all the three specimens, especially in the upper layers, but its average value varies only between 0.60 and 0.62 (Figure 5.9(b)). The normalised vertical stress, averaged over the floor, assumes a value ranging from 0.94 to 0.99 (Figure 5.9(c)). In summary, although a certain variability is observed, the fluctuations of the results balance out, so that different initial particle configurations generate similar specimens at the end of the gravitational deposition process. This is also facilitated by the large number of particles used for these analyses.

5.1.2 CPUs and computational time

Deposition tests were performed under identical conditions using various numbers of processors. The aim was to assess the optimum number of processors to be used for each simulation, to reduce the computational time to the minimum. The information on the performance of the DEM code for this type of simulation could also be used to predict performance in the pipe–soil simulations, where large domains were employed, and long simulation times were expected.

The tests consisted of generating of identical samples of about 37 000 non-contacting spheres, and letting them settle under gravity until a final configuration under static equilibrium was reached. The initial positions of the spheres in the samples were exactly the same, as the random generation process was performed using the same seed number. In fact the results of the tests, expressed in terms of specimen height against time, were very close to each other. These were not identical because of non-deterministic solution expected when running numerical simulations on multiple processors. The order of floating point operations is different in every parallel simulation, so round-off errors are accounted for in a non-deterministically manner.

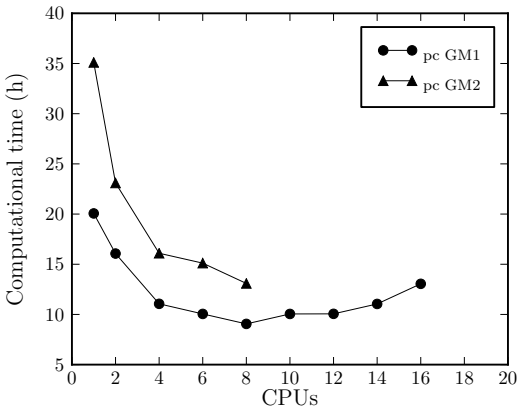

Figure 5.10: Performance of deposition tests on the two workstations pc GM1 and pc GM2.

Two workstations were used to measure the performance of the deposition script. These were the same as presented in Section 3.2.2: pc GM1 with 16 processors, and pc GM2 with 8 processors. The computational times are shown in Figure 5.10. The run time is higher for a small number of processors, then decreases as the number of CPUs increases, but when CPUs$>$ 8 the time begins to slightly increase again. Hence it is evident that the optimal number of processors for this specific simulation is 8, for both the workstations. For the workstation with 16 CPUs (pc GM1) the computational time is expected to increase slightly when two simulations are performed at the same time with 8 CPUs each.

The trend just described is in agreement with the results obtained from the general performance test illustrated in Section 3.2.2. Analogous results are obtained because of the similarities of the two tests. However, it should be considered that the tests illustrated (whose computational times vary between 10 and 35 h) are performed only to prepare the numerical specimen. Because of the length of the entire simulations (specimen preparation and pipe loading), and the large number of tests expected to be completed for this work, it was crucial to assess, for the specific simulation objective

of this study, the way of obtaining the best performance from the DEM code. Other simulations with different numbers of bodies and other loading conditions may require a different number of processors to make optimum use of the available computational power.

5.1.3 Specimens of different relative densities

Numerical specimens with different relative densities can be obtained by settling the particles as described at the beginning of Section 5.1, but with a fictitious value of the interparticle friction angle during deposition (Cundall, 1988).

Two numerical specimens were generated with non-contacting spheres located at initial identical position. These specimens differed from the friction angle ϕ_μ of all the spheres, being 0.1 and 70° respectively. Gravity was gradually applied on both specimens, and the particles were let to settle, as described earlier. Depending on the friction angle of the particles in each specimen, the particles settled in a denser or in a looser packing. After the particles had settled in static equilibrium, the real value of interparticle friction calibrated from the triaxial tests ($\phi_\mu = 26°$, Chapter 4) was assigned and kept constant during the subsequent pipe–soil interaction analyses described in the next chapters of this thesis. This procedure was chosen as it was regarded the most suitable for obtaining specimens at different densities changing only one parameter at the time. The procedures reviewed earlier did not allow to generate specimens with such a big range of porosity.

The results of the deposition are summarized in Table 5.1 and presented in Figure 5.11. The particles with the 70° friction angle led to the loosest specimen, with a final porosity of 0.497. Where the 0.1° friction angle was used, the particles settled

Table 5.1: Summary of the deposition of specimens consisting of sand of different interparticle friction angle.

Friction angle ϕ_μ (°)	Runtime (h)	Height (m)	Final porosity (-)
70	16.25	0.223	0.497
0.1	54.29	0.184	0.390

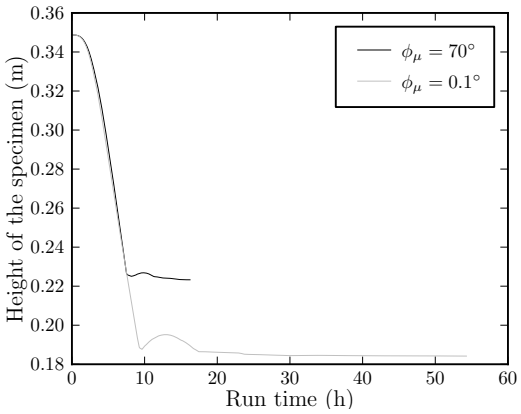

Figure 5.11: Variation of the height of the specimen during the deposition for samples with different interparticle friction angles ($\phi_\mu = 70$ and 0.1°).

in their densest configuration, with the final porosity of the numerical specimen being 0.390. This simulation was considerably longer compared to the one performed to obtain a loose specimen (more than 3 times longer), as the equilibrium was reached after a larger number time increments. Figure 5.12 shows the position of the particles after the deposition for the two specimens with the highest and the lowest interparticle friction angles. It is evident the difference in heights due to the different interparticle friction angles.

The two numerical samples at the end of the deposition were regarded as the benchmark specimens at the loosest and densest states, which could be obtained numerically using the described procedure. The relative density was assigned as the lowest ($RD = 0\,\%$) for the loosest specimen and highest ($RD = 100\,\%$) for the densest speci-

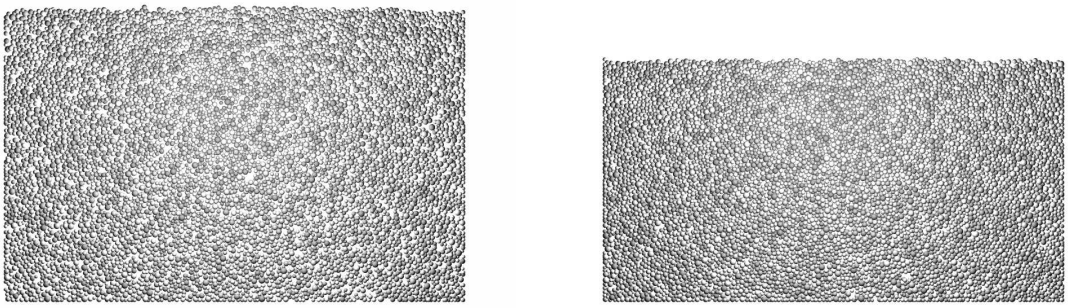

(a) (b)

Figure 5.12: Specimens obtained from deposition of particles with (a) high interparticle friction angle ($\phi_\mu = 70°$, $RD = 0\,\%$) and (b) low interparticle friction angle ($\phi_\mu = 0.1°$, $RD = 100\,\%$).

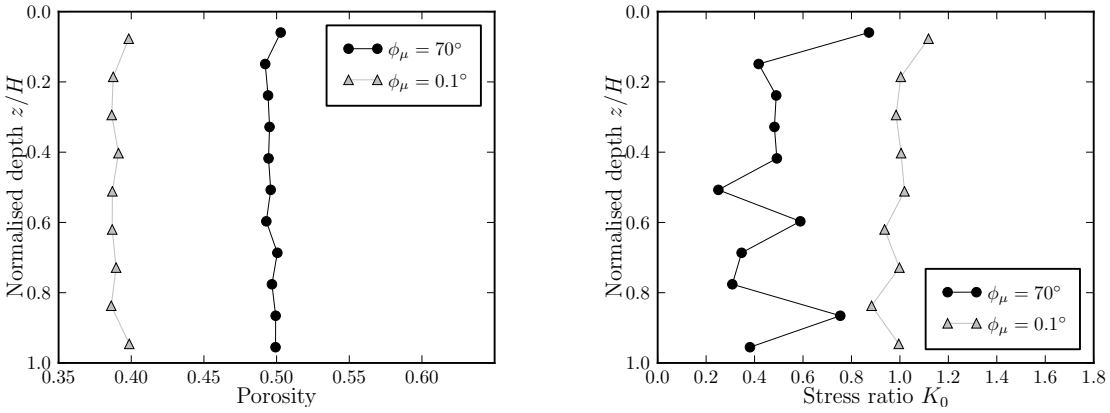

(a) (b)

Figure 5.13: Distribution of the porosity and of the ratio of the lateral and vertical stresses for various values of the interparticle friction angle.

men. Hence, given the porosity n of a specimen generated from deposition of particles with a certain interparticle friction angle ϕ_μ (where $0.1° < \phi_\mu < 70°$), the relative density RD of that specimen was evaluated as

$$RD = \frac{(n_{\max} - n)(1 - n_{\min})}{(n_{\max} - n_{\min})(1 - n)} \tag{5.2}$$

where $n_{\max}$ and $n_{\min}$ are the maximum and minimum porosities of the specimen obtained from the highest and lowest interparticle friction angle.

As expected, the porosity within horizontal layers is relatively uniform for the

two specimens, increasing for high initial interparticle friction angles (Figure 5.13(a)). The ratio between the horizontal and vertical stresses is higher for denser specimens (Figure 5.13(b)), which is due to the higher lateral stresses.

5.1.4 Effect of damping

A review was carried out on the use of damping by other researchers when generating numerical specimens with the gravitational method. The findings revealed the use of either viscous or non-viscous damping, but without thorough investigation of the effects. The majority of researchers used the non-viscous type, for example, Marketos and Bolton (2010) used the PFC^{3D} Itasca (2008) with local non-viscous damping set to the default value of $\alpha = 0.7$. Yade with local non-viscous damping was used by Nitka et al. (2013) ($\alpha = 0.08$) and by Tran et al. (2014) ($\alpha = 0.2$).

It is worth mentioning also the work of Zhang et al. (2001b), which analysed the effect of viscous damping during the generation of a specimen by pouring uniform spheres from different dropping heights. They used a formulation of damping force as in Eq. 3.41 and 3.42, but a different formulation for the damping constants C_n and C_s. They observed a distinct dependence of packing density on the damping constants ($C_n = C_s$) when these are greater of about 0.25. Although it is an interesting result, it is not applicable to the work of this thesis. That finding is valid for their specific specimen generation procedure and for a viscous damping formulation different from the one used in this work.

For the analyses in this thesis, damping was used during both the sample preparation simulations (presented in this chapter) and the pipe–soil interaction analyses (in Chapter 6 and 7) to dissipate kinetic energy among particles. Non-viscous damping

Table 5.2: Summary of the deposition of specimens with various damping ratio.

Damping ratio ζ (-)	Runtime (hh)	Height (m)	Porosity (-)	Stress ratio (-)
0.5	21.27	0.221	0.490	0.50
0.0	39.61	0.200	0.438	0.99

was discarded, as the gravitational deposition was not in quasi-static conditions, and it would have led to non-physical behaviours. Local viscous damping has been used in the literature (Brilliantov et al., 1996; Antony and Kuhn, 2004) to replicate the physical phenomenon of energy dissipation. Whether viscous damping is able to replicate those phenomena is still an open question and needs further research. Nevertheless, local (contact) viscous damping (Section 3.3.3) was used for the sample preparation and pipe–soil interaction analyses to facilitate the attainment of equilibrium states within a reasonable computational time. As will shown in detail in Section 6.4.4, viscous damping has almost no influence on the pipe response when it is loaded. However, it has a great influence during specimen preparation.

In this work, the damping ratio $\zeta = \zeta_n = \zeta_s$ (Eq. 3.48 and 3.49) was varied between 0 and 0.5. Particles were created in specimens with identical initial positions. Then gravity was gradually applied, and the particles were allowed to settle. A summary of the tests performed is presented in Table 5.2, and the height of the samples during the deposition is shown in Figure 5.14(a).

When damping is present, the specimen obtained is looser, which is consistent with the results of Zhang et al. (2001b). When no damping is used, the runtime is longer. This is because the particles dissipate kinetic energy only through friction, hence the condition of equilibrium is achieved after a longer time. Bouncing of the

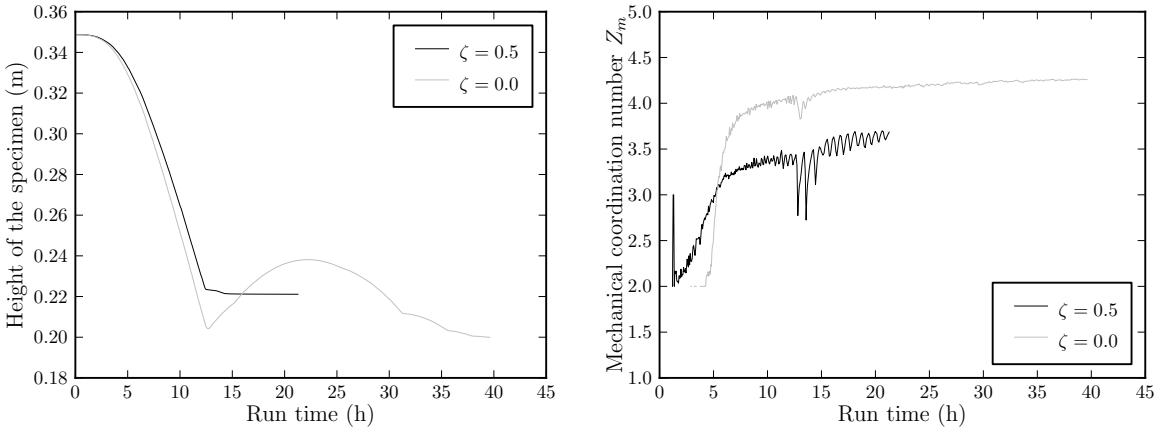

(a) Height of the sample

(b) Mechanical coordination number

Figure 5.14: Evolution of the numerical sample during the deposition with various value of the damping ratio.

surface particles is also more evident, which is reflected in a non-monotonic decrease of the sample's height. This could be avoided by applying gravity even more slowly, but since it occurs only for a very small number of particles, it will not change the final height of the sample.

It is also interesting to note the evolution of the mechanical coordination number during the deposition of the particles (Figure 5.14(b)). This number quantifies the average number of contacts per particle, and it is calculated by the formula (Thornton, 2000):

$$Z_m = \frac{2C - N_1}{N - N_0 - N_1} \tag{5.3}$$

where C is the total number of contacts, N the number of particles, N_1 and N_0 the number of particles with one or no contacts. It starts from a value equal to 2, as the particles with no contacts or with one contact are excluded. Then it gradually increases, reaching a higher value (4.2) when no damping is used, and a smaller value (3.6) when a damping coefficient of 0.5 is used.

The damping ratio may be related to the coefficient of restitution through a non-

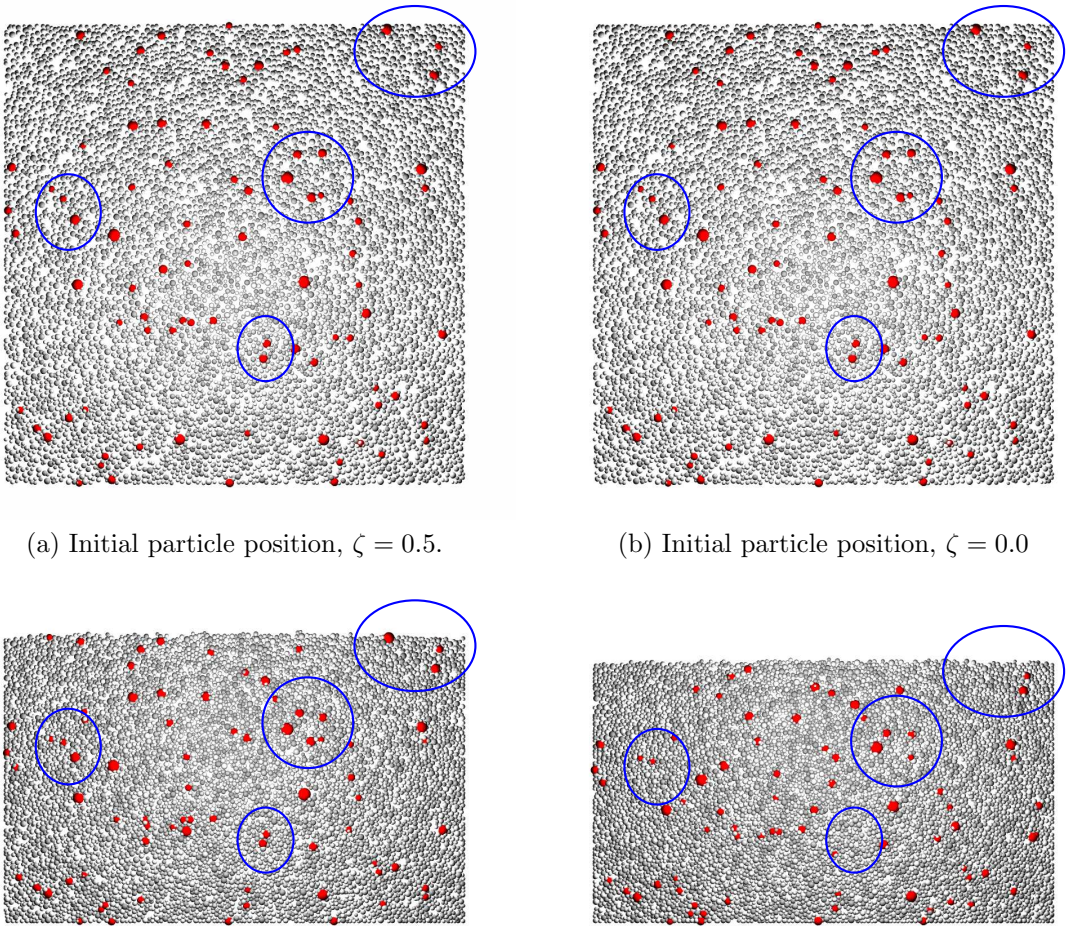

(a) Initial particle position, $\zeta = 0.5$.

(b) Initial particle position, $\zeta = 0.0$

(c) Particle position after deposition, $\zeta = 0.5$.

(d) Particle position after deposition, $\zeta = 0.0$.

Figure 5.15: Particle positions (top) before and (bottom) after the deposition, for simulations with various damping ratios: (left) $\zeta = 0.5$ and (right) $\zeta = 0.0$. The particles in red have their radius increased by a factor of 2 only for visualization purposes.

linear relationship (Tsuji et al., 1992; Antypov and Elliott, 2011). The implication is that when the damping ratio is higher, the coefficient of restitution is lower, suggesting that the particles lose part of their kinetic energy, decreasing the energy available for their rearrangement. This can be better visualised by the representation of the particle positions before and after the deposition, in the damped and non-damped specimens (Figure 5.15).

The positions of the particles whose centre is in the central region of thickness $1.1D_{50}$ are shown in the snapshots. In addition, some particles are shown in red, with a

radius two times bigger, so that their movements can be followed during the deposition. The radius is increased in the figures only for easier visualization, and not during the simulation. When viscous damping was included in the contact law (Figure 5.15(a) and (c)) the particle movement was essentially downwards, with almost no rearrangement. It is straightforward to follow the movements of the majority of the particles in the planes shown in the figure. Instead, when no damping was used (Figure 5.15(b) and (d)), the particles did not remain in the central region during their settlement, and tracking them is more arduous. In summary, the effect of local viscous damping on an assembly of particles falling under gravity is to hinder their rearrangements.

5.2 Pipe segment implementation

The numerical object replicating the pipeline was implemented in the Yade code as a cylinder. For the sake of completeness, it should be mentioned that another cylindrical object was already available in the code, the facet cylinder.

The facet cylinder consists of a set of facets (the lateral surface) around two polygonal surfaces (the top and bottom surfaces), with a number of edges defined by the user. Its drawback is that it does not allow creation of a smooth circular surface at the contact between the pipeline and the spheres. This feature is crucial during the movement of the pipe, as it affects the number of particles in contact with the pipe. The discrepancy between a circular and non-circular surface would increase with increasing size of the sand particles. Moreover, facets are used in the Yade code mainly as a type of boundary, e.g. as a container for particles. This implies that facets are implemented in the code to be massless, so that they cannot move as a result of dynamic impacts,

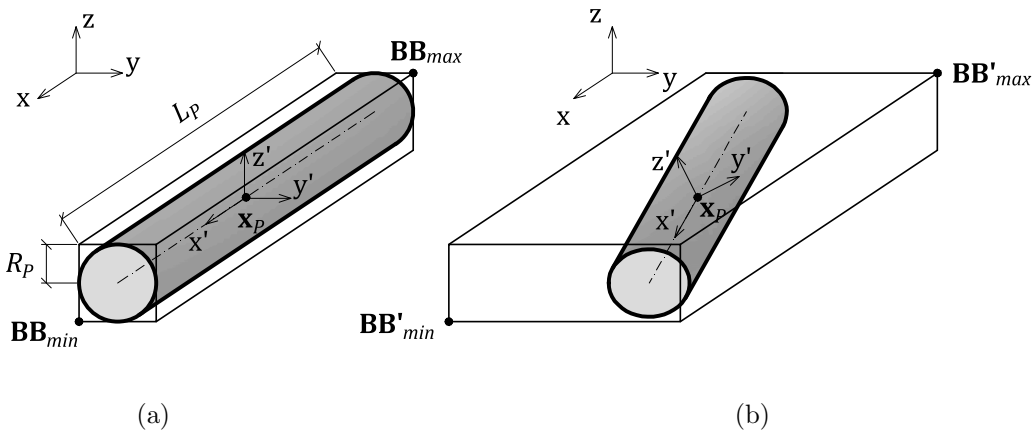

(a) (b)

Figure 5.16: The pipeline object implemented in the code Yade. (a) Initial geometry and (b) enlargement of the bounding box to follow the pipe's movements and rotations.

but only if a velocity is applied to them. Hence the pipe would have not been able to move as a result of the interaction with the spheres representing the sand.

A new object replicating the pipeline was therefore implemented in the code. This was done on the basis of a pre-existing object, and a brief description follows here.

The pipeline segment is a three-dimensional body defined by the coordinates of its center $\mathbf{x}_P$, the radius R_P, and the length L_P (Figure 5.16). Assuming it is a solid body, it has a volume V_P and principal moments of inertia I_1, I_2 and I_3:

$$V_P = \pi (R_P)^2 L_P \tag{5.4}$$

$$I_1 = \frac{1}{2}(R_P)^2 \rho V_P \tag{5.5}$$

$$I_2 = I_3 = \frac{\rho V}{12}[3(R_P)^2 + (L_P)^2] \tag{5.6}$$

where ρ is the density. The definition of the pipe from its center, rather than from the beginning and the end, allowed a more efficient location of the object during contact detection, for example when periodic boundary conditions were used.

Contact detection is performed through an axis-aligned bounding box, defined by

its minimum and maximum corners

$$\mathbf{BB}_{\min} = \mathbf{x}_P - \mathbf{BB}_{size} \tag{5.7}$$

$$\mathbf{BB}_{\max} = \mathbf{x}_P + \mathbf{BB}_{size} \tag{5.8}$$

where $\mathbf{x}_P$ is the location of the centre of the pipe, and $\mathbf{BB}_{size}$ is half of the size of the bounding box. The size varies in order to follow the pipe movements and rotations, in such a way that the bounding box remains aligned to the global axes without rotating itself (Figure 5.16(b)), through the formula:

$$\mathbf{BB}_{size} = \mathbf{R}_1 L_P/2 + \mathbf{R}_2 R_P + \mathbf{R}_3 R_P \tag{5.9}$$

where $\mathbf{R}_1, \mathbf{R}_2$ and $\mathbf{R}_3$ are the columns of the rotation matrix $\mathbf{R}$. This matrix, also called the direction cosine matrix, is a 3×3 matrix defining the orientation of the rotated pipe axes $x'y'z'$ with respect the original non-rotated (global) coordinate system xyz. In general $\mathbf{R}$ is constructed from the quaternions representation of the pipe orientation. For a more exhaustive description of quaternion and 3D rotations refer to Hanson (2006).

5.2.1 Pipe and sphere interaction

The geometrical part of the contact between the spherical particles (representing sand grains) and the pipe was modelled as an interaction between two solid spheres: one representing a sand particle, and one having the same radius and mechanical properties as the pipe, projected along the pipe axis at the minimum distance from the sand sphere (Figure 5.17).

The projection on the pipe axis of the branch vector connecting the centres of the

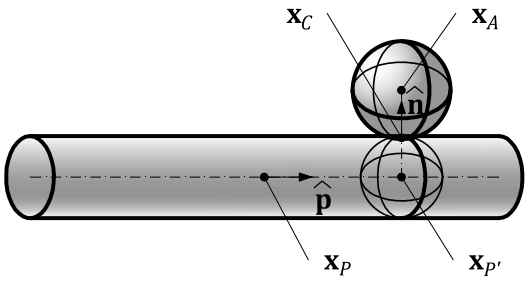

Figure 5.17: Geometrical contact between the pipe and one sphere.

pipe and a generic sphere is defined in the form

$$x_P x_A = \widehat{\mathbf{p}} \cdot (\mathbf{x}_P - \mathbf{x}_A) \tag{5.10}$$

where $\mathbf{x}_P$ and $\mathbf{x}_A$ are the positions of the pipe and the sphere, and $\widehat{\mathbf{p}}$ is the unit vector of the current pipe axis. Hence the sphere with the pipe's radius and properties, projected on the pipe axis, is located at

$$\mathbf{x}_{P'} = \mathbf{x}_P + \widehat{\mathbf{p}} \cdot x_P x_A. \tag{5.11}$$

The contact between the projected sphere with centre $\mathbf{x}_{P'}$ and the sand sphere with centre $\mathbf{x}_A$ is then treated simply as a contact between two spheres. The branch vector connecting the centres of the two spheres is

$$\mathbf{x}_{P'}\mathbf{x}_A = \mathbf{x}_{P'} - \mathbf{x}_P \tag{5.12}$$

The interaction is defined by the contact normal $\widehat{\mathbf{n}}$, the overlapping U_n and the location of the contact point $\mathbf{x}_C$, expressed as

$$\widehat{\mathbf{n}} = \frac{\mathbf{x}_{P'}\mathbf{x}_A}{|\mathbf{x}_{P'}\mathbf{x}_A|} \tag{5.13}$$

$$U_n = R_P + R_A - |\mathbf{x}_{P'}\mathbf{x}_A| \tag{5.14}$$

$$\mathbf{x}_C = \mathbf{x}_P + \widehat{\mathbf{n}} \cdot (R_P - 0.5\, U_n) \tag{5.15}$$

In this way the pipe was essentially reduced to an object consisting of a series of spheres at an infinitesimal distance from each other, with the total volume, mass, and inertia of a cylinder. Only the contact between the pipe and the sand spheres was implemented, as the pipe–pipe and pipe–wall interactions were not necessary for the simulations performed in this work.

The mechanical part of the pipe–sand contact was implemented with a Hertz–Mindlin no micro-slip solution and a moment–relative rotation contact law, in the same way as already discussed for the contact between sand spheres (Section 3.3.2). For each contact, the geometrical and the elastic parameters are calculated as equivalent radius R^*, Young's modulus E^* and shear modulus G^* between the pipe sphere and the sand sphere:

$$\frac{1}{R^*} = \frac{1}{R_P} + \frac{1}{R_A} \tag{5.16}$$

$$\frac{1}{E^*} = \frac{1-\nu_A^2}{E_P} + \frac{1-\nu_B^2}{E_A} \tag{5.17}$$

$$\frac{1}{G^*} = \frac{2-\nu_A}{G_P} + \frac{2-\nu_B}{G_A}. \tag{5.18}$$

The moment–relative rotation law was still used in the contact between the two bodies, but the resistance moment was only applied to the spheres in contact with the pipe. The moment is added to account for the non-sphericity of the spherical particles representing sand grains of irregular shapes. The non-sphericity of the pipe, instead, is directly taken into consideration by calculating moments of inertia and torques, and applying the contact forces at the center of gravity of the object.

From the contact forces and contact moments, the equations of motion are integrated to calculate the accelerations, velocities, displacements and rotations of the pipe, as already described in Section 3.3.5. Since the pipe is not a spherical body,

the principal moment of inertia about the pipe axis is different from the other two ($I_1 \neq I_2 = I_3$). Hence the rotational equation of motion remains in the generic form:

$$T_i = I_i \dot{\omega}_i + (I_k - I_j)\omega_j \omega_k \tag{5.19}$$

where T is the torque generated at the contact, I is the principal moment of inertia, $\dot{\omega}$ and ω are the angular acceleration and velocity, and i, j, k are indices for the dimensions $x', y',$ and z' in the rotated (local) coordinate system of pipe. As the current values of both $\dot{\omega}$ and ω are needed, the code uses another algorithm to evaluate the rotations of non-spherical bodies. It is based on the algorithm proposed by Allen and Tildesley (1991) and documented in Šmilauer et al. (2010).

It should be pointed out that the pipe–soil interaction analyses performed during this work, and described in the next two chapters, were carried out on a pipeline with blocked rotational degrees of freedom. Hence the algorithm for non-spherical bodies was not used. It was still worth mentioning that algorithm in case future work will be carried out with the pipe allowing movements with six degrees of freedom.

The implementation of the pipeline was verified by performing a simple test where one sphere was moved against the pipe in an oblique direction along the global coordinate system. The geometrical and physical parameters of the interaction were calculated analytically and then compared with the values obtained from the code. The interaction forces were then calculated and applied to the bodies. The forces calculated analytically on the bodies were then compared with the ones calculated by Yade. As the pipe is not a spherical body, an additional verification was made by checking that the total moment on the pipe calculated by Yade on the pipe was exactly equal to the cross product of the contact force and the distance vector between the centre and the

contact point.

5.3 Summary

Two features of the DEM model were presented in this chapter. Firstly, the preparation of the numerical specimen was described. The DEM parameters calibrated in Chapter 4 were employed to replicate soil particles settling under gravity. The procedure allowed for the preparation of homogeneous numerical samples at a range of relative densities, by varying the interparticle friction angle during deposition. Secondly, the features of the geometrical object replicating a pipeline segment were illustrated. Its implementation in the DEM code Yade was necessary in order to treat the pipeline as a solid body with a continuously curved surface.

The numerical soil specimen and the specifically implemented pipeline object will be employed in the two following chapters to perform pipe–soil interaction analyses.

Chapter 6

Pipe–soil interaction: small displacement analyses

This chapter presents the results of analyses conducted to investigate the DEM parameters necessary to perform stable and accurate numerical pipeline simulations. A dimensional analysis is briefly proposed, to identify the key parameters in the pipe–soil interaction problem. The results of a sensitivity analysis are then presented, to choose suitable values of the key parameters controlling the numerical simulations. To reduce the computational effort, the analyses are conducted on small specimens.

6.1 Dimensional analysis

In order to compare results from different loading tests (e.g. from numerical and experimental tests) it is necessary to define some dimensionless groups. These groups will be used in this chapter and the next.

Dimensional analysis suggests that the vertical force V and horizontal force H on

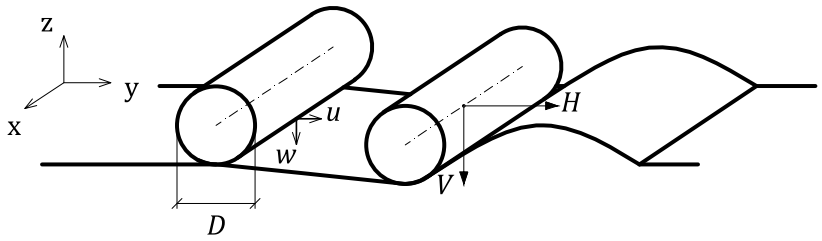

Figure 6.1: Geometry of the pipeline loading test.

the pipe can be scaled by the soil unit weight γ', and by the pipe's dimensions D and L, forming the dimensionless groups:

$$\frac{V}{\gamma' D^2 L} = f_A\left(\frac{w}{D}, \phi_\mu, \delta\right) \tag{6.1}$$

$$\frac{H}{\gamma' D^2 L} = f_B\left(\frac{u}{D}, \phi_\mu, \delta\right) \tag{6.2}$$

where u and w are respectively the lateral pipe displacement and the depth of penetration of the invert (bottom of pipe) relative to the undisturbed seabed, ϕ_μ is the interparticle friction angle of the sand, and δ is the interparticle angle of friction between the pipe and the sand (Figure 6.1). The ratio w/D is usually referred to as the embedment ratio.

It is also worth considering the effect of parameters related to the numerical simulation, such as the damping ratio ζ (Eq. 3.48 and 3.49), the size of the sand particles D_{50} and the loading velocity v, so that the Eq. 6.1 and 6.2 become:

$$\frac{V}{\gamma' D^2 L} = f_A\left(\frac{w}{D}, \phi_\mu, \delta, \zeta, \frac{D}{D_{50}}, \frac{v\Delta t}{D}\right) \tag{6.3}$$

$$\frac{H}{\gamma' D^2 L} = f_B\left(\frac{u}{D}, \phi_\mu, \delta, \zeta, \frac{D}{D_{50}}, \frac{v\Delta t}{D}\right). \tag{6.4}$$

6.2 Boundary conditions and number of dimensions

6.2.1 Test setup

A study on the effect of the boundary conditions was conducted by performing vertical loading tests on a packing of spheres enclosed by rigid walls and periodic boundaries. These 3D simulations were then compared with a pseudo 2D test.

Yade is only developed for DEM analysis in 3D. In order to run 2D simulations spherical particles were created with their centres lying in a common plane, and displacements along the out-of-plane direction and rotations around the in-plane axes were inhibited. In this way, the test replicates the behaviour of rods with their axes aligned in the out-of-plane direction. This is a common expedient used in DEM to simulate 2D tests with a software developed for 2D simulations (Thornton and Zhang, 2006). Pseudo 2D simulations were here preferred to real 2D simulations (using disks instead of spheres) available with DEM softwares developed specifically for this purpose, so that the same numerical tool could be used for 3D and 2D tests.

Rigid walls are replicated in the DEM by non-dynamic planar surfaces with no mass or inertia. The term non-dynamic means that forces and torques, calculated from the interaction with the spherical particles, are used to update the particle positions and orientations only, without being used in the equations of motion integration (Eq. 3.1 and 3.2). Hence rigid walls do not move; their motion occurs only if movement is imposed, but not as consequence of a contact. The term rigid is used here as opposed to flexible: the walls have a finite stiffness, but do not allow localised deformations of the boundary itself. For the simulations described in this thesis, the elastic properties of the walls were taken to be the same as the sand particles, such that a small penetration of

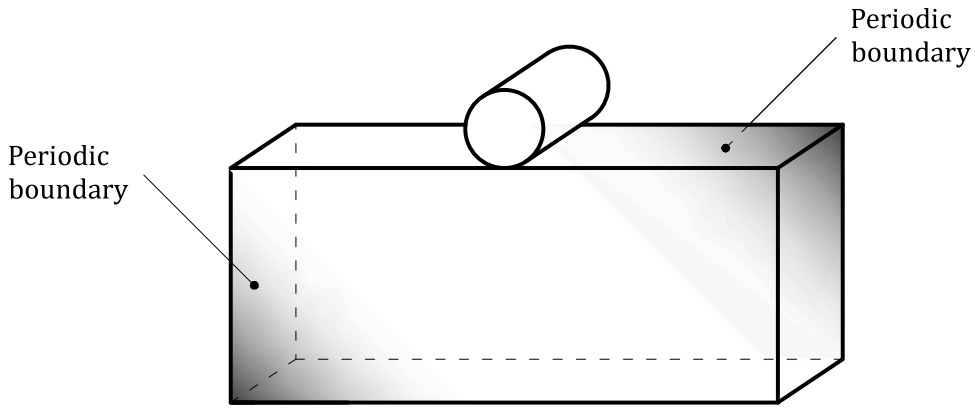

Figure 6.2: Geometry of the loading test of the pipe on a sphere packing enclosed by periodic boundaries.

the sand particles into the walls themselves was allowed. The particle-boundary friction coefficient was set equal to zero to avoid introducing non-homogeneous deformations.

For the 3D simulation only, periodic boundaries were initially included on the container planes perpendicular to the pipe axis, in order to reduce the numerical sample to a thin slice (Figure 6.2). Ketterhagen et al. (2008) demonstrated that a model with a thickness of 2.1 times the median sand diameter (D_{50}) between two parallel periodic boundaries can adequately reproduce the plane strain problem of a granular material flowing from a hopper.

In this research, two types of 3D samples were used. One sample was contained all around by frictionless rigid walls, with the two planes parallel to the pipe axis at a distance of $20D_{50}$. The other sample was contained by frictionless rigid walls along the planes parallel to the pipe axis, and periodic boundaries in the planes perpendicular to the pipe axis. A width of $5D_{50}$ between the two parallel periodic boundaries was selected.

The periodic sample, as well as the one enclosed by rigid planes, aim to replicate plane strain conditions. Although the interaction of the pipeline with the surrounding

Table 6.1: Summary of tests performed.

Test	Number of dimensions	Boundary conditions	Spheres
ST-2D	2	Rigid walls	795
ST-3D-RW	3	Rigid walls	15843
ST-3D-PB	3	Periodic boundaries	3964

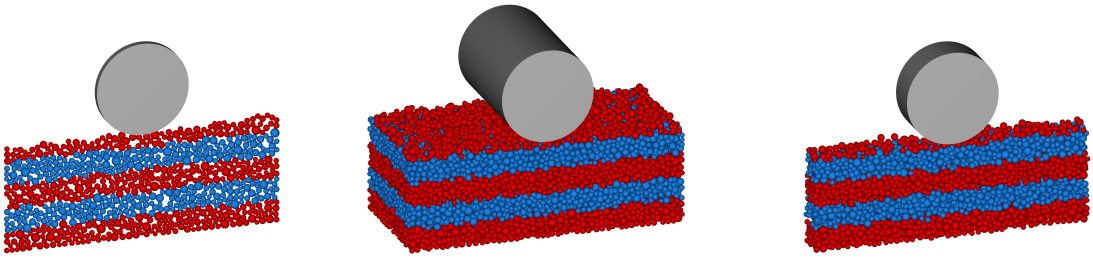

(a) (b) (c)

Figure 6.3: Geometries analysed: (a) Test ST-2D: pseudo 2D sample, (b) Test ST-3D-RW: 3D sample enclosed by rigid walls, and (c) Test ST-3D-PB: 3D sample enclosed by periodic boundaries in the direction perpendicular to the pipe axis.

soil is a 3D problem, the assumption of plane strain conditions is very common in the field of pipeline research. The assumption implies that the curvature of the pipeline is negligible, so that the pipe–soil interaction can be analysed in distinct cross-sectional planes.

A summary of the main features of the test is given in Table 6.1. The domain is only three pipe diameters wide and one pipe diameter high, to reduce the computational cost. The pipe diameter is never changed in all the tests presented in this thesis, and is set equal to $D = 0.05\,\mathrm{m}$. This is taken as the diameter of a pipe used in small-scale laboratory tests performed by Sandford (2012), against which the DEM model is validated in Chapter 7. The geometries of the three tests after the sand deposition and the pipeline generation are presented in Figure 6.3. In the snapshots, as in all the following figures, the particles are coloured according to their position just before the

penetration of the pipe had started. For reference, the height of each layer was taken as $D/4$ (12.5 mm). For clarity, the walls are not included in these figures.

In each test, the pipe was generated at a level higher than the seabed surface, and then pushed vertically into the seabed at a constant velocity until it reached an embedment of at least $0.15D$ (7.5 mm). A velocity of $v = 0.005$ m/s was used here as a reference value. The influence of the velocity on the numerical results is covered in Section 6.4.3.

6.2.2 Presentation of results

Data from these numerical simulations, and from all the other pipe loading tests presented in this thesis, were recorded at a frequency depending on the loading velocity. In this way an equal amount of data was available for tests with the same penetration depth. Data were recorded to obtain 100 data points for a pipe displacement of $0.1D$. Therefore, for a pipe of velocity $v = 0.005$ m/s and diameter $D = 0.05$ m, a data acquisition frequency of 100 Hz was used.

The results of the loading tests on the pipe described in this section, and also throughout the thesis, are presented in terms of normalised vertical pipe–soil load $V/(\gamma' D^2 L)$ versus normalised embedment w/D.

The embedment w is defined as the depth of the penetration of the invert (the bottom) of the pipe relative to the undisturbed seabed. This definition requires a precise definition of the initial seabed surface level. Since the random generation and the subsequent gravity deposition generates a slightly non-flat surface, the height of the sample at the undisturbed level is taken over an average of 10 vertical columns across the packing. The pipeline embedment is recorded from the moment when two

conditions are satisfied. These are when the pipe invert has reached the calculated seabed surface level, and when the pipe is in contact with more than one sand sphere. The second condition was added to avoid the particular, but possible, condition at the very beginning of the penetration, in which the pipe touches the surface through one particle only for a relatively large embedment, causing unrealistically small pipe–soil loads for increasing penetration depths.

As the measured load fluctuates significantly, the mean value and the standard deviation are also plotted. The standard deviation was calculated over an interval of $w/D = 0.01$ and it quantifies the amplitude of the oscillations around the mean value. For each interval σ was evaluated as:

$$\sigma = \sqrt{\frac{1}{n}\sum_{i=1}^{n}(V_i - \overline{V})^2} \tag{6.5}$$

where n is the number of data points in each interval, V_i is the value for each embedment depth, and $\overline{V}$ is the mean vertical load in the interval.

For the purpose of calculating the normalised force during the 2D test, the dimension of the out-of-plane direction was taken to be the median particle diameter ($L = D_{50}$). Table 6.1 shows that the 2D test employed a number of particles almost 20 times smaller than the 3D test with rigid walls, and 5 times smaller than the 3D test with periodic boundaries. These two tests were performed on specimens with thicknesses of $20D_{50}$ and $5D_{50}$ respectively. Therefore normalising by the thickness of the specimen may be regarded as a normalisation with respect the number of particles, given that the width and height of the sample are the same in all three cases.

6.2.3 Results

The results of the three simulations during vertical penetration are presented in Figure 6.4. For all the tests, the normalised pipe–soil load increases approximately linearly as the penetrations proceeds. For small embedment depths, the pipeline response is generally unaffected by the boundary conditions. The test with periodic boundaries can be regarded as the closest one to representing plane strain conditions. The test with rigid walls exhibits a similar response, especially for a penetration depth of less than $0.1D$. For the 2D test, however, although the evolution of vertical load is similar to the test with periodic boundaries, the response at shallow penetration depths is characterised by high fluctuations, occasionally reducing the load to zero.

For embedment depths greater than $0.1D$, the fluctuations in all the tests are too large to make any meaningful comparison. In fact, it is important to recall that these analyses are only valid for very limited range of penetration depths, as these tests are performed on a reduced sample height in comparison with the small-scale laboratory tests.

The tests were carried out under displacement control, hence the pipe was moved at a constant vertical velocity, while keeping the lateral and longitudinal movements fixed. It is worth analysing and comparing the reaction forces in these two directions to understand the effect of the different boundaries. Figure 6.5 presents the pipe–soil force in the longitudinal and horizontal directions. In ideal plane strain conditions, these forces should both be equal to zero. In these tests, however, the forces tend to fluctuate around zero. Therefore their distance from zero is a measure of the accuracy of the test, and hence of the divergence from the plane strain conditions. The longitudinal force is not evaluated during the 2D test, as the out-of-plane dimension is zero. For the

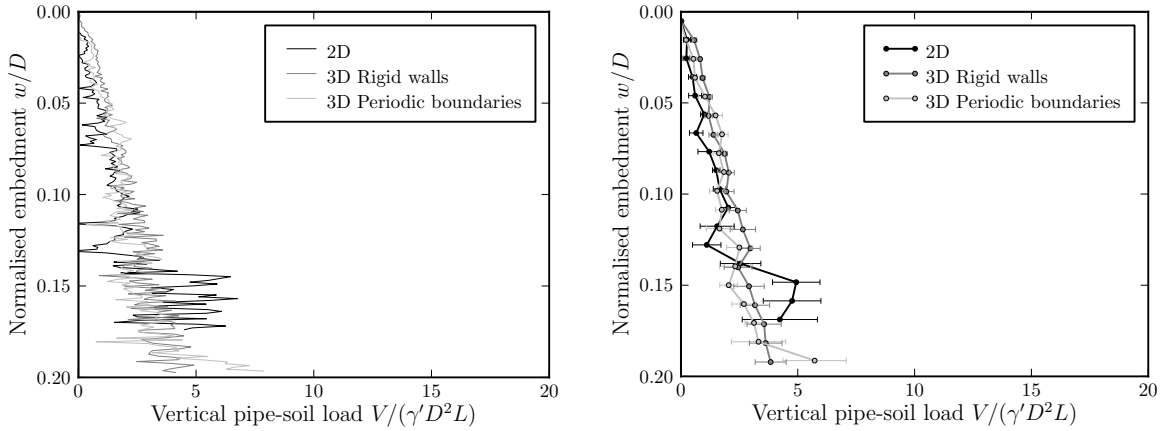

Figure 6.4: Normalised pipe–soil interaction force during the penetration on samples with various boundary conditions (Tests ST-2D, ST-3D-RW and ST-3D-PB).

3D test with rigid walls, however, the longitudinal force is slightly uneven, reaching a maximum value of approximately 4.5 % of the maximum vertical force. The test with periodic boundaries produces a very limited longitudinal force, suggesting that the effect of the boundaries is indeed negligible.

The horizontal force fluctuates around zero, with a greater amplitude for the 2D test, reaching almost 10 % of the maximum vertical force. The horizontal forces from the 3D tests are of similar magnitude for both rigid walls and periodic boundaries.

In conclusion, these findings indicate that the 2D test is not able to correctly reproduce the behaviour obtained from a 3D test. Instead, the 3D test with rigid walls is able to better replicate plane strain conditions (as simulated by the periodic boundaries).

Although the three-dimensional simulation performed with periodic boundaries was proven to be more stable and close to the plane strain conditions than the simulation with rigid walls, the periodic boundary conditions were not used elsewhere for the analyses in this thesis. The reason was that the DEM code Yade was not yet developed to deal with large bodies such as the walls and the pipeline in a periodic domain.

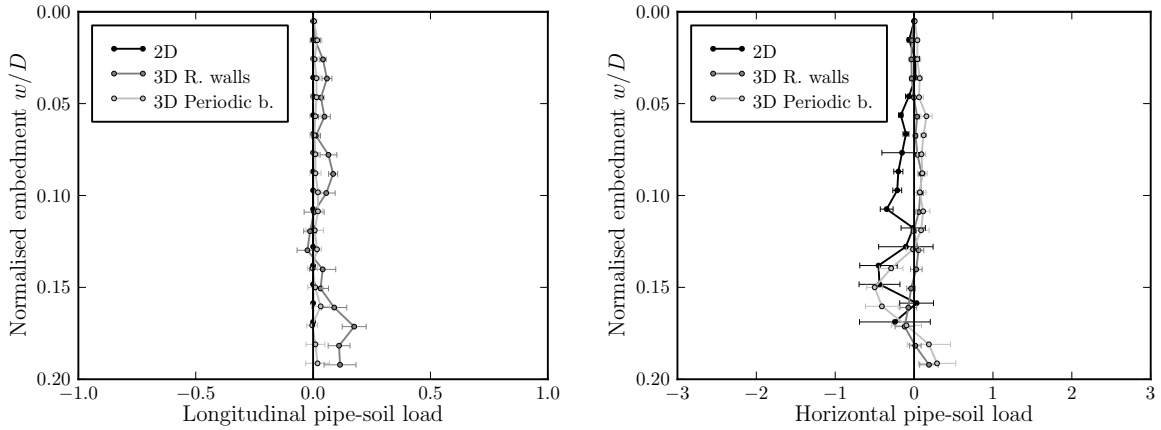

Figure 6.5: Forces during the penetration on samples with various boundary conditions (Tests ST-2D, ST-3D-RW and ST-3D-PB): (a) longitudinal force and (b) horizontal force.

To address this issue, some changes were made to the code, together with the main developers. These changes, however, prevented the simulations from being saved and reloaded for continuing or changing a previous simulation. This became impractical in the long run, when analyses lasting 30 to 40 days were performed. For this reason, only small tests could be run with periodic boundary conditions, such as the one described in this section (Figures 6.4 and 6.5). Therefore all the remaining tests were performed on specimens enclosed exclusively by smooth rigid walls.

6.3 Large and small domain

An additional preliminary test was performed to verify whether the analyses performed on the small domain were representative of the pipe response. Therefore the results obtained with the small domain were compared with the ones obtained under the same conditions in a larger domain. Loading tests of the pipe were performed on two different numerical specimens: one consisted of 3964 spheres enclosed by frictionless walls in a

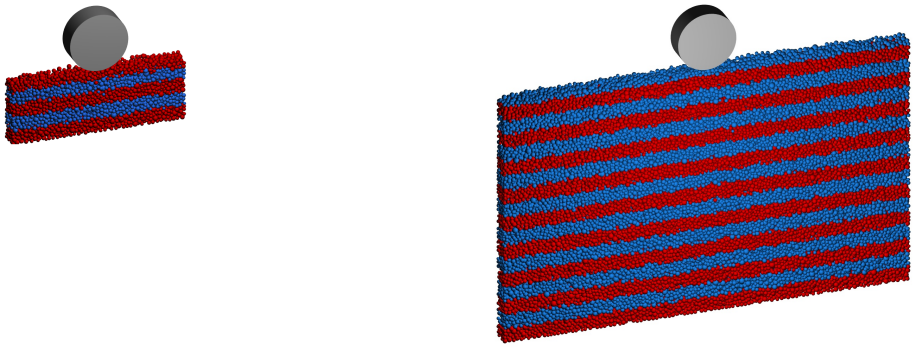

(a) (b)

Figure 6.6: Snapshot of simulations before penetration: (a) Test ST1 in the small domain, and (b) Test LT1 in the large domain.

domain of reduced dimensions, $3D \times 1D \times 5D_{50}$ (Small Test 1, ST1, Figure 6.6(a)); the other consisted of 36 961 enclosed in a domain large enough to accommodate the expected failure mechanism, $7D \times 4D \times 5D_{50}$ (Large Test 1, LT1, Figure 6.6(b)).

The pipe was pushed at a constant vertical velocity 0.005 m/s to an embedment depth of $0.2D$ (10 mm), similar to the analyses described in the previous section. It was then moved laterally at the same rate while keeping the embedment depth constant, until a final lateral displacement of $0.1D$ (5 mm) was reached. Although the velocity of the pipe was of the same magnitude in both tests, 5.3 h were required to move the pipe of $0.1D$ vertically in the small domain test (ST1), while 136.3 h in the large domain test (LT1). Therefore there was an obvious computational benefit in performing the sensitivity analysis (Section 6.4) on small domains.

The vertical penetration results are presented in Figure 6.7. The measured load fluctuates significantly during the simulation, hence the mean value and the standard deviation are also plotted. The mean values for the two tests are very similar, suggesting that the small test captures the pipe–soil load accurately. However, ST1 generates

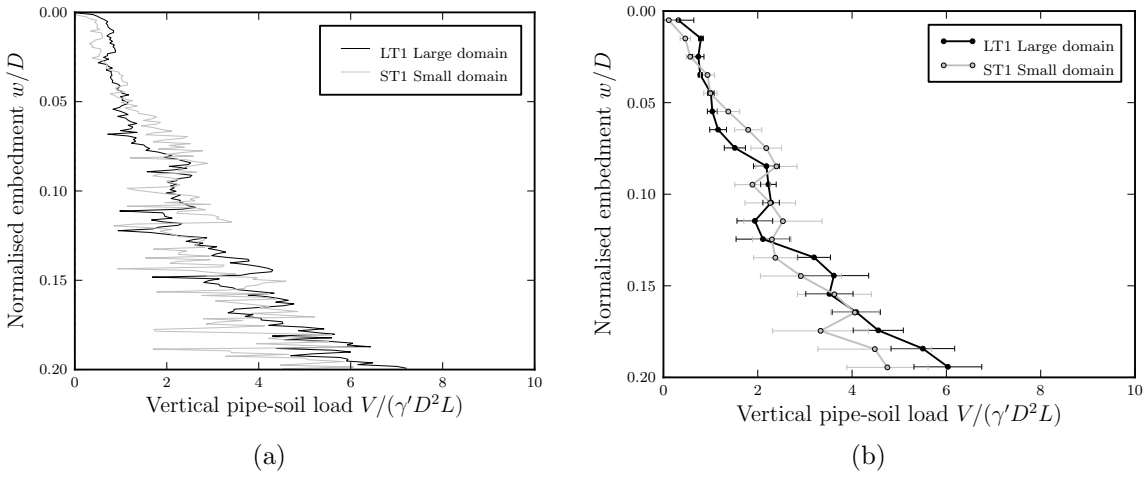

Figure 6.7: Influence of the dimension of the domain on the numerical solution during vertical penetration. (a) Raw data and (b) mean and standard deviation.

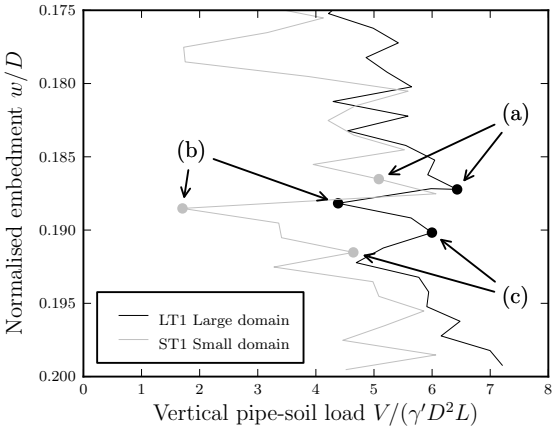

Figure 6.8: Load–displacement curve during some stages of Test LT1 and Test ST1.

greater fluctuations of the load, such that the standard deviation of $V/(\gamma' D^2 L)$ reaches a value of 1.96. The maximum standard deviation for LT1 is lower and equal to 1.20. Such instability in the small test is due to the close proximity of the boundaries (the floor and the lateral walls).

It is now relevant to understand the nature of these load fluctuations. Figure 6.8 highlights three stages of the pipe penetration in the small and large domains, corresponding to a few steps before, during, and after a sudden drop of the vertical force occurs. The instantaneous force chains at these three stages for both tests are presented

(a) $F_{n,max} = 1.806\,\mathrm{N}$ (b) $F_{n,max} = 0.946\,\mathrm{N}$ (c) $F_{n,max} = 1.471\,\mathrm{N}$

Figure 6.9: Contact force network at different stages (see Figure 6.8) during the penetration of Test ST1. The value of the maximum force at the contact in the normal direction $F_{n,max}$ is also specified.

(a) $F_{n,max} = 2.018\,\mathrm{N}$ (b) $F_{n,max} = 1.382\,\mathrm{N}$ (c) $F_{n,max} = 1.737\,\mathrm{N}$

Figure 6.10: Contact force network at different stages (see Figure 6.8) during the penetration of Test LT1. The value of the maximum force at the contact in the normal direction $F_{n,max}$ is also specified.

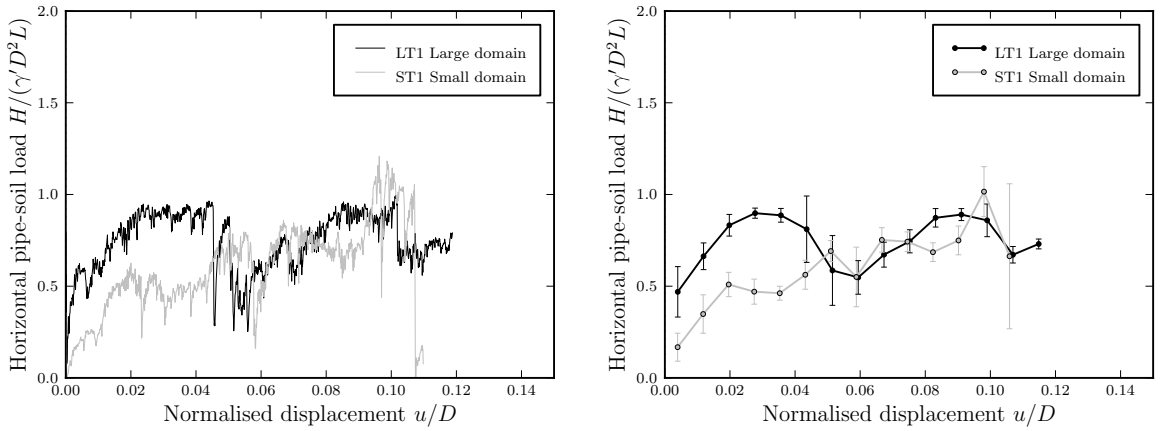

Figure 6.11: Influence of domain dimensions on the numerical solution during lateral movement. (a) Raw data and (b) mean and standard deviation.

in Figure 6.9 and 6.10. The force network in the small domain (Figure 6.9) shows that where the pipe–soil load is high (at (a) and (c)) a structured contact force network develops underneath the pipe. However, when the vertical force drops (at (b)), a weaker force network is developed. A thick network is also visible close to the lower boundary, indicating that the domain is not sufficiently large. The weaker force network is also observed during a drop of the load in the large domain (Figure 6.10), but in this case no large forces at the boundaries develop. The difference between the high force ((a) and (c)) and the drop (b) is limited, as the fluctuation itself is of smaller amplitude (as anticipated by Figure 6.8). These two figures demonstrate that the fluctuations in the pipe–soil response are directly related to the development of the contact forces within the soil. These fluctuations develop during the numerical simulations, and their amplitude is greater when the domain is smaller.

The normalised horizontal force during the lateral movement of the pipe is shown in Figure 6.11. It is evident that the load is slightly different during the first phases of the lateral movement, but it then reaches similar values of the horizontal load for

larger displacements. However, greater fluctuations are observed in the small domain test, especially as lateral motion proceeds, as the pipe becomes closer to the boundary.

Summarizing, these analyses have shown that numerical tests on small domains are a valid compromise between accuracy and computational effort, if a limited amount of pipe displacement is investigated. Hence small domains are employed in the rest of this chapter to study the effect of various input parameters on the pipe–soil interaction. Fluctuations are expected to be greater than in larger domains. However, the shorter computational time from performing simulations on small domains is considered as a greater benefit.

6.4 Sensitivity analysis on small sand geometries

A sensitivity analysis was performed to investigate the effect of various input parameters on the numerical simulations. Other sensitivity analyses for DEM analyses can be found in the literature (Ng, 2006; Widuliński et al., 2009), but none of the findings from those studies can be directly applied to the specific problem examined in this work.

The influence of parameters such as the dimensions of the domain, the size of the spheres, the damping coefficient and the loading velocity was investigated. The study was conducted mainly during the vertical penetration phase and for small embedment depths. This limited loading path allowed the use of a smaller domain. The advantage was a substantial reduction of the computational time, as already mentioned in the previous section. Moreover, some of the tests performed for the sensitivity analysis required such computational effort that they could have not been performed on a larger

Table 6.2: Summary of the tests performed on small geometries.

Test	Spheres	PSD scaling factor	Median particle size D_{50} (mm)	Domain width $\times D_{50}$	Damping ratio ζ	Loading velocity (m /s)
LT1	36 961	4	3.2	5	0.3	0.005
ST1	3964	4	3.2	5	0.3	0.005
ST2	15 843	2	1.6	5	0.3	0.005
ST3	63 360	1	0.8	5	0.3	0.005
ST4	2379	4	3.2	3	0.3	0.005
ST5	15 843	4	3.2	20	0.3	0.005
ST6	3964	4	3.2	5	0.7	0.005
ST7	3964	4	3.2	5	0.5	0.005
ST8	3964	4	3.2	5	0.1	0.005
ST9	3964	4	3.2	5	0.0	0.005
ST10	3964	4	3.2	5	0.5, 0.0*	0.005
ST11	3964	4	3.2	5	0.3	0.05
ST12	3964	4	3.2	5	0.3	0.001

* Two values of the damping ratio were used during the test: $\zeta = 0.5$ for the deposition and $\zeta = 0.0$ during the loading phase.

domain and for a longer loading path with the available computer resources. These tests are those with the smallest particles and the smallest loading velocity (Tests ST2 and ST12 in Table 6.2).

Once the effect of this first set of parameters was assessed for small domains and limited pipe displacements, the findings were applied to larger simulations. In fact, for parameters such as the relative density of the soil and the pipe–soil friction angle, it is more relevant to understand their effect at deeper embedments and larger lateral movements. The results of simulations examining these variables will be presented in Chapter 7.

The geometry of the benchmark test consisted of a domain three times the pipe diameter wide, one pipe diameter high and five times the mean particle diameter thick (shown in Figure 6.6(a)). Hence 3964 spheres were created within a domain of size

$3D \times 1D \times 5D_{50}$. The parameters investigated were the number of the particles, the thickness of the domain, the damping coefficient and the loading velocity (Table 6.2). Starting from the reference Test ST1, one parameter was varied in each test.

6.4.1 Dimension of the sand particles

The size of the particles plays a crucial role in the study of the pipe–soil interaction. Particle dimension affects the number of bodies in contact with the pipe. It also affects the critical time step, which decreases with the minimum radius of all particles in a simulation (Eq. 3.53), increasing the computational time. Therefore the particle size should be a compromise between a realistic response and computational effort.

Starting from the particle size distribution of the Leighton Buzzard sand (Section 4.1), two other grading curves were created by scaling up the original one by factors of 2 and 4. The width and height of the domain were left unchanged, but, because of the scaling factors, a different thickness ($5D_{50}$) was used. A different number of particles was generated each time, varying from about 4000 for the highest scaling factor, to about 63 000 for the real PSD.

It is worth considering the ratio D/D_{50}, between the pipe diameter and the median particle size, which depends on the scaling factor of the PSD. For the tests presented in this work, the pipe diameter was kept constant and equal to 50 mm, which is also the dimension used in the small-scale experiments (Sandford, 2012) against which the DEM model will be validated in the next chapter. Hence the pipe/particle size ratio D/D_{50} varied between 15.6 for the larger particle size (PSD×4, Test ST1) and 62.5 for the particles where no scaling factor was applied (Test ST3). A summary of the particle dimensions and pipe/particle size ratio used here is presented in Table 6.3.

Table 6.3: Summary of tests performed with different particle dimensions.

Test	PSD scaling factor	Spheres	Median particle size D_{50} (mm)	D/D_{50}	Runtime up to $w/D = 0.1$ (h)
ST1	4	3,964	3.2	15.6	4
ST2	2	15,843	1.6	31.2	41
ST3	1	63,360	0.8	62.5	565

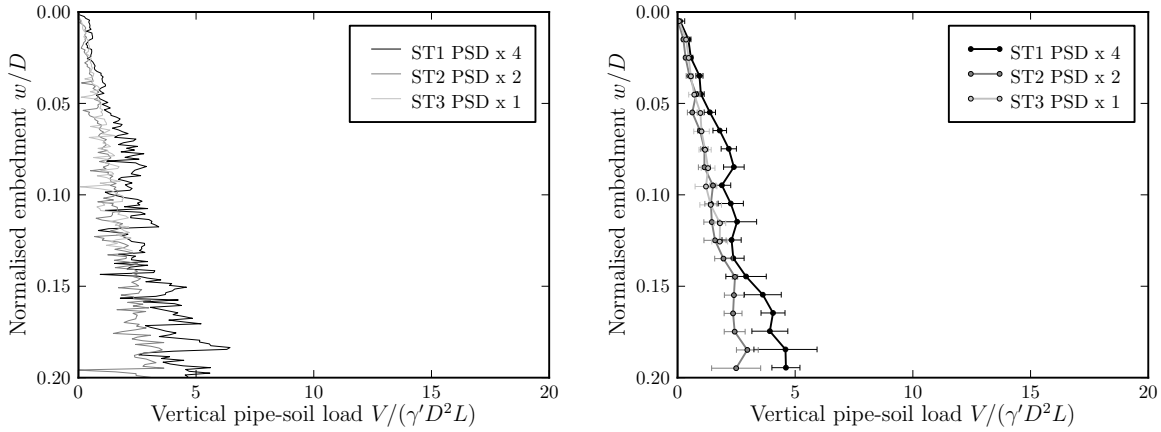

Figure 6.12: Pipe response during vertical loading tests with different particle dimensions (Tests ST1, ST2 and ST3).

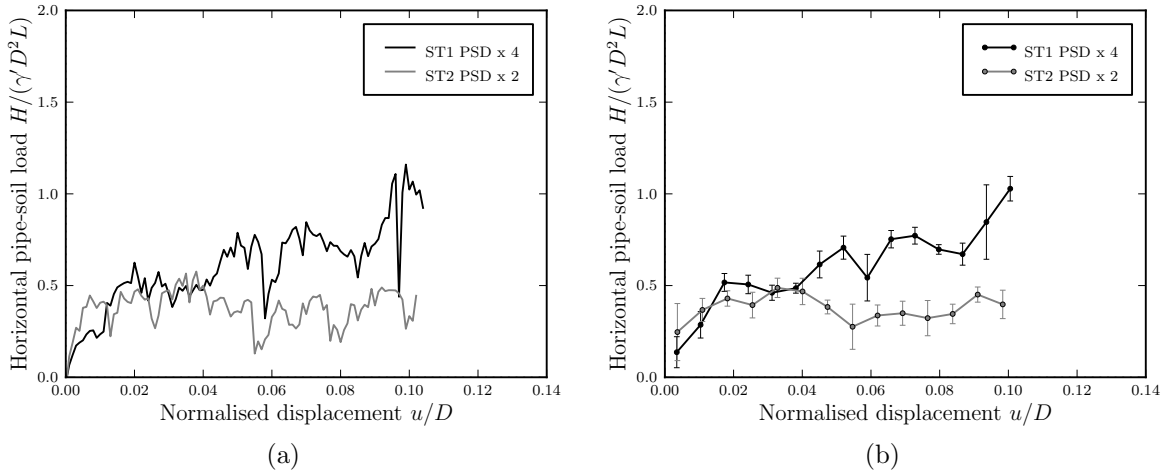

Figure 6.13: Pipe response during lateral loading tests with different particle dimensions (Tests ST1 and ST2).

After generation and deposition, the porosity of the numerical sample varied within a small range, from 0.495 to 0.485, suggesting that the arrangement of the grains is independent of the PSD scaling ratio. This condition is valid as long as the domain is sufficiently large.

The results of the vertical loading tests are shown in Figure 6.12. These show a different pipe response for certain particle dimensions. The assemblies made of larger particles ($D_{50} = 3.2\,\text{mm}$, PSD×4) react with a higher force. This trend was expected, as the smaller particles can easily rearrange themselves under the pipe load. Instead, the assemblies consisting of larger particles have less freedom, and they oppose the pipe movement with a higher force.

The results also show that for a D_{50} smaller than 1.6 mm (PSD×2), no changes are observed. This is an important result, as it indicates the maximum allowable scaling factor. The use of smaller particle sizes would lead to unnecessarily long run times. Instead, increasing the scaling factor from 1 to 2 allows the run time necessary to move the pipe through a vertical displacement of $0.1D$ (0.005 m) to be reduced from 565 to 41 hours. This is also why the test with small particles was run only up to a penetration of $0.125D$.

Figure 6.13 shows the horizontal pipe–soil load during the lateral displacement of the pipe for the tests with the two larger particle sizes (ST1 and ST2). The test with the smallest particle size (ST3) was intentionally not run for the lateral phase as it has already shown that it provides no additional better results, yet is computationally extremely expensive. The pipe–soil load differs depending on the particle size, with smaller particles exhibiting a smaller force. This is in accordance with the findings from the vertical phase.

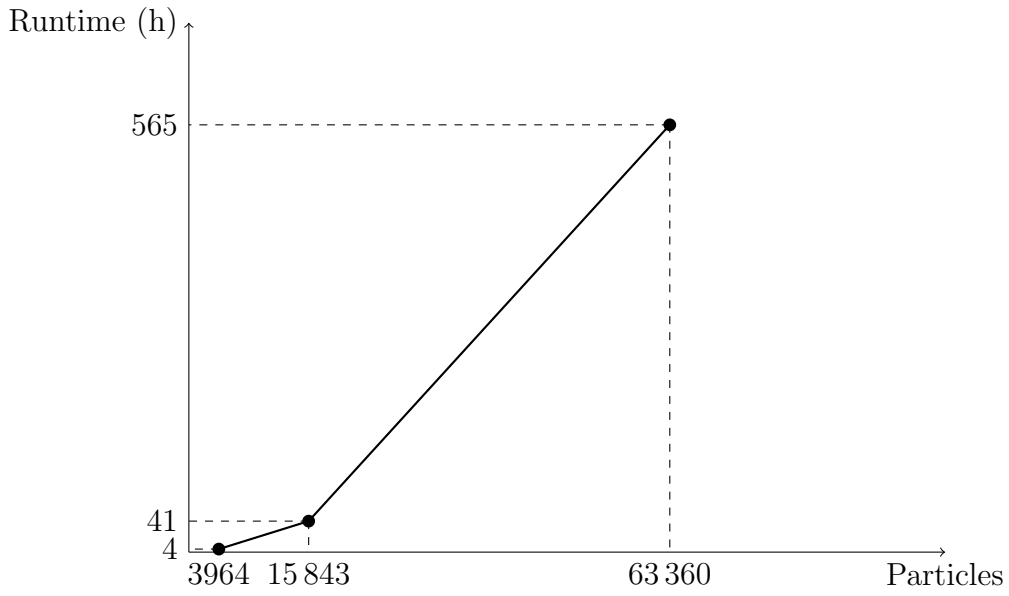

Figure 6.14: Computational time for vertical loading tests (up to $w = 0.1D$) with increasing number of particles.

Table 6.3 includes the computational time required to move the pipe to a penetration depth of $0.1D$. The runtime against the number of particles in each simulation is also plotted in Figure 6.14. For an increase in the number of particles from about 4000 to about 16 000, the runtime is 10 times bigger. For a further increase in the number of particles by a factor of 4, the runtime is instead 14 times bigger. This is due to two factors controlling the computational time: the number and the size of particles. The non-linearity relationship between number of particles and computational time was already considered in Section 3.2.2 and Figure 3.6. The computational time is influenced by particle size through the initial time step as defined in Eq. 3.53. Although this is not relevant for short tests, it should be taken into account when longer simulations on larger domains are performed (described, for instance, in Chapter 7).

Overall, these results demonstrate that the particles should be scaled up only by a factor of 2 and, more importantly, that a pipe/particle size ratio of 31.2 reproduces the pipe response realistically. For a PSD scaling factor smaller than 2, the computational

time increases enormously, with no significant difference in the results. These findings are in disagreement with DEM analyses of buried pipes subject to uplift by Calvetti et al. (2004) and Yimsiri and Soga (2006). Although upwards movements were investigated, the pipe and the particle dimension can still be compared with those used in this thesis. Those researchers both scaled their actual PSD by 50, obtaining D/D_{50} ratios of 2.5 (Calvetti et al., 2004) and 4.8 (Yimsiri and Soga, 2006), which are much smaller than desirable ratio suggested in this thesis. No justification was provided for their choice, and only preliminary analyses were mentioned, stating a negligible or limited influence of the particle size.

Although the scaling factor of 2 ($D/D_{50} = 31.2$) is suggested here as being optimal, the majority of the DEM analyses described in this thesis were performed with a scaling factor of 4 ($D/D_{50} = 15.6$). The reason was essentially to find a compromise between accuracy and computational time. It should be pointed that this D/D_{50} ratio, although smaller than the actual one, was still considerable greater than the ratios that have been used by previous researchers.

6.4.2 Thickness of the domain

The effect of the thickness of the domain was investigated by performing loading tests on assemblies with different thicknesses. Values of 3, 5, and $20D_{50}$ were used (Table 6.4). As shown in Section 6.2, the sample with a thickness of $20D_{50}$ is taken as the baseline reference for replicating plane strain conditions in numerical simulations. Hence the aim of these tests was to chose an appropriate width for the sample, that could produce results as close as possible to the ones obtained for the plane strain conditions.

Table 6.4: Summary of tests performed with different domain thicknesses.

Test	Spheres	Domain thickness $\times D_{50}$	Domain thickness (mm)	L/D
ST4	2379	3	9.6	0.19
ST1	3964	5	16	0.32
ST5	15 843	20	64	1.28

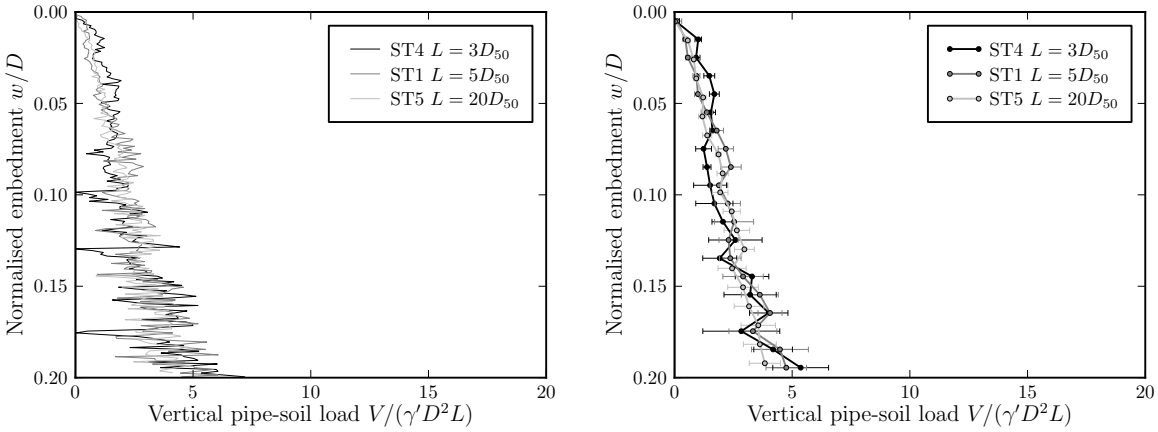

Figure 6.15: Normalised vertical pipe–soil interaction force during the penetration on samples with various thicknesses (Tests ST4, ST1, ST5).

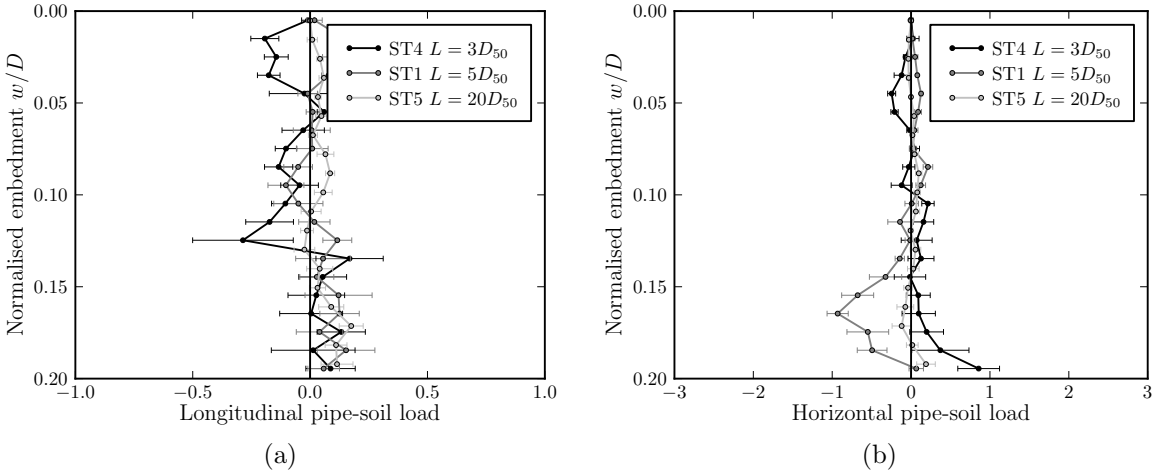

Figure 6.16: Normalised longitudinal and horizontal pipe–soil interaction force during the penetration on samples with various thicknesses (Tests ST4, ST1, ST5).

The results presented in Figure 6.15 show a very good agreement of the vertical pipe–soil load between the medium and the thicker domain. In contrast, the thinner domain, which was only $3D_{50}$ thick produced a slightly different response. The key difference here is the amplitude of the oscillations, which increases with decreasing thickness of the domain and with increasing penetration depth (due to the limited specimen depth, see Section 6.2). In fact, the maximum standard deviation of $V/(\gamma' D^2 L)$ increases from 11.0, to 15.95 and 19.02 as the thickness decreases from 20 to 5 to $3 \times D_{50}$.

The longitudinal (in the out-of-plane direction) and the horizontal force on the pipe during the vertical penetration are plotted in Figure 6.16. As expected, they all balance out, and again, their amplitude decreases with increasing thickness of the domain. The mean longitudinal force goes from a maximum of 0.465 to a minimum of 0.284, and the mean horizontal force varies in the range 1.392 to 0.307.

In summary, a domain with a thickness of $5D_{50}$ is capable of reproducing the same vertical response of the pipe in plane strain conditions. A thicker domain significantly increases the number of particles but does not alter the vertical response, instead only stabilizing the pipe in the lateral and out-of-plane directions. Hence, the medium thickness of $5D_{50}$ was chosen as a compromise between a stable simulation and the computational effort required.

6.4.3 Loading velocity

The velocity at which the pipe was pushed into the numerical sample was then varied between 0.05 and 0.001 m/s (Tests ST11, ST1 and ST12). It is important to note that these tests were run on the same initial numerical sample; after the gravity deposition,

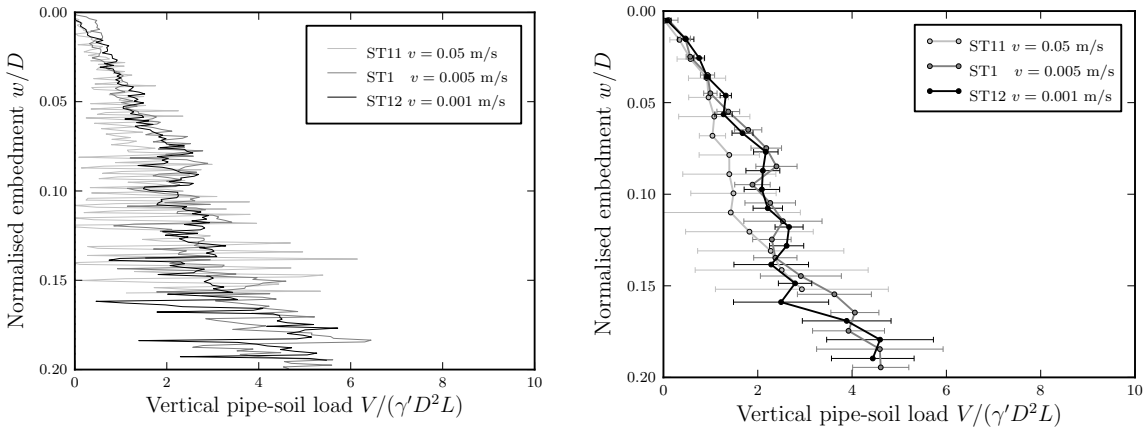

Figure 6.17: Pipeline response during the penetration at various loading velocities (Tests ST11, ST1, ST12).

the numerical sample was saved and reloaded to perform various simulations with different values of the loading velocity.

The results presented in Figure 6.17 show that at the highest velocity of $v = 0.05\,\mathrm{m/s}$ (Test ST11), the response is different. For the medium and small values, however, the only effect of the loading velocity is to decrease the amplitude of the fluctuations: the maximum standard deviations for the tests at 0.005 and $0.001\,\mathrm{m/s}$ are 1.34 and 1.13 respectively.

A further investigation was carried out by analysing the evolution of the number of contacts between the pipe and the sand particles, together with the mechanical coordination number, as shown in Figure 6.18. As expected, the number of spheres in contact with the pipe increases proportionally with the penetration of the pipe, almost irrespective of the loading velocity (if the fluctuations are neglected). In contrast, the coordination numbers, which all start from the same value (as the tests all start from an identical sample), remain nearly constant for small velocities, and decrease considerably for higher velocities. It should be noted that the mechanical coordination number gives

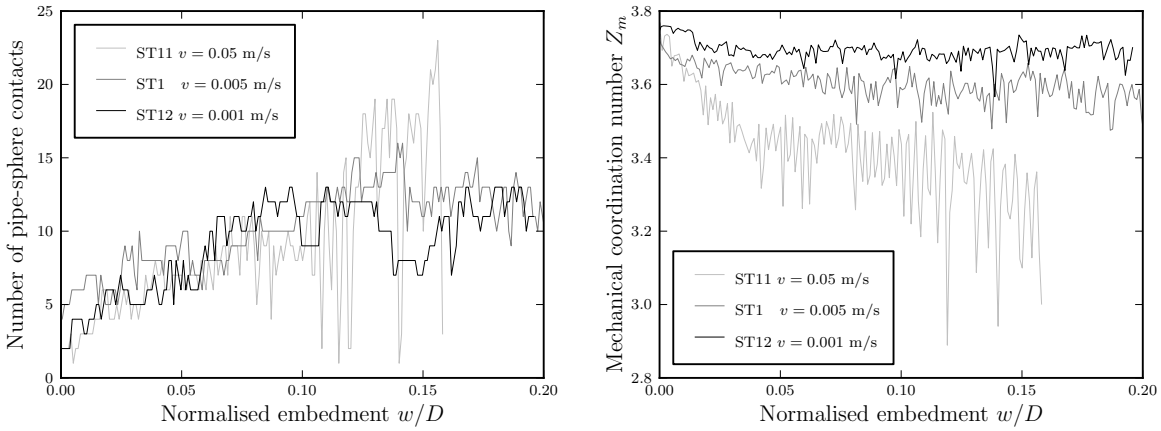

(a) (b)

Figure 6.18: Evolution of contacts during the penetration at various loading velocities (Tests ST11, ST1, ST12).

the average number of interactions per particle in the specimen, and hence reflects the arrangement of the particles within the packing. The trends described suggest that when a higher velocity is used, the number of spheres in contact with the pipe is similar to the test with a slow velocity. On the other hand, looking at the coordination number, it seems that in the fast test the particles do not have time to rearrange themselves.

Lateral loading tests at constant embedment were also performed using the different loading velocities. These tests were carried out from the same initial conditions (i.e. same pipe vertical position and same particle arrangement inside the soil). This could not be guaranteed if the pipe had been pushed vertically into the sand at different velocities (as shown in Figure 6.18(b)). Hence the three lateral tests were performed starting from the point in Test ST1 where the pipe had already been penetrated to an embedment depth $w = 0.2D$.

The results of these lateral tests are presented in Figure 6.19(a). As already anticipated from the results of the vertical phase, when the loading velocity increases, the

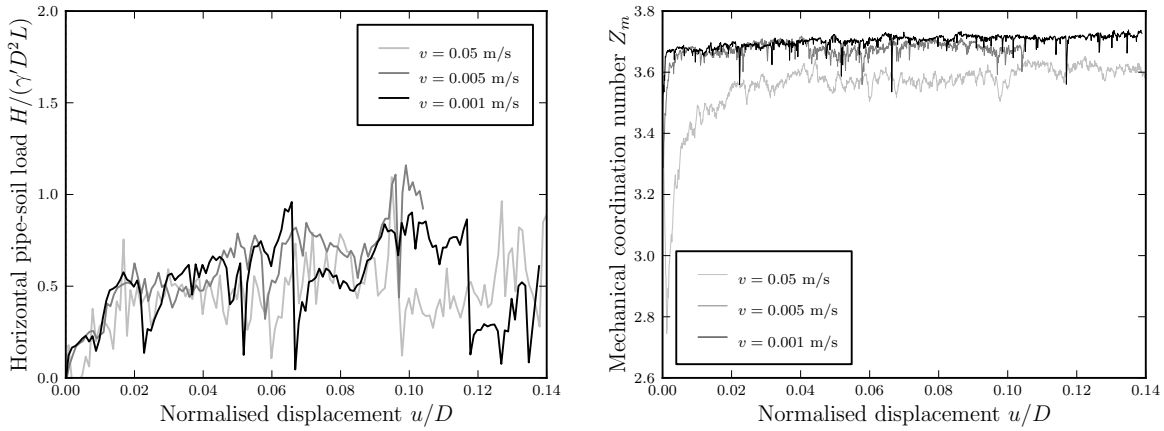

(a) (b)

Figure 6.19: Pipeline response during the lateral phase for various loading velocities.

pipe response changes slightly, and the fluctuations increase accordingly. The effect of the loading velocity is also visible from Figure 6.19(b), where the mechanical coordination number is shown. This parameter is lower when $v = 0.05\,\text{m/s}$ meaning that the particle arrangement within the soil is different when the loading velocity is too high.

Concluding, as the results from the vertical and lateral tests performed with the two smallest velocities did not differ excessively, the one equal to 0.005 m/s (Test ST1) was considered sufficient to be employed in the subsequent analyses.

6.4.4 Viscous damping ratio

Local viscous damping was used for the loading tests on the pipe. Although there is a physical meaning behind the use of viscous damping, its formulation, and the appropriate value of the damping coefficient, is still an object of study by various researchers (see Section 3.3.3).

As shown in Figure 5.14 of the previous chapter, the effect of damping is observed in the preparation of the sample, as a packing prepared with more damping has a greater height (hence a looser state). A series of penetration tests was performed, where the

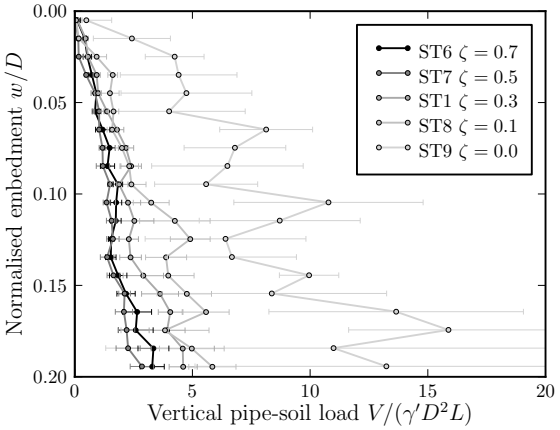

Figure 6.20: Results of penetration tests with various damping coefficients during deposition (Tests ST6, ST7, ST1, ST8, ST9).

pipe was loaded on specimens prepared using different damping ratios, varying ζ from 0.7 to 0.0 (Tests ST6, ST7, ST1, ST8 and ST9). The same values of damping were used during the loading phase of the tests. The damping ratios in the normal and tangential directions were assumed to be the same ($\zeta_n = \zeta_s = \zeta$).

As the tests start from samples with different arrangements, different behaviour during the vertical penetration is expected. The pipeline response presented in Figure 6.20 confirms a stiffer response for the non-damped (denser) sample, and a weaker response for the damped (looser) samples.

In addition, a test was performed starting from a sample prepared as in Test ST7, but where the penetration was carried out without any damping. The results show that no major differences are found in the average pipeline response (Figure 6.21(a)). The damping only attenuates the fluctuations of the pipe–soil force, reducing the maximum standard deviation over the entire penetration depth almost by half (Figure 6.21(b)). A maximum standard deviation of 0.93 was observed when no damping was used during the loading stage. Instead, when damping was kept throughout the simulation, a maximum standard deviation of only 0.51 was recorded.

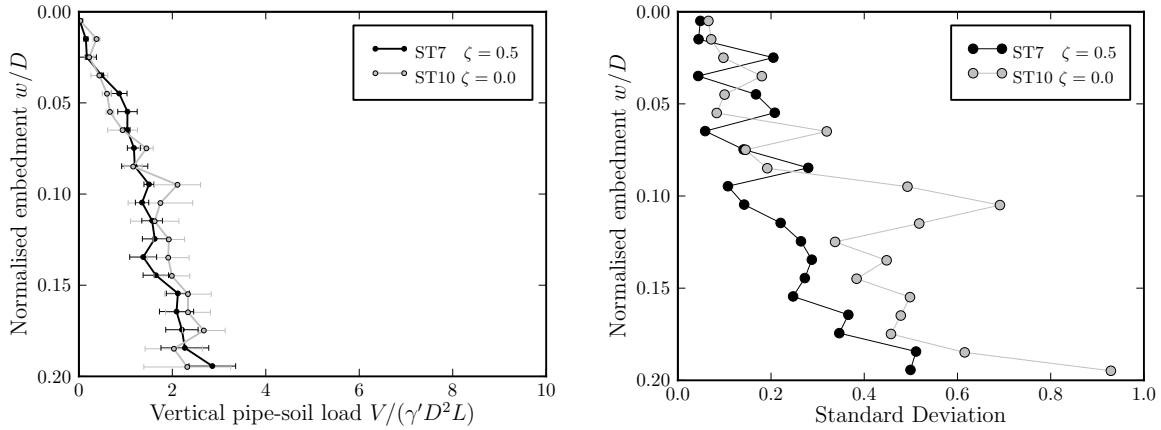

Figure 6.21: Results of the penetration stage of loading tests on identical specimens, but with various damping ratios during loading (Tests ST7, ST10).

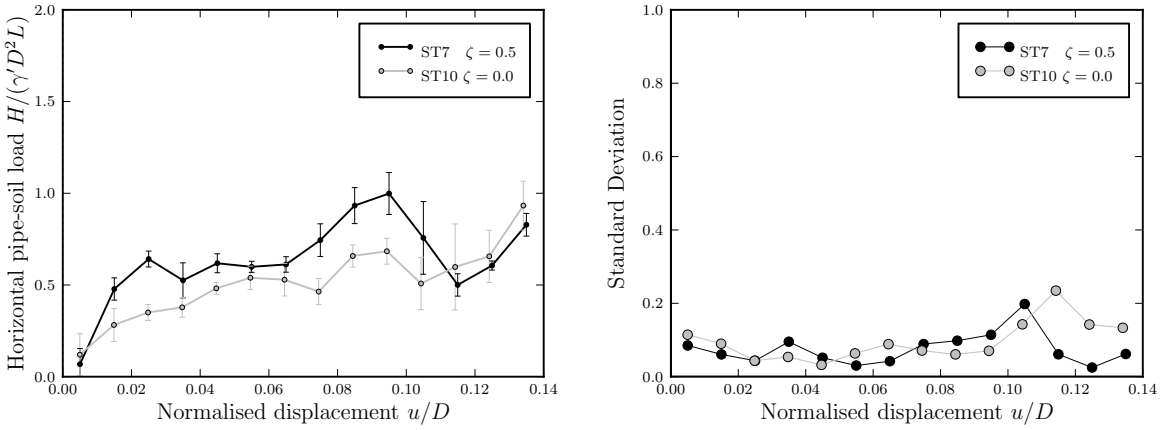

Figure 6.22: Results of the lateral stage of loading tests on identical specimens, but with various damping ratios during loading (Tests ST7, ST10).

The results of the lateral loading phase are shown in Figure 6.22. Unlike the vertical phase, there is not a clear influence of the damping. Also, the standard deviation oscillates in both tests, without a clear pattern as the lateral movement of the pipe proceeds.

In summary, viscous damping mainly influences the preparation phase of the specimen and, as consequence, the subsequent loading phase as well. As it aims at replicating the physical viscous dissipations occurring at a particle level, it should be included in

the contact law formulation. However, no recommendations could be deduced from the presented results, nor in related literature. In fact, it is common among DEM researchers to use a certain damping coefficient (either viscous or non-viscous) as long as simulations are stable. Therefore, a damping ratio of $\zeta = 0.2$ was chosen, and kept constant throughout the remainder of study.

6.5 Summary of results and compromises

This chapter has presented numerical analyses of pipe sections loaded on a small numerical sample replicating a sandy seabed. To reduce the computational demand, most tests were performed on small samples consisting of about 4000 particles (instead of 37 000, Section 6.3), allowing only limited amounts of vertical and lateral pipe movement ($0.2D$ in each direction, as against $2D$ and $4D$ in the tests to be described in Sections 7.4.2 and 7.4.1). The analyses aimed at exploring the influence of significant numerical parameters, such as particle dimension, domain thickness, loading velocity of the pipe and damping ratio.

The analyses have provided useful recommendations for performing pipe loading tests on larger specimens and for larger pipe movements. These recommendations should be followed in ideal cases, where computational times are not a issue. However, due to the computational demand of this type of analysis, some of these recommendations are impractical in some of the large simulations, and compromises must be found.

In this case, the additional value of these tests is to provide information on the pipe response when the recommendations cannot be followed. In other words, to anticipate the different response when the simulation is not performed in ideal conditions.

Below is a summary of the main findings from the small displacement tests, and a list of the compromises that had to be made to perform the tests presented in the next chapter.

- The domain size should be large enough to contain the failure mechanism, i.e. $7D \times 4D \times 5D_{50}$. Sometimes a smaller domain was used to reduce the number of particles and hence the computational demand. The drawback is that the pipe–soil force becomes less stable. This effect increases as the pipe penetrates into the sand, because the pipe becomes closer to the boundary.
- The particle size influences the pipe–soil response during both vertical and lateral motion of the pipe. The particle size distribution may be scaled up by a factor of 2, giving a pipe/particle size ratio $D/D_{50} = 31.2$. With such a scaling factor, numerical tests in the large domain would have required about 150 000 particles. This number is roughly 10 times larger than 15 843, the number of particles used in the small domain test with the same PSD (Test ST2). These two tests differ only in the number of particles. As the dependency between number of particles and computational time is not strictly linear (Figure 3.6 and Table 6.3), the test on the large domain would require a computational time more than 10 times longer than 22 days, which is the time required to move the pipe of $w = 0.1D$ in the small domain test ST2.

  This was obviously impractical, and instead a compromise between accuracy and computational time was necessary. Therefore only one of the tests described in the next chapter was performed with the ideal PSD scaling factor of 2. Whenever larger particles were used, a slightly different response was expected.
- A domain thickness of $5D_{50}$ is sufficient to model plane strain conditions. This

thickness was used in all the remaining analyses.

- The effect of the loading velocity is that larger velocities vary the pipe–soil response, whereas velocities smaller than a certain limit only affect the amplitude of the fluctuations in the pipe–soil interaction forces. This limit value was found to be 0.005 m/s, hence it is chosen for the remaining analyses. This value does not influence the pipe response on average, but still gives large fluctuations of the load.

  The chosen value was used for the vertical loading–unloading test and for the vertical and lateral monotonic tests (Sections 7.2 and 7.3). When tests involving lateral pipe displacements larger than $1D$ (50 mm) were carried out, a faster loading velocity was preferred (Section 7.4). For these analyses, larger fluctuations and instabilities of the solution were expected.

- The damping influences mainly the preparation of the numerical specimen by varying the arrangement of particles. During movement of the pipe, for the same specimen, the effect of damping is to attenuate the fluctuations of the pipe–soil force. In the absence of a specific calibration, and of detailed recommendations in the literature, a value of the viscous damping ratio of 0.2 is considered to be realistic and is used in the remaining simulations.

Chapter 7

Pipe–soil interaction: large displacement analyses

This chapter describes the simulations performed using a 3D domain and under loading conditions comparable to those experienced by the pipe during small-scale model tests. The pipe–soil interaction is investigated under four different types of loading conditions: (i) vertical loading and unloading, (ii) monotonic vertical and lateral loading, (iii) cyclic large lateral displacement at constant vertical penetration and (iv) cyclic large lateral displacement under constant vertical load. Results are presented both in terms of force–displacement curves and in a graphical fashion (particle plots, velocity vectors, and contact forces) to highlight the mechanisms occurring at a particle level.

7.1 Tests setup

The geometry and mechanical parameters of the numerical model were taken from the analyses presented in Chapters 4, 5 and 6. Those values were used in most of the DEM

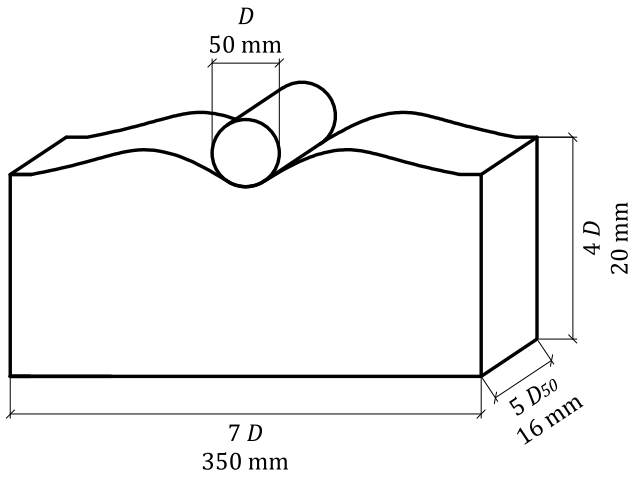

Figure 7.1: Geometry of domain for large displacement analyses.

analyses presented in this chapter, unless otherwise specified.

The chosen dimension of the specimen was large enough to include the expected failure mechanism due to vertical and lateral loading of the pipe. A width of $7D$ and a height of $4D$ was chosen (Sandford, 2012). The thickness of the numerical specimen was taken as $5D_{50}$ as assessed from the sensitivity analysis described in Section 6.4.1. The specimen was enclosed by rigid frictionless walls. The geometry is sketched in Figure 7.1 and a view of the simulation before commencing any pipe loading tests is shown in Figure 7.2.

7.1.1 DEM soil parameters

The parameters of the modelled soil were calibrated using triaxial tests in Chapter 4 and are summarised in Table 7.1 The viscous damping ratio $\zeta = 0.2$ was taken as assessed in the sensitivity analysis (Section 6.4.4).

The particle size distribution (PSD) of Leighton Buzzard (LB) sand 14/25 was used in the numerical model. From the sensitivity analysis presented in Section 6.4.1, a scaling factor of the PSD equal to 2 should have chosen. However, such a scaling

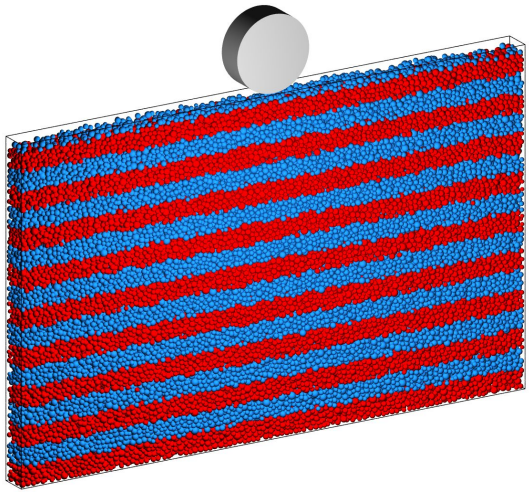

Figure 7.2: Typical initial geometry of large displacement analyses.

factor would have required an extensive computational effort. A domain of dimensions $7D \times 4D \times 5D_{50}$ would have needed of about 150 000 spheres to fill the volume. In an attempt to find a compromise between accuracy and computational effort, a scaling factor of 4 was chosen instead (Section 6.5). With the chosen value of $D_{50} = 3.2\,\text{mm}$, the total number of particle was of 36 961 and the thickness of the specimen was 16 mm (Figure 7.1). It is important to note that, even with these relatively large particles, the simulation took approximately 7 days to run the penetration phase until an embedment depth of $w = 0.2D$ on 8 cores of a 16 core workstation with 32 GB of available RAM.

7.1.2 DEM pipeline parameters

The choice of the numerical parameters of the pipeline (Table 7.2) was made in order to replicate the solid steel pipe usually employed in small-scale tests on sandy seabeds, as in those performed by Sandford (2012). The pipe diameter D was taken of 50 mm and its length equal to the thickness of the domain, $L = 5D_{50}$, as described in Section 6.2. The pipe density was taken as that of a generic steel material ($7850\,\text{kg/m}^3$).

The contact law parameters of the pipeline were taken from the elastic properties of

Table 7.1: Input parameters of DEM soil.

Parameter	Symbol	Units	Value
Median particle size	D_{50}	mm	3.2 *
Particle density	ρ	kg/m^3	2650
Young's modulus	E	GPa	70 **
Poisson's ratio	ν		0.3
Interparticle friction coefficient	ϕ_μ	°	26
Rolling stiffness coefficient	β_r		0.05
Plastic moment coefficient	η		0.3
Viscous damping ratio	ζ		0.2

* $D_{50} = 1.6$ mm in the cyclic large lateral displacement test at constant embedment (Section 7.4.1).

** $E = 70$ MPa in the three cycle tests at constant vertical load (Section 7.4.3 and 7.4.4)

Table 7.2: Input parameters of DEM pipeline.

Parameter	Symbol	Units	Value
Pipe diameter	D	mm	50
Pipe length	L		$5D_{50}$
Pipe density		kg/m^3	7850
Young's modulus	E_p	GPa	200 *
Poisson's ratio	ν_p		0.3
Pipe–soil interface angle of friction	δ		2/3 ϕ_μ
Rolling stiffness coefficient			0.05
Plastic moment coefficient			0.3
Viscous damping ratio			0.2

* $E_p = 200$ MPa in the three cycle tests at constant vertical load (Section 7.4.3 and 7.4.4)

the steel ($E_P = 200$ GPa, $\nu_P = 0.3$). The angle of friction at the pipe–soil interface was assumed to be a fraction of the interparticle friction angle of the sand, $\delta = {}^2/_3\ \phi_\mu$. This value is a very rough estimate originally suggested by Potyondy (1961), who proposed ratios of ${}^\delta/_{\phi_\mu} = 0.54$ for dry sand on smooth polished steel and ${}^\delta/_{\phi_\mu} = 0.76$ for dry sand on rough rusted steel. Further analyses with a different interface friction angle are presented in Section 7.3.4. The rolling coefficients were taken as those of the sand. These were used to calculate the interacting moment, which was only applied to the sand particles (Section 5.2.1).

7.2 Vertical loading–unloading test

An initial test was performed to explore the pipe response and to validate the DEM approach during a cycle of vertical loading and unloading. Although lateral loading was not performed during this test, the numerical sample was the same as that used for the vertical and lateral tests described in the next section.

7.2.1 Loading history

The pipe was pushed into the numerical specimen at a constant rate $v = 0.005\,\mathrm{m/s}$. When it reached an embedment depth of 10 mm ($w = 0.2D$), the pipe was lifted upwards at a rate 10 times slower, i.e. $v = 0.0005\,\mathrm{m/s}$, until it reached zero vertical load. Then it was pushed again vertically at the same rate as the initial loading. These values of the loading rate were taken from the results of the sensitivity analysis (Section 6.4). However, they are different from those used in the laboratory experiment against which these results are compared. The experimental values were 0.1 mm/s and 0.001 mm/s for loading and unloading respectively (Sandford, 2012). Hence the numerical loading rates are 50 and 500 times larger than the experimental ones. If those realistic loading rates were used, the numerical simulation would have taken 50 and 500 times longer.

7.2.2 Results and comparison with experiment

The numerical results were validated against a small-scale model test performed by Sandford (2012) using a 50 mm pipe on Leighton Buzzard sand, grade DA30 ($D_{50} = 0.5\,\mathrm{mm}$). This sand differs from the LB sand grade 14/25 (used here in the numerical

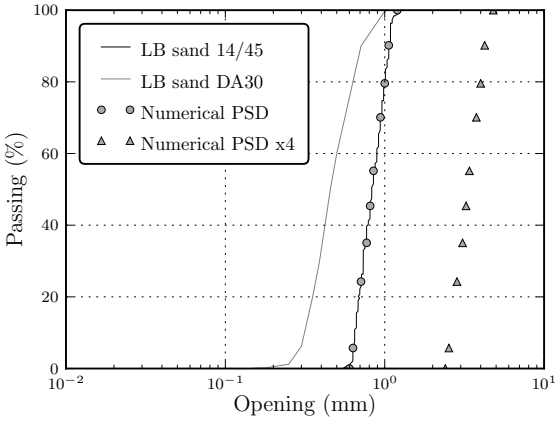

Figure 7.3: Grading curves of experimental and numerical sands.

model and calibrated against experimental triaxial tests) only by its PSD. As shown in Figure 7.3, the scaling factor between the adopted numerical PSD (×4) and the LB sand grade DA30 is 6.4. The LB sand DA30 also has a slightly larger portion of small grains. However, this should not have any influence during the pipe loading test as the load in a DEM simulation is usually taken by the larger particles, through which the "strong" contact force network is formed (Thornton, 2000). In this regard, O'Sullivan (2011b) suggests that, although smaller particles do not contribute to the response of the material, they increase the computational cost of the simulation.

Force and displacement data from the numerical simulation were recorded at a frequency of 100 Hz, such that 100 data points were recorded over the time the pipe moved $0.1D$ (5 mm). In Figure 7.4 the results from the DEM simulation are compared with the loading and unloading laboratory test performed by Sandford (2012).

The vertical load–penetration curve shows a typical response of a sandy seabed, confirming the linear relationship proposed by Zhang (2001):

$$V/L = k_p w \tag{7.1}$$

where k_p is the vertical plastic stiffness, here found to be 36.6 kPa. This is close to

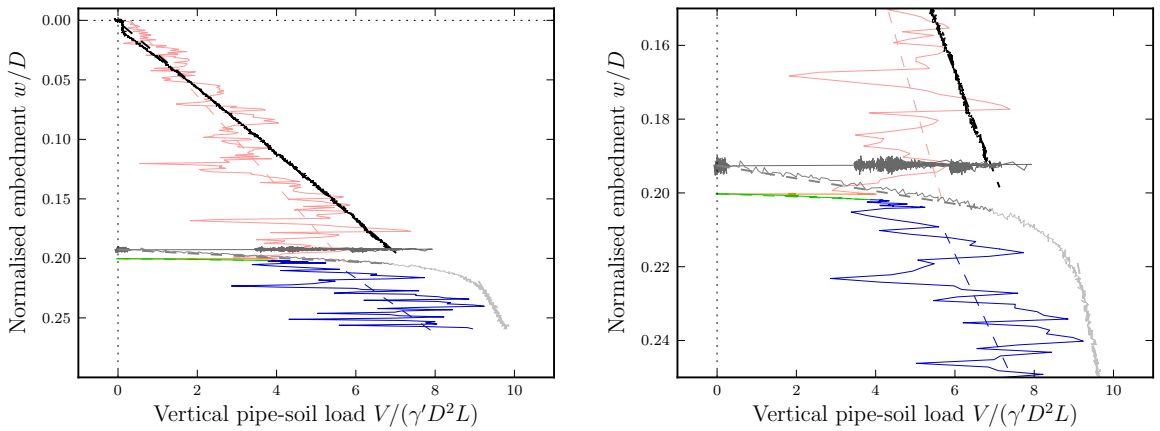

Figure 7.4: Vertical loading–unloading test: (coloured lines) DEM results and (grey-scale lines) experimental results (Sandford, 2012). (a) Entire test and (b) enlargement of the unload–reload phase.

the experimental value of $k_p = 41.2\,\text{kPa}$, especially considering that Sandford (2012) obtained a variability in observed plastic stiffness of $35.5 < k_p < 54.3\,\text{kPa}$ when repeating the same loading test. This result shows the capability of the DEM model to reproduce the vertical response in an accurate way. It is worth stressing here that no further calibration was necessary to replicate numerically the experimental pipe–soil load with such accuracy. The mechanical parameters of the numerical particles were calibrated from the triaxial tests (Chapter 4). The sensitivity analysis presented earlier in Chapter 6 was only necessary to tune parameters affecting the numerical simulation such as domain dimensions, particle size and loading velocity. No further adjustments were made. Hence this result (i) confirms that the preliminary work presented early in this thesis was needed for replicating experimental data correctly, and (ii) validates the DEM approach as an appropriate method to analyse the pipe–soil interaction during a loading event.

During the unloading stage, the vertical load–displacement curve is extremely stiff, both in the numerical and in the experimental test. On reloading, the pipe–soil curve

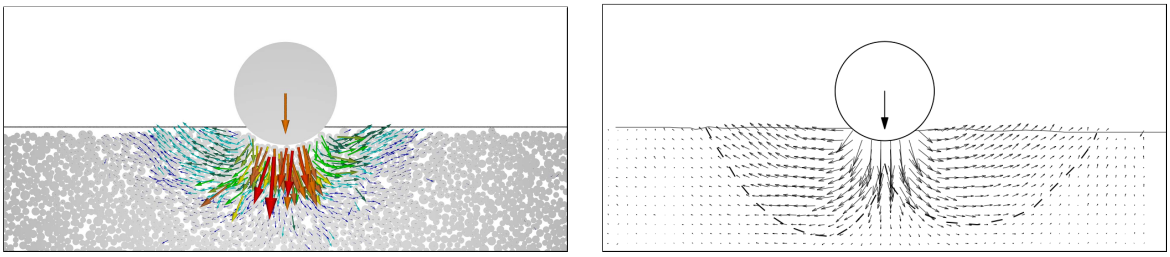

(a) (b)

Figure 7.5: Velocity field at $w = 0.1D$: (a) DEM simulation and (b) as obtained from PIV analysis during the laboratory test (Sandford, 2012).

has a greater stiffness than during the virgin loading. The plastic stiffness in the numerical and in the experimental tests is 3195 and 682 kPa respectively.

After reaching approximately the same vertical load recorded before unloading commenced, the load–displacement curve proceeds with a slope close to that of the virgin line. This is observed both in the numerical test and in the experimental test.

7.2.3 Failure mechanism

The failure mechanism within the soil during vertical penetration in the numerical and experimental tests is deduced from analysis of the velocity field.

For the numerical test, those particles lying within a vertical slice of thickness $1.1D_{50}$ passing through the centre of the sample are considered for the evaluation of the velocity vectors. Then these velocity vectors are determined by considering the change of displacement over the time required for the pipe to move throughout a distance of $0.1D$, and are shown in Figure 7.5(a). They exhibit a punching shear failure mechanism, dominated by compression of the underlying soil, and little movement of soil particles at the surfaces adjacent to the pipe. A slightly asymmetric field is developed, as would be expected due to the non-homogeneity of the natural soil.

The computed velocity field from the numerical test is compared with experimental

results obtained by particle image velocimetry (PIV) as shown in Figure 7.5(b). Good agreement is observed, showing a clear failure surface during the vertical penetration, and the same limited amount of soil movement towards the surface.

7.3 Vertical and lateral loading test

7.3.1 Validation test

A series of analyses was performed to investigate the pipe response during both vertical and lateral movement, and to validate it against experimental data.

The geometry, the pipe and soil properties were as described above. In fact, the generation of the numerical sample and the initial vertical penetration until $w = 0.2D$ were performed only once. Then the simulation was reloaded to perform both the vertical loading–unloading test described above and the vertical and lateral tests described below. This is one advantage of DEM over experiments, that the same simulation can be reloaded several times, to perform different tests starting from the same pipe position on identical specimens.

In all of the tests in this section, the pipe was penetrated to an invert embedment depth of 12.5 mm ($w = 0.25D$) and was moved laterally until a displacement of 45 mm ($u = 0.9D$) while keeping the embedment depth constant.

7.3.1.1 Comparison with experiment

The results from the DEM simulation are compared with the results of the small-scale experimental test (Sandford, 2012) in Figure 7.6. For clarity, the numerical results are shown through their raw data, recorded at data acquisition frequency of 100 Hz, and

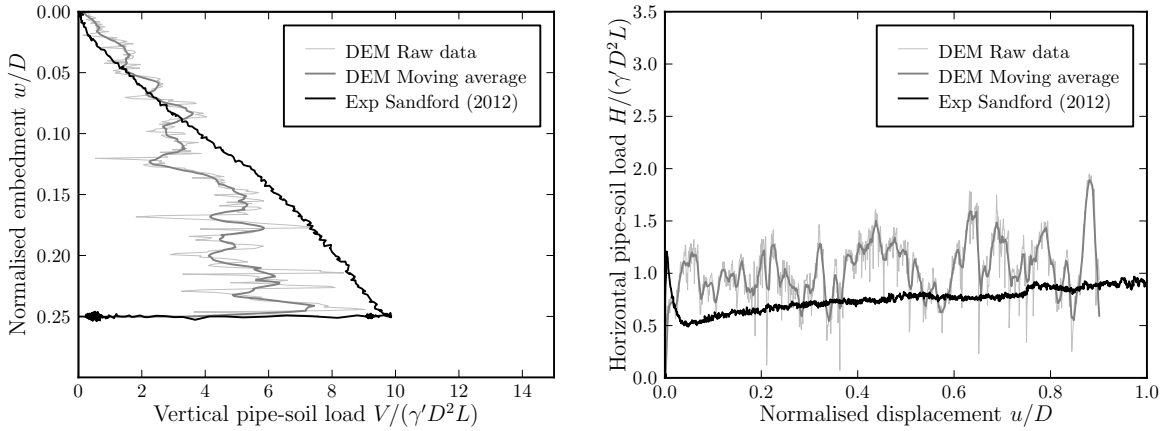

Figure 7.6: Vertical and lateral load–displacement responses from DEM simulation and laboratory test.

the moving average based on a window of 10 data points. The vertical load–penetration curve in Figure 7.6 shows the same linear relationship as described in Section 7.2.2. Hence the plastic stiffness is still $k_p = 36.6\,\text{kPa}$. The experimental value for this test was found to be equal to 50 kPa, which is still broadly comparable with the numerical value. The results during the lateral movement phase are less accurate, as the initial increase and the sudden drop of the lateral resistance were not replicated. A likely reason is that in the numerical test the pipe was moved at a fixed lateral velocity, which might have been to fast for high passive resistance to develop and subsequently dissipate in the sand. A large oscillation amplitude is observed in the numerical test, which could be reduced by increasing the damping ratio.

7.3.1.2 Pipe–soil interaction at a particle scale

Figure 7.7 shows the front views of the sample at various stages of loading. The particles are coloured according to their initial position prior to vertical loading. The height of each layer is taken as 12.5 mm ($D/4$). The surface level at the start of the

loading and the instantaneous pipe velocity vector are also depicted.

As the pipe moves downwards it compresses the sand underneath it, with minimal heave at the surface. As the test proceeds and the pipe moves laterally, it scrapes away a thin layer of sand, and a berm builds up in front of it.

The network of contact forces at various stages of the simulation is shown in Figure 7.8. During initial penetration, the contact forces are symmetrically distributed, radially decreasing away from the pipe. Calvetti et al. (2004) observed that, when the distance between the pipe and the rigid base of the soil domain is too small, the forces are transmitted vertically and a type of bearing "column" is formed. In this analysis, it was observed that the vertical stresses calculated along the bottom boundary were reasonably uniform, suggesting that the modelled depth of sand is sufficient. The dominant internal forces change to a diagonal pattern as the pipe moves laterally. It is interesting to observe how the chain of contact forces thickens and rotates during the lateral movement of the pipe (Figure 7.9). As the pipe moves laterally, the initial force chain decreases its thickness, indicating a reduction of load on the particles forming that chain (Figure 7.9(a) to 7.9(b)). The load is then shared between the observed force chain as well as other chains forming and thickening in front of the pipe (Figure 7.9(b) to 7.9(c)). Thereafter, the pipe's lateral movement is resisted by a transfer of force chains.

The corresponding particle velocity fields, determined by considering the change of displacement over the time required for the pipe to move through a distance of $0.1D$, are shown in Figure 7.10. These confirm a punching shear failure mechanism during the vertical penetration, with compression of the underlying soil and practically no movement of the soil particles at the surface adjacent to the pipe. The pattern of the

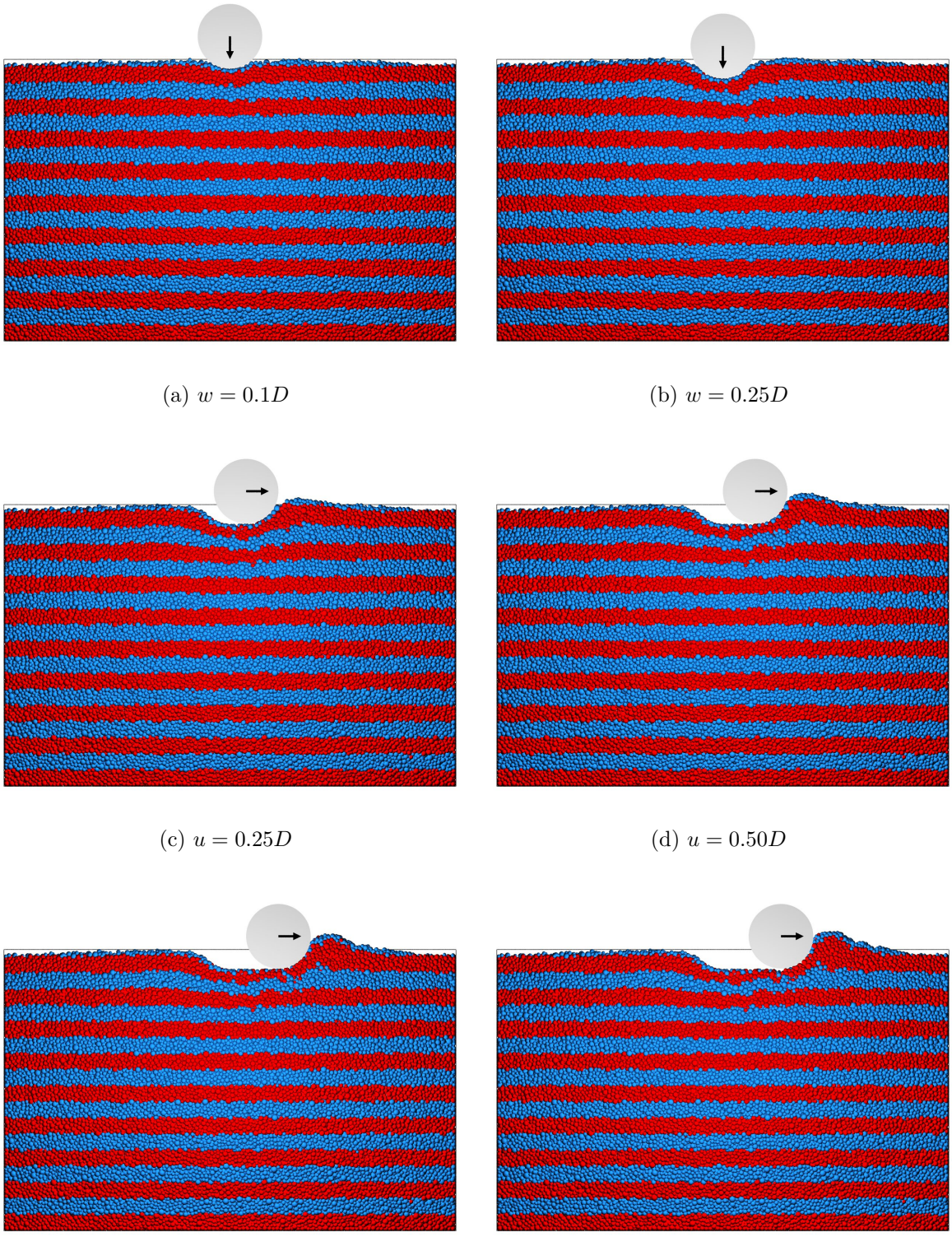

(a) $w = 0.1D$

(b) $w = 0.25D$

(c) $u = 0.25D$

(d) $u = 0.50D$

(e) $u = 0.75D$

(f) $u = 0.9D$

Figure 7.7: Snapshots of the simulation at various stage of loading.

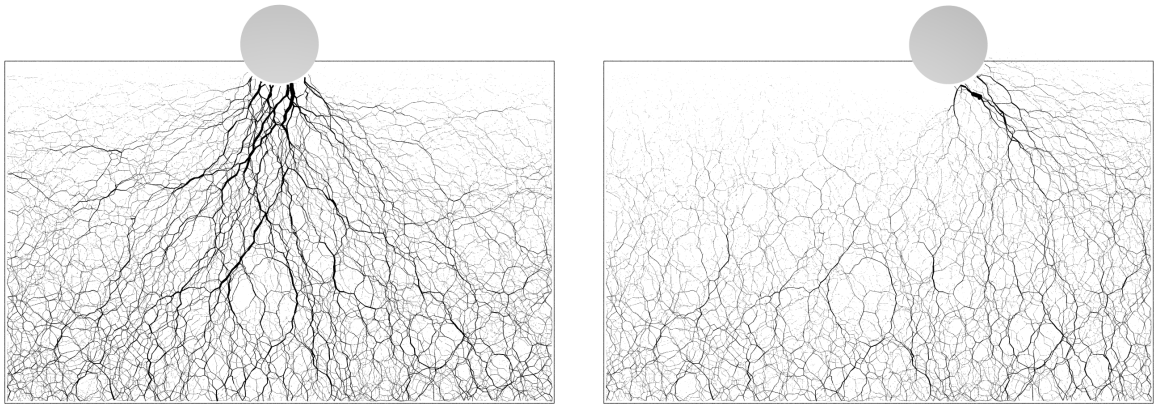

(a) $w = 0.25D$ (b) $u = 0.9D$

Figure 7.8: Contact force network (a) at maximum penetration and (b) at maximum lateral displacement.

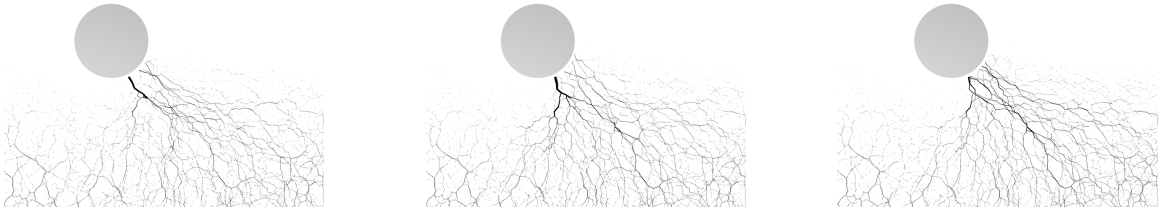

(a) $u = 0.64D$ (b) $u = 0.66D$ (c) $u = 0.68D$

Figure 7.9: Enlargement of contact force network at different pipe positions.

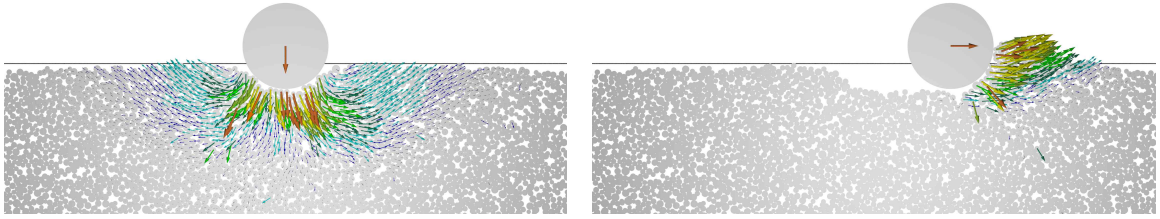

(a) $w = 0.25D$ (b) $u = 0.9D$

Figure 7.10: Velocity field (a) at maximum penetration and (b) at maximum lateral displacement. Only a portion of the entire domain is shown.

velocities during the lateral displacement clearly indicates that soil motion is restricted to a region in front of the pipe. This finding suggests that during lateral displacement, only the soil near the seabed surface is affected by pipeline motion, and the soil below the pipe invert level is practically undisturbed. Moreover, the velocities are essentially horizontal, while the pattern produced by the force chains (Figure 7.9) is more inclined.

7.3.2 Effect of rolling resistance

The influence of the rolling resistance component of the contact law during monotonic vertical and lateral loading was investigated. The aim was to assess whether or not the moment–relative rotation contact law was essential to the DEM model. This contact law was introduced in Section 3.3.2.2 and the rolling coefficients β_r and η defined in Equations 3.23, 3.31 and 3.32.

A vertical and lateral loading test was performed with both the rolling stiffness coefficient β_r and the plastic moment coefficient η equal to zero, i.e. the particles were free to roll. All the other mechanical parameters were taken from the analyses presented in Chapters 4, 5 and 6, and used in the previous tests presented in this chapter. The applied pipe displacement was the same as in the validation test (Section 7.3.1), so that results could be compared. The validation test used rolling coefficients as estimated by the calibration procedure described in Section 4.4, i.e. $\beta_r = 0.05$ and $\eta = 0.3$.

Throughout this section, the numerical test with particles free to roll will be referred to as "rolling free test", whereas the validation test will be referred to as "rolling restricted test".

The numerical specimen was prepared using the usual process of generation and gravitational deposition of the particles. In the rolling free test, the deposition occurred

Table 7.3: Rolling coefficients and specimen parameters after sample preparation.

Test	β_r	η	Height (m)	Porosity
Rolling restricted	0.05	0.3	0.217	0.480
Rolling free	0	0	0.198	0.433

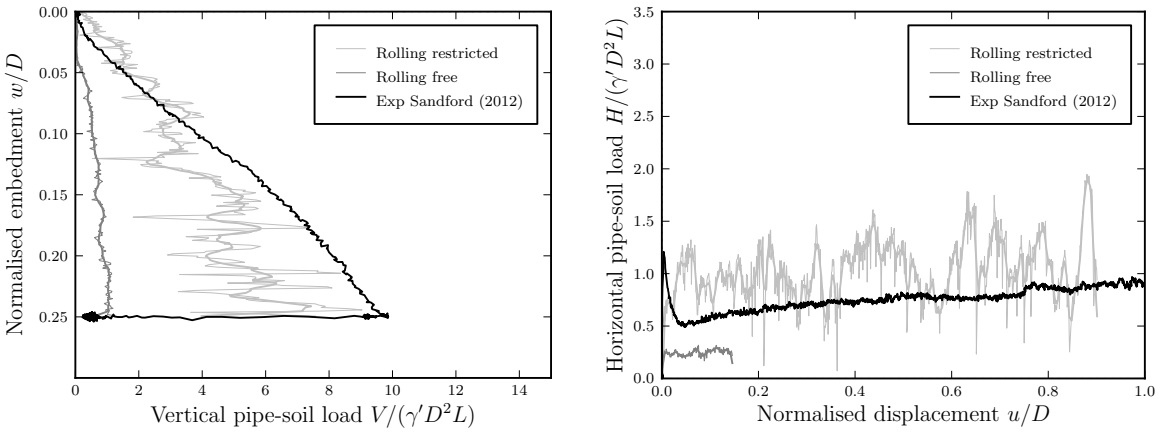

Figure 7.11: Vertical and lateral load–displacement response of numerical samples with and without the moment–relative rotation contact law.

with more bouncing of the particles, which is expected. At the end of the deposition, the sample height and the porosity were larger than in the rolling restricted test. These values are summarized in Table 7.3. The difference is in agreement with findings from the analysis of the generation procedure using various interparticle friction angles ϕ_μ (Section 5.1.3). Lower friction, either rolling friction β_r or interparticle friction ϕ_μ, lets the particles arrange themselves in a denser state.

Figure 7.11 shows the results of the vertical and lateral loading tests with and without the moment–relative rotation contact law. The numerical results are also compared against the small-scale laboratory test results from Sandford (2012).

The response during vertical loading is much softer in the rolling free test than where the rolling is restricted. This occurs even though the specimen where the particles are

free to roll has a smaller initial porosity, hence it is expected to behave as a denser material. This finding demonstrates that it is not possible, with the chosen mechanical parameters, to reproduce the soil specimen realistically. It is important to stress that the calibration procedure (Chapter 4) was carried out using a realistic interparticle friction angle, Young's and Poisson's modulus, and calibrating the coefficient of the moment–relative rotation contact law. If the particles were let free to roll, a different calibration procedure would have been necessary. However the discrepancy seems too large to be overcome by the limited variability that can be offered by tuning the contact law parameters. This is why the moment–relative rotation contact law is essential to replicate pipe–soil interaction in a realistic way.

The magnitude of the oscillations observed in the rolling free test does not depend directly on the contact law. Instead, the oscillations are related to the stiffness of the material. In other words, when the soil behaves as softer, the pipe penetrates easily into it. Whereas where the soil is stiffer, it opposes to the pipe motion more, and in a more unstable way.

The response during lateral movement reflects the results of the vertical phase. As the rolling free test gives rise to a smaller vertical pipe–soil load during penetration, the horizontal force during the lateral movement is smaller. The test was run for a short displacement only, as the trend was already evident from the first stages of the lateral motion.

7.3.3 Effect of relative density

Two further tests were performed to evaluate the effect of the initial relative density of the numerical specimen on the pipe–soil interaction. The pipe was subjected

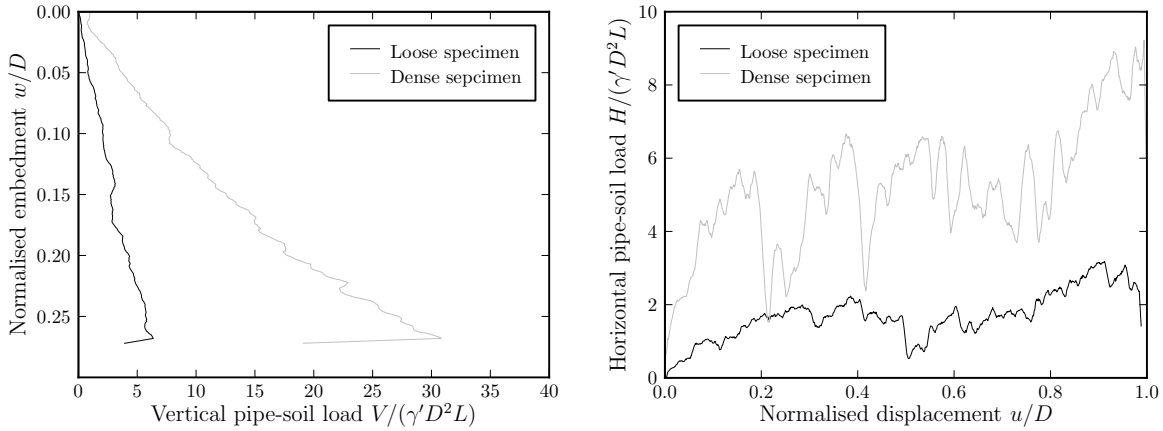

(a) (b)

Figure 7.12: Vertical and lateral load–displacement responses for specimens with different relative densities.

to a similar displacement path to before (maximum penetration of $w = 0.27D$ and maximum lateral displacement of $u = 1.0D$), on specimens generated with different friction angles during the deposition phase (described in Section 5.1.3). Friction angles of 40° and 10° were used to generate loose and dense specimens with relative densities of 11.8 % and 63.5 % respectively. After the particles had settled, the usual value of interparticle friction ($\phi_\mu = 26°$) was assigned and the pipe was loaded. In order to speed up the simulations, numerical non-viscous damping ($\alpha = 0.5$, Eq. 3.40) was used for these tests. It was anticipated that the results would be affected by the numerical damping, as it is a non-physical parameter, and usually is not recommended unless the simulation is quasi-static. However, the comparison between these two loading tests only, performed in both cases with the same type of damping, was still meaningful and indicative of the effect of the relative density of the samples.

The vertical and horizontal force–displacement responses of the pipeline are shown in Figure 7.12. As expected, the vertical plastic stiffness increases for the denser specimen (k_p changes from 31 to 151 kPa). In the same way the denser sample results

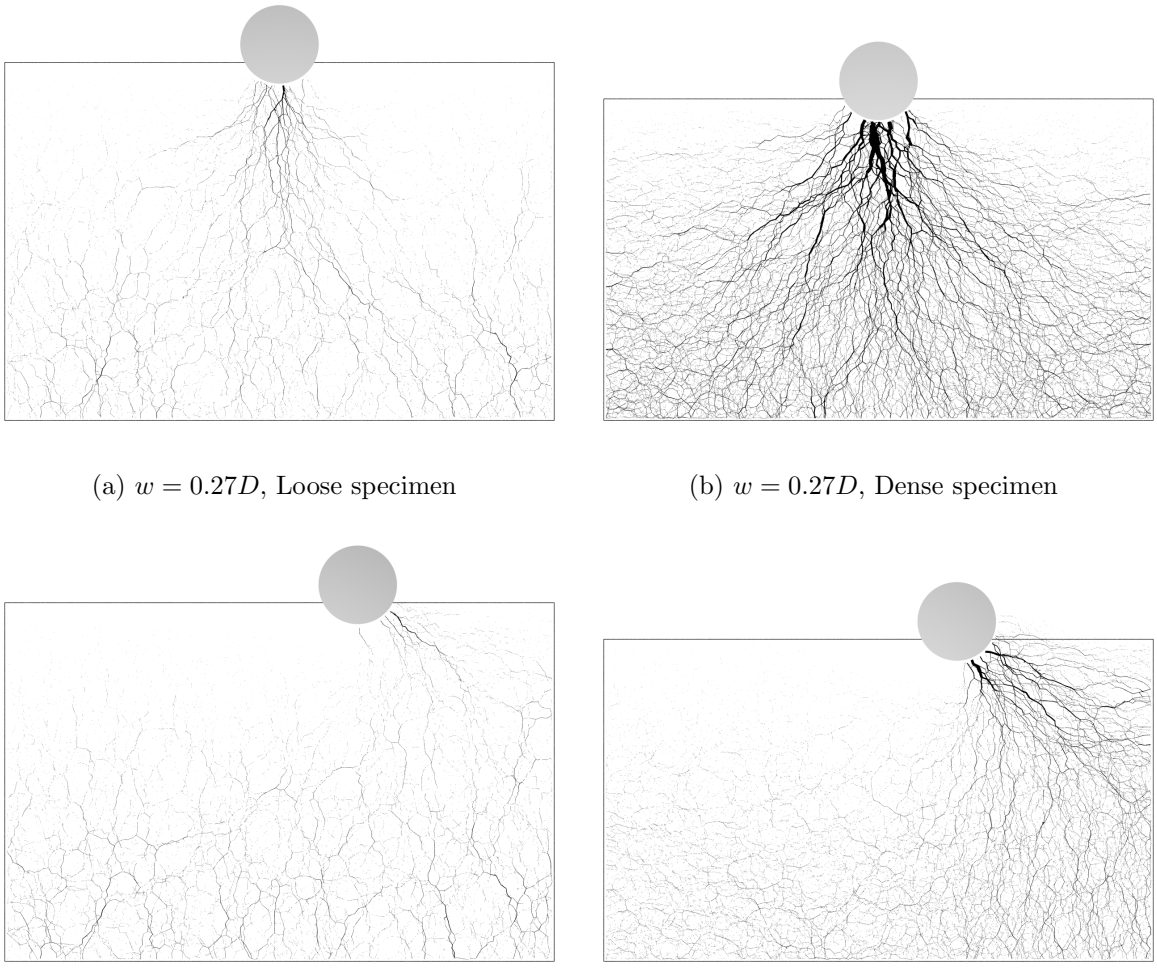

(a) $w = 0.27D$, Loose specimen

(b) $w = 0.27D$, Dense specimen

(c) $u = 1.0D$, Loose specimen

(d) $u = 1.0D$, Dense specimen

Figure 7.13: Contact force network at different pipe positions for specimens with different relative densities (force chains are all scaled to the same maximum value).

in a markedly higher horizontal resistance during the lateral displacement phase.

The contact force network and the velocity field are shown in Figures 7.13 and 7.14, at the maximum vertical penetration and at the maximum lateral displacement, for a loose and a dense sample. The contact forces were all scaled to the same maximum value to allow a direct graphical comparison. A similar scaling procedure was applied to the velocity fields of the two tests.

The distribution of the contact forces confirms the observations from the force–displacement curves. In the loose sample the force networks are very sparse, and during

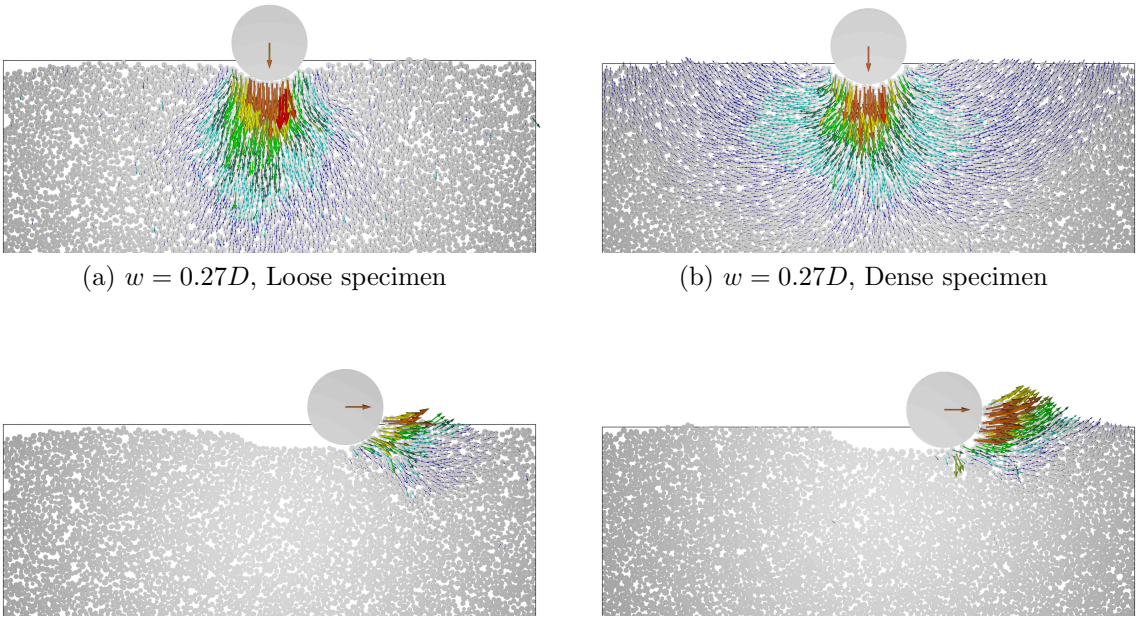

(a) $w = 0.27D$, Loose specimen

(b) $w = 0.27D$, Dense specimen

(c) $u = 1.0D$, Loose specimen

(d) $u = 1.0D$, Dense specimen

Figure 7.14: Velocity field at different pipe positions for specimens with different relative densities (velocities are all scaled to the same maximum value). Only a portion of the entire domain is shown.

the penetration they are aligned with the direction of loading. In the dense sample the force chains are thicker and spread further around the pipe, especially during the penetration.

The various modes of failure within the sand can be better observed from the velocity fields in Figure 7.14. At the end of vertical penetration into the looser sample there is a clear punching shear mechanism, with the pipe compressing the soil beneath it. The failure mode becomes more localised in the denser specimen, where the velocity vectors adjacent to the pipe are directed towards the free surface. During the lateral displacement phase the same trend is observed: the soil is predominantly compressed as the pipe is moved in the loose specimen, whilst in the denser case dilation occurs and a berm of soil forms.

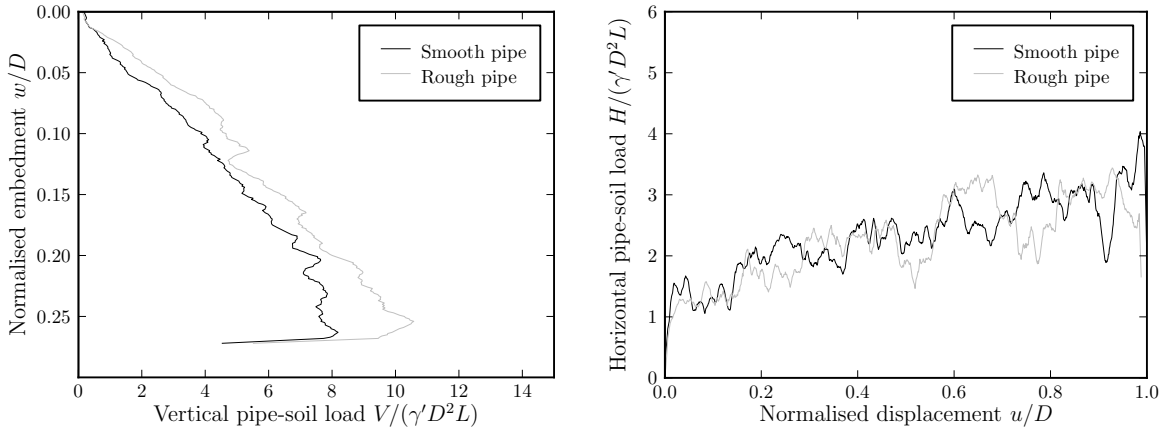

Figure 7.15: Vertical and lateral load–displacement responses for specimens with different values of pipe–soil interface friction angle.

7.3.4 Effect of pipe–soil interface friction angle

Tests with different interface friction angles were also performed, to investigate the role of pipe surface roughness. The interface friction angle δ was varied to replicate a smooth pipe ($\delta = 0°$) and a rough pipe ($\delta = \phi_\mu = 26°$). As for the previous two tests, numerical non-viscous damping ($\alpha = 0.5$) was used.

The smooth and rough pipes were simulated in precisely the same numerical soil specimen, which was prepared in advance, saved and reloaded to be used in the different tests. In this way, any small variations in the initial relative density of the soil were eliminated. The interparticle friction angle in the contact law was the only parameter that changed.

Although the load–displacement curves are substantially similar for the smooth and rough pipes (Figure 7.15), analysis of the results at a particle level highlights interesting differences. Figure 7.16 shows that the smooth pipe generates a fairly uniform distribution of forces across the contact zone. The rough pipe, however, transmits the major forces in the direction of loading. A similar trend is observed in the velocity

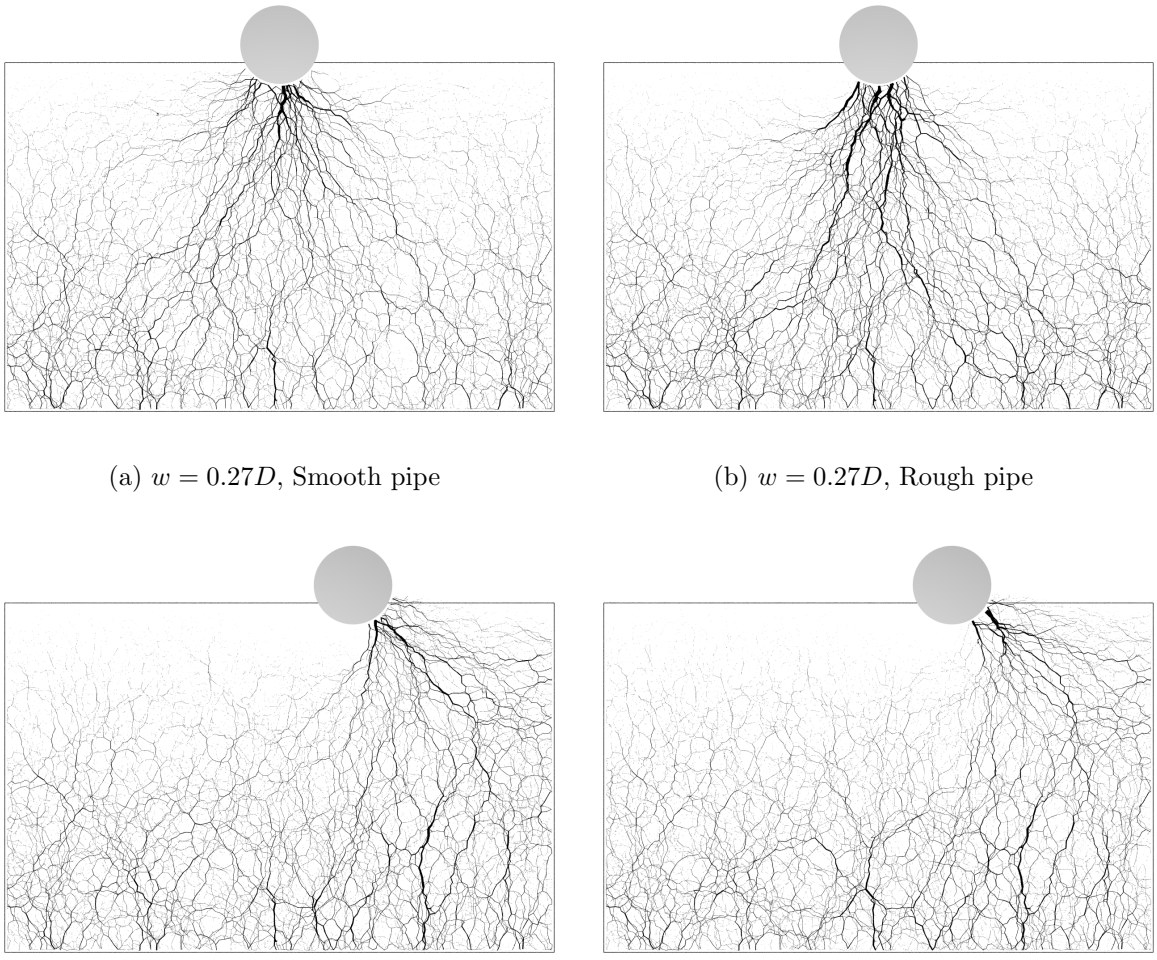

(a) $w = 0.27D$, Smooth pipe

(b) $w = 0.27D$, Rough pipe

(c) $u = 1.0D$, Smooth pipe

(d) $u = 1.0D$, Rough pipe

Figure 7.16: Contact force network at different pipe positions for specimens with different values of pipe–soil interface friction angle (force chains are all scaled to the same maximum value).

fields (Figure 7.17). The smooth pipe gives rise to a slightly more localised failure mechanism, compressing the sand and moving it radially away from the pipe. On the other hand, the rough pipe compresses the soil in a narrower region along the direction of motion.

The likely reason is that the roughness of the pipe loosens the soil on the surface in the vicinity of the pipe–sand interface. Therefore the rough pipe compresses the sand (which now has become slightly looser), in a punching shear mechanism, typical of the

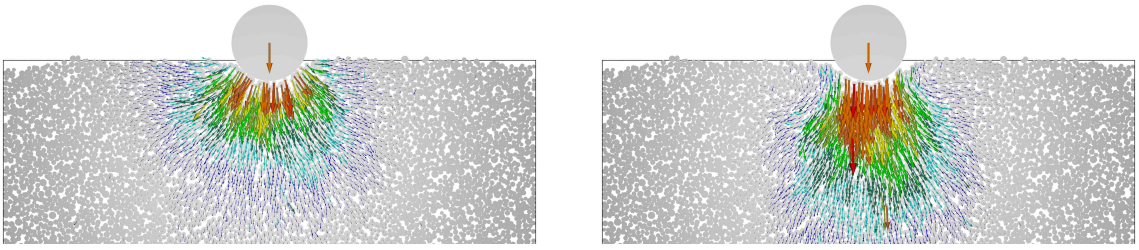

(a) $w = 0.27D$, Smooth pipe

(b) $w = 0.27D$, Rough pipe

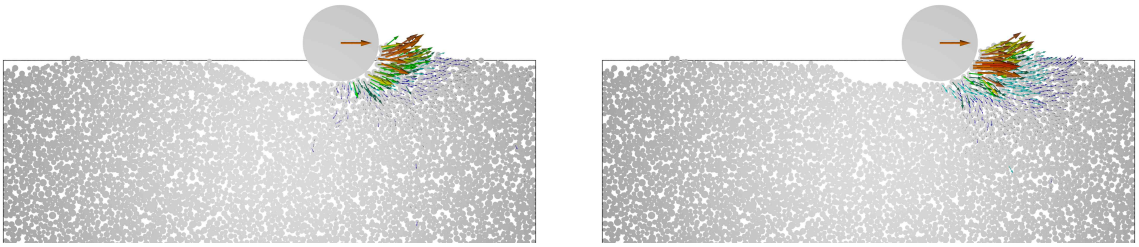

(c) $u = 1.0D$, Smooth pipe

(d) $u = 1.0D$, Rough pipe

Figure 7.17: Velocity field at different pipe positions for specimens with different values of pipe–soil interface friction angle (velocity vectors are all scaled to the same maximum value). Only a portion of the entire domain is shown.

loose specimens (Section 7.3.3 and Figure 7.14(a)). This phenomenon, however, does not occur with the smooth pipe, which gives rise to a more localised failure mechanism. The process described depends on the very specific way the pipe is loaded, and it occurs because the pipe is placed upon the sand surface, as also seen in Yoshimi and Kishida (1981).

7.3.5 Combined effect of density and roughness

The findings obtained from the loading tests with different relative densities and different pipe roughnesses suggest that both these factors have a significant effect on the results. Firstly, it was shown that they both depend on the interparticle friction angle. Varying the interparticle friction angle of the sand (ϕ_μ) yields specimens at different relative densities. Varying the friction angle of the pipe (δ) controls its roughness.

It is worth stressing that the specimen density and the pipe roughness both have an effect on the failure mechanism and dilatant behaviour. Loose specimens (large ϕ_μ during deposition) and rough pipes (large δ) are characterised by a punching shear mechanism, in which the pipe compresses the sand in the direction of motion. Conversely, dense specimens (small ϕ_μ during deposition) and smooth pipes (small δ) are characterised by a local and more dilatant failure mechanism, where the pipe pushes the sand and moves it towards the surface.

Therefore it can be inferred that the failure mechanism, either punching shear or localised, is directly related to the interparticle friction, both at the sand–sand and at the pipe–sand contact.

7.4 Cyclic large lateral displacement tests

7.4.1 Constant embedment test

A cyclic large lateral displacement test was performed were the pipe was moved up to $4D$ horizontally from its initial position. The test was performed to validate the DEM approach for simulations involving large lateral displacement of a pipe on a granular material. Moreover, it is of fundamental importance to observe the formation of the soil berm, and the collection of the dormant berm as the pipe encounters it in consecutive cycles.

Due to the different displacement path, the specimen geometry was adjusted. The width of the domain remained of $7D$ (even though this was expected to be slightly small for the given displacement of $4D$). The height was reduced to $0.8D$, based on previous analyses where it was observed that only the soil near the seabed surface was

affected by the pipe's lateral motion (Section 7.3 and Figure 7.10(b)). The thickness of the domain was kept at $5D_{50}$. It should be stressed that this domain remains extremely small for the amount of pipe displacement carried out during this test. However, this size was chosen to limit the number of particles necessary to fill the domain, and hence the computational time required to perform the test.

The PSD of the sand was scaled up by a factor of only 2, and not 4, as in the tests previously described in the Sections 7.2 and 7.3. The reason was that smaller (hence more realistic) particles would be necessary to capture the interaction of the pipe with the soil surface. It should be mentioned again that practically no difference was observed in the results of the loading test when a scaling factor smaller than 2 was used for the PSD (Section 6.4.1). Hence the PSD used for this test was believed to be representative of the actual sand grains. With this scaling factor and domain size, 29 569 spheres were used for this test.

The material properties were chosen from the calibration, and were unchanged from those used in all the previous pipe loading tests. Local viscous damping was used, with a coefficient $\zeta = 0.2$ (see Section 7.3 and Eq. 3.48-3.49). The pipe was moved at a velocity of 0.01 m/s, which was larger than that suggested from the sensitivity analysis, but chosen for computational efficiency reasons.

The test was performed under displacement control, with the prescribed path as follows (Figure 7.18).

- Section A→B: the pipe was moved at a constant velocity at an angle of 20° to the horizontal surface, until a penetration of $0.1D$.
- Section B→C: lateral movement of the pipe at constant embedment, for a distance of $2D$.

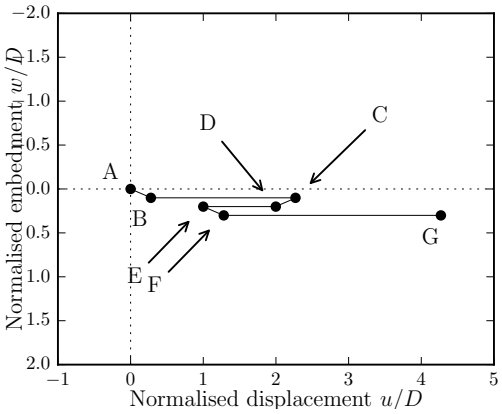

Figure 7.18: Displacement path of the large lateral cyclic test.

- Section C→D: the pipe is pushed at an angle of 20° until a further penetration of $0.1D$.
- Section D→E: the pipe is moved laterally backwards at constant embedment for a distance of $1D$.
- Section E→F: the pipe is pushed another time at an angle of 20° until a further penetration of $0.1D$.
- Section F→G: lateral movement of the pipe at constant embedment, for a distance of $3D$ in the initial direction.

This pipe trajectory was chosen as it was regarded as a good test for validation of the DEM model during a large displacement test. The key points were (i) the backwards pipe motion while the soil berm was left dormant (point C), (ii) the collection of the dormant berm during the second leg of the forward motion (section F→G) and (iii) the large lateral movement of the pipe, up to several pipe diameters (points C, G).

Although the test was performed on a smaller domain and using a high pipe velocity, the simulation time was still large, taking 43 days, using 8 of the 16 cores available in the workstation with 32 GB of RAM. Modifications to parameters such as geometry, velocity or loading path, in order to reproduce more realistic loading conditions, would

have increased the computational time even further.

7.4.1.1 Results

The results of the tests are presented in Figure 7.19, in terms of normalised horizontal load, and snapshots from the simulations are shown in Figure 7.20. In general, the horizontal load, which corresponds to the passive resistance mobilised during the lateral pipe movement, increases as the pipe is pushed into the sand and the size of the berm increases.

At the beginning, the lateral resistance increases as the pipe is pushed into the sand at a slope of 20°. As the test proceeds (B→C) the pipe is moved laterally at constant embedment. It scrapes the surface, building a berm of soil ahead of it, hence increasing the passive resistance from the soil. After a displacement of $2D$, its trajectory is reversed, and it is pushed deeper into the sand. The berm built is left "dormant", hence the lateral resistance returns to zero. As the pipe is pushed into the sand, in the opposite direction the lateral resistance starts gradually increasing with the opposite sign (C→D). When the pipe is moved backwards at constant $w = 0.2D$ another berm forms on what is now the leading side of the pipe, increasing the lateral resistance (D→E). The load changes sign again when the pipe is reversed: it increases to zero, and continues to increase rapidly while the pipe is pushed into the sand until $w = 0.3D$, and moved laterally (F). When the pipe is moved laterally for a further $3D$ the lateral resistance is higher than the first cycle (B→C). This is due to another berm of soil forming and merging with the dormant berm (Figure 7.21). The large oscillations in the lateral resistance towards the end of the test are due to the proximity of the domain boundary as the pipe was subjected to large lateral displacement.

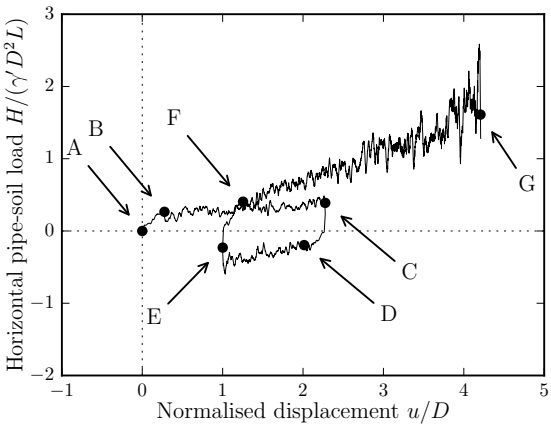

Figure 7.19: Lateral load–displacement response of the cyclic large lateral embedment test.

Observation of the velocity field (Figure 7.22), averaged over the time required to move the pipe through a displacement of $0.1D$, allows the following conclusions to be drawn:

- Almost the entire soil domain is affected by the pipe vertical movement (Figure 7.22(b)), indicating that the height of the numerical sample is not sufficient even for the small amount of vertical displacement to which the pipe was subjected. Although this was anticipated, the small domain was chosen for the computational reasons mentioned previously. During the lateral displacement, on the other hand, only the superficial soil was mobilised.
- The very large red vectors are not fluctuations or numerical instabilities, but the expected very high velocities of particles falling from the top of the berm (Figure 7.22(e), (g) and (l)). This is a realistic mechanism, occurring also in real conditions, which cannot be captured from continuum-based element analysis.
- When the dormant berm is collected, the particles of the new berm initially slide over those is the dormant berm (Figure 7.22(k)). Then they all move together, sliding above the soil underneath the pipe and the berm, which remains practic-

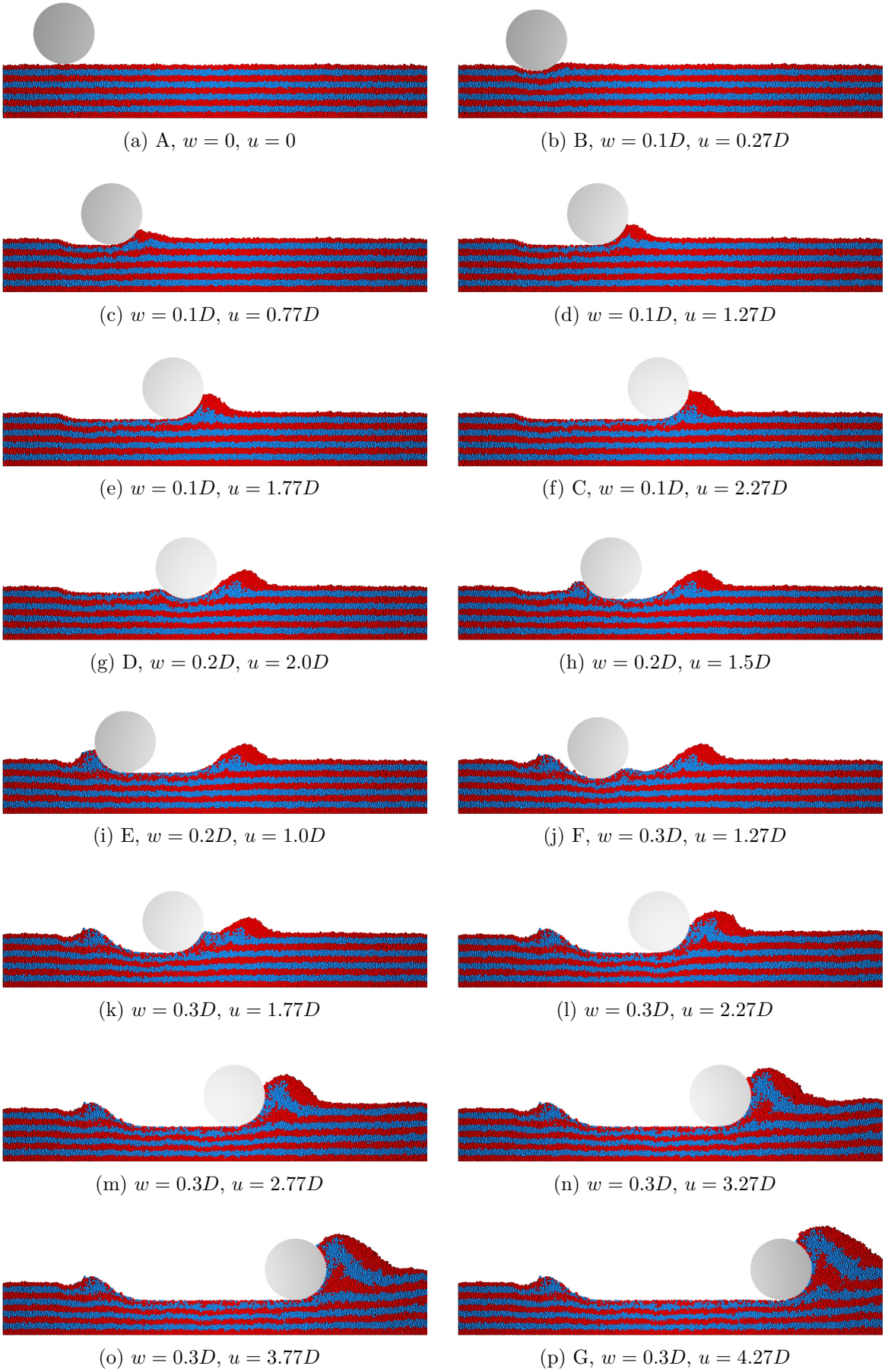

(a) A, $w = 0$, $u = 0$

(b) B, $w = 0.1D$, $u = 0.27D$

(c) $w = 0.1D$, $u = 0.77D$

(d) $w = 0.1D$, $u = 1.27D$

(e) $w = 0.1D$, $u = 1.77D$

(f) C, $w = 0.1D$, $u = 2.27D$

(g) D, $w = 0.2D$, $u = 2.0D$

(h) $w = 0.2D$, $u = 1.5D$

(i) E, $w = 0.2D$, $u = 1.0D$

(j) F, $w = 0.3D$, $u = 1.27D$

(k) $w = 0.3D$, $u = 1.77D$

(l) $w = 0.3D$, $u = 2.27D$

(m) $w = 0.3D$, $u = 2.77D$

(n) $w = 0.3D$, $u = 3.27D$

(o) $w = 0.3D$, $u = 3.77D$

(p) G, $w = 0.3D$, $u = 4.27D$

Figure 7.20: Snapshots at various stages of the large displacement test. The figures show the entire domain.

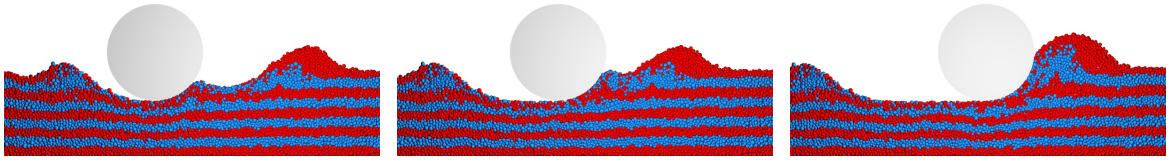

(a) $w = 0.3D$, $u = 1.38D$ (b) $w = 0.3D$, $u = 1.73D$ (c) $w = 0.3D$, $u = 2.34D$

Figure 7.21: Enlargement of the new berm merging with the dormant berm during the large displacement test.

ally stationary (Figure 7.22(l)).

- The particles in the central part of the berm all move together (the orange arrows in Figure 7.22(o) and (p)), with the particles at the top and at the bottom moving at a slower velocity. This is due to the middle particles moving with the pipe, the lower particles being constrained by the stationary soil beneath, and the highest particles being the ones in between those which have already fallen from the top of the berm.

The plot of cumulative particle rotations, recorded from the beginning of the loading phase (Figure 7.23), is also a useful means to obtain an interesting insight into the mechanisms occurring during the pipe movement. In the figure, red represents positive (anti-clockwise) particle rotation, and blue represents negative (clockwise) particle rotation. As the pipe moves laterally in the forward direction (towards the right end of the domain), the particles below the pipe rotate anti-clockwise. In general, the majority of the particles in front of the pipe rotate in the same direction. It is also evident that as the berm grows due to the large pipe displacement, the particles rotate anti-clockwise essentially on its centre. Two regions of blue particles are forming and growing along the two sides of the berm. These consist of the particles falling from the top of the berm along the free lateral surfaces. However, on one side their path is

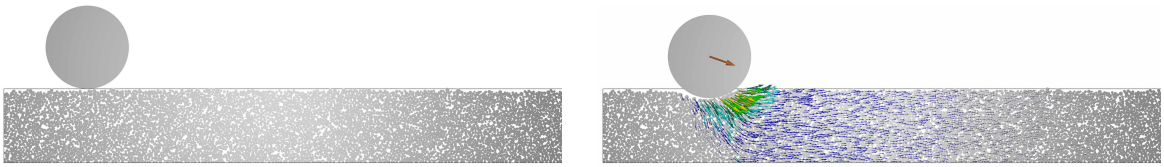

(a) A, $w = 0$, $u = 0$

(b) B, $w = 0.1D$, $u = 0.27D$

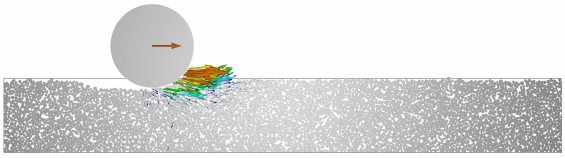

(c) $w = 0.1D$, $u = 0.77D$

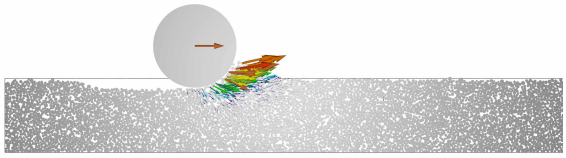

(d) $w = 0.1D$, $u = 1.27D$

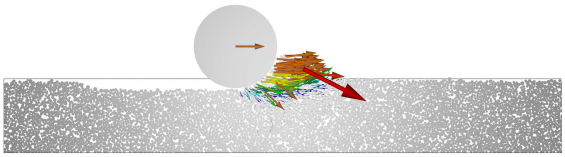

(e) $w = 0.1D$, $u = 1.77D$

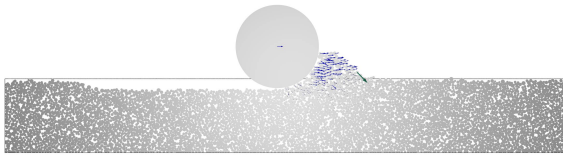

(f) C, $w = 0.1D$, $u = 2.27D$

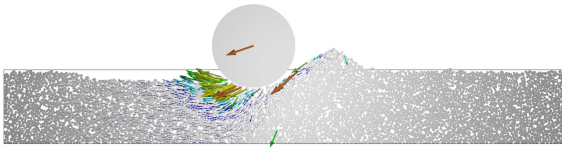

(g) D, $w = 0.2D$, $u = 2.0D$

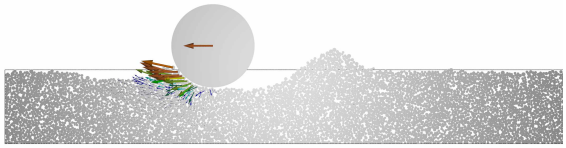

(h) $w = 0.2D$, $u = 1.5D$

(i) E, $w = 0.2D$, $u = 1.0D$

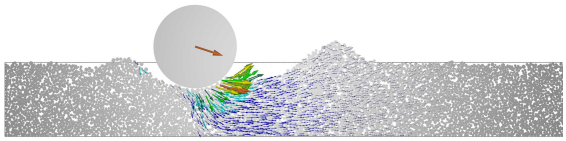

(j) F, $w = 0.3D$, $u = 1.27D$

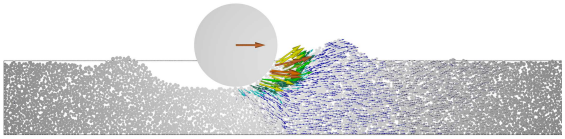

(k) $w = 0.3D$, $u = 1.77D$

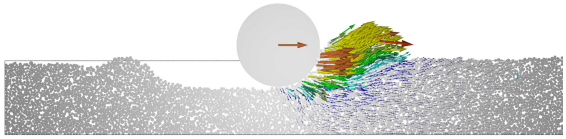

(l) $w = 0.3D$, $u = 2.27D$

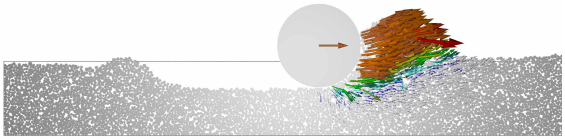

(m) $w = 0.3D$, $u = 2.77D$

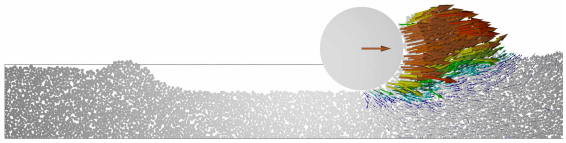

(n) $w = 0.3D$, $u = 3.27D$

(o) $w = 0.3D$, $u = 3.77D$

(p) G, $w = 0.3D$, $u = 4.27D$

Figure 7.22: Velocities at various stages of the large displacement test. The entire domain is shown here.

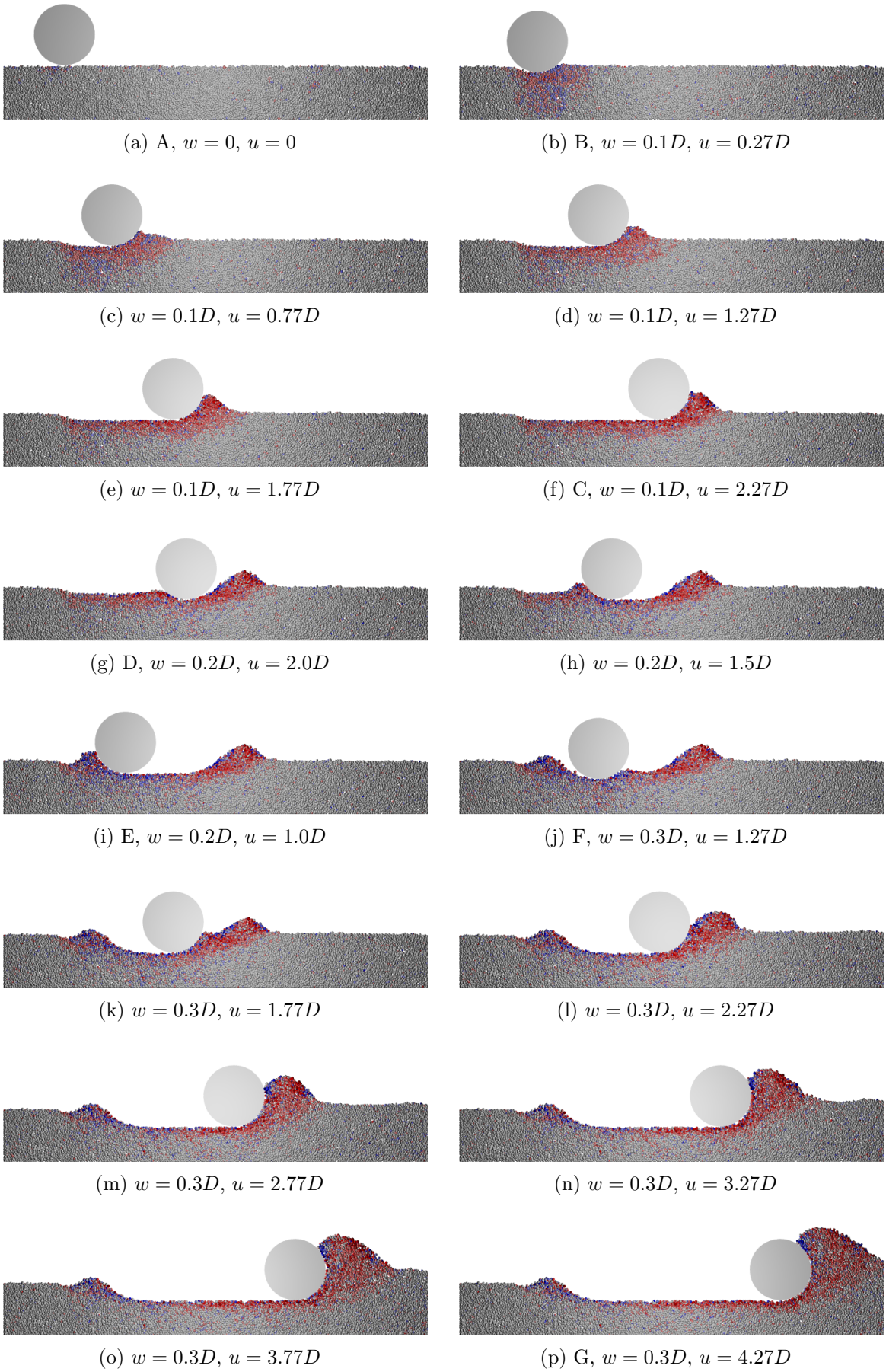

(a) A, $w = 0$, $u = 0$

(b) B, $w = 0.1D$, $u = 0.27D$

(c) $w = 0.1D$, $u = 0.77D$

(d) $w = 0.1D$, $u = 1.27D$

(e) $w = 0.1D$, $u = 1.77D$

(f) C, $w = 0.1D$, $u = 2.27D$

(g) D, $w = 0.2D$, $u = 2.0D$

(h) $w = 0.2D$, $u = 1.5D$

(i) E, $w = 0.2D$, $u = 1.0D$

(j) F, $w = 0.3D$, $u = 1.27D$

(k) $w = 0.3D$, $u = 1.77D$

(l) $w = 0.3D$, $u = 2.27D$

(m) $w = 0.3D$, $u = 2.77D$

(n) $w = 0.3D$, $u = 3.27D$

(o) $w = 0.3D$, $u = 3.77D$

(p) G, $w = 0.3D$, $u = 4.27D$

Figure 7.23: Cumulative rotation at various stages of the large displacement test. The entire domain is shown here. Red represents positive (anti-clockwise) particle rotation and blue represents negative (clockwise) particle rotation.

interrupted by the pipe and they rotate in place.

It should be noted that a direct comparison of the information obtained by the velocity and rotations is not appropriate. This is because the velocity field was based on the average velocity, over a particular displacement interval centred on the moment of interest, while the rotation was cumulative, recorded from the beginning of the pipe movement.

It is important to stress that the above mechanisms were observed for one specific test, but as previous tests have shown (Section 7.3.3 and 7.3.4) the pipe–soil interaction is dependent on the pipe roughness and the specimen density. Hence, it is reasonable to expect slightly different kinematics when the pipe–sand interface friction angle and the sand interparticle friction angles are varied.

7.4.2 Constant V test: one cycle test

7.4.2.1 Test geometry and load control

A cyclic large displacement test at constant vertical load was conducted. The aim of this test was to replicate more realistically the loading conditions experienced by the pipeline during its operating life on the seabed.

As the numerical tests carried out under load control are computationally more expensive, various simplifications were necessary. These concerned the size of the domain and the dimensions of the particles.

The dimensions of the specimen were chosen as the smallest that would accommodate the expected displacement. Hence a domain $5D$ wide, $2D$ high, and $5D_{50}$ thick (in the out-of-plane direction) was prepared. The particle size was larger than the recommendations from the sensitivity analysis, with the real PSD scaled up by a factor of 4.

This allowed reduction of the number of particles to 13 201. On the other hand, the small number of particles prevented detailed observations of the kinematics in small areas.

The test consisted of vertical penetration until an embedment depth of $w = 0.17D$ (8.5 mm), performed at a velocity of 0.01 m/s. The pipe was then unloaded at a rate 10 times slower, i.e. 0.001 m/s, until it reached a vertical force corresponding to 0.1 of the maximum value recorded during the penetration. This was chosen to provide an overloading ratio $R = 10$ before the lateral displacement took place. This is the ratio between the maximum vertical force previously experienced by the pipeline and the current vertical force. The load was then maintained constant (see below) and the pipe was moved laterally at a velocity of 0.01 m/s. One cycle of lateral movement was imposed on the pipe. It was initially moved to a lateral displacement of $u = 2D$ (100 mm). The direction of the lateral displacement was then reversed and the pipe was moved back to the initial position $u = 0$, all the while maintaining constant vertical load.

The vertical load was controlled through a servo-control algorithm. Its formulation was derived assuming that the difference of the resultant force on the pipe between the current V and the desired value V_0 was equal to the sum of the inertial forces developed to move the sand particles in contact with the pipe:

$$V - V_0 = \sum_{i=1}^{N_p} m_i \frac{\Delta v}{\Delta t} \tag{7.2}$$

where N_p is the particles in contact with the pipe, and Δv is the difference between the current v and the previous velocity v_{prev} of the pipe along the vertical direction. The algorithm may be called after a certain number τ of time steps. In this case, a

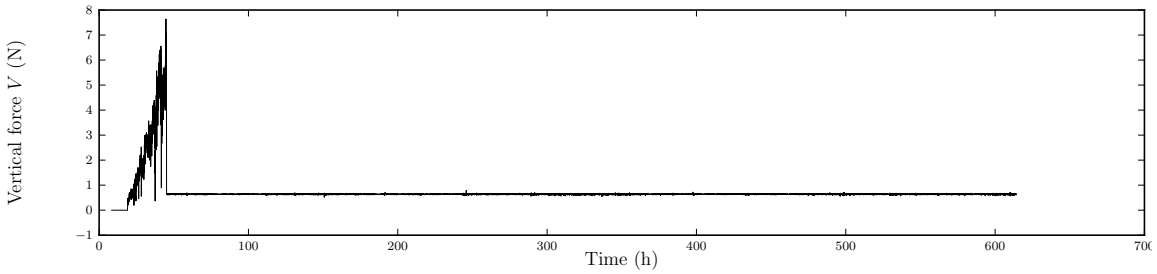

(a)

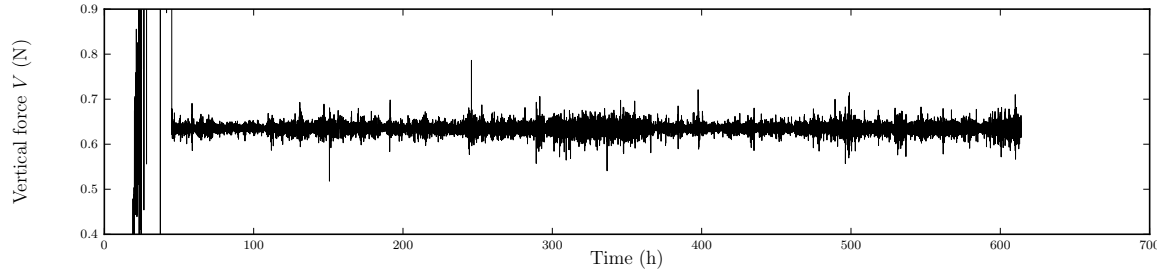

(b)

Figure 7.24: Record of the vertical force during the vertical and lateral phase of the constant V test: (a) entire amplitude and (b) enlargement.

gain parameter α_g is needed. Adjusting the previous equation, the current velocity is estimated as:

$$v = v_{prev} + \alpha_g \frac{\tau \Delta t}{\sum_{i=1}^{N_p} m_i} \left(V - V_0 \right). \tag{7.3}$$

By trial and error analysis, it was found that the fastest simulation could be obtained when the function was called every $\tau = 50$ time steps, and the gain parameter was $\alpha_g = 0.5$.

The algorithm allowed an approximately constant force to be maintained throughout the lateral test, as shown in Figure 7.24. In fact, for a desired constant force of 0.635 N, only a few major oscillations were observed. The maximum and minimum values of the vertical force were respectively 0.786 N and 0.518 N. The relative error between the desired V_0 and the recorded vertical load V was calculated from the

formula

$$\epsilon = \frac{|V_0 - V|}{V_0}. \tag{7.4}$$

For the maximum and minimum recorded force the percentage error was only of 23.8 % and 18.4 % respectively. Therefore the numerical algorithm was capable of maintaining the load constant in a more precise way than in the laboratory tests, where an error up to 40 % may be expected (Sandford, 2012). In those experimental tests large instabilities of the vertical load occurred on approaching the extremities of the cycle.

7.4.2.2 Results

The results of the lateral test at constant vertical load are presented in terms of force–displacement curves in Figure 7.25 and particle plots in Figure 7.26. Data and pictures from an experimental test are also shown. This was a small-scale $1g$ model test performed by Sandford (2012), and belongs to the same series of tests mentioned in Section 7.3. The loading history was identical to the numerical test described here, although, the velocities were different: they were 0.1 mm/s during the vertical penetration, 0.001 mm/s for the unloading, and 0.05 mm/s for the lateral velocity. In addition, a smaller loading velocity of 0.001 mm/s was used during the early movements along each direction to assist the vertical load control system.

The pipe starts the lateral movement from a vertical position of $w = 0.17D$ (8.5 mm). Initially it follows a slight downwards trajectory, reaching a maximum embedment depth of 10 mm ($0.2D$) when it has moved 37.5 mm ($0.75D$) laterally. The horizontal force H increases as the pipe builds up a berm of soil at its front while scraping the surface. Then the pipe starts moving along an upwards trajectory, to reach, by the end of the first leg ($u = 2D$), the initial vertical position of 8.5 mm. The

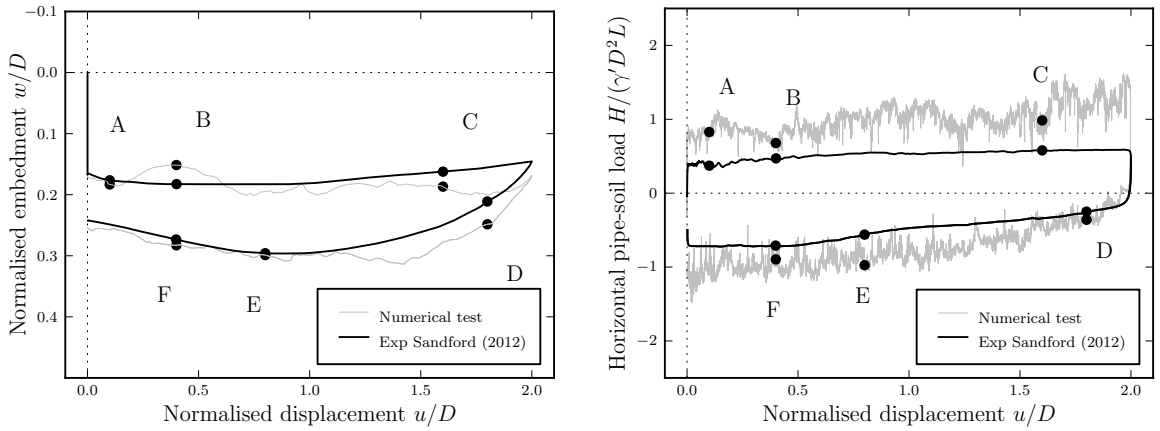

(a) (b)

Figure 7.25: Results of one cycle of the constant V test: (a) displacement path and (b) horizontal force-lateral displacement relationship.

occurrence of uplift and the amount of uplift depends on the overloading ratio R. In this case, $R = 10$ implied a small vertical force on the pipe before the lateral movement commenced. In fact, as the berm increases its volume and pushes towards the pipe, the pipe has to move upwards to maintain the same vertical force. When reversing the direction of movement, the pipe experiences a rapid increase of penetration, and the horizontal force increases but in the opposite direction. Then, as in the previous leg, the pipe moves slightly upwards to keep the vertical load constant.

The numerical results compare well with the experiment. The pipe trajectory can be almost superimposed with very limited differences. The pipe position at the end of the first lateral movement is 8.5 mm in the simulation and 7.5 mm in the experiment. At the end of the second leg, the pipe vertical position is 12.7 mm in the simulation and 12.1 mm in the experiment. The horizontal force increases constantly during the pipe motion. The numerical force during the forward motion is larger than the experimental force by at least a factor of two. This discrepancy is mainly due to the smaller dimensions of the numerical specimen. At the closest point, the pipe is only $1D$ distant

from the wall. The horizontal force becomes more unstable as the pipe comes closer to the rigid boundary.

The velocity field at various points of the test is shown in Figure 7.27. In the same way as for the tests presented earlier in this thesis, the velocity vectors were calculated over the time required for the pipe to move through a distance of $0.1D$. The pipe and the particle locations are also shown, to provide information about the soil profile throughout the test. Although this analysis was performed as a 3D, only the velocity vectors of those particles whose centres fell within a thin centred slice were considered. The figure also shows the velocity field obtained from processing experimental data using PIV.

From Figure 7.27, it is evident that the numerical simulation replicates, with an excellent match, the experimental velocity field. As the pipe starts its lateral motion, the sand appears to follow a predominantly horizontal trajectory (points A, B and C). The pipe scrapes the soil surface, forming a berm of soil. The soil particles initially move upwards towards the free surface (point A), then horizontally with the pipe (points B and C). At point D, the pipe has just been reversed. Some high velocity vectors are observed from particles falling from the internal edge of the berm, in both the numerical and the experimental results. Even the velocities underneath and on the left hand side of the pipe moving can be observed in both the numerical and experimental tests. A good match is observed at the following step (point E). Even the active and the small dormant berm (and the space in the soil profile between them) can clearly be observed in both the numerical and experimental. The same match is evident at the end of the cycle (point F).

In summary, these results show that the numerical model can replicate with good

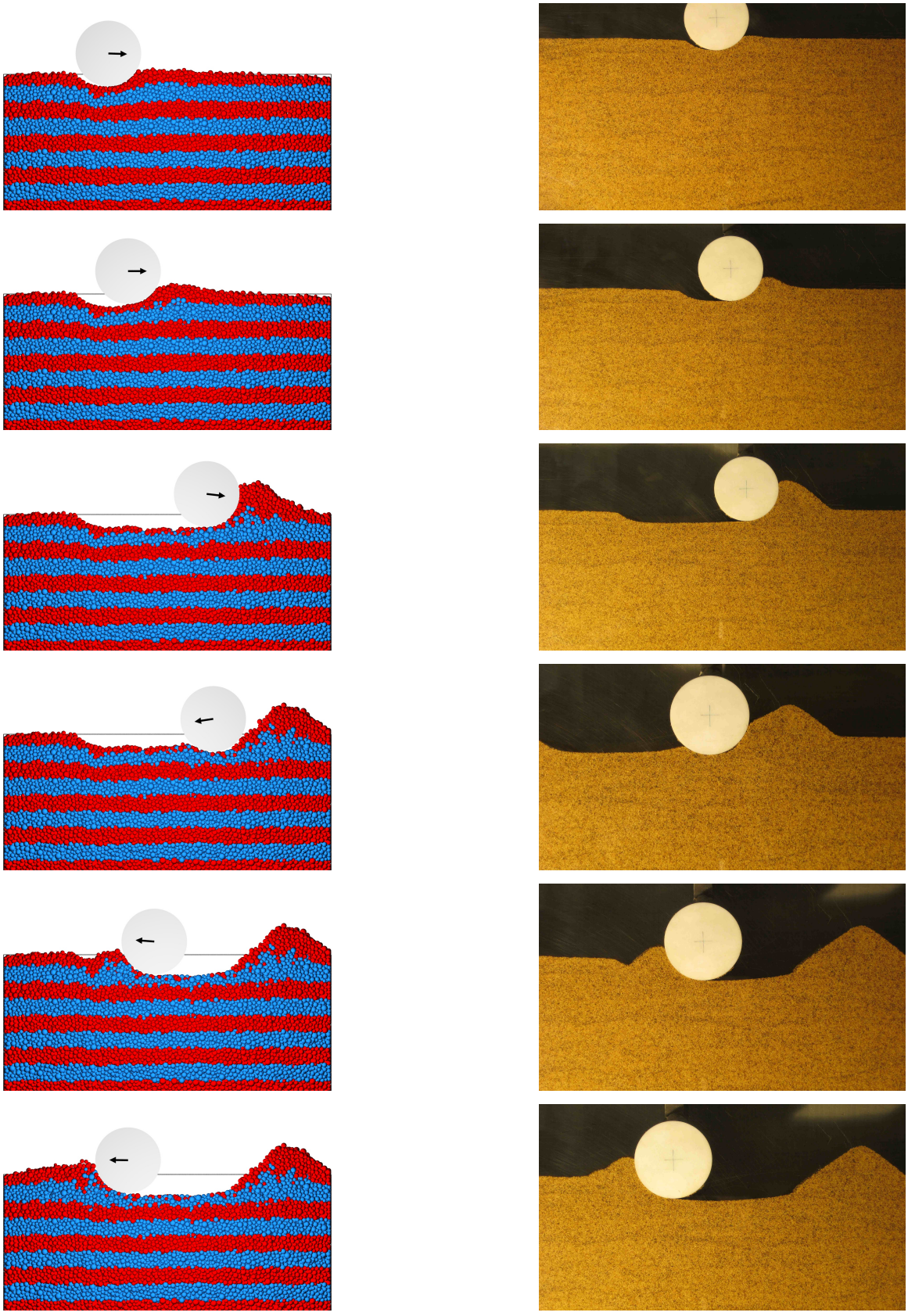

Figure 7.26: Pipe position and soil bed profile from (a) numerical simulation and (b) experimental test (Sandford, 2015). The figures from DEM simulation show the entire domain, the photos from the experiment show only a limited amount of a larger domain.

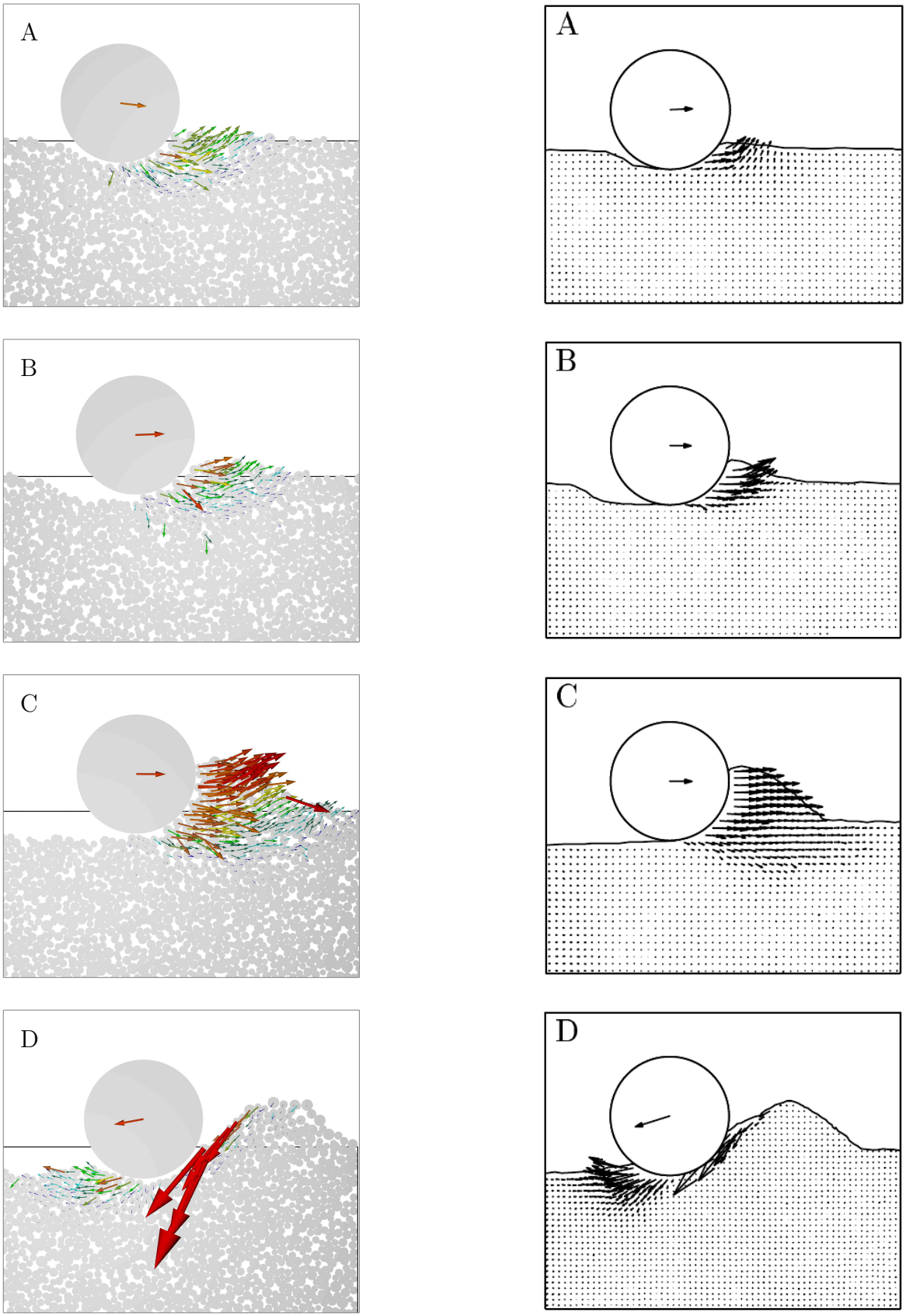

Figure 7.27: Velocity field from (a) numerical simulation and (b) experimental test (Sandford, 2012) .

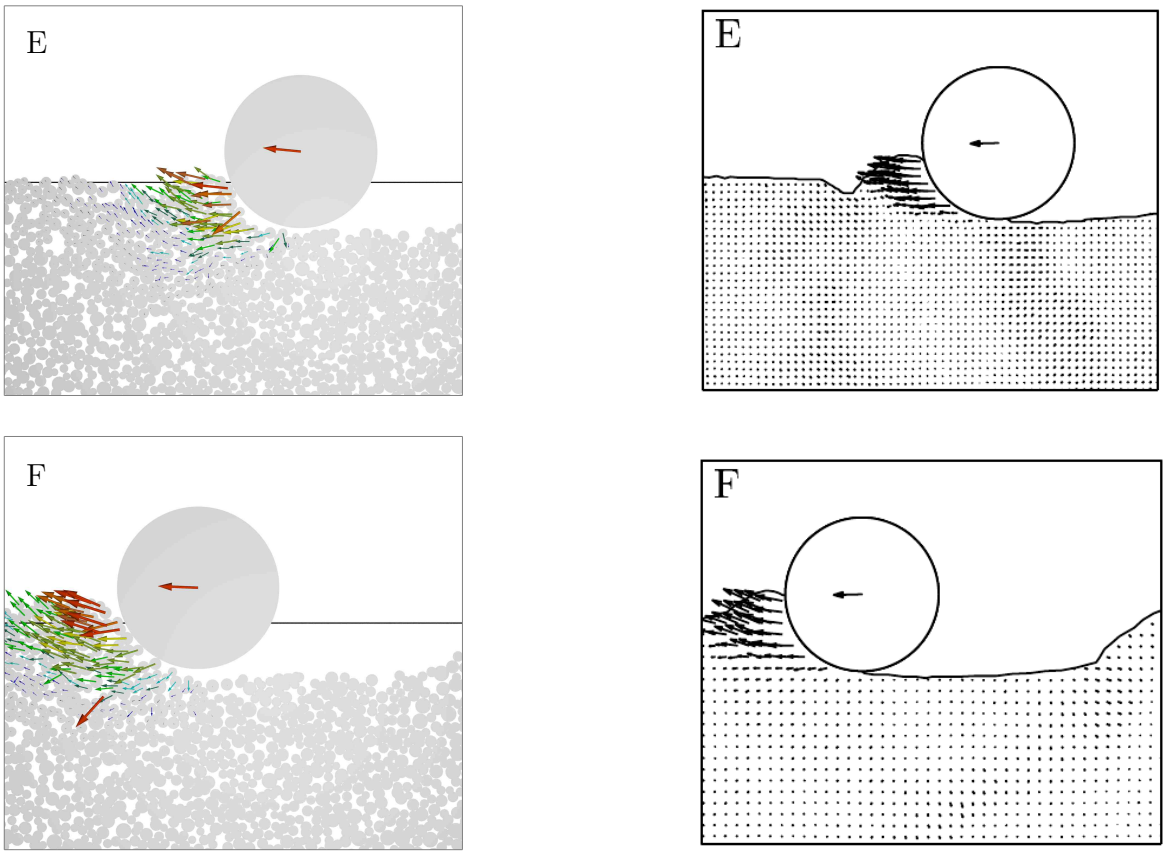

Figure 7.26: Velocity field from (a) numerical simulation and (b) experimental test (Sandford, 2012) (continued).

accuracy the pipe trajectory, the soil profile and the velocity field in the soil during a lateral test at constant vertical load. However, computational time remains the biggest limitation. It required 11.2 hours to move the pipe laterally through 5 mm ($0.1D$), which corresponds to more than 18 days to move the pipe for a full cycle of $2D$ in each leg.

7.4.2.3 Effect of contact stiffness

The same vertical loading and constant V test was performed using particles with a smaller contact stiffness. The aim of this test was to establish whether a smaller stiffness could be used for analysing the pipe response during a cyclic lateral loading test at constant vertical load. The advantage would have been a larger critical time

step and hence a shorter computational time.

The contact stiffnesses were taken three orders of magnitude smaller than the actual ones used previously. Hence the Young's moduli were $E = 70\,\text{MPa}$ and $E_p = 200\,\text{MPa}$, for sand and pipeline respectively. Although these are unrealistic values, the ratio between the two remained constant, which is relevant for the development of contact forces. The geometry of the numerical specimen, the loading history, and the loading velocities were kept unchanged. Throughout this section, the test will be referred to as "soft test" and the test performed with the higher Young's moduli, and already described in the previous section, will be referred to as "stiff test".

Generation of a new specimen with soft particles was necessary for the soft test. At the end of the deposition the soft and the stiff specimen had approximately the same height and the same porosity. The porosity in the soft sample was 0.474, and in the stiff sample was 0.484. The height varied from 0.107 m ($2.14D$) to 0.110 m ($2.20D$), with the minimum required height being $2D$ (0.1 m). It is reasonable that the specimen of the soft test is characterized by a slightly lower porosity, i.e. it is denser, as it consists of softer particles that can overlap more, hence the final porosity after deposition is smaller. However, this can be considered as a small difference, if looking at the range of porosities that was obtained, for example, by using a low or a high interparticle friction angle during the deposition (Section 5.1.3).

Figures 7.27 and 7.28 show the comparison between the soft and stiff tests. The experimental results are also plotted for reference. The results in the V–w plane show that the response during vertical loading is very close for the soft and the stiff test. Fluctuations are observed more in the stiff test, as anticipated, because the particles are stiffer, and hence penetration is more unstable. However, the domain is

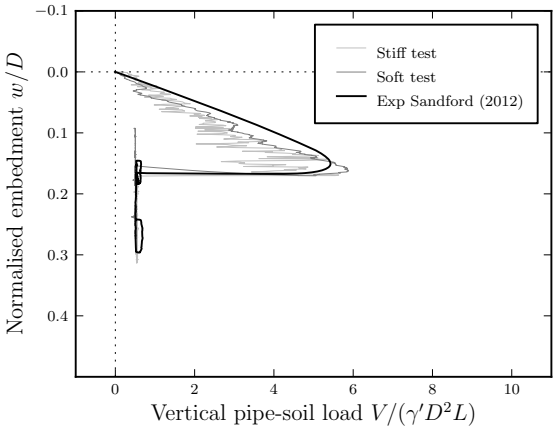

Figure 7.27: Influence of contact stiffness on the one cycle constant V test: vertical force-embedment depth relationship.

of small size in both tests: its height is only $2D$. This contributes to an increase in the oscillations. At the end of vertical penetration, the maximum vertical load is only slightly different between the two tests, that is $V = (\gamma' D^2 L) = 5.23$ for the soft test, and $V = (\gamma' D^2 L) = 5.67$ for the stiff test.

During the unloading stage, the stiffness of the vertical load–embedment depth curve is very large in the stiff test. This is consistent with what was observed in the vertical loading–unloading test (Section 7.2). In the soft test, instead, the pipe experiences a measurable uplift during unloading. This occurs because the soft specimen is able to recover a small part of the deformation elastically.

The lateral movement was carried out at constant vertical loadsof $V/\gamma' D^2 L = 0.523$ for the soft test, and $V/\gamma' D^2 L = 0.562$ for the stiff test. They are slightly different, but this should not affect the behaviour of the pipe in the two tests. During the first leg of the lateral movement, the plot in the u–w plane shows a slightly upwards trajectory for the soft test, which corresponds to a slightly smaller horizontal force. Instead the elevation of the pipe in the stiff test remains nearly constant. As the trajectory is reversed, the pipes tend to move along a downwards trajectory. The comparison with

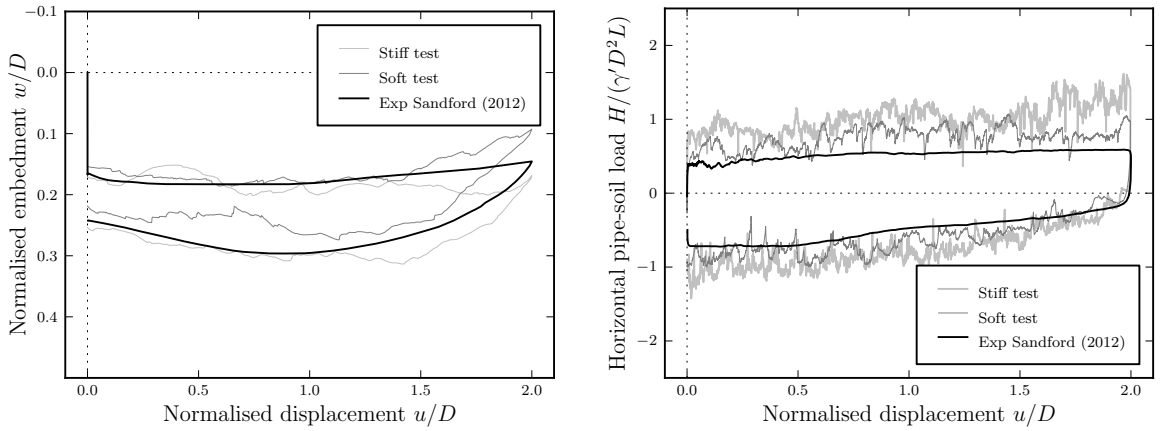

(a) (b)

Figure 7.28: Influence of contact stiffness on the one cycle constant V test: (a) displacement path and (b) horizontal force-lateral displacement relationship.

the experimental results shows that, although the actual pipe trajectory is replicated better in the stiff test, the results from the soft test and the stiff test do not differ enormously.

Overall, in the stiff test the pipe tends to move deeper than in the soft test. This might be due to recovery of elastic deformation in the soft test. A great difference is found in terms of computational time. Load-controlled tests such as these ones require an adjustment of the vertical velocity given to the pipe every 50 steps. Hence they are computationally more expensive than the other type of pipe loading test presented in this thesis, which are purely displacement-controlled. The time required to move the pipe $0.1D$ was 0.87 h in the soft test and 12.23 h in the stiff test. These numbers provide an estimation of the amount of time required to perform a constant V simulation for more than one cycle.

As the pipe response in the stiff test was not substantially different from the response observed in the soft test, further constant V tests were carried out with the reduced Young's moduli. This simplification was merely to limit the computational demand of

the simulations.

7.4.2.4 Effect of rolling resistance

The same soft test was repeated with the particles free to roll. The aim was to investigate whether or not the pipe–soil interaction during a constant V test could be simulated accurately without the moment–relative rotation contact law. The pipe was again subjected to vertical loading up to $w = 0.17D$, unloading to 0.1 of the maximum vertical load, and then to a cycle of $2D$ lateral displacement at constant vertical load.

Figures 7.29 and 7.30 present the results of the constant V test with soft bodies for the rolling free and the rolling restricted test. The experimental results are also plotted for comparison. In the rolling free test, the maximum vertical load during penetration, $V/\gamma' D^2 L$=0.91, is considerably lower than in the rolling restricted test, $V/\gamma' D^2 L$=5.23. This is because the particles free to roll can offer less resistance to the penetration of the pipe, as was already discussed in Section 7.3.2. The same overloading ratio is applied to the pipes, i.e. $R = 10$, so the vertical loads during the lateral phase are very different. As a consequence, the pipe trajectory and the horizontal force during lateral movement differ between the two tests as well. While the pipe in the rolling restricted test follows a very slight upward trajectory, the pipe trajectory in the rolling free test is moving upwards with a steeper slope. The lateral force in the rolling free test is between 6 and 11 times smaller than in the rolling restricted test.

As already demonstrated for the vertical and lateral test at constant embedment (Section 7.3.2), these results demonstrate that the moment–relative rotation contact law is necessary for simulating lateral displacement tests at constant vertical load. The additional rolling resistance is fundamental for replicating the pipe–soil interaction with

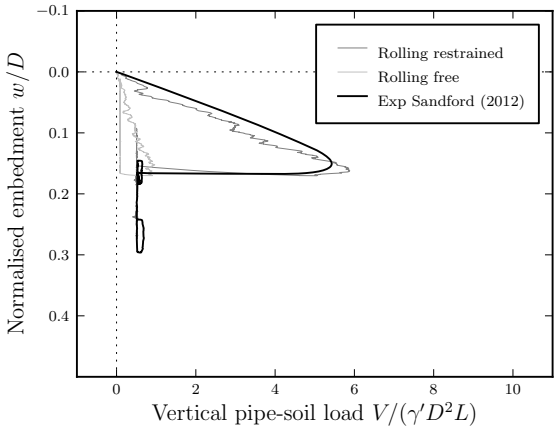

(a)

Figure 7.29: Influence of rolling resistance on the one cycle constant V test: vertical force-lateral displacement relationship.

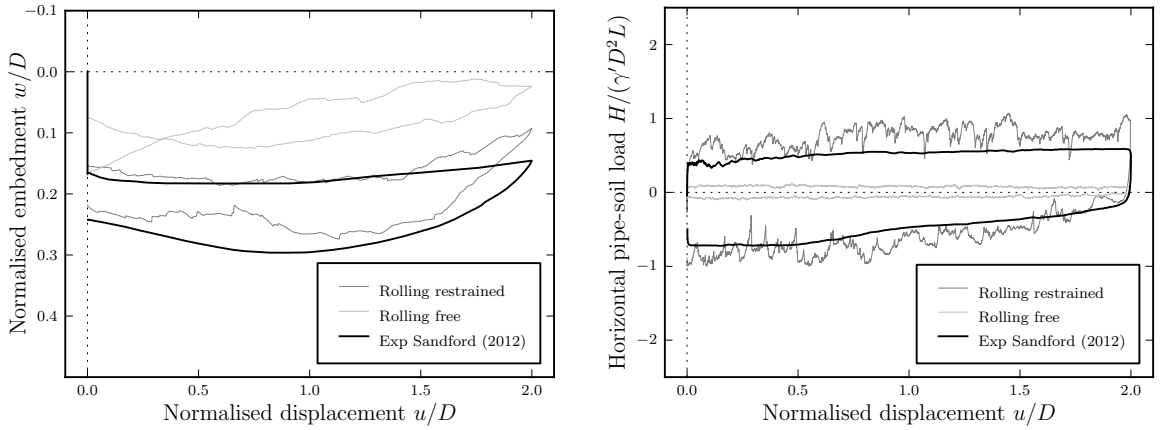

(a) (b)

Figure 7.30: Influence of rolling resistance on the one cycle constant V test: (a) displacement path and (b) horizontal force-lateral displacement relationship.

good accuracy. Hence it is of primary importance to include it in the contact law.

7.4.3 Constant V test: three cycle test

Sections 7.4.2.3 and 7.4.2.4 demonstrated that although the moment–relative rotation contact law is fundamental for replicating the pipe–soil interaction correctly, smaller contact stiffnesses could be used to save computational time. Hence the simplification regarding the contact stiffnesses was used for the simulations presented in this section

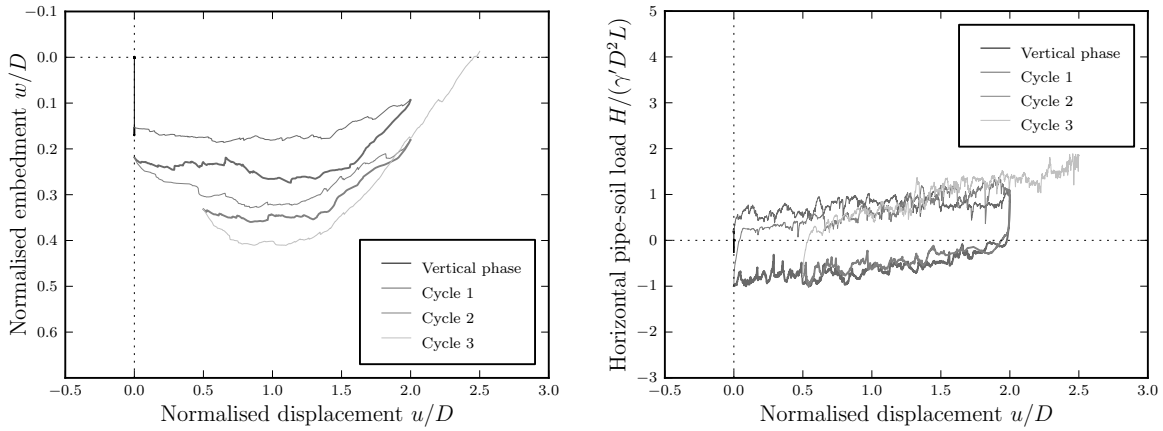

(a) (b)

Figure 7.31: Results of the three cycle constant V test: (a) displacement path and (b) horizontal force-lateral displacement relationship. In the displacement plot, the axes are not to the same scale.

and in Section 7.4.4. The stiffnesses were taken three orders of magnitude smaller than the real ones, hence the Young's moduli were $E = 70\,\text{MPa}$ and $E_p = 200\,\text{MPa}$, for the sand and the pipeline respectively.

A cyclic lateral displacement path was imposed on the pipe. The first cycle was as described in the previous constant V test. That is, the pipe was initially moved until a displacement of $u = 2D$ (100 mm). The direction of the lateral displacement was then reversed and the pipe was moved back to the initial lateral position $u = 0$. Then the pipe was moved for two additional cycles. The direction was reversed until a displacement of $u = 2D$ (100 mm). Then the pipe was moved backwards through a displacement of $1.5D$ (75 mm), and finally moved forwards through a lateral displacement of $2D$ (final location $u = 2.5D$ from its initial position).

Figure 7.31 shows the results in terms of pipe trajectory and horizontal pipe–soil force during the cyclic lateral motion. For a more efficient visualization of the different cycles, each of them is plotted with a different colour. Particle plots are shown in Figure 7.32. This figure is particularly relevant for the analysis of the evolution of the

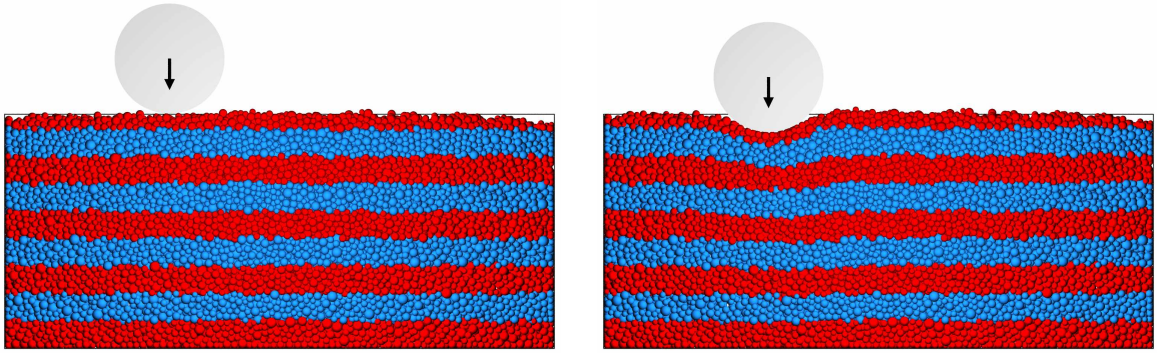

(a) $w = 0, u = 0$

(b) $w = 0.17D, u = 0$

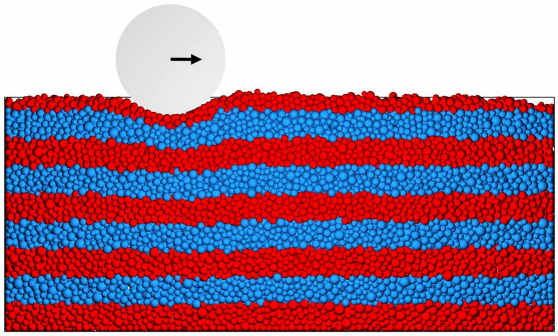

(c) Cycle 1, $u = 0$

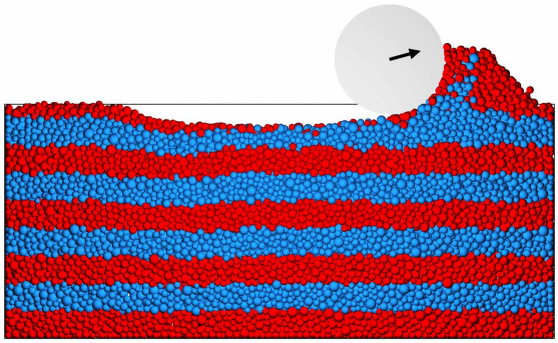

(d) Cycle 1, $u = 2D$

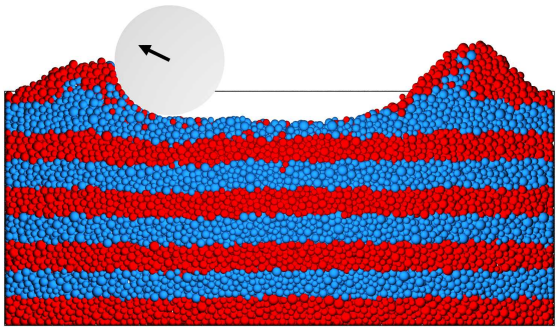

(e) Cycle 2, $u = 0$

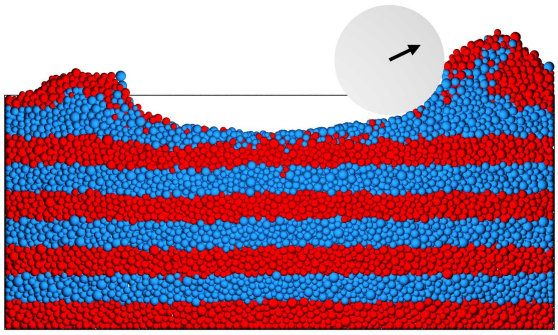

(f) Cycle 2, $u = 2D$

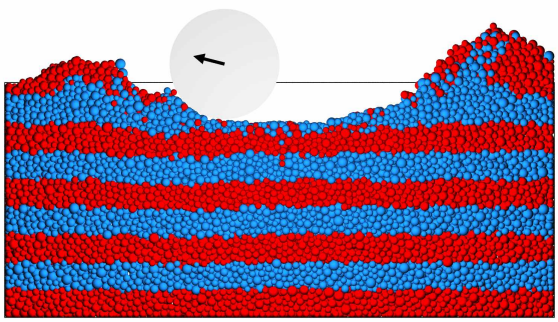

(g) Cycle 3, $u = 0.5D$

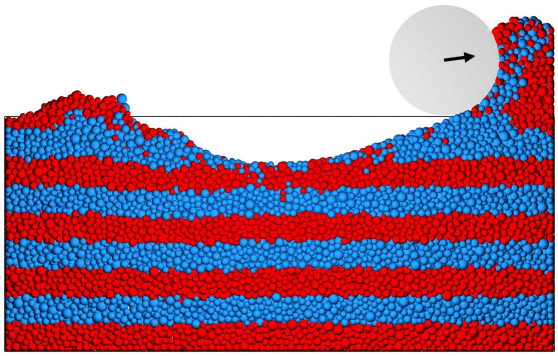

(h) Cycle 3, $u = 2.5D$

Figure 7.32: Soil profile and pipe position during the three cycle constant V test.

soil profile during the test.

The pipe starts the lateral movement at an embedment depth of 8 mm ($0.16D$). At the start of the first cycle, the pipe remains approximately at the same vertical level. The horizontal force H increases as the pipe scrapes the surface and builds up a berm of soil at its front. After reaching a displacement of 71 mm ($1.42D$), the pipe starts moving along an upwards trajectory. When reversing the direction of movement, the pipe experiences some penetration, and the horizontal force increases but in the opposite direction. Then, as in the previous leg, the pipe moves slightly upwards to maintain a constant V.

At the start of the second cycle, the pipe undergoes a rapid penetration, reaching a peak of 16.5 mm ($0.33D$). The lateral load increases, but with a smaller initial stiffness. Then the pipe starts rising to maintain the vertical load. As the simulation proceeds further, the pipe penetrates deeper into the soil, scraping the soil surface, and forming a small trench. The maximum embedment becomes deeper, and the position at the end of each segment is slightly deeper than the previous one. The $u - H$ curves becomes steeper for each segment where the pipe is moved in the forward direction, whereas they remain essentially unchanged during the backwards motion.

During the third cycle, the pipe reaches a maximum embedment depth of 20.5 mm ($0.41D$). By the end of the last leg, it rises again, reaching a higher position than its initial one. The rapid increase of the lateral load is due to the proximity of the boundary. The boundary also affects the occurrence of the uplift in this final leg of the cycle. In fact, with the wall such close to the pipe, the berm grows much more that it would do if the domain were larger. Then the pipe is forced to move upwards to maintain a constant vertical load. If the domain were larger, the soil in the berm would

have spread more, and the berm itself would have been smaller. As a consequence, the pipe would have not experienced such a large horizontal force, and it would have experienced smaller uplift.

7.4.4 Constant V tests at different overloading ratios

Two more lateral tests at constant vertical load were performed. The loading conditions were as per the previous test, except for the value of the constant vertical load. Hence the domain size was $5D \times 3D \times 5D_{50}$, and the pipe and particles were soft, i.e. the Young's moduli of the pipe and the sand particles were $E_p = 200\,\text{MPa}$ and $E = 70\,\text{MPa}$.

The aim of these tests was to use the DEM model to predict lateral constant V tests under various overloading ratios. The terms normally and overloaded pipeline are analogous to the concepts of normal consolidation and over-consolidation in classical soil mechanics. According to previous analyses (Zhang, 2001; Sandford, 2012) when $R < 10$ the pipe is normally loaded or slightly overloaded, and, during lateral loading, experiences an initial downward movement. Instead when $R > 10$ the pipe is overloaded and experiences an initial upward movement.

To verify these experimental observations, numerical tests were performed at different overloading ratios. Tests were performed with $R = 5$ ($V = 0.2V_{\text{max}}$) to replicate the behaviour of a lightly overloaded pipe, and with $R = 20$ ($V = 0.05V_{\text{max}}$) to replicate a heavily overloaded pipe.

Figure 7.33 shows the vertical load recorded during these tests as a function of the embedment. In the figure, the curve obtained from the test described in the previous section, where $R = 10$, is also included as reference. As anticipated, the vertical load is nearly constant throughout the lateral phases of the three tests. During those phases,

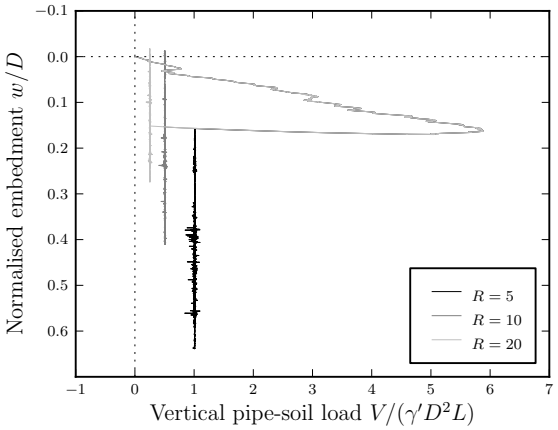

Figure 7.33: Vertical load recorded during constant V tests at different overloading ratios R.

the penetration depth is decreasing or increasing in relation to the overloading ratio of the pipe.

The pipe trajectory and the $u - H$ curve for the heavily overloaded and the slightly overloaded tests are presented in Figures 7.34 and 7.35 respectively. The particle plots of the three tests are illustrated in Figure 7.36.

The heavily overloaded pipe was subjected to a constant vertical load $V = 0.296\,\mathrm{N}$ ($R = 20$) throughout the lateral motion. Figures 7.34 and 7.36(a) show that during the first cycle the pipe experiences gradual uplift up to an embedment depth of 1.5 mm ($0.03D$) due to the small value of the constant vertical load. When reversing the lateral direction, the pipe penetrates into the soil for a limited depth, and then rises gently. During the second cycle, the pipe moves deeper into the sand, increasing the maximum embedment depth to 11.5 mm ($0.23D$). During the backward movement, the pipe follows the same trajectory as the previous leg, and then reaches its maximum penetration in the forward movement of the third cycle (14 mm, $0.28D$). The $u - H$ plot shows a gradual increase of the horizontal load at the beginning of each segment, followed by an almost constant resistance.

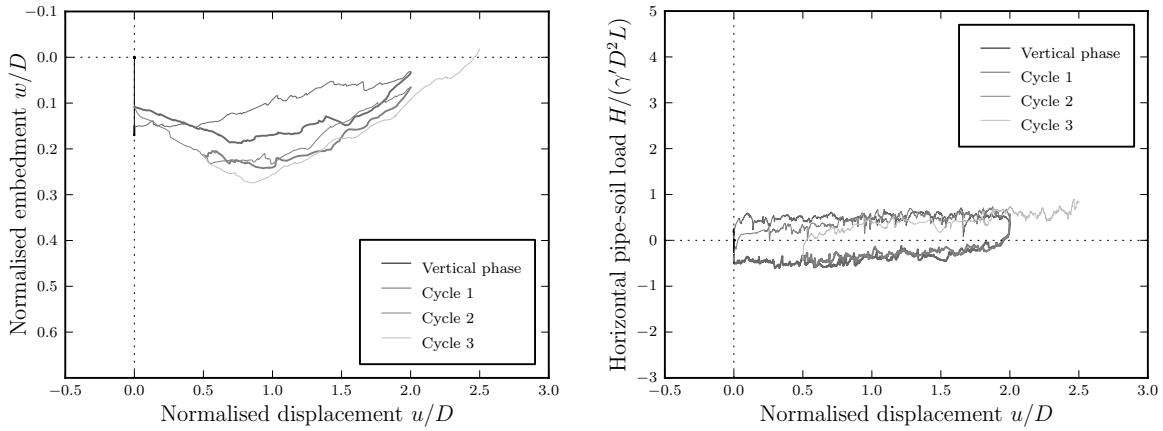

(a) (b)

Figure 7.34: Result of the constant V test on the heavily overloaded pipe ($R = 20$).

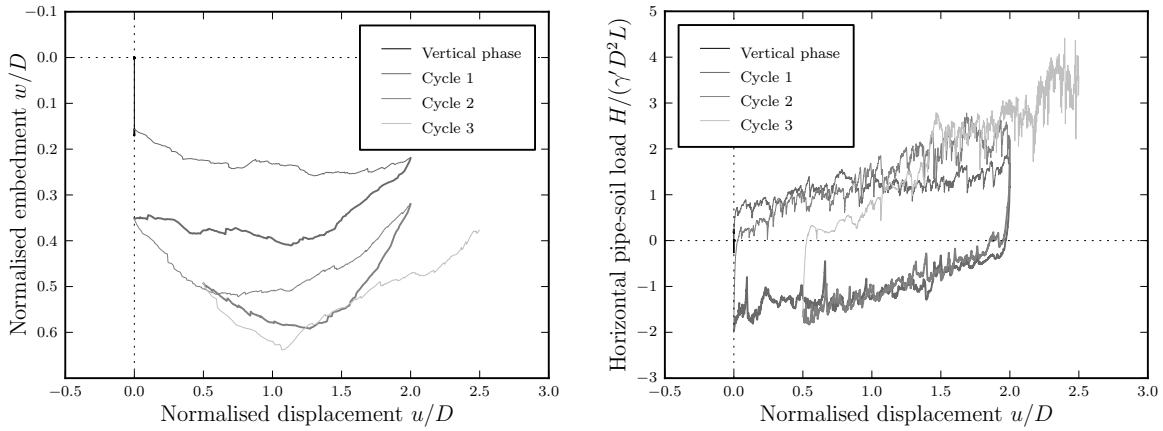

(a) (b)

Figure 7.35: Result of the constant V test on the slightly overloaded pipe ($R = 5$).

The results from the test on the lightly overloaded pipe are shown in Figures 7.35 and 7.36(c)). This test was conducted with a constant vertical load of $V = 1.184\,\mathrm{N}$ ($R = 5$). From the figures, it is evident that, from the first cycle, the pipe follows a downwards trajectory, reaching a penetration of 11 mm ($0.22D$), while the horizontal load gradually increases. This initial penetration is deeper than what was observed in the previous two tests. This is consistent with the higher vertical load applied in this test. When reversing the direction of motion, the pipe undergoes rapid further penetration, and rises slightly only at the end of the segment. At the start of the

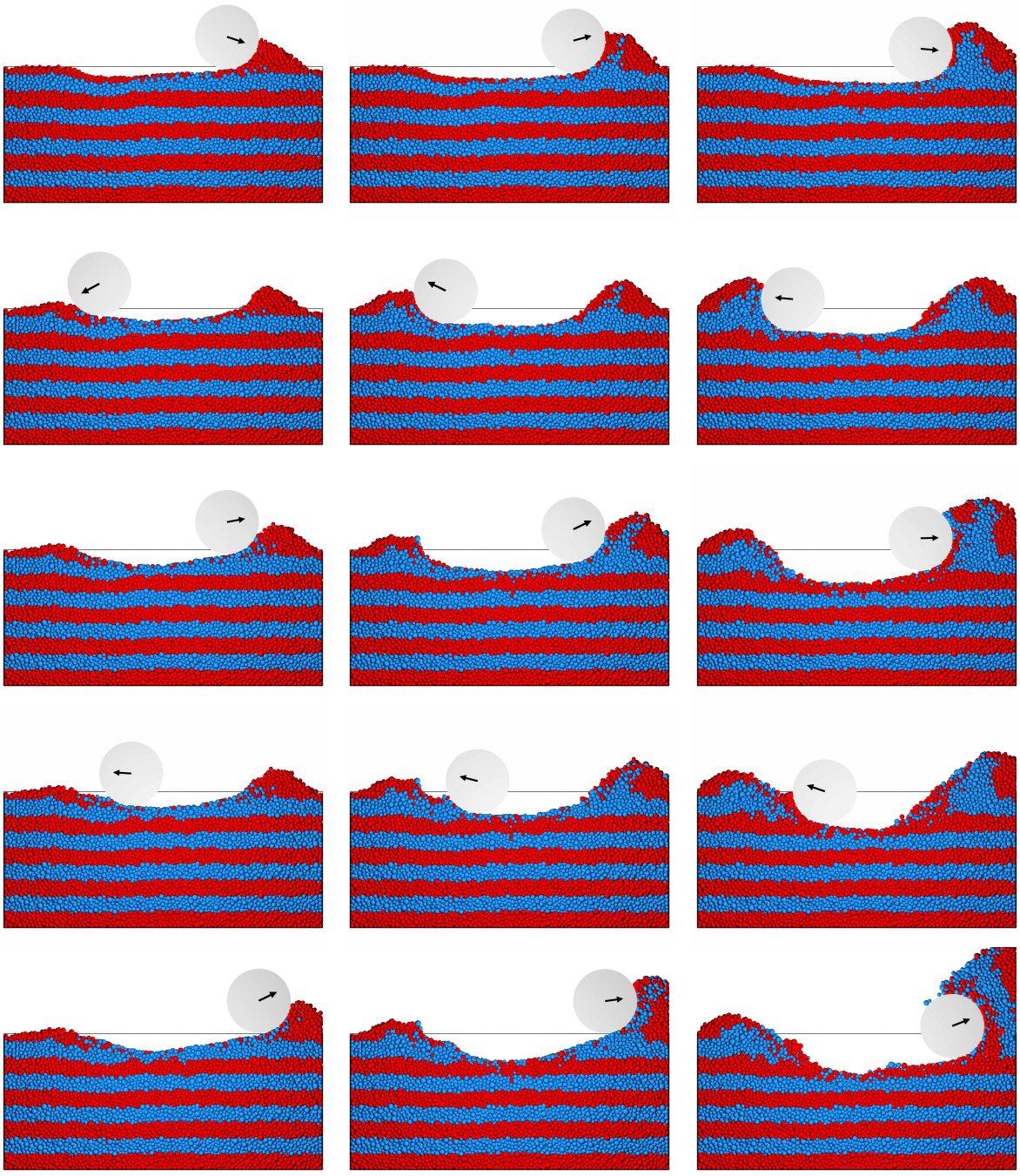

(a) $R = 20$, heavily overloaded pipe

(b) $R = 10$, moderately overloaded pipe

(c) $R = 5$, lightly overloaded pipe

Figure 7.36: Soil surface and pipe position during the constant V tests at different overloading ratios R.

second cycle, the pipe penetrates deeper into the soil. The corresponding horizontal load increases more slowly than in the first cycle, and then it reaches a value higher than before. As the simulation proceeds, the pipe forms a trench, scraping the soil surface deeper and steeper, reaching a maximum embedment of 32 mm ($0.64D$). At the end of the simulation, it rises up reaching a depth of 19 mm ($0.38D$).

The soil profiles illustrated in Figure 7.36 allow a comparison among the tests performed at different overloading ratios. The heavily overloaded pipe follows an approximately horizontal trajectory, with only a lightly penetration in the centre of each cycle, and an uplift on the sides. As expected, the lightly overloaded pipe experiences a deeper penetration throughout the cyclic motion. As it moves downwards, the slightly overloaded pipe forms a trench and scrapes the soil surface, building up a larger berm than the heavily overloaded pipe.

7.4.5 Concluding remarks

DEM simulations have shown that the pipe trajectory during a constant V test depends on the overloading ratio. Heavily overloaded pipes ($R = 20$) experience an initial uplift, whereas lightly overloaded pipes ($R = 5$) move along a downward trajectory. Moderately overloaded pipes ($R = 10$), instead, moves laterally with nearly constant elevation. These simulations were performed in small domains and with the pipe and particle Young's moduli three orders of magnitude smaller than the real one. Because of these approximations, accurate quantitative comparisons with experimental data are not meaningful.

However, qualitative comparisons can be made with the findings from experimental constant V tests performed by Zhang et al. (2001a) and Sandford (2012). These re-

searchers found that a critical value around $R = 10$ controls the occurring of uplift or penetration during the initial lateral movement of the pipe.

The numerical results were able to replicate such behaviour. In conclusion, these final analyses have demonstrated the capability of the DEM model to replicate realistically the influence of R on the pipe response during lateral constant V tests.

Chapter 8

Conclusions

8.1 Summary and main findings

The purpose of the research presented in this thesis was to provide a numerical tool for the study of pipe–soil interaction for offshore pipelines on sandy seabeds. The distinct element method (DEM) was identified as a viable alternative to laboratory tests and continuum-based numerical analyses for the study of this problem. The main research stages and the key findings are summarised here.

8.1.1 Contact of sand grains

Evidence was provided on the particulate nature of soils, and the distinct element method (DEM) was introduced as a suitable method for addressing geotechnical problems where large deformations are involved. The main features of the DEM code are summarised here.

- Parallelisation is allowed through the OpenMP environment, where the optimal number of processors is around 8.

- The Hertz–Mindlin no micro-slip solution is chosen as contact law, as it realistically replicates the non-linear elastic behaviour of sand grains in contact.
- The moment–relative rotation contact law is added to mimic the contact between irregular shaped grains. The law is based on other moment–relative rotation contact laws available in the literature. However, the rolling coefficients are implemented specifically to maintain the consistency with the non-linear behaviour described by the contact force.

8.1.2 Mechanical behaviour of a sand sample

Triaxial tests simulations were performed on cubic periodic assemblies to calibrate the DEM model. The following conclusions were drawn.

- A representative element volume (REV) of 5000 particles is sufficiently large to replicate the macroscopic response of the sand accurately.
- The inertial number should be $I \leq 4 \times 10^{-4}$ to ensure stable and accurate simulations, i.e. quasi-static and strain rate independent. The inertial number suggested in the literature, $I \leq 1 \times 10^{-3}$, guarantees stable simulations only.
- The moment–relative rotation contact law increases the strength of the numerical material and allows a realistic critical state friction angle to be reproduced. In this way, the proposed calibration procedure provides a numerical model able to capture the macroscopic response of the sand at different relative densities.
- The validation on specimens at another relative density and various confining pressures demonstrates that the DEM model is capable of predicting the soil response without any further adjustments of the calibrated parameters.
- The investigation of the numerical results at a particle level has shown that the

microscopic response is strictly dependent on the boundary conditions. A further discussion on the ability of the DEM to replicate the micro- and macro-response of a granular material suggests that it is challenging to develop a numerical model reproducing them both. In general each model is developed to analyse the soil behaviour at a specific scale, replicating either the experimental stress–strain curve (macroscopic scale), or the kinematics of the soil particles (microscopic scale).

8.1.3 Soil specimen preparation and pipeline implementation

The gravitational deposition approach was found to be the most suitable technique to prepare a numerical assembly within the geometrical limitations of the domain. Improvements over the techniques available in literature were made to obtain homogeneous specimens.

- The proposed method allows numerical specimens to be created at various relative densities with a minimal difference in the procedure.
- The coefficient of viscous damping has a great influence on particle rearrangement, and hence on the relative density of the specimen.

A cylindrical object was implemented to model a segment of the pipeline. The implementation was essential to treat the pipeline as a body with a continuous curved external surface and a specific mass, rather than a massless polygonal prism.

8.1.4 A numerical approach for studying pipe–soil interaction

Small displacement loading tests simulations were performed with a segment of the pipeline in a 3D prismatic soil domain. The aim was to gain understanding of signi-

ficant parameters controlling the numerical simulation, and to find a reasonable compromise between numerical accuracy and computational effort. The results provided the following recommendations.

- The particle size distribution may be scaled up by a factor of 2 to reduce the number of particles filling the domain. This allows a ratio between the pipe diameter and the median particle size of $D/D_{50} = 31.2$.
- When modelling plane strain conditions, the thickness of the domain may be as small as $5D_{50}$. Even without periodic boundary conditions, such a small thickness ensures a limited influence of the walls in the out-of-plane direction.
- The loading velocity and the viscous damping control the amplitude of the oscillations of the force–displacement curve during loading. For stable and accurate results, $v = 0.005\,\mathrm{m/s}$ and $\zeta = 0.2$ should be used.

Some compromises had to be made between these recommendations and their high computational demand. Those preliminary DEM analyses had a significant value, that is to predict and anticipate the different response when these recommendations cannot be fulfilled.

8.1.5 Modelling of pipe–soil interaction by DEM analyses

Large displacement loading simulations were performed to validate the DEM model against a small-scale $1g$ model test. An initial test was performed to explore the pipe response during a cycle of vertical loading and unloading. The novelties of the DEM approach and the main findings from the analysis are summarised as follows.

- The DEM is capable of replicating the macroscopic behaviour of the laboratory test. For the first time, a quantitative comparison of the force–displacement

curves is carried out.

- Good qualitative agreement for failure mechanisms within the soil is found between numerical simulation and experimental test.

A monotonic vertical and lateral loading test simulation at constant embedment was performed. Validation results and findings from a parametric analysis are summarised.

- Good quantitative agreement of the macroscopic pipe behaviour is found with results from small-scale laboratory tests. The moment–relative rotation contact law implemented during this work is essential to replicate realistic behaviour with such accuracy.
- The failure mechanism is investigated directly from particle plots, velocity field and contact force network. These figures provide valuable insights into the underlying mechanics of the soil at a particle level. They reveal a punching shear failure mechanism during penetration, dominated by compression of the underlying soil, whereas during the lateral phase the motion of soil particles is restricted to the superficial region in front of the pipe.
- The type of failure is dependent on the friction angles at sand–sand and pipe–sand contact. For large friction angles – either ϕ_μ (loose specimen) or δ (rough pipe)– the system is characterised by a punching shear mechanism. In contrast, for small friction angles – either ϕ_μ (dense specimen) or δ (smooth pipe) – the system is characterised by a local failure mechanism and more dilatant behaviour.

A cyclic large lateral displacement test was also performed. The pipe was pushed into the sand and then cyclically moved at constant embedment up to a lateral displacement of 4 pipe diameters.

- The formation and growth of the soil berm as the pipe moves laterally, and its

collection after one cycle is clearly reproduced by the DEM approach.

- Large deformations in the soil are directly captured by the DEM. These cannot be captured by continuum-based numerical analyses without remeshing or further numerical adjustments. For instance, the particle velocities and the particle rotation plots allow the observation of particles falling from the top of the berm at high velocities.

A simulation was conducted to replicate realistically the conditions experienced by a buckling pipeline in the field. The pipeline was preloaded and then subjected to a cycle of lateral displacement at a constant vertical load. The novel features of the method are summarised.

- The vertical load is maintained at a constant value through a servo-control algorithm. The load oscillates around the desired value with an error less than 24 %. Such small variability cannot be obtained in laboratory tests.
- The DEM simulations realistically reproduce the pipe trajectory and the pipe–soil load observed in experimental tests.
- The failure mechanism is revealed from particle position plots and the particle velocity field. Excellent agreement was found between numerical and experimental results.

A larger test programme was carried out to simulate three cycles of lateral displacement at a constant vertical load. The effect of the overloading ratio was also investigated.

- The DEM model captures the effect of the overloading ratio. The response of the pipe depends on the maximum vertical load experienced by the pipe prior to the lateral movement.
- Overloaded pipes are subjected to uplift, whereas slightly overloaded pipes follow

a downwards trajectory, forming a deep and steep trench.

8.2 Recommendations for further research

This thesis has illustrated the capability of the proposed DEM model to replicate the mechanical behaviour of granular soils and, for the first time, to analyse the pipe–soil interaction for offshore pipelines on sand. Since this was the very first attempt to combine distinct element modelling and on-bottom offshore pipelines, there is still room for improvements and further research. The limitations raised during this work, together with some recommendations for further analyses are presented in this section.

- The effect of particle shape was taken into account through a fictitious moment–relative contact law. However, this may be not be sufficient to replicate the arrangement of physical specimens, and hence the soil behaviour realistically. Non-spherical particles should be used, such as clumps, spheropolygons, ellipsoids, potential particles, or the real sand grain geometry should be reproduced by non-uniform rational basis-splines (known as NURBS).
- The proposed calibration procedure allowed the response of a sand specimen during triaxial tests to be replicated at a macroscopic scale. However, at the microscopic scale, differences were found in the physical response. The possible reason was identified in the periodic boundary conditions. Hence further analyses are recommended using either rigid aperiodic or flexible boundaries so that both the stress–strain curves and the deformations occurring at a particle level are reproduced.
- The influence of the viscous damping ratio on the specimen preparation and on

the pipe loading test was investigated, but an appropriate value was chosen only as a compromise between computational cost and influence on the numerical results. The damping ratio, in fact, is not a physical constant, hence no realistic value could be assigned to it. A more realistic contact model should include a formulation relating the damping to the coefficient of restitution, which is a physical variable. Although various formulations of this type of damping can be found in the literature, e.g. in Antypov and Elliott (2011), the coefficient of restitution would still require a preliminary calibration.

- The comparison between the numerical and the experimental results were limited to one type of sand. To investigate the pipe–soil interaction under a larger variety of soil conditions, the proposed method can be also used with different types of sands and at various relative densities. However, to replicate the quantitative response, a preliminary calibration for the different soil type is necessary.
- The computational cost remains the primary limitation of the pipe loading tests. Runtimes of about one month on a 16-core workstation with 32 GB of RAM were necessary for a domain of approximately 37 000 particles of large size. It was found that simulations should be performed with a smaller particle size, employing about 150 000 particles. This size is still impractical with the available computer resources.

  The choice of loading velocity is made depending on the computational time. Although a loading velocity of 0.005 m/s was used for the presented tests, a smaller velocity, especially when varying the load direction, would simulate the laboratory conditions more realistically.

  The use of other DEM codes, based not on OpenMP but on MPI parallelisation,

should be evaluated, to exploit the faster runtimes that are currently possible on high performance shared-memory clusters.

- Since this thesis has demonstrated the DEM capability at analysing pipe–soil interaction, the method could be applied to study a larger variety of loading tests, replicating more realistically the loading conditions experienced by the pipelines in the field. Several cycles of vertical unloading and reloading tests should be performed to explore the pipe response to the accumulated vertical settlements induced by cyclic loading. Lateral displacement analyses should also investigate the pipe response after a larger displacement and for longer sequence of cycles, as offshore on-bottom pipelines may be subject to lateral displacements of up to 10 or $20D$, for up to 1000 cycles.
- The DEM could be employed to analyse pipe–soil interaction for buried pipelines subjected to upheaval buckling. In fact, from a micro-mechanical point of view, the two problems have several similarities. The only difference would be the specimen preparation procedure, as the buried pipeline is already in place.

8.3 Concluding remarks

This thesis has demonstrated that the distinct element method can be employed as a numerical tool for modelling the interaction between granular soils and on-bottom offshore pipelines.

The calibration and the validation of the soil properties provided a numerical model replicating the behaviour of the sand. The preliminary small displacements analyses on the pipe provided recommendations for performing DEM simulations of a pipeline

segment loaded on a numerical specimen. The large displacement analyses demonstrated the validity of the DEM approach for investigating the interaction between the pipeline and the sand.

The analysis of pipe–soil interaction was carried out through cyclic vertical simulations, monotonic vertical and lateral simulations, and cyclic lateral simulations both at constant embedment and at constant vertical load. At a macroscopic scale, although further adjustments of the model should be made, good agreement was found with experimental results. At the microscopic scale, results were obtained from particle plots, particle velocities, and contact forces in a manner not easily accessible with continuum-based numerical analyses.

The study has also shown that although realistic quantitative conditions are replicated for particular conditions, the model is not yet ready to provide detailed and accurate quantitative predictions. The DEM model still remains a simplification of the physical system. Differences between the physical and the numerical model are, for instance, the contact law, the particle shape and the domain dimensions.

In conclusion, the DEM is capable of simulating large displacements of the pipe and of modelling large deformations in sand. It replicates the macroscopic behaviour observed from laboratory tests, and provides microscopic details beyond both laboratory and continuum-based numerical tests. Hence this research leads the way for the application of the distinct element method to the analysis of a large variety of loading conditions for offshore pipelines on granular soils.

Appendix A

List of publications

The following publications have been produced during the completion of this thesis:

- Macaro, G. and Utili, S. (2012). DEM triaxial tests of a seabed sand. In Wu, C. Y., editor, *Discrete Element Modelling of Particulate Media. Proceedings of the International Symposium on Discrete Element Modelling of Particulate Media.*, pages 203–211. The Royal Society of Chemistry.

- Macaro, G., Utili, S., and Martin, C. M. (2015a). DEM analyses of pipe–soil interaction for offshore pipelines on sand. In Soga, K., Kumar, K., Biscontin, G., and Kuo, M., editors, *Geomechanics from Micro to Macro. Proceedings of the TC105 ISSMGE International Symposium on Geomechanics from Micro to Macro, IS-Cambridge 2014*, volume 1, pages 595–600, London, UK. Taylor & Francis Group.

- Macaro, G., Utili, S., and Martin, C. M. (2015b). Distinct element modelling of pipe–soil interaction for offshore pipelines on sand. *Computers and Geotechnics*. (Invited paper under review, submitted June 2015).

Bibliography

Ai, J., Chen, J.-F., Rotter, J. M., and Ooi, J. Y. (2011). Assessment of rolling resistance models in discrete element simulations. *Powder Technology*, 206(3):269–282.

Alder, B. J. and Wainwright, T. E. (1959). Studies in molecular dynamics. I. General method. *The Journal of Chemical Physics*, 31(2):459–466.

Allen, D. W., Lammert, W. F., Hale, J. R., and Jacobsen, V. (1989). Submarine pipeline on-bottom stability: recent AGA research. In *Proceedings of the 21st Offshore Technology Conference*, Paper OTC 6055, Houston, Texas, USA.

Allen, M. P. and Tildesley, D. J. (1991). *Computer simulation of liquids*. Clarendon Press.

Andrade, J. E., Lim, K.-W., Avila, C. F., and Vlahinić, I. (2012). Granular element method for computational particle mechanics. *Computer Methods in Applied Mechanics and Engineering*, 241:262–274.

Antony, S. J. and Kuhn, M. R. (2004). Influence of particle shape on granular contact signatures and shear strength: new insights from simulations. *International Journal of Solids and Structures*, 41(21):5863–5870.

Antypov, D. and Elliott, J. A. (2011). On an analytical solution for the damped hertzian spring. *EPL (Europhysics Letters)*, 94(5).

Aubeny, C. P., Shi, H., and Murff, J. D. (2005). Collapse loads for a cylinder embedded in trench in cohesive soil. *International Journal of Geomechanics*, 5(4):320–325.

Bagi, K. (2005). An algorithm to generate random dense arrangements for discrete element simulations of granular assemblies. *Granular Matter*, 7(1):31–43.

Bai, Y. (2001). *Pipelines and risers*, volume 5 of *Elsevier Ocean Engineering Book Series*. Elsevier.

Bardet, J. P. and Huang, Q. (1993). Rotational stiffness of cylindrical particle contacts. In Thornton, C., editor, *Powders & Grains 93: Proceedings of the Second International Conference on Micromechanics of Granular Media*, pages 39–43, Birmingham, UK. Balkema, Rotterdam, The Netherlands.

Bardet, J. P. and Proubet, J. (1992). Shear-band analysis in idealized granular material. *Journal of Engineering Mechanics*, 118(2):397–415.

Barrett, P. J. (1980). The shape of rock particles, a critical review. *Sedimentology*, 27(3):291–303.

Beaubouef, B. (2014). Operators planning more than 7,000 miles of offshore pipelines through 2018. *Offshore Magazine*, 74(8).

Belheine, N., Plassiard, J.-P., Donzé, F.-V., Darve, F., and Seridi, A. (2009). Numerical simulation of drained triaxial test using 3D discrete element modeling. *Computers and Geotechnics*, 36(1):320–331.

Braestrup, M. W., Andersen, J. B., Andersen, L. W., Bryndum, M., Christensen, C. J., and Nielsen, N.-J. R. (2005). *Design and installation of marine pipelines*. Blackwell Science.

Brennodden, H., Sveggen, O., Wagner, D. A., and Murff, J. D. (1986). Full-scale pipe–soil interaction tests. In *Proceedings of the 18th Annual Offshore Technology Conference*, Paper OTC 5338, Houston, Texas, USA.

Brilliantov, N. V., Spahn, F., Hertzsch, J.-M., and Pöschel, T. (1996). Model for collisions in granular gases. *Physical Review E*, 53(5):5382.

Bromwell, L. G. (1966). The friction of quartz in high vacuum. Technical report, Massachusetts Institute of Technology, Dept of Civ. Eng Research Report.

Bruton, D. A. S. and Carr, M. (2011). Overview of the SAFEBUCK JIP. In *Proceedings of the Offshore Technology Conference*, Paper OTC 21671, Houston, Texas, USA. Offshore Technology Conference.

Bruton, D. A. S., Carr, M., Crawford, M., and Poiate, E. (2005). The safe design of hot on-bottom pipelines with lateral buckling using the design guideline developed by the safebuck joint industry project. In *Proceedings of the Deep Offshore Technology Conference*, Vitoria, Espirito Santo, Brazil.

Bruton, D. A. S., Carr, M., and White, D. J. (2007). The influence of pipe–soil interaction on lateral buckling and walking of pipelines: the SAFEBUCK JIP. In *Proceedings of the 6th International Offshore Site Investigation and Geotechnics Conference*, pages 133–150, London, UK.

Cabalar, A. F. (2010). Applications of the oedometer, triaxial and resonant column tests to the study of micaceous sands. *Engineering Geology*, 112(1):21–28.

Calvetti, F., di Prisco, C., and Nova, R. (2001). Modelling of pipeline–landslide interaction. In Kishino, Y., editor, *Powders and Grains 2001*, pages 304–307. CRC Press.

Calvetti, F., di Prisco, C., and Nova, R. (2004). Experimental and numerical analysis of soil–pipe interaction. *Journal of Geotechnical and Geoenvironmental Engineering*, 130(12):1292–1299.

Cardoso, C. O. and Silveira, R. (2010). Pipe–soil interaction behavior for pipelines under large displacements on clay soils — A model for lateral residual friction factor. In *Proceedings of the Offshore Technology Conference*, Paper OTC 20767, Houston, Texas, USA. Offshore Technology Conference.

Catalano, E., Chareyre, B., and Barthélémy, E. (2014). Pore-scale modeling of fluid-particles interaction and emerging poromechanical effects. *International Journal for Numerical and Analytical Methods in Geomechanics*, 38(1):51–71.

Cavarretta, I., Coop, M. R., and O'Sullivan, C. (2010). The influence of particle characteristics on the behaviour of coarse grained soils. *Géotechnique*, 60(6):413–423.

Chakrabarti, S. (2005). *Handbook of offshore engineering*, volume 1. Elsevier.

Chapman, B., Jost, G., and Van Der Pas, R. (2008). *Using OpenMP: portable shared memory parallel programming*. MIT Press, Cambridge, Massachusetts.

Chareyre, B. and Villard, P. (2005). DEM modelling of soil structures reinforced with geosynthetics. In Garca-Rojo, R., Hermann, H., and Mc Namara, S., editors, *Powders and Grains 2005: Proceedings of the 5th International Conference on Micromechanics of Granular Media*. Balkema, Rotterdam, The Netherlands.

Cheuk, C. Y., White, D. J., and Bolton, M. D. (2007). Large-scale modelling of soil–pipe interaction during large amplitude cyclic movements of partially embedded pipelines. *Canadian Geotechnical Journal*, 44(8):977–996.

Cheuk, C. Y., White, D. J., and Bolton, M. D. (2008). Uplift mechanisms of pipes buried in sand. *Journal of Geotechnical and Geoenvironmental Engineering*, 134(2):154–163.

Cheung, G. and O'Sullivan, C. (2008). Effective simulation of flexible lateral boundaries in two- and three-dimensional DEM simulations. *Particuology*, 6(6):483–500.

Cho, G.-C., Dodds, J., and Santamarina, J. C. (2006). Particle shape effects on packing density, stiffness, and strength: natural and crushed sands. *Journal of Geotechnical and Geoenvironmental Engineering*, 132(5):591–602.

Clayton, C. R. I., Abbireddy, C. O. R., and Schiebel, R. (2009). A method of estimating the form of coarse particulates. *Géotechnique*, 59(6):493–501.

Cui, L. and O'Sullivan, C. (2003). Analysis of a triangulation based approach for specimen generation for discrete element simulations. *Granular Matter*, 5(3):135–145.

Cundall, P. A. (1971). A computer model for simulating progressive, large-scale movements in blocky rock systems. In *Proceedings of an International Symposium on Rock Fracture*, pages II–8, Nancy, France.

Cundall, P. A. (1987). Distinct element models of rock and soil structure. *Analytical and computational methods in engineering rock mechanics*, 4:129–163.

Cundall, P. A. (1988). Computer simulations of dense sphere assemblies. *Micromechanics of Granular Materials*, 4:113–123.

Cundall, P. A. (2001). A discontinuous future for numerical modelling in geomechanics? *Proceedings of the ICE-Geotechnical Engineering*, 149(1):41–47.

Cundall, P. A. and Hart, R. D. (1992). Numerical modelling of discontinua. *Engineering computations*, 9(2):101–113.

Cundall, P. A. and Strack, O. D. L. (1979). A discrete numerical model for granular assemblies. *Géotechnique*, 29(1):47–65.

de Josselin de Jong, G. and Verruijt, A. (1969). Etude photo-elastique d'un empilement de disques, *Cahiers du Groupe Francais de Rheologie II* **2**: 73–86. In Schotting, R. J., Duijn, H. C., and Verruijt, A., editors, *Soil Mechanics and Transport in Porous Media: Selected Works of G. de Josselin de Jong* (2006). Springer.

DEM Solutions (2013). *EDEM 2.5 User Guide*. Edinburgh.

Di Prisco, C., Nova, R., and Corengia, A. (2004). A model for landslide–pipe interaction analysis. *Soils and Foundations*, 44(3):1–12.

Di Renzo, A. and Di Maio, F. P. (2004). Comparison of contact-force models for the simulation of collisions in DEM-based granular flow codes. *Chemical Engineering Science*, 59(3):525–541.

Duran, J. (2000). *Sands, powders, and grains — An Introduction to the physics of granular materials*. Springer, New York.

Edison (2010). Sustainability report. Technical report, Edison.

Erik, P. and Stokke, R. (2009). Assessment of impacts of offshore oil and gas activities in the North-East Atlantic. Technical report, OSPAR Commission.

Espoo (2009). Nord Stream Espoo Report. Chapter 4. Description of the project. Technical report, Nord Stream AG.

Feda, J. (1982). *Mechanics of particulate materials — The principles*. Elsevier Scientific Publishing Company.

Feng, Y. T., Han, K., and Owen, D. R. J. (2003). Filling domains with disks: an advancing front approach. *International Journal for Numerical Methods in Engineering*, 56(5):699–713.

Gottardi, G., Houlsby, G. T., and Butterfield, R. (1999). Plastic response of circular footings on sand under general planar loading. *Géotechnique*, 49(4):453–469.

Guo, B., Song, S., Ghalambor, A., and Chacko, J. (2005). *Offshore pipelines*. Elsevier.

Hanson, A. J. (2006). *Visualizing Quaternions*. Elsevier.

Harkness, J. (2009). Potential particles for the modelling of interlocking media in three dimensions. *International Journal for Numerical Methods in Engineering*, 80(12):1573–1594.

Hart, R., Cundall, P. A., and Lemos, J. (1988). Formulation of a three-dimensional distinct element model — Part II. Mechanical calculations for motion and interaction of a system composed of many polyhedral blocks. *International Journal of Rock Mechanics and Mining Sciences & Geomechanics*, 25(3):117–125.

Hertz, H. (1881). On the contact of elastic solids, *Journal Reine und angewandte Mathematik* **92**: 156–171. In Jones, D. E. and Schott, G. A., editors, *Miscellaneous Papers* (1896). Macmillan, London.

Houlsby, G. T. (2009). Potential particles: a method for modelling non-circular particles in DEM. *Computers and Geotechnics*, 36(6):953–959.

Itasca (2008). *PFC3D Particle Flow Code in 3 Dimensions*. Itasca Consulting Group Inc., Minneapolis, Minnesota.

Iwashita, K. and Oda, M. (1998). Rolling resistance at contacts in simulation of shear band development by DEM. *Journal of Engineering Mechanics*, 124(3):285–292.

Jiang, M. J., Konrad, J. M., and Leroueil, S. (2003). An efficient technique for generating homogeneous specimens for DEM studies. *Computers and geotechnics*, 30(7):579–597.

Jiang, M. J., Yu, H., and Harris, D. (2005). A novel discrete model for granular material incorporating rolling resistance. *Computers and Geotechnics*, 32(5):340–357.

Johnson, K. L. (1985). *Contact mechanics*. Cambridge University Press.

Ketterhagen, W. R., Curtis, J. S., Wassgren, C. R., and Hancock, B. C. (2008). Modeling granular segregation in flow from quasi-three-dimensional, wedge-shaped hoppers. *Powder Technology*, 179(3):126–143.

Kloss, C. and Goniva, C. (2011). LIGGGHTS–Open source discrete element simulations of granular materials based on Lammps. *Supplemental Proceedings: Materials Fabrication, Properties, Characterization, and Modeling, Volume 2*, pages 781–788.

Konuk, I. and Yu, S. (2007). Continuum FE modeling of lateral buckling: study of soil effects. In *ASME 2007 26th International Conference on Offshore Mechanics and Arctic Engineering*, OMAE2007-29376, pages 347–354. American Society of Mechanical Engineers.

Kozicki, J. and Donzé, F.-V. (2008). A new open-source software developed for numerical simulations using discrete modeling methods. *Computer Methods in Applied Mechanics and Engineering*, 197(49):4429–4443.

Kozicki, J., Tejchman, J., and Mróz, Z. (2012). Effect of grain roughness on strength, volume changes, elastic and dissipated energies during quasi-static homogeneous triaxial compression using DEM. *Granular Matter*, 14(4):457–468.

Kozicki, J., Tejchman, J., and Mühlhaus, H.-B. (2014). Discrete simulations of a triaxial compression test for sand by DEM. *International Journal for Numerical and Analytical Methods in Geomechanics*, 38(18):1923–1952.

Kuhn, M. R. (1999). Structured deformation in granular materials. *Mechanics of Materials*, 31(6):407–429.

Kuhn, M. R. (2006). Oval and ovalplot: Programs for analyzing dense particle assemblies with the discrete element method.

Lambe, T. W. and Whitman, R. V. (1969). *Soil mechanics*. John Wiley and Sons, Inc.

Lambrakos, K. F. (1985). Marine pipeline soil friction coefficients from *in-situ* testing. *Ocean Engineering*, 12(2):131–150.

Lin, X. and Ng, T.-T. (1997). A three-dimensional discrete element model using arrays of ellipsoids. *Géotechnique*, 47(2):319–329.

Lyons, C. G. (1973). Soil resistance to lateral sliding of marine pipelines. In *Proceedings of the Fifth Annual Offshore Technology Conference*, Paper OTC 1876, Houston, Texas, USA.

Macaro, G. and Utili, S. (2012). DEM triaxial tests of a seabed sand. In Wu, C. Y., editor, *Discrete Element Modelling of Particulate Media. Proceedings of the International Symposium on Discrete Element Modelling of Particulate Media.*, pages 203–211. The Royal Society of Chemistry.

Macaro, G., Utili, S., and Martin, C. M. (2015a). DEM analyses of pipe–soil interaction for offshore pipelines on sand. In Soga, K., Kumar, K., Biscontin, G., and Kuo, M., editors, *Geomechanics from Micro to Macro. Proceedings of the TC105 ISSMGE International Symposium on Geomechanics from Micro to Macro, IS-Cambridge 2014*, volume 1, pages 595–600, London, UK. Taylor & Francis Group.

Macaro, G., Utili, S., and Martin, C. M. (2015b). Distinct element modelling of pipe–soil interaction for offshore pipelines on sand. *Computers and Geotechnics*. (Invited paper under review, submitted June 2015).

Marketos, G. and Bolton, M. D. (2010). Flat boundaries and their effect on sand testing. *International Journal for Numerical and Analytical Methods in Geomechanics*, 34(8):821–837.

Martin, C. M. (1994). *Physical and numerical modelling of offshore foundations under combined loads*. D.Phil. Thesis, University of Oxford.

Martin, C. M., Kong, D., and Byrne, B. W. (2013). 3D analysis of transverse pipe–soil interaction using 2D soil slices. *Géotechnique Letters*, 3(July-September):119–123.

Martin, C. M. and White, D. J. (2012). Limit analysis of the undrained bearing capacity of offshore pipelines. *Géotechnique*, 62(9):847–863.

Merifield, R. S., White, D. J., and Randolph, M. F. (2008). The effect of pipe–soil interface conditions on the undrained breakout resistance of partially-embedded pipelines. In *The 12th International Conference of International Association for Computer Methods and Advances in Geomechanics (IACMAG)*. IACMAG.

Mindlin, R. D. (1949). Compliance of elastic bodies in contact. *Journal of Applied Mechanics*, 16.

Mindlin, R. D. and Deresiewicz, H. (1953). Elastic spheres in contact under varying oblique forces. *Journal of Applied Mechanics*, 20.

Mitchell, J. and Soga, K. (2005). *Fundamentals of soil behavior*. John Wiley and Sons, Inc., Hoboken, NJ.

Mitchell, R. F. (2006). *Drilling engineering*, volume 2 of *Petroleum Engineering Handbook*. Society of Petroleum Engineers, Richardson, TX.

Mohamed, A. and Gutierrez, M. S. (2010). Comprehensive study of the effects of rolling resistance on the stress–strain and strain localization behavior of granular materials. *Granular Matter*, 12(5):527–541.

Nash, I. F. J. and Roberts, P. M. (2011). MEIDP — The deep sea gas route to India. In *Proceedings of the Offshore Technology Conference*, Paper OTC 21259, Houston, Texas, USA. Offshore Technology Conference.

Ng, T.-T. (2006). Input parameters of discrete element methods. *Journal of Engineering Mechanics*, 132(7):723–729.

Nitka, M., Tejchman, J., and Kozicki, J. (2013). Investigations of micro-structure evolution in granular shear zones using DEM. In Bischoff, M., Oñate, E., Owen, D. R. J., Ramm, E., and Wriggers, P., editors, *III International Conference on Particle-based Methods – Fundamentals and Applications - PARTICLES*.

Nova, R. and Montrasio, L. (1991). Settlements of shallow foundations on sand. *Géotechnique*, 41(2):243–256.

Oda, M. and Iwashita, K. (2000). Study on couple stress and shear band development in granular media based on numerical simulation analyses. *International Journal of Engineering Science*, 38(15):1713–1740.

Oda, M. and Kazama, H. (1998). Microstructure of shear bands and its relation to the mechanisms of dilatancy and failure of dense granular soils. *Géotechnique*, 48(4):465–481.

Oda, M., Konishi, J., and Nemat-Nasser, S. (1982). Experimental micromechanical evaluation of strength of granular materials: effects of particle rolling. *Mechanics of Materials*, 1(4):269–283.

O'Sullivan, C. (2002). *The application of discrete element modelling to finite deformation problems in geomechanics*. Ph.D. Thesis, University of California, Berkeley.

O'Sullivan, C. (2011a). Particle-based discrete element modeling: geomechanics perspective. *International Journal of Geomechanics*, 11(6):449–464.

O'Sullivan, C. (2011b). *Particulate discrete element modelling*. Taylor & Francis.

O'Sullivan, C. (2015). Advancing geomechanics using DEM. In Soga, K., Kumar, K., Biscontin, G., and Kuo, M., editors, *Geomechanics from Micro to Macro - Proceedings of the TC105 ISSMGE International Symposium on Geomechanics from Micro to Macro, IS-Cambridge 2014*, volume 1, pages 21–32, London, UK. Taylor & Francis Group.

O'Sullivan, C. and Bray, J. D. (2003). Modified shear spring formulation for discontinuous deformation analysis of particulate media. *Journal of Engineering Mechanics*, 129(7):830–834.

Palmer, A. C. (2008). *Dimensional analysis and intelligent experimentation*. World Scientific.

Palmer, A. C. and King, R. A. (2008). *Subsea pipeline engineering*. PennWell Books, Tulsa, Oklahoma, USA.

Palmer, A. C., Steenfelt, J. S., Steensen-Bach, J. O., and Jacobsen, V. (1988). Lateral resistance of marine pipelines on sand. In *Proceedings of the 20th Annual Offshore Technology Conference*, Paper OTC 5853, Houston, Texas, USA.

Pasqualino, I. P., Alves, J. L. D., and Battista, R. C. (2001). Failure simulation of a buried pipeline under thermal loading. In *Proceedings of OMAE'01, 20th International Conference on Offshore Mechanics and Arctic Engineering*, pages 3–8, Rio de Janeiro, Brazil.

Persistence of Vision Pty. Ltd. (2004). *Persistence of Vision Raytracer (Version 3.6) (POV-Ray)*. Williamstown, Victoria, Australia.

Plassiard, J.-P., Belheine, N., and Donzé, F.-V. (2009). A spherical discrete element model: calibration procedure and incremental response. *Granular Matter*, 11(5):293–306.

Potyondy, J. G. (1961). Skin friction between various soils and construction materials. *Géotechnique*, 11(4):339–353.

Pournin, L., Weber, M., Tsukahara, M., Ferrez, J.-A., Ramaioli, M., and Liebling, T. M. (2005). Three-dimensional distinct element simulation of spherocylinder crystallization. *Granular Matter*, 7(2-3):119–126.

Procter, D. C. and Barton, R. R. (1974). Measurements of the angle of interparticle friction. *Géotechnique*, 24(4):581–604.

Radjaï, F. and Dubois, F. (2011). *Discrete-element modeling of granular materials*. Wiley-ISTE.

Randolph, M. F. and Gourvenec, S. M. (2011). *Offshore geotechnical engineering*. Taylor & Francis Group.

Roux, J.-N. (2005). The nature of quasistatic deformation in granular materials. In *Powders and Grains 2005: Proceedings of the 5th International Conference on Micromechanics of Granular Media*, pages 261–265.

Roux, J.-N. and Combe, G. (2002). Quasistatic rheology and the origins of strain. *Comptes Rendus Physique*, 3(2):131–140.

Roux, J.-N. and Combe, G. (2010). How granular materials deform in quasistatic conditions. In Goddard, J., Jenkins, J. T., and P, G., editors, *Proceedings of the IUTAM-ISIMM Symposium on Mathematical Modeling and Physical Instances of Granular Flow*.

Rowe, P. W. (1962). The stress-dilatancy relation for static equilibrium of an assembly of particles in contact. *Proceedings of the Royal Society of London. Series A. Mathematical and Physical Sciences*, 269(1339):500–527.

Salot, C., Gotteland, P., and Villard, P. (2009). Influence of relative density on granular materials behavior: DEM simulations of triaxial tests. *Granular matter*, 11(4):221–236.

Sandford, R. J. (2012). *Lateral buckling of high pressure/high temperature on-bottom pipelines*. D.Phil. Thesis, University of Oxford.

Sandford, R. J. (2015). Personal communication.

Santamarina, J. C. and Cho, G. C. (2004). Soil behavior: The role of particle shape. In *Advances in Geotechnical Engineering: The Skempton Conference*, volume 1, pages 604–617, London, UK. Thomas Telford.

Schnaid, F. (1990). *A study of the cone-pressuremeter test in sand*. D.Phil. Thesis, University of Oxford.

Schotman, G. J. M. (1989). The effects of displacements on the stability of jackup spudcan foundations. In *Proceedings of the 21st Offshore Technology Conference*, Paper OTC 6026, Houston, Texas, USA.

Shell (2009). Five-year fact book — Shell financial and operational information 2005–2009. Technical report, Royal Dutch Shell plc.

Shi, G.-H. and Goodman, R. E. (1985). Two dimensional discontinuous deformation analysis. *International Journal for Numerical and Analytical Methods in Geomechanics*, 9(6):541–556.

Small, S. W., Tamburello, R. D., and Piaseckyj, P. J. (1971). Submarine pipeline support by marine sediments. In *Proceedings of the Third Annual Offshore Technology Conference*, Paper OTC 1357, Houston, Texas, USA.

Šmilauer, V. (2010). *Cohesive Particle Model using the Discrete Element Method on the Yade Platform*. Ph.D. Thesis, Czech Technical University in Prague.

Šmilauer, V., Catalano, E., Chareyre, B., Dorofenko, S., Duriez, J., Gladky, A., Kozicki, J., Modenese, C., Scholtès, L., and Sibille, L. (2010). *Yade Documentation. The Yade Project, 2010*.

Tan, F. S. C. (1990). *Centrifuge and theoretical modelling of conical footings on sand*. Ph.D. Thesis, University of Cambridge.

Terzaghi, K. (1920). Old earth pressure theories and new test results. *Engineering News Record*, 85(14):632–637.

Terzaghi, K. (1925). Principles of soil mechanics: V — Physical differences between sand and clay. *Engineering News Record*, 96:912–915.

Thoeni, K. and Eulitz, A. (2014). Multicore & performance benchmarks. In Chareyre, B. and Chalak, C., editors, *1st YADE Workshop*, pages 462–501.

Thomas, P. A. (1997). *Discontinuous deformation analysis of particulate media*. Ph.D. Thesis, University of California, Berkeley.

Thornton, C. (2000). Numerical simulations of deviatoric shear deformation of granular media. *Géotechnique*, 50(1):43–53.

Thornton, C. and Antony, S. J. (1998). Quasi-static deformation of particulate media. *Philosophical Transactions of the Royal Society A: Mathematical, Physical and Engineering Sciences*, 356(1747):2763–2782.

Thornton, C., Cummins, S. J., and Cleary, P. W. (2011). An investigation of the comparative behaviour of alternative contact force models during elastic collisions. *Powder Technology*, 210(3):189–197.

Thornton, C. and Zhang, L. (2006). A numerical examination of shear banding and simple shear non-coaxial flow rules. *Philosophical Magazine*, 86(21-22):3425–3452.

Tian, Y. and Cassidy, M. J. (2010). The challenge of numerically implementing numerous force–resultant models in the stability analysis of long on-bottom pipelines. *Computers and Geotechnics*, 37(1):216–232.

Tian, Y. and Cassidy, M. J. (2011). Pipe–soil interaction model incorporating large lateral displacements in calcareous sand. *Journal of Geotechnical and Geoenvironmental Engineering*, 137(3):279–287.

Tormodsgard, Y. (2014). Facts. The Norwegian petroleum sector. *Norwegian Petroleum Directorate*.

Tran, V. D. H., Meguid, M. A., and Chouinard, L. E. (2014). Discrete element and experimental investigations of the earth pressure distribution on cylindrical shafts. *International Journal of Geomechanics*, 14(1):80–91.

Tsuji, Y., Tanaka, T., and Ishida, T. (1992). Lagrangian numerical simulation of plug flow of cohesionless particles in a horizontal pipe. *Powder Technology*, 71(3):239 – 250.

Verley, R. L. P. and Sotberg, T. (1994). A soil resistance model for pipelines placed on sandy soils. *Journal of Offshore Mechanics and Arctic Engineering*, 116(3):145–153.

Wagner, D. A., Murff, J. D., Brennodden, H. A., and Sveggen, O. A. (1987). Pipe–soil interaction model. In *Proceedings of the 19th Annual Offshore Technology Conference*, Paper OTC 5504, Houston, Texas, USA.

Wang, D., White, D. J., and Randolph, M. F. (2010). Large-deformation finite element analysis of pipe penetration and large-amplitude lateral displacement. *Canadian Geotechnical Journal*, 47(8):842–856.

Weatherley, D., Hancock, W., and Boros, V. (2014). Esys-particle tutorial and user's guide version 2.3.1.

White, D. J. (2010). SAFEBUCK Joint Industry Project — Pipe–soil interaction models for lateral buckling design — Phase IIa data review. Technical Report Report GEO: 09497v2, University of Western Australia.

White, D. J. and Gaudin, C. (2008). Simulation of seabed pipe–soil interaction using geotechnical centrifuge modelling. In Conference Advisory Board, editor, *Proceedings of the Deep Offshore Technology Conference (Asia-Pacific)*, Perth, Australia. PennWell Corporation.

Widuliński, Ł., Kozicki, J., and Tejchman, J. (2009). Numerical simulations of triaxial test with sand using DEM. *Archives of Hydro-Engineering and Environmental Mechanics*, 56(3-4):3–26.

Yimsiri, S. and Soga, K. (2006). DEM analysis of soil–pipeline interaction in sand under lateral and upward movements at deep embedment. *Geotechnical Engineering*, 37(2):83–94.

Yoshimi, Y. and Kishida, T. (1981). A ring torsion apparatus for evaluating friction between soil and metal surfaces. *ASTM Geotechnical Testing Journal*, 4(4).

Yu, S. and Konuk, I. (2007). Continuum FE modeling of lateral buckling. In *Proceedings of the 2007 Offshore Technology Conference*, Paper OTC 18934.

Zdravkovic, L. and Carter, J. (2008). Contributions to géotechnique 1948–2008: Constitutive and numerical modelling. *Géotechnique*, 58(5):405–412.

Zhang, J. (2001). *Geotechnical stability of offshore pipelines in calcareous sand*. Ph.D. Thesis, University of Western Australia.

Zhang, J. and Erbrich, C. T. (2005). Stability design of untrenched pipelines–geotechnical aspects. In *Proceedings of the International Symposium on the Frontiers in Offshore Geotechnics: ISFOG 2005*. Taylor and Francis Perth, Australia.

Zhang, J., Randolph, M. F., and Stewart, D. P. (1999). An elasto-plastic model for pipe–soil interaction of unburied pipelines. In *Proceedings of the Ninth (1999) International Offshore and Polar Engineering Conference*, Brest, France. International Society of Offshore and Polar Engineers.

Zhang, J., Stewart, D. P., and Randolph, M. F. (2001a). Centrifuge modelling of drained behaviour for pipelines shallowly embedded in calcareous sand. *International Journal of Physical Modelling in Geotechnics*, 1:25–39.

Zhang, J., Stewart, D. P., and Randolph, M. F. (2002a). Kinematic hardening model for pipeline–soil interaction under various loading conditions. *The International Journal of Geomechanics*, 2(4):419–446.

Zhang, J., Stewart, D. P., and Randolph, M. F. (2002b). Modeling of shallowly embedded offshore pipelines in calcareous sand. *Journal of Geotechnical and Geoenvironmental Engineering*, 128(5):363–371.

Zhang, W., Wang, J., and Jiang, M. (2013). DEM-aided discovery of the relationship between energy dissipation and shear band formation considering the effects of particle rolling resistance. *Journal of Geotechnical and Geoenvironmental Engineering*, 139(9):1512–1527.

Zhang, Z. P., Liu, L. F., Yuan, Y. D., and Yu, A. B. (2001b). A simulation study of the effects of dynamic variables on the packing of spheres. *Powder Technology*, 116(1):23–32.

Zhu, H. P., Zhou, Z. Y., Yang, R. Y., and Yu, A. B. (2007). Discrete particle simulation of particulate systems: theoretical developments. *Chemical Engineering Science*, 62(13):3378–3396.

Zhu, H. P., Zhou, Z. Y., Yang, R. Y., and Yu, A. B. (2008). Discrete particle simulation of particulate systems: a review of major applications and findings. *Chemical Engineering Science*, 63(23):5728–5770.